Antiproton reactions at 6 and 9 geV/c

Nigel Butler

ANTIPROTON   REACTIONS   AT   6   AND   9   GeV/c

A   thesis   presented

by

Nigel   Butler   B.A.

for   the

Degree   of   Doctor   of   Philosophy

at   the

University   of   Durham

June   1982

ABSTRACT

Interactions of antiprotons on protons at 6 and 9 GeV/c are investigated from a 520K picture exposure at the SLAC Hybrid Facility, using a baryon-exchange trigger. Double-differential cross-sections are presented for the inclusive processes $\bar{p}p \rightarrow \pi^{\pm}X$, and fits are made to the statistical thermodynamic model of Hagedorn and Hoang, where the shortcomings of the model are pointed out. Cross-section data are also given for exclusive annihilation channels.

In the channel $\bar{p}p \rightarrow \pi^{+}\pi^{+}\pi^{-}\pi^{-}$ copious production of ρ and f mesons is observed. A Van Hove analysis indicates that:(i) there is a pronounced "leading particle" effect; (ii) resonances are favourably produced in the central region; (iii) there is associated production of resonances; and (iv) Δ exchange makes only a small contribution. Two simple amplitude models incorporating these features are proposed and compared : one where the dominant process is a leading pion recoiling from a loose "cluster" of pions; in the other, where both vertices produce peripheral pions, with a centrally produced resonance. The latter model is found to describe the data much better. Figures for spin-density matrices and cross-sections are given and compared with previous data.

Preliminary results of a search for narrow exotic mesons are given. For this, data taken with a deuterium target (amounting to 566K pictures) is also used. Upper cross-section limits are given for inclusive processes. A number of narrow effects are reported in exclusive channels, the most significant being in the channel $\bar{p}p \rightarrow p_{f}\bar{n}\pi^{+}\pi^{-}\pi^{-}$ where a 6 standard deviation enhancement in the $p_{f}\bar{n}$ mass is seen at 2.02 GeV/c^2, the mass of a previously found state. The cross-section is greater than 1 μb and the width is consistent with resolution (20 MeV/c^2). Initial indications are that this state is also produced centrally.

"The Shepherds, I say, whose names were Knowledge, Experience, Watchful, and Sincere, took them by the hand, and had them to their tents, and made them partake of that which was ready at present. They said, moreover, We would that you should stay here awhile, to be acquainted with us, and yet more to solace yourselves with the good of these Delectable Mountains ... .

Then I saw in my dream, that in the morning the Shepherds called up Christian and Hopeful to walk with them upon the mountains. So they went forth with them, and walked a while, having a pleasant prospect on every side. Then said the Shepherds one to another, Shall we show these pilgrims some wonders? . So, when they had concluded to do it, they had them first to the top of a hill called Error, which was very steep on the farthest side, and bid them look down to the bottom. So Christian and Hopeful looked down, and saw at the bottom several men dashed all to pieces by a fall that they had from the top. Then said Christian, What meaneth this?... .

Then I saw that they had them to the top of another mountain, and the name of that is Caution, and bid them look afar off; which when they did, they perceived, as they thought, several men walking up and down among the tombs that were there: and they perceived that the men were blind, because they stumbled sometimes upon the tombs, and because they could not get out from among them. Then said Christian, What means this?".

from "The Pilgrim's Progress" by John Bunyan

CONTENTS

CHAPTER 2 : THE SLAC HYBRID FACILITY

CHAPTER 3 : DATA PROCESSING

CHAPTER 4 :

ACCEPTANCE CONSIDERATIONS AND DETERMINATION OF CROSS-SECTIONS

CHAPTER 5 : THE FOUR PION FINAL STATE

CHAPTER 6 : SEARCH FOR NARROW MESON STATES

LIST OF FIGURES

LIST   OF   TABLES

LIST OF TABLES (Cont.)   Page

INTRODUCTION AND OUTLINE OF THESIS

This thesis describes an experiment (BC68) to investigate $\bar{p}N$ interactions at 6 and 9 GeV/c and, in particular, the analysis carried out by the author on the data obtained. The experiment was performed at Stanford Linear Accelerator Centre (SLAC) using the SLAC Hybrid Facility (SHF) and was in two phases, Phase I in April 1978, using a hydrogen target; and Phase II in March-June 1979, partly with hydrogen and partly with deuterium. Six collaborating laboratories were involved: Imperial College, London; the Rutherford Laboratory, U.K.; CEN Saclay, France; SLAC, California; Tohoku University, Japan; and Tufts University, Massachusetts. The work for this thesis was done in association with the Rutherford Laboratory.

The main purpose of the experiment was to search for exotic meson states, especially the kind known as "baryonium". There are theoretical predictions for such states and, within the context of the quark model, their existence would imply that quark structures other than $q\bar{q}$ and qqq (for normal mesons and baryons) are possible. They should be most readily observed in the baryon-antibaryon system, where indeed a number of candidates has already been found by previous experiments. However, much of the evidence is contradictory, and this experiment was proposed in order to clarify the situation.

In a production experiment, baryonium should be best observed in reactions proceeding via baryon-exchange. To suppress the more usual meson-exchange interactions, a trigger was used in the BC68 experiment. This accepted only events with a forward going π^+, π^-, K^+, or proton with laboratory momentum greater than 2.5 (4.0) GeV/c at incident momentum of 6.1 (8.9) GeV/c respectively. In this way, annihilation reactions were enhanced by the meson-triggered events, providing

opportunity to observe baryonium produced centrally or at the bottom (proton) vertex; while the proton-triggered events are very promising candidates for baryonium produced at the top (antiproton) vertex (since protons are normally only produced backwards relative to the incident antiproton).

Because of the baryon-exchange trigger there is a plentiful supply of annihilation events, valuable for alternative physics analyses, independent of baryonium. The processes involved in annihilations are still poorly understood, and here two specific phenomenological models are investigated in the light of data from inclusive differential cross-sections and from the particular channel $\bar{p}p \rightarrow \pi^+\pi^+\pi^-\pi^-$. Complications are encountered because of the limited acceptance of the apparatus, and these are considered in some detail. Since a very pure sample of events is needed for the baryonium search, it has taken a considerable time to achieve the necessary degree of refinement, and it is only possible to present the initial findings here. However, for the alternative physics mentioned above, a more thorough investigation has been made.

The first chapter describes the theoretical and experimental background of baryonium physics. The second chapter gives details of the SLAC Hybrid Facility, the beam, trigger, and the data-taking. Chapter 3 pursues the subsequent analysis from scanning and measuring through to the stage of a Data Summary Tape, with detailed descriptions of the optical system of the bubble chamber and of the downstream Cerenkov detector, as these provide essential information for the off-line analysis.

The fourth chapter gives details on cross-section normalisation and acceptance corrections. Double-differential cross-section results are presented for inclusive data and for exclusive annihilation channels.

The former are fitted to the statistical thermodynamic model of Hagedorn

and Hoang. In chapter 5 there is a brief review of annihilation

mechanisms, and a summary of previous work on the four pion final

state, with comprehensive references. This is followed by a detailed

investigation of this reaction from the present data, and the fitting

to two variants of an amplitude model. The sixth and final chapter

deals with the baryonium search and presents the preliminary findings

for inclusive, central, and exclusive processes.

This thesis is generally concerned only with data taken with a

hydrogen target, the exception being in the last chapter where some

results from deuterium reactions are recorded.

CHAPTER 1

EXOTIC MESONS AND BARYONIUM

In this Chapter, a brief overview of the current status of baryonium physics is presented. More detailed reviews of the subject are readily available (e.g. ref. 1.1), and many papers (theoretical and experimental) have appeared in the last decade, during which there has been a significant reappraisal of the subject. Here, the pertinent features are highlighted, notably where the predictions and observations can be investigated in the present experiment (as described in Chapter 6). The first part of the Chapter deals with the theoretical aspects, and then the experimental situation is summarised, followed by a discussion.

1.1 EXOTIC PARTICLES

In the quark model, all well-established hadrons are described by the simplest of quark structures; baryons are composed of three quarks (qqq) and mesons are composed of one quark and one anti-quark ($q\bar{q}$). Limitations on the allowable quark combinations are imposed by attributing the quarks with a property called "colour", with the rule that all observable (i.e. free) particles are colour singlets. This ensures that all free particles have integral charge, baryon number and strangeness. In particular, no free quarks are allowed. Nevertheless, more complex colour singlet combinations are allowed, such as

$$qq\bar{q}\bar{q} \qquad \text{exotic meson}$$

$$qqqq\bar{q} \qquad \text{exotic baryon}$$

$$qqq\bar{q}\bar{q}\bar{q} \qquad \text{exotic meson}$$

$$qqqqqq \qquad \text{dibaryon}$$

Such particles are called "exotic". The first and third combinations have baryon number zero, and so are called exotic mesons and these are

the only exotic states considered here. Some states may be explicitly exotic, that is, they have quantum numbers unobtainable for the "normal" particles: such as a doubly charged meson, or a strangeness +1 baryon. Other states may not be explicitly exotic and so will be difficult to distinguish from normal particles.

Within the current theory of the quark model and of strong interactions, there is no binding reason why exotic states should not exist. Indeed, in one development of the theory, their existence is required, as will now be described.

1.2 PREDICTION OF $q\bar{q}q\bar{q}$ STATES FROM DUALITY

Two-component duality is a property based on finite-energy sum rules in Regge theory. Amongst its predictions are the exchange degeneracy of the ρ, f^o, ω and A_2 mesons, and the mixing angle of the octet and singlet states in the ω meson. Clearly, it is a powerful tool that one would not wish to abandon.

In 1968 Rosner (ref. 1.2) showed that duality led to the prediction of "mesons" decaying mainly into a baryon (B) and an anti-baryon ($\bar{B}$). Harari (ref. 1.3), in 1969, derived the same prediction by his invention of duality diagrams, which show the continuity of quarks throughout an interaction. As an example, the case of $\pi\pi \rightarrow KK$ scattering is illustrated in figure 1.1 (a) by Harari-Rosner duality diagrams. According to two-component duality, the amplitude for an interaction is completely determined by knowledge of either all directly produced resonances in the s-channel, or Regge pole exchanges in the t-channel. Thus, in figure 1.1(a), we say that the s-channel resonances (e.g. the ρ meson) are dual to the t-channel resonances (K*), and the existence of one implies the existence of the other. For meson-meson and meson-baryon scattering there is no difficulty; however, consider now the case of $B\bar{B}$ scattering (fig. 1.1 (b)).

5
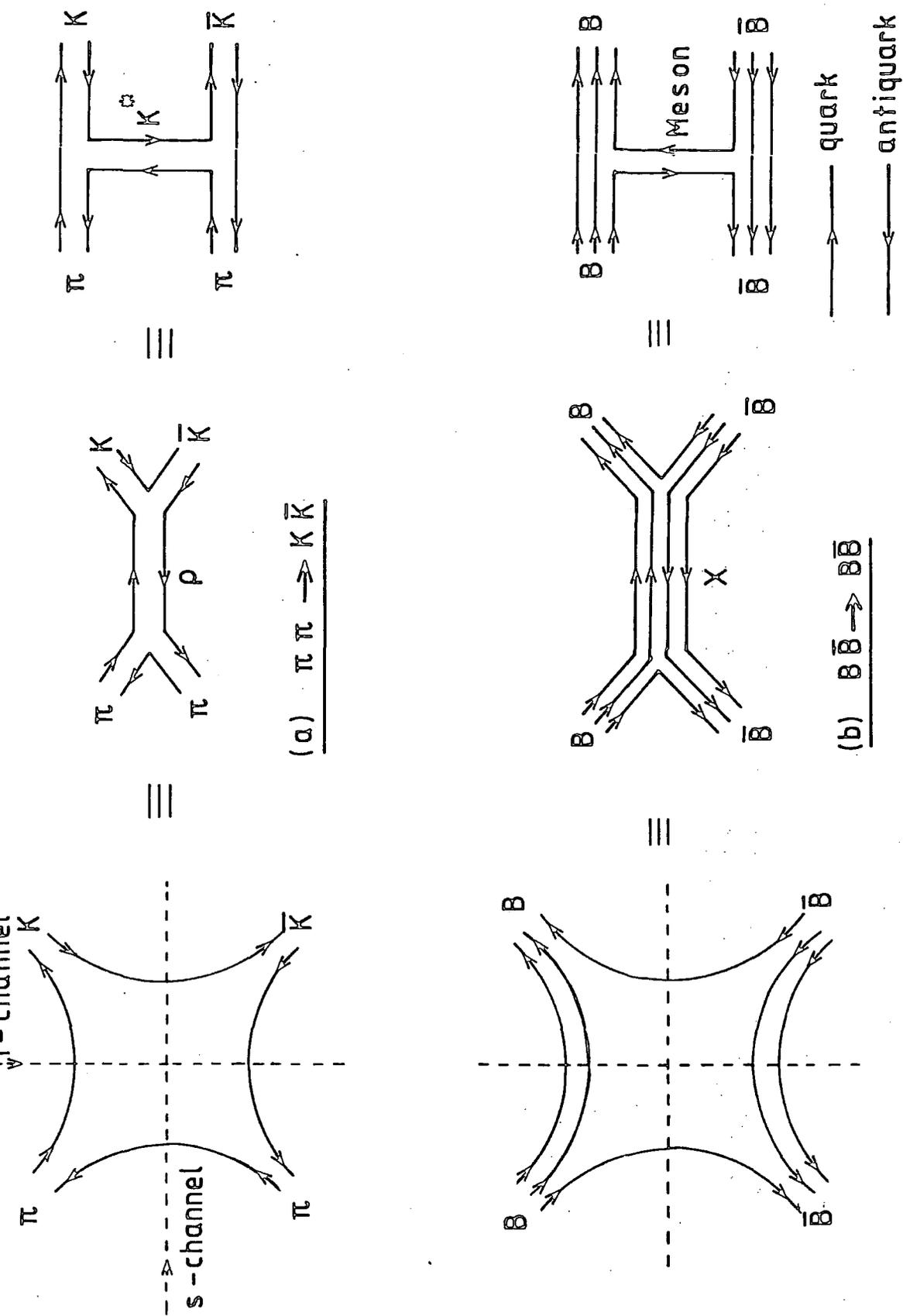
Fig. 1.1   Duality diagrams

In the s-channel we have a $q\bar{q}q\bar{q}$ state, dual with normal mesons in the t-channel. Furthermore, the four quark state is expected to couple strongly to $B\bar{B}$, both in formation and decay.

1.3 PREDICTION OF BOUND $N\bar{N}$ STATES FROM NUCLEAR PHYSICS

In an independent line of research, Shapiro and co-workers (refs. 1.4 - 1.6) have shown that nuclear physics leads to the prediction of non-relativistic bound $N\bar{N}$ states, appearing as heavy mesonic resonances. The nucleon (N) and antinucleon ($\bar{N}$) are considered to be confined in a nuclear potential, such as the two nucleons of the deuteron (NN). Interaction is via normal meson exchange (such as π) over a range $\sim \hbar/mc$ where m is the mass of the exchanged particle. Unlike the deuteron, there is the possibility of annihilation occuring, via baryon exchange; but over a much shorter range because of the heavier mass of baryons compared with the pion (this being the predominant meson exchanged). In the potential model, it is generally assumed that there is an orbital angular momentum between the two constituents, keeping them well separated ("centrifugal barrier") and hence away from the annihilation zone.

Within the context of the quark model, these $N\bar{N}$ states have the quark structure $qqq\bar{q}\bar{q}\bar{q}$ and are therefore classed as exotic. As with the four quark states expected by duality, they would be characterised by decaying mainly in to $B\bar{B}$ rather than into mesons.

1.4 BARYONIUM

The states predicted in sections 1.2 and 1.3 have become known as "baryonium". In the original use of the word, Chew (ref. 1.7) defines baryonium as a particle whose coupling to $B\bar{B}$ channels is substantially larger than to channels made up entirely from normal mesons, and this is the sense used in this thesis. The qualification that coupling to $B\bar{B}$

is larger than to mesons is a crucial one, as some theorists are now claiming that duality may be fulfilled by four-quark states which couple predominantly to mesons (see, for example, ref. 1.8). If baryonium exists there must be some "selection rule" inhibiting its decay to mesons. There have been three main attempts to explain this:

(i)   The well known Okubo-Zweig-Iizuka (OZI) rule has been invoked to explain the suppression of decays such as $\phi \rightarrow$ non-strange mesons (and, more recently, $J/\psi \rightarrow$ non-charmed mesons). This essentially forbids quark diagrams in which the initial and final states are not connected by quark lines. In an attempt to incorporate the baryonium selection rule, Freund, Waltz and Rosner (ref. 1.9) have generalised the OZI rule as follows:

1. No quark line is connected with an antiquark line from the same hadron.

2. Each of the three hadrons meeting at a vertex exchanges at least one quark line with each of the remaining two hadrons.

This effectively forbids crossing quark lines (that is, non-planar diagrams). Figure 1.2 shows the allowed decay into $B\bar{B}$ and the "forbidden" decays to mesons.

(ii) In the nuclear potential model, stability against annihilation is predicted if one neglects the imaginary part of the potential. Whether this is permissible is a matter of some dispute amongst theorists (this is considered in ref. 1.6).

(iii) For high spin states, it is reasonable to expect a significant centrifugal barrier effect. This overrides the point made in (ii), and is also useful in four-quark models in which the two diquarks are separated by an orbital angular momentum, forming a "diquonium".
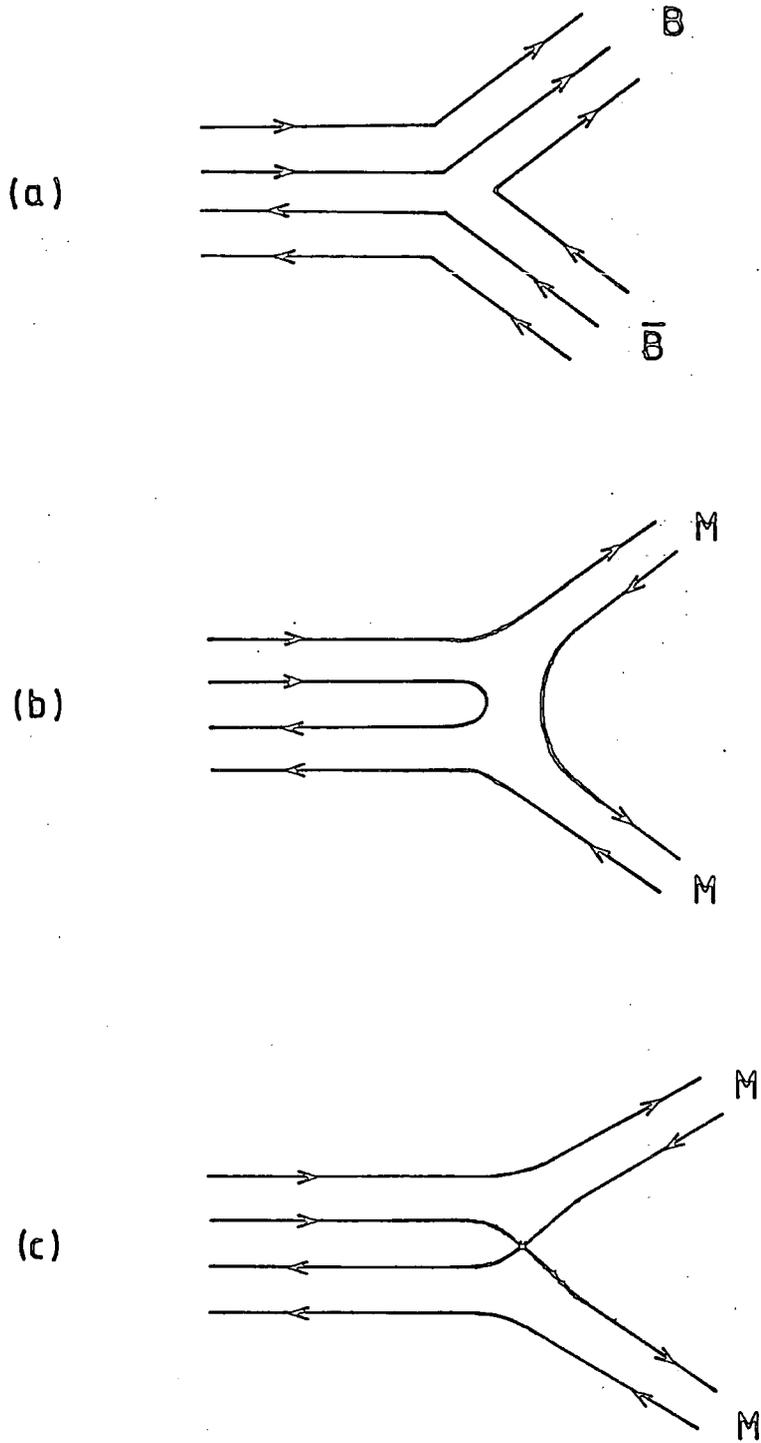
Fig. 1.2   Quark line diagrams showing decays of
a $qq\bar{q}\bar{q}$ state:

(a)   allowed decay to $B\bar{B}$

(b) & (c)   "forbidden" decays to mesons

1.5 MODELS OF qq̄qq̄ STATES

Three particular models of four-quark exotic mesons are now considered.

1.5.1 MIT Bag model

Four-quark states, and baryonium in particular, are readily accommodated by the MIT bag model (ref. 1.10). In the spinless state (fig. 1.3(a)), the two quarks and two antiquarks are confined in a roughly spherical bag. Since a quark and antiquark may group to form a normal meson, the two qq̄ pairs are bound relatively weakly by colour-magnetic forces, and the bag is very prone to fission into two qq̄ mesons.

Considering angular momentum excitations changes the picture dramatically. The bag is now imagined to be long and thin (fig. 1.3 (b)), with the diquark and anti-diquark well separated. The centrifugal barrier inhibits movement of a quark from one end to the other, so decay is predominantly by creation of a qq̄ pair in the middle, producing a baryon and anti-baryon. This is a model for baryonium, and predicts such states to have non-zero (and preferably high) spin. The model is also capable of predicting mass spectra, as many authors have done (e.g. ref. 1.11).

1.5.2 String model

In the string model, the colour flux is simply represented by strings connecting the quarks. Thus, ordinary mesons have one string connecting the quark and antiquark (fig. 1.4 (a)), while baryons have three strings connected at a junction. In the model for baryonium there are two junctions (fig. 1.4 (b)), thus naturally allowing a decay to BB̄.

It has been pointed out (ref. 1.12) that a junction can be considered in some respects like a particle, so that it is conserved in quark line diagrams. The Freund-Waltz-Rosner selection rules may then be replaced by a simpler rule: No internal loops are allowed for quark/junction lines.
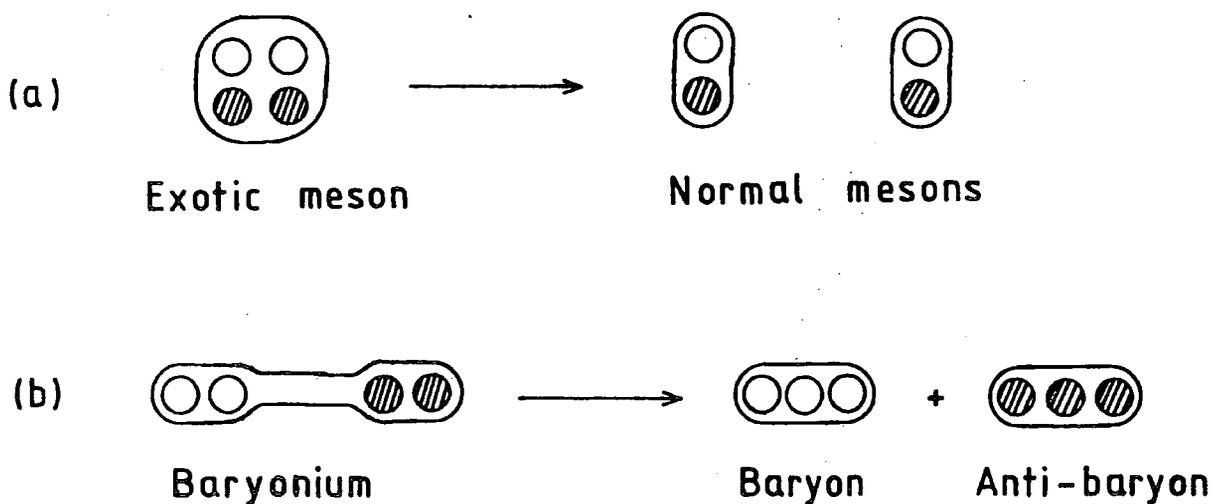
Fig. 1.3   Decays of qqq̄q̄ states in the bag model
(a)   spinless state
(b)   with spin
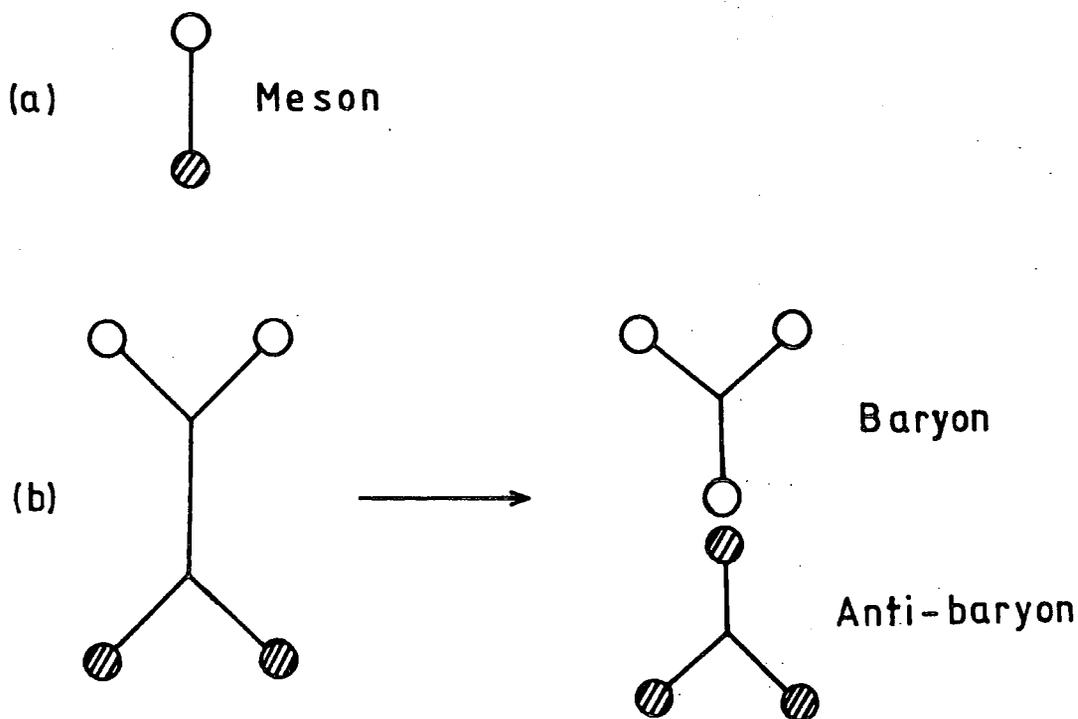
Fig. 1.4   String model pictures for (a) a meson
and (b) baryonium decaying to B B̄

Attempts have been made to derive this junction conservation rule from quantum chromodynamics (QCD) (ref. 1.13). While a mechanism has been found, it can hardly rate as a prediction. Furthermore, the same theory also 'predicts' $q\bar{q}\bar{q}$ states with no junctions, which would decay mainly to the multi-meson channel (see also ref 1.8).

1.5.3 Colour Chemistry

Colour, according to our present understanding, is a fundamental source of force, and is the basis of QCD theory. So called constituent quarks can have one of three colours and are therefore in a colour group 3 (antiquarks being in a $\bar{3}$), and combinations should satisfy the rules of SU(3) group theory. The observable hadrons, being free particles must be in a colour singlet. Thus, we have for mesons and baryons:

$$q\bar{q} \quad : \quad 3 \otimes \bar{3} \quad = \quad 8 \oplus 1$$

$$qqq \quad : \quad 3 \otimes 3 \otimes 3 \quad = \quad 10 \oplus 8 \oplus 8 \oplus 1$$

only the singlet states existing as free particles. Using this colour model, Chan and Hogaasen (ref. 1.14) have shown that certain exotic configurations emerge naturally as observable hadrons. In particular, they consider a "diquonium" state, that is, a diquark bound to an anti-diquark. Diquarks are either in a colour $\bar{3}$ or a 6 :

$$qq : 3 \otimes 3 \quad = \quad \bar{3} \oplus 6$$

giving rise to two kinds of diquonium:

$$q q \bar{q} \bar{q} : 3 \otimes \bar{3} \quad = \quad 8 \oplus 1 \qquad \text{(T-diquonium)}$$

$$\text{or} \quad \bar{6} \otimes 6 \quad = \quad 27 \oplus 8 \oplus 1 \qquad \text{(M-diquonium)}.$$

The combinations $6 \otimes 3$ and $\bar{6} \otimes \bar{3}$ do not correspond to observable particles since there is no singlet state ($6 \otimes 3 = 10 \oplus 8$). The two kinds of diquonium are called T (True) and M (Mock) and are predicted to have

very different properties. This is because colour $\bar{3}$ diquarks can unite with another quark to form a free baryon, whereas colour 6 diquarks can not be so combined (because 6 ⊗ 3 does not give a singlet). Therefore, it is expected that T-diquonium couples strongly to the $B\bar{B}$ channel, whereas M-diquonium can not couple to $B\bar{B}$ except by colour mixing (gluon exchange). The degree of mixing should be less for higher angular momentum states which, in the diquonium model, also have suppressed mesonic decays, thus leading to very narrow decay widths. These high angular momentum states of M-diquonium are also predicted to decay via cascade to lower mass states, and so have a very clear signature.

These ideas concerning quark combinations and the forces between them suggest the possibility of a "colour chemistry", in which many more complex quark structures are allowed. Certainly, the observation of states predicted by this model (e.g. M-diquonium) would be strong evidence that colour is a real quantum number.

1.6 ARE $B\bar{B}$ STATES EXPECTED TO HAVE NARROW DECAY WIDTHS?

If the decay width of a resonance is narrow, compared with typical widths for hadronic processes, it means that the decays are suppressed; either because of kinematic (threshold) effects, or because of genuinely weak couplings to the decay channels. If a resonance in a $B\bar{B}$ state is narrow, this implies that both mesonic decays and baryon-antibaryon decays are suppressed.

Considering mesonic decays, one would expect that threshold effects would play no part, since $B\bar{B}$ states are expected to have a mass around, or greater than, two nucleon masses. However, Karlsson and Kerbikov (ref. 1.15) have claimed that quasi-nuclear $B\bar{B}$ states may exist with strong couplings to the annihilation channels, but with narrow widths, provided such a state is near to several successive decay thresholds. With this exception, the existence of narrow $B\bar{B}$ states requires some

baryonium selection rule, as discussed in section 1.4. Such a rule is readily accommodated by existing theories, but there is no firm prediction (such that the non-existence of narrow states would be inconsistent with theory).

Now considering baryon-antibaryon decays, states are expected with masses near threshold (~ 2 GeV/c^2), and so these would have narrow widths, provided mesonic decays are also suppressed. If narrow states exist at high masses, there must be some mechanism preventing the decay to B$\bar{\text{B}}$. Such a mechanism is provided by the M-diquonium model mentioned in the last section. However, it has been pointed out (ref. 1.16) that, according to QCD, the force between two quarks in a colour 6 state is repulsive in the one-gluon exchange approximation, which would mean that M-diquonium is unstable. Furthermore, Barbour and Ponting (ref. 1.17) find that, using a confining potential model, M-diquonium should have a strong tendency to decay into multimeson final states.

Therefore, the theoretical situation is highly uncertain. The observation of narrow B$\bar{\text{B}}$ states would be of great theoretical significance, especially at high mass: however, the non-observation would not be greatly detrimental to existing theory. It can always be claimed that exotic mesons do exist, but with broad widths and/or decaying predominantly to normal mesons.

1.7 EXPERIMENTAL OBSERVATIONS

1.7.1 Formation experiments

In the wake of the theoretical predictions about baryonium, a number of experiments reported observations of effects which were naturally inter-preted as resonances coupled to B$\bar{\text{B}}$. These were first clearly seen in formation experiments, the most celebrated being the S-meson. The S has been observed in several experiments, with a very narrow width, and is therefore a strong candidate for baryonium. Unfortunately recent experiments

have given conflicting results on the mass, width, and cross-section of

the S, and there is now much uncertainty about the true nature of this

enhancement.

Carroll et al (ref. 1.18) first reported structures in the total

$\bar{p}p$ and $\bar{p}d$ cross-sections, shown in figure 1.5, at a mass of 1932 MeV/c^2.

Similar effects were seen by: Kalogeropoulos and Tzanakos (ref. 1.19) in

the $\bar{p}n$ annihilation cross-section; d'Andlau et al (ref. 1.20) in $\bar{p}p$ back-

ward elastic scattering; Chaloupka et al (ref. 1.21) in $\bar{p}p$ total and

elastic cross-section (shown in fig. 1.6); Brückner et al (ref. 1.22) in

$\bar{p}p$ elastic and charged annihilation cross-section (shown in fig. 1.7);

and Sakamoto et al (ref. 1.23) in the total $\bar{p}p$ cross-section. These

results are given in table 1.1 and, despite some discrepancies, they pro-

vide strong evidence for the existence of the S-meson.

However, no narrow enhancements were observed by Alston-Garnjost et al

in the $\bar{p}p$ charge-exchange cross-section (ref. 1.24), nor in the backward

elastic-scattering cross-section (ref. 1.25). In a later and more sensitive

experiment, Hamilton et al confirmed the absence of a signal in the charge-

exchange channel (ref. 1.26), and cast doubt on the enhancement in the

total $\bar{p}p$ cross-section (ref. 1.27). The cross-section variation is shown

in fig. 1.8(a) and does not display any narrow structure (the results of

Carroll et al are shown by the dashed line). However, if a smooth back-

ground is subtracted (fig. 1.8(b)) a broader and gentle enhancement is

indicated at about the same mass (1939 MeV/c^2) as previous observations.

A similar effect is apparent in the charged annihilation cross-section

(fig. 1.8(c)), where the dashed line represents the results of Bruckner

et al. No structure is seen in the $\bar{p}d$ data.

Clearly, the claims of these experiments are conflicting, particularly

regarding the cross- section of the resonance. A recent experiment by

Kamae et al (ref. 1.28) does not yield any enhancement in the total $\bar{p}p$
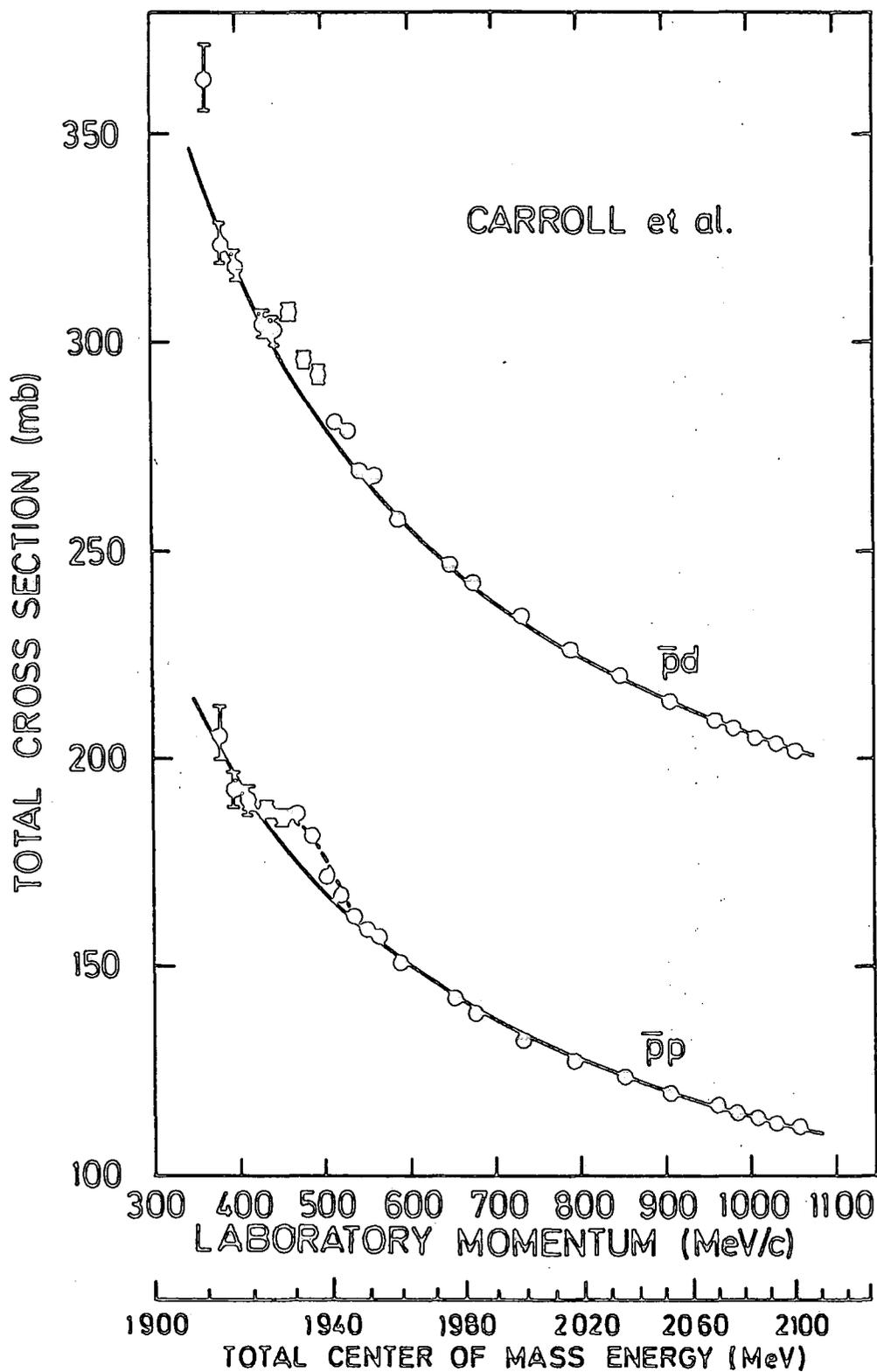
Fig. 1.5   Total cross-sections for p̄p and p̄d (from ref. 1.18).
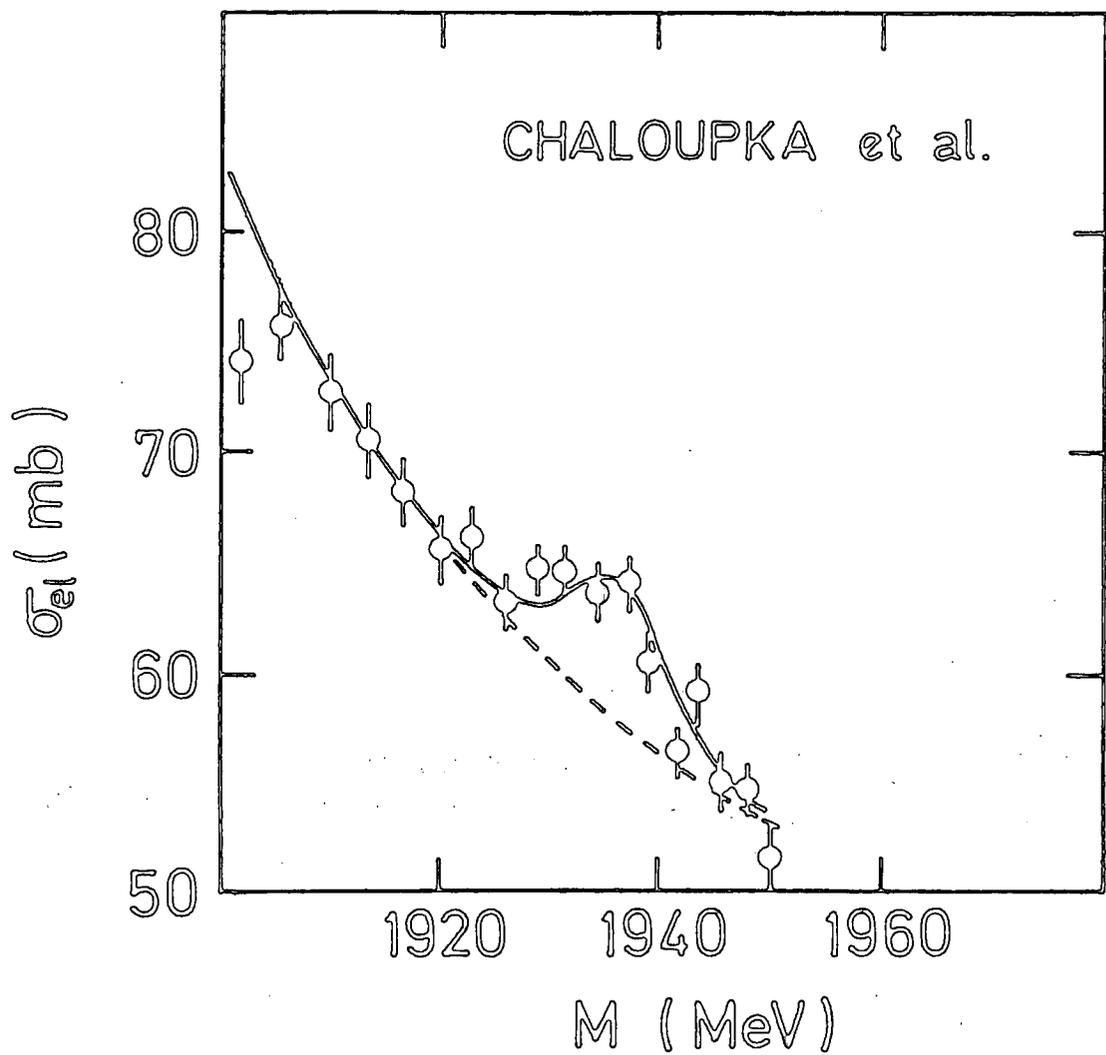
Fig. 1.6 Elastic cross-section for p̄p (ref. 1.21)
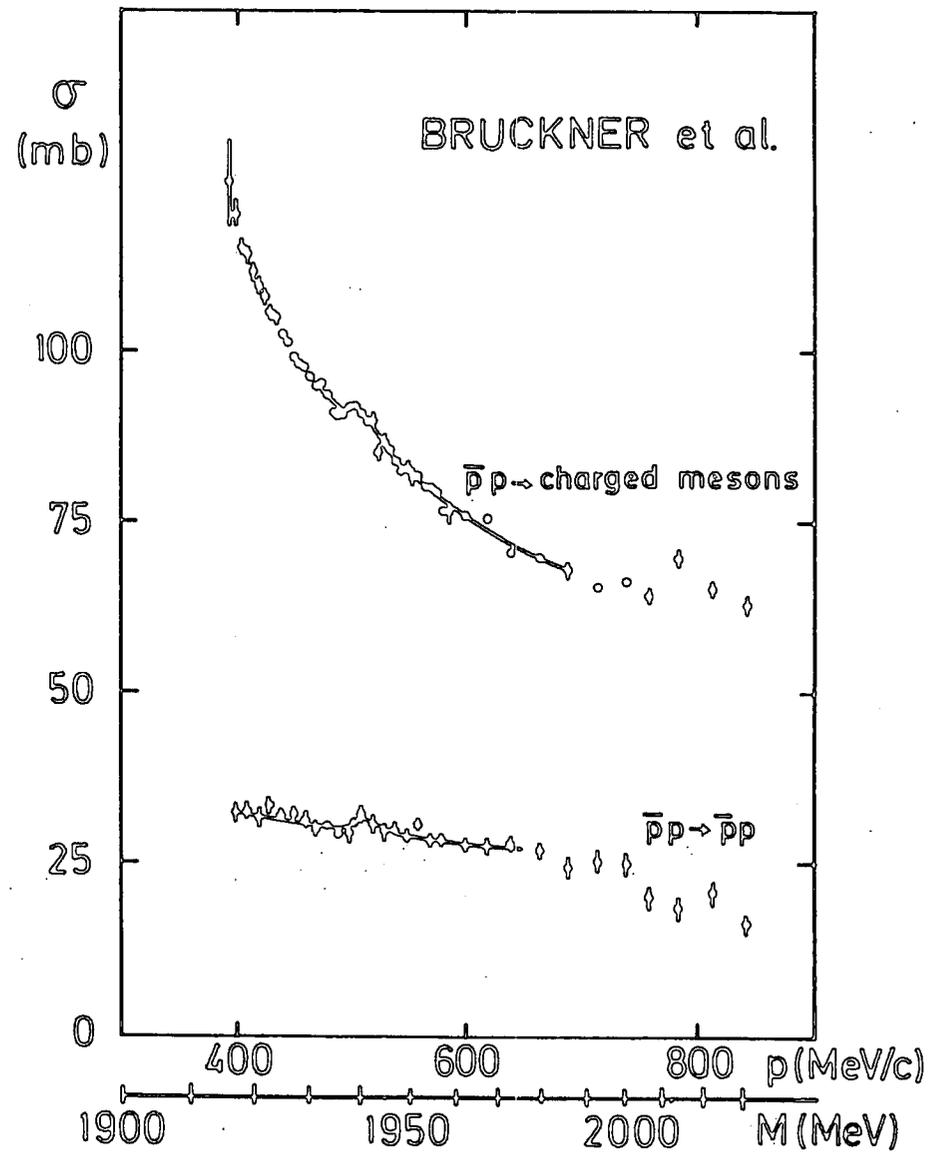
Fig. 1.7 Cross-sections for p̄p charged annihilation
and p̄p elastic (ref. 1.22).
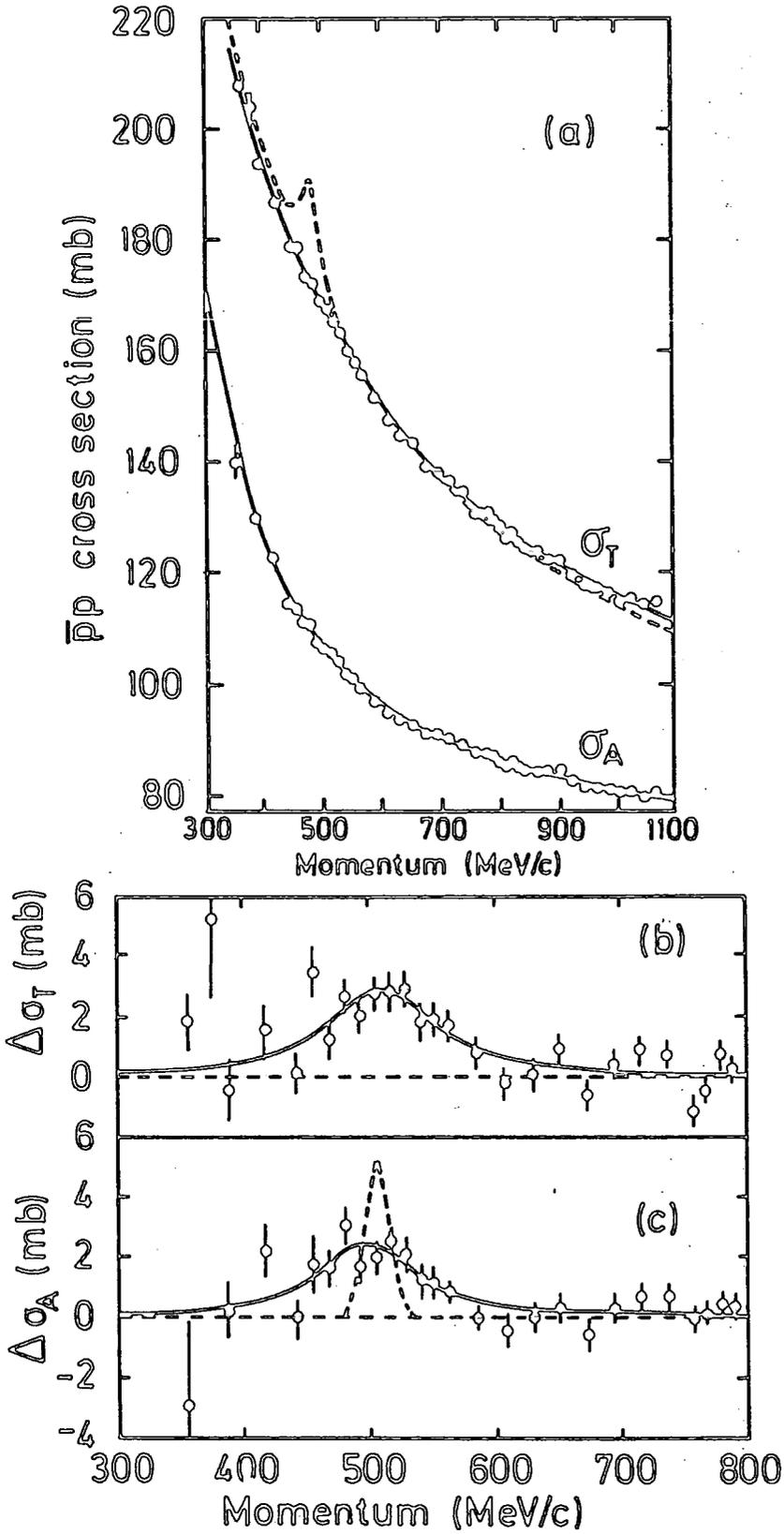
Fig. 1.8 (a) The p̄p total and charged annihilation cross-sections

(b) The background-subtracted total cross-section

(c) The background-subtracted charged annihilation cross-section (ref. 1.27).

TABLE 1.1   NEAR-THRESHOLD $\overline{N}N$ STATES SEEN IN FORMATION EXPERIMENTS

Mass (MeV/c^2)	Γ (MeV/c^2)	Reactions	$\Delta\sigma$ (mb)	Reference
1932 $\pm$ 2	9 $^{+4}_{-3}$	$\overline{p}p$ total $\overline{p}d$ total	18 $^{+6}_{-3}$	Carroll et al (1.18)
1932 $^{+2.4}_{-0.4}$	4.5 $\pm$ 4	$\overline{p}n$ total	–	Kalogeropoulos et al (1.19)
1942 (split)	57.5 $\pm$ 5	$\overline{p}p$ backward elastic	$\sim$ 5	d'Andlau et al (1.20)
1936 $\pm$ 1	9 $^{+4}_{-3}$	$\overline{p}p$ total $\overline{p}p$ elastic	10.6 $\pm$ 2.4 7.0 $\pm$ 1.4	Chaloupka et al (1.21)
1939 $\pm$ 3	$\lesssim$ 4	$\overline{p}p$ elastic $\overline{p}p$ charged annih.	4 $\pm$ 2 9 $\pm$ 2 (total)	Bruckner et al (1.22)
1936 $\pm$ 1	2.8 $\pm$ 1.4	$\overline{p}p$ total	14.5 $\pm$ 3.9	Sakamoto et al. (1.23)
1939	22 $\pm$ 6	$\overline{p}p$ total $\overline{p}p$ charged annih.	3 $\pm$ 0.7	Hamilton et al (1.27)
1949 $\pm$ 10	80 $\pm$ 20	$\overline{p}p \rightarrow 5\pi$	5.5 $\pm$ 1.5	Defoix et al. (1.30)

cross-section; while a report by Jastrzembski et al (ref. 1.29) does not claim any evidence for the S-meson, despite apparent structure in their total cross-section measurements at about 1937 MeV/c^2. Finally, an s-channel resonance has been observed by Defoix et al (ref. 1.30) in the reaction $\bar{p}p \rightarrow 2\pi^+ 2\pi^- \pi^o$, shown in figure 1.9. The peak is at rather too high a mass (1949 MeV/c^2) and is too wide (80 MeV/c^2) to be identified with the S-meson. Nevertheless, the effect is clearly significant.

The narrowness of the S-meson is not unexpected, as it is close to the N$\bar{\text{N}}$ threshold. Broader structures have been seen at higher masses, named the T and U mesons to indicate they are in the same sequence. As with the S, they have been observed by a number of experiments as gentle wiggles in the cross-section curve. The peaks are more pronounced after subtracting a smooth background curve (fig. 1.10); they have normal hadronic widths and are centred on about 2190 and 2350 MeV/c^2 respectively. More details are given in ref. 1.1.

1.7.2 Production experiments

Production experiments provide good hunting ground for exotic particles; especially since, unlike formation experiments, it is possible to detect off-mass-shell annihilations, and explicitly exotic states.

The S-meson has not been convincingly observed in production. A claim by Daum et al (ref. 1.32) for a 4 standard deviation peak at 1940 MeV/c^2 in

$$pp \rightarrow \bar{p}p + X$$
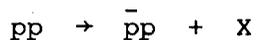
was effectively nullified when the same experimenters repeated the experiment with 20 times more events, using a beryllium target instead of hydrogen (ref. 1.33); no enhancement was observed. Upper cross-section limits for S-meson production have been given by two experiments:

$pp \rightarrow pp\bar{p}p$ at 11.75 GeV/c, $\sigma < 10$ nb   (ref. 1.34)

$\pi^+ p \rightarrow (\bar{p}p)_f \Delta^{++}$ at 9.8 GeV/c, $\sigma < 20$ nb   (ref. 1.35)

Fig. 1.9   The cross-section for $\bar{p}p \to 2\pi^+2\pi^-\pi^o$ multiplied by the $\bar{p}$ incident momentum plotted against the C.M. energy (ref. 1.30).
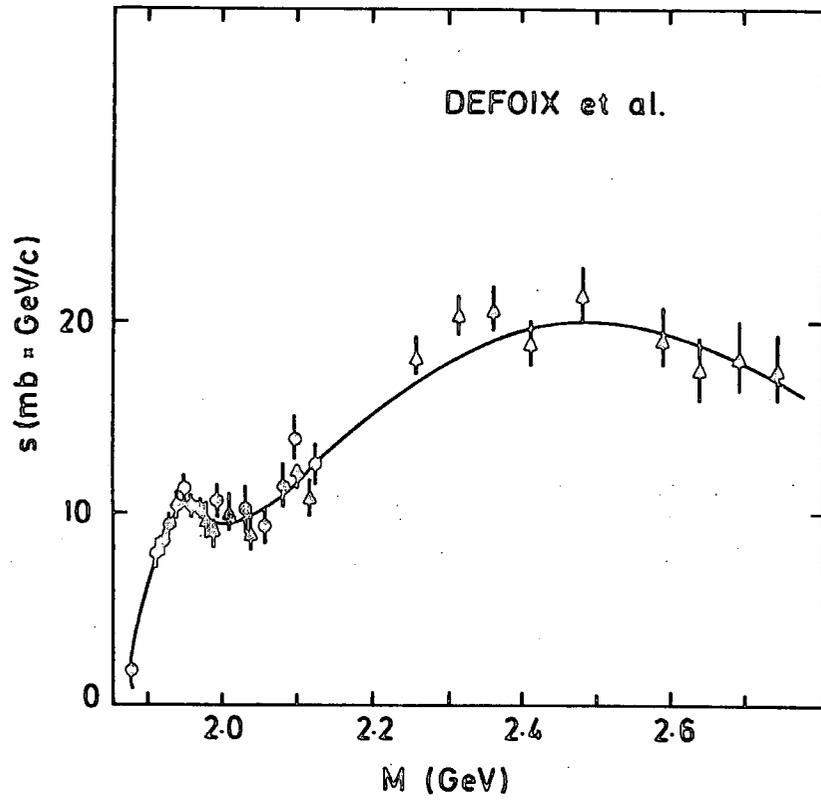
Fig. 1.10   The $\bar{p}p$ elastic cross-section with a smooth background-subtracted, in the T, U region (ref. 1.31).

DEFOIX et al.

s (mb ¤ GeV/c)

M (GeV)

Lab. momentum GeV/c

EISENHANDLER et al.

$\bar{p}p$ elastic cross-section (background subtracted) mb

Mass GeV
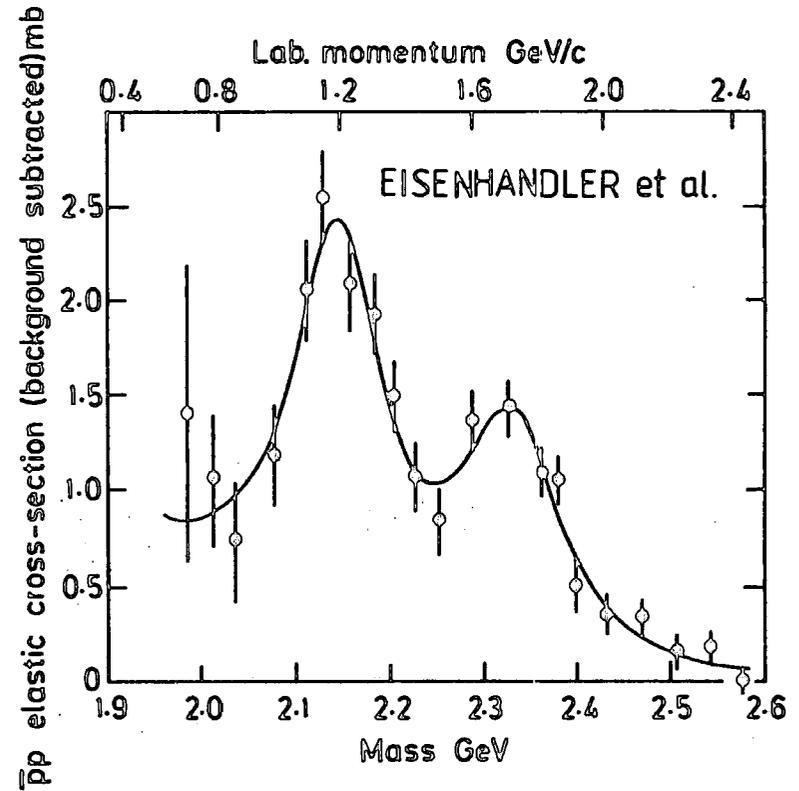
However, resonant-like structure has been seen in inclusive $\bar{p}p$ photo-production with mass 1930 ± 2 MeV/c^2 and width 12 ± 7 MeV/c^2 (ref. 1.36). As with formation, the experimental status of the S in production experiments needs further clarification.

Of the other narrow peaks found in production, the strongest candidates are the 2020 and 2204 MeV/c^2 states observed by Benkheiri et al (ref. 1.37). These were seen in the channel $\pi^- p \rightarrow p_f \pi^- \bar{p}p$ at 9 and 12 GeV/c, where p_f is the fast forward proton which triggered the apparatus. The narrow peaks appear in the $\bar{p}p$ mass spectrum, and are enhanced (to about 7 standard deviations above background) by selecting events with a $p_f \pi^-$ mass in the range of the Δ^0 (1232) or N* (1520). The peaks are further enhanced by selecting the backward part of the decay angular distribution in the $\bar{p}p$ rest frame (fig. 1.11). If genuine, this would be evidence for baryonium resonances, produced by baryon exchange, and in association with a forward Δ^0 or N*. Details of the 2020 and 2204 MeV/c^2 states are given in table 1.2. A state of mass 1930 MeV/c^2 is also indicated, but is not statistically significant.

TABLE 1.2   PROPERTIES OF THE 2020 AND 2204 MeV/c^2 STATES (ref. 1.37)

Mass (MeV/c^2)	2020 ± 3	2204 ± 5
Width (MeV/c^2)	24 ± 12	$16 ^{+20}_{-16}$
$\sigma(\pi^- p \rightarrow \Delta^0 M)$ (9 GeV/c	18 ± 5	17 ± 5
(nb) (12 GeV/c	10 ± 4	21 ± 5
$\sigma(\pi^- p \rightarrow N^* M)$ (9 GeV/c	30 ± 12	–
(nb) (12 GeV/c	26 ± 8	–

No peaks were found in the $\bar{p}p \pi^-$ mass from the same reaction, nor in the $\bar{p}n$ mass in the reaction $\pi^- p \rightarrow p_f \bar{p}n$ (ref. 1.38) from which the authors conclude that nucleon exchange dominates over Δ exchange. This is confirmed by Pennington (ref. 1.39) on theoretical grounds who also predicts cross-sections for the M (2.02) and M (2.20) states to be found in other experiments, including the present $\bar{p}p$ experiment.

Fig. 1.11 The distribution of p$\bar{\text{p}}$ mass decaying
           backwards, and produced in association with
         a Δ^O, for π$^-$p at 9 and 12 GeV/c
           (ref. 1.37).
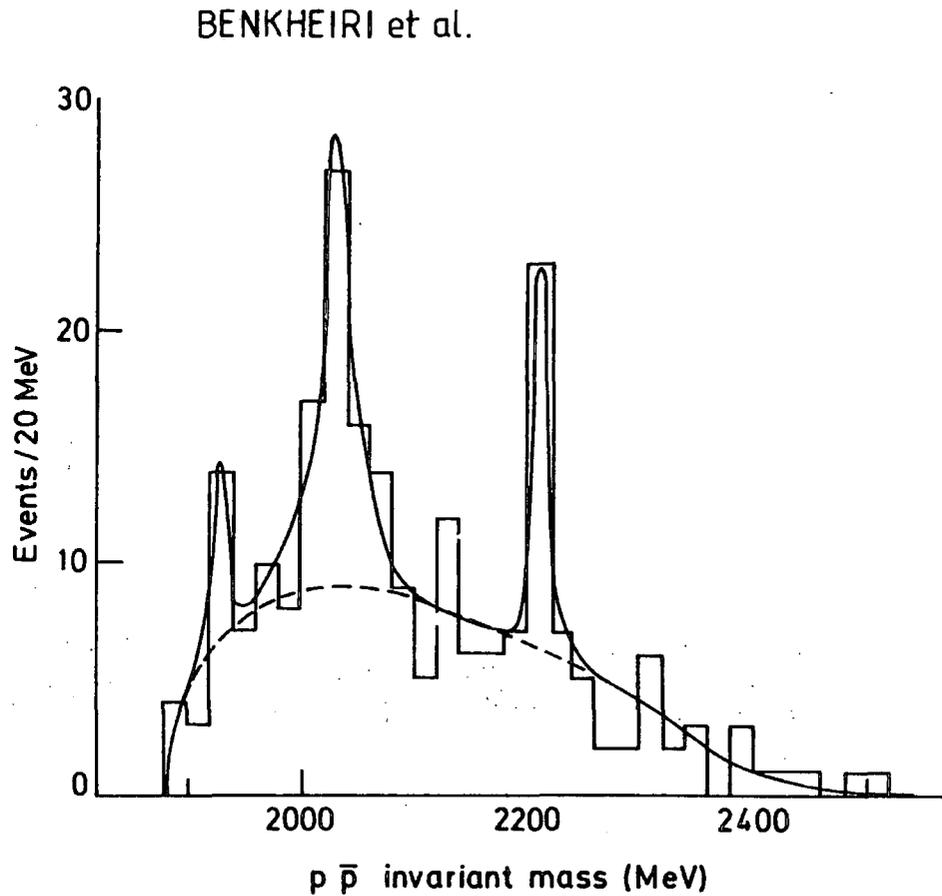
Fig. 1.12 The $\bar{\text{p}}$p mass decaying backwards produced
           in association with Δ^O + N*,
           for π$^-$p at 16 GeV/c (ref. 1.38).
           The dashed curve is from the previous
           figure.

BENKHEIRI et al.
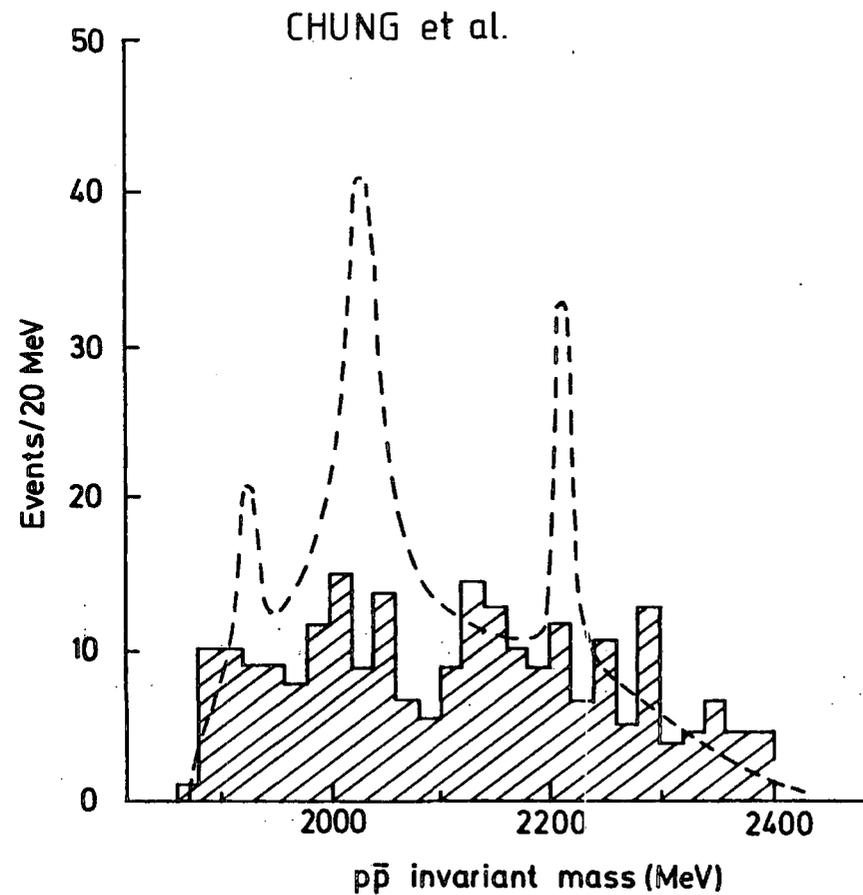
CHUNG et al.

Unfortunately, the experimental results since Benkheiri et al have

been overwhelmingly negative. In particular, Chung et al (ref. 1.40)

have essentially repeated the experiment, though using different apparatus

and a higher beam momentum (16 GeV/c). Their results, shown in fig. 1.12,

do not indicate any significant structure. Assuming a cross-section vary-

ing as $p_{lab}^{-2.5}$ (typical of baryon-exchange processes), the effects seen

by Benkheiri et al would appear as >5 standard deviations. Cross-section

limits at the 95% confidence level are of the order of 3 nb. In another

$\pi^- p$ experiment at 8.1 GeV/c, Carroll et al (ref. 1.41) see no structure in

the $\bar{p}p$ mass spectra produced inclusively, and give upper cross-section

limits of 46 and 71 nb for the 2.02 and 2.20 GeV/c^2 states respectively

(no specific decay mode required for the associated Δ or N^*).

Evangelista et al (ref. 1.42) have examined the reaction

$\pi^- p \rightarrow \bar{p}p_f \pi^- p$ at 10 GeV/c and do not observe any peaks in the $\bar{p}p_f$

spectrum, even after selecting an associated Δ^0 or N^*. However, this is

perhaps to be expected, as Benkheiri et al saw no peaks in $\bar{p}p_f$, and such

a state would have to be coupled strongly to mesons as well as to $\bar{p}p$ (it

being produced at the top vertex).

In other types of interaction, the evidence is likewise conflicting:

Gibbard et al (ref. 1.43) have observed weak (3 s.d.) effects in the $\bar{p}p$

mass at 2.02 and 2.20 GeV/c^2 in virtual photoproduction; and Green

(ref. 1.44) has reported an enhancement at 2207 MeV/c^2 in $\bar{p}p \rightarrow \pi_f^+ X^-$

at 6 GeV/c (the effect seems to be mainly connected with the $\pi^- K^+ K^-$

system, but the claim has not been subsequently confirmed). Other results

are negative: Banks et al (ref. 1.45) have observed no narrow structures

in the $\bar{p}p$ mass produced in $\bar{p}p$ interactions at 12 GeV/c with a fast proton

or K^+. The cross-section limit is 40 nb (99.6% confidence level), compared

with the prediction of 100 $\pm$ 40 nb from ref. 1.39. Finally, Bionta et al

(ref. 1.46) have looked at the $\bar{p}p$ system recoiling off a forward Δ^{++} in π^+p interactions at 9.8 GeV/c. Assuming nucleon exchange, they predict cross-sections for the 2.02 and 2.20 GeV/c^2 states from isospin consider-ations. They would appear as >11 s.d. enhancements in the $\bar{p}p$ mass; but nothing is seen.

Many other baryonium candidates have been reported in the literature; some of the outstanding ones are listed in table 1.3. None of these states have been substantiated by other experiments.

TABLE 1.3. SOME BARYONIUM CANDIDATES SEEN IN PRODUCTION EXPERIMENTS

Mass (GeV/c^2)	Width (MeV/c^2)	Reaction	State, X	Reference
2.08	110	$\pi^-d \to n_s n\ X$ $\pi^-d \to p_s \pi^- n\ X$	$\bar{p}p$ "	1.47
2.85 3.05	<39 <20	$\bar{p}n \to \pi^-\ X$	$\bar{N}N,\ \bar{N}N\pi$	1.48
2.235	200	$K^-p \to p\ X^-$	$\Lambda\bar{p}$	1.49
2.26, 2.32 2.49	broad	$K^+p \to p\ X^+$ $K^-p \to p\ X^-$	$\bar{\Lambda}p$ $\Lambda\bar{p}$	1.50
1.92, 2.02 2.11, 2.26	broad	$\pi^-p \to n\ X$	$\bar{p}p$	1.54

It is worth noting, as a precaution, that several narrow effects have been observed of high statistical significance, which have disappeared with subsequent higher statistics: a $K^o\pi\pi$ state at 2.6 GeV/c^2 (ref. 1.51); a $\bar{p}p\pi^-$ state at 2.95 GeV/c^2 (ref. 1.52); and $\bar{\Lambda}\ \Delta^{++}$ (1232) and $\bar{\Sigma}^+$ (1385) p states at 2.46 GeV/c^2 (ref. 1.53). Statistical anomalies

are a particular problem in searches for narrow states, and any such
observations should be assessed in terms of the number of histograms
scanned, and the recurrence of effects at the same mass in different
histograms.

1.8   THE ROLE OF THE PRESENT EXPERIMENT

The present experiment is aimed specifically at investigating narrow
meson states, such as those described above. The use of an antiproton
beam has a great kinematic advantage over meson beams : simply because of
the masses of the particles involved, the square of the four-momentum
transfer from beam to an outgoing meson reaches positive values and is
substantially nearer to the exchanged baryon pole than for meson beams
(favourable t_{min} effect), resulting in much larger cross-sections for
baryon-exchange processes. This is illustrated by Pennington's cross-
section predictions for the 2020 and 2204 MeV/c^2 states of ref. 1.37 to
be seen in the present experiment:

				M (2020)	M(2204)
$\bar{p}p$	$\rightarrow$	π^- M$^+$		6 GeV/c	6.0 $\pm$ 2.5 μb	14.7 $\pm$ 7.2 μb
		$\hookrightarrow$ $\overline{NN}$	9 GeV/c	1.1 $\pm$ 0.5 μb	2.5 $\pm$ 1.2 μb

(ref. 1.39).

These cross-sections are 2 to 3 orders of magnitude higher than those given
in the original $\pi^- p$ experiment.

The choice of beam momenta (6 and 9 GeV/c) is highly suitable for
investigating baryonium states in the mass range 2 to 3.5 GeV/c^2, which is
the band favoured by most theorists in their mass spectra predictions, and
is where most observations have so far been made. The trigger on a fast,
forward meson or proton is mainly to reduce background from normal meson-
exchange processes, which frequently have a fast outgoing antiproton.

A large part of the data was taken with a deuterium target. This enabled the detection of explicitly exotic states, e.g. $\bar{p}d \rightarrow p_s \pi^+ X^{--}$. While the experiment is mainly aimed at observing baryonium states, it is also highly suitable for detecting narrow resonances decaying to mesons.

1.9 SUMMARY AND OUTLOOK

An outstanding problem in hadron physics is the need for four-quark states to build meson exchange in the standard duality scheme. However, the properties of these states are by no means certain. They may not be narrow, as was initially expected, and some theorists (e.g. Gavai and Roy, ref. 1.55) are now predicting a large number of broad $B\bar{B}$ states in the S, T, U region. If this is so, they will be very difficult to detect and will require a high statistics partial wave analysis. Others (e.g. Pennington, ref. 1.8) claim that duality is mainly fulfilled by states coupling to multi-mesons, and only weakly by baryonium states.

To achieve this level of statistics, we will have to wait for the proposed LEAR facility (low energy antiproton ring), when a high antiproton flux will become available. Till then, production experiments will be mainly useful for finding narrow states, though there have been some promising results regarding broad states (table 1.3).

Despite conflicting evidence, the most favourable baryonium candidate is still the S(1936), since effects have been seen at this mass in a number of experiments*. The T and U states are firm, but may well not be exotic. Of the effects seen in production experiments, the most striking are the

---

*   At the time of writing (April 1982), a new result from a transmission experiment by the Heidelberg-Saclay-Strasbourg collaboration indicates a peak followed by a dip at the S mass, which may explain previous observations and non-observations.

2020 and 2204 MeV/c^2 states of Benkheiri et al. Recent experiments appear to dispute this finding, but the original observations have not been explained away and seem to be too significant to be statistical fluctuations.

In conclusion, there is need for more experiments with high statistics and good resolution to search for exotic states, and to confirm effects discovered previously. This is where the present experiment can make a valuable contribution.

CHAPTER 2

THE SLAC HYBRID FACILITY

The exposure BC68 took place at SLAC (Stanford Linear Accelerator

Centre) in two phases: phase I was in April 1978, with the bubble chamber

filled with hydrogen; phase II was in March - June 1979, part of the data

taken with hydrogen and part taken with deuterium filling the chamber.

Just over one million pictures were taken in all, about half of which were

with hydrogen and half with deuterium.

This chapter starts with a general review of hybrid systems, and then

describes in detail the SLAC Hybrid Facility as used in BC68. This is

followed by a description of the beam and trigger and, finally, considera-

tions of the efficiency, with a statistical summary of the data obtained.

2.1 HYBRID SYSTEMS

Most high energy physics experiments fall into two categories : those

using bubble chambers and those employing electronic detectors (counters).

Although it has had a very fruitful life of nearly 20 years, the bubble

chamber in its conventional form is now being used less and less compared

to counter techniques. This is for two main reasons : firstly, there is

now a greater need for high statistics experiments which enable rare

processes to be observed. Conventional bubble chambers can only gather

data at a rate of about one event/second, thus demanding long exposure

times at the accelerator. Also, an exposure of more than about 10^6

pictures would require an enormous effort to process the film, taking a

large collaboration several years to complete the measurements. Counter

experiments, on the other hand, take data at a much greater rate, and the

measurements are made at the time of detection. As a result, counter

experiments often have an order of magnitude more events than bubble

chamber experiments.

Secondly, advances in physics have led to greater interest in very high energy interactions. These are best observed in colliding beam machines, where bubble chambers can not be used. In stationary target machines, the problem of measuring the momenta of fast particles, which leave tracks too straight to be measured accurately in a conventional bubble chamber, cannot be overcome. (In this thesis, the words "fast" and "slow" are used in abbreviation for high and low momentum). Moreover, it is then not possible to make unambiguous identification of particles. The difficulty of measuring very high momenta can be surmounted in counter experiments and, also particle identification is much easier.

Because of these factors of time and precision, counter experiments have largely superseded conventional bubble chambers. This is not without loss: bubble chambers are excellent vertex detectors, especially useful for observing strange particle decays; there is 4π angular detection of charged particles, giving precise topological information: and in contrast to counter methods, tracks of slow and stopping particles can be seen and measured ($\beta \lesssim 0.8$).

In an attempt to combine the merits of bubble chambers with the advantages of electronic detectors, hybrid systems have been developed. A hybrid system (refs. 2.1, 2.2) consists of a bubble chamber (acting as both target and track detector) surrounded by electronic detectors (for triggering, counting, measurement and identification of fast particles).

To increase the data taking rate, bubble chambers have been developed which are made to pulse as rapidly as is mechanically feasible. The Rapid Cycling Bubble Chamber (RCBC) is used in many hybrid systems and is technically the most difficult part of the system to construct and run. An RCBC pulsing at 10 Hz or more performs a very large number of oscillations in its lifetime and the dynamic parts have to be extremely reliable (notably the expansion valve and seals). In addition the rapid

movement of liquid creates a large heat load which must be conducted away with high efficiency. A piston made of metal helps to do this, but it can make the problem worse, since a moving conductor in the bubble chamber magnetic field creates eddy currents and hence extra heating. The design and operation of a RCBC is therefore crucial to the success of a hybrid system.

The electronic detectors can flank the bubble chamber on as many sides as possible, but they are usually placed upstream and downstream of the beam, to intercept the beam and the fast, forward particles. Any of the standard techniques of counter experiments may be used : scintillation counters, proportional wire chambers (PWC's), spark chambers, drift chambers, Cerenkov detectors etc. These can be used in any configuration, and serve a variety of functions: (a) counters, which simply send a signal to indicate the passage of a charged particle; (b) hodoscopes, which give coarse positional information of the tracks; (c) spectrometers, which determine the paths of the particles and hence their momenta (in a known magnetic field); (d) calorimeters, which determine the total energy possessed by the particles, including neutral ones; (e) particle identifiers, which distinguish the particles on the basis of mass or velocity; (f) triggers, which use the information obtained from the detectors to decide whether or not to accept the event.

A RCBC pulses so rapidly that, without a trigger, a great number of pictures would soon be taken, mostly with no, or uninteresting, events. Therefore, a picture is taken only when the detectors indicate that, apparently, a wanted event has occurred. This reduces the background substantially, so much less time is spent scanning the film - a great advantage over conventional bubble chambers. However, triggering does introduce biasses in the data; to correct for this, and for normalisation, the acceptance must be known.

"Acceptance" is defined as the fraction of events taking place in the fiducial volume of the bubble chamber that are accepted by the trigger. Since the trigger is normally set up to select events of a particular kinematic configuration, the acceptance will be a function of many of the physical parameters that are of interest, and is often zero for a large region of phase space - so that no correction is possible in that region. The acceptance depends on (a) the geometrical configuration and size of the detectors; (b) the efficiency of each of these elements; (c) the precise algorithm that is used for the trigger. The acceptance can therefore only be properly corrected for by using a sophisticated Monte Carlo method which accurately simulates these three properties. This is a principal disadvantage of triggered experiments.

To implement the trigger and perform other control functions, a hybrid system is interfaced with an on-line minicomputer.

Many systems use two triggers : a fast trigger and a camera trigger. The fast (or hardware) trigger uses the instantly-available information from the detectors and makes a quick (typically 20 nS) decision whether or not to proceed with the slow trigger algorithm. This is done using coincidence units, logic gates and discrimination units. This is necessary to avoid overloading the computer and consequently inhibiting triggers from other events which follow shortly after. The fast trigger is necessarily fairly simple.

If an event is accepted by the fast trigger, the complete information from the detectors is read into the computer and is processed (during the bubble growth time) through a program written for the particular experiment (called the "algorithm"). An "accept" decision by the algorithm causes the chamber lights to be flashed, thus recording the event on photographic film. This is called a camera (or software) trigger.

In practise, a trigger will never work perfectly and there are always a certain number of unwanted events recorded. This is for a number of reasons: interactions occurring outside the fiducial volume, in the chamber walls, or in the detectors; particles decaying in flight; "noise" from delta-rays produced along the paths of the tracks, or from random sources such as cosmic rays; and inefficiencies in the detectors.

In summary, hybrid systems constitute a powerful facility for high energy, high statistics experiments needing good vertex detection, and the development of RCBC's represents a significant technological advance. Developments are also proceeding with T.S.T.'s (composite chambers), high resolution bubble chambers (such as LEBC) and the application of holographic techniques, thus enabling the decays of charmed particles to be observed. The future of bubble chambers is thus ensured for a good many more years yet.

2.2 THE SLAC HYBRID FACILITY

The SLAC Hybrid Facility (SHF) is shown schematically in fig. 2.1. The components are (in order, going downstream): beam counter (S1), first beam proportional wire chamber (P1), beam Cerenkov counter (CB), beam hodoscope (BH), second beam PWC (P2), bubble chamber (BC), three downstream PWC's (α, β, γ), downstream Cerenkov counter (Canute), and beam veto counter (DV).

The axes used throughout this thesis are shown in fig. 2.1. They form a right-handed system with x in the (horizontal) beam direction, Y vertically upwards, and Z horizontal and pointing towards the bubble chamber cameras. The origin is situated on the inside surface of the BC window on the axis of the cylindrical chamber body. The axes are precisely defined relative to certain fixed locations on the camera plate, and are used to calibrate the optical parameters (see Chapter 3).

Fig. 2.1   SLAC Hybrid Facility

S1 P1 CB   BH P2   BC

DV

α β γ Canute

Y

X (Beam)

Z
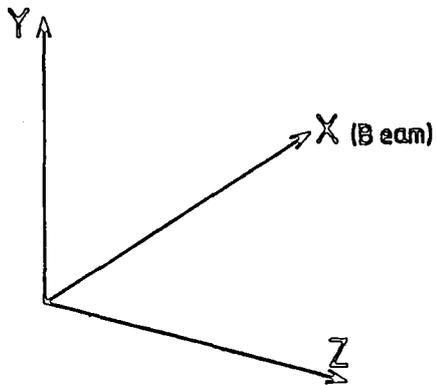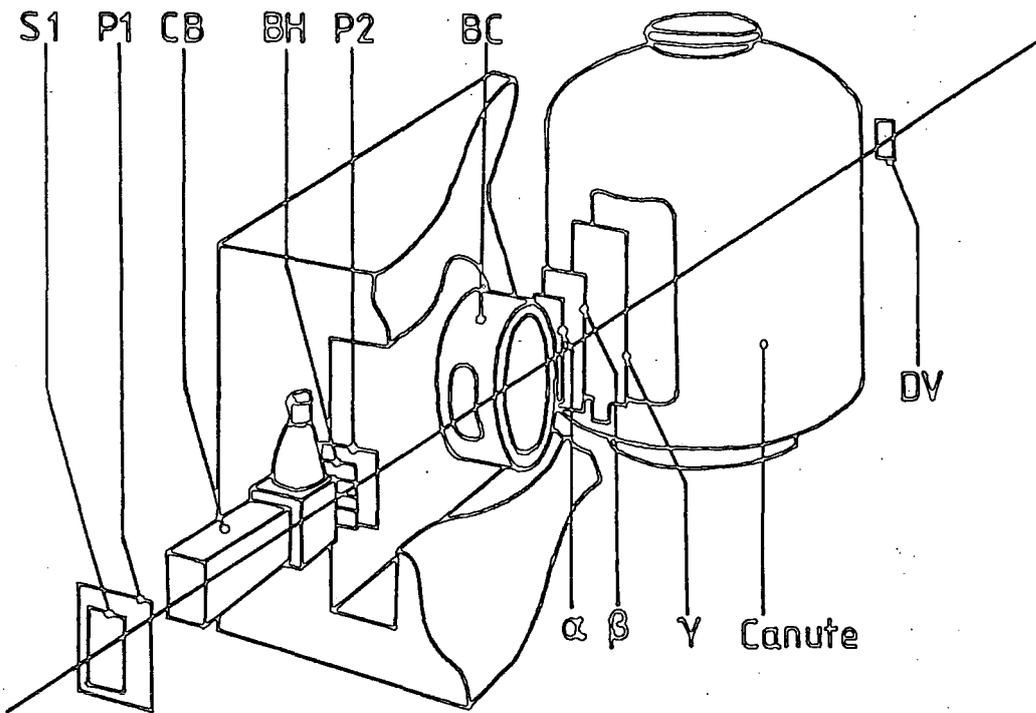
The bubble chamber magnetic field is such that negatively charged particles going downstream are deflected upwards (positive Y direction).

The components of the SHF will now be described in detail (refs. 2.2, 2.3). The positions and dimensions are given in table 2.1.

TABLE 2.1 POSITIONS AND DIMENSIONS OF PRINCIPAL COMPONENTS OF THE SHF

(Phase II Figures, if different, are given in brackets)

Element	X (cm)	Width (cm)	Height (cm)
S1	-899	bigger than beam cross-section	
P1	-863.9	"	
CB mirror	-393.5	"	
BH	-365.5	"	
P2	-327.2	"	
BC centre	O	"	
PWC α	78.4	21.5	72
PWC β	119.9 (120.9)	33	104
PWC γ	202.0 (203.5)	60	168
Canute mirrors	492 (521)	140	330
DV	∿600	5.6 (7.6)[*]	15.9 (27.9)[*]

( )[*] after roll 7221

2.2.1   The 1 metre Bubble Chamber

At the centre of the SHF is the 1 metre bubble chamber which is shown in fig. 2.2. The main specifications are given in table 2.2, and the operating conditions used in BC68 in Table 2.3.
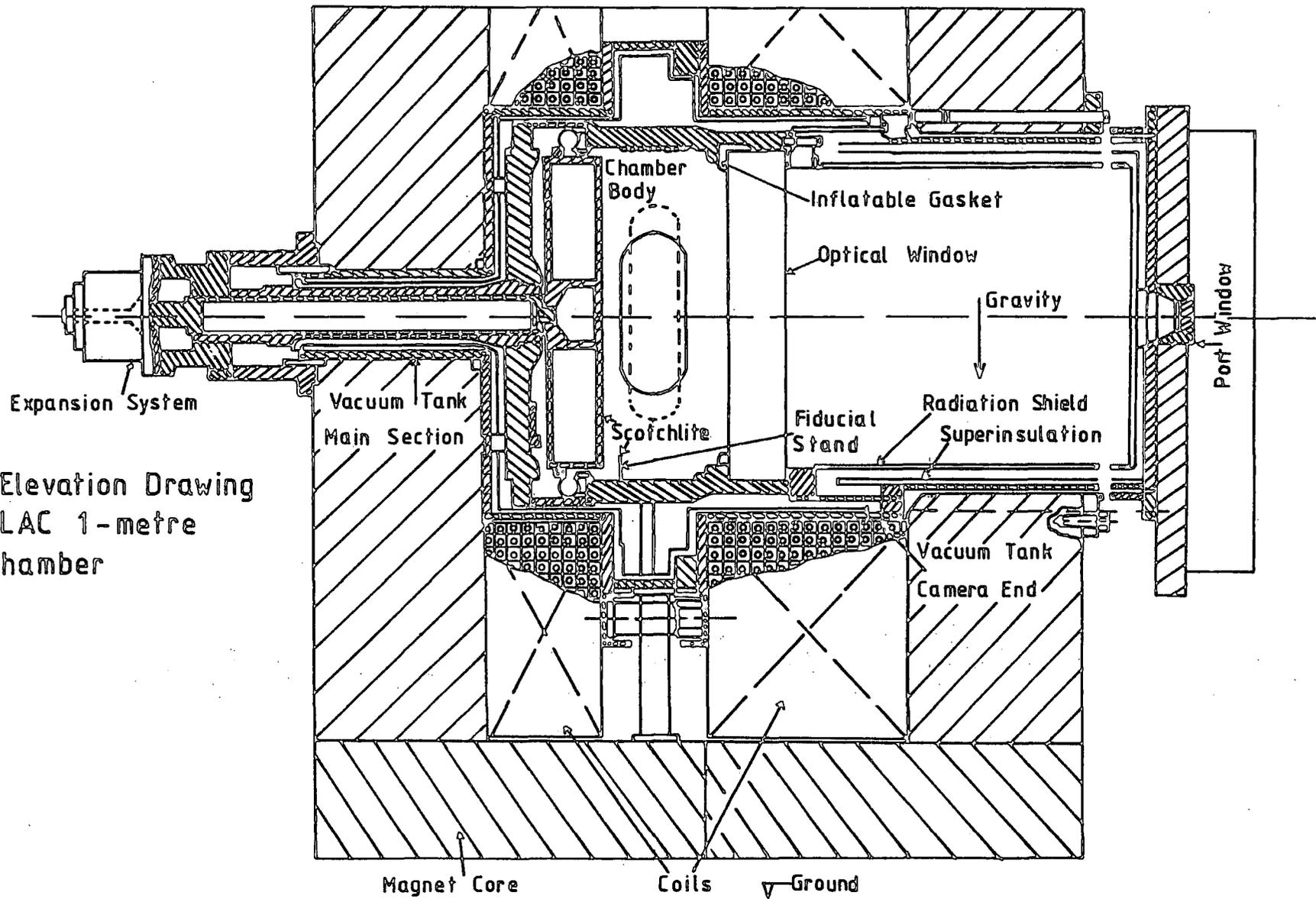
Fig. 2.2 Elevation Drawing
of the SLAC 1-metre
Bubble Chamber

Chamber Body

Inflatable Gasket

Optical Window

Gravity

Expansion System

Vacuum Tank
Main Section

Scotchlite

Fiducial Stand

Radiation Shield
Superinsulation

Port Window

Vacuum Tank
Camera End

Magnet Core

Coils

Ground

35

TABLE 2.2   PRINCIPAL SPECIFICATIONS OF THE SLAC 1m RCBC

Chamber diameter	110 cm
Chamber depth	43 cm
Visible volume	0.360 m^3
Piston diameter	102 cm
Piston movement	4.6 mm
Window thickness	19.5 cm
Beam window thickness	1.6 mm

TABLE 2.3   OPERATING CONDITIONS OF THE 1m   RCBC

	H_2	D_2
Liquid used		
Cycling frequency (normal)	15 Hz	8.5 Hz
Liquid vapour pressure	4.0 atm	5.3 atm
Liquid temperature	26.5 K	31.5 K
Density	62 Kg m^{-3}	140 Kg m^{-3}
Refractive index	1.098	1.110
Bubble growth time	3.5 m sec.	
Bubble diameter	300 - 450 μm	
Bubble density (at β= 1)	$\sim$ 10 cm^{-1}	
Magnetic field strength	18 Kgauss	

The chamber body is cylindrical with the cylinder axis horizontal and perpendicular to the beam. It is made from stainless steel and is milled down to a thickness of 1.6 mm where the beam enters and leaves the chamber, to minimise interactions in the walls. The chamber is placed inside a large, roughly rectangular, vacuum tank to prevent heat flow into the chamber.

The illumination system is Bright Field by means of three flash tubes concentric with the camera lenses, which are arranged in an equilateral triangle facing the bubble chamber window. The inside surface of the piston is covered with "scotchlite", a composite of small ($\sim$30μm) glass beads fixed in an adhesive matrix and covered by a thin layer of mylar for protection. This has the property of reflecting light retrodirectively, so that a scattering centre - such as a bubble - appears dark on a bright background. The optical system is fully described in Chapter 3.

A typical picture taken in the 1 metre RCBC is shown in fig. 2.3. The three straight lines perpendicular to the beam are the edges of the scotchlite strips (30 cm wide) which are not allowed to overlap since this would cause pluming (i.e. local boiling that takes place along any sharp edges or roughness; this is a problem particularly acute in RCBC's). Below one of the chamber views (not shown in the figure) is the data box which contains such information as: roll-frame number, time and date, magnetic field, pressure, beam hodoscope and downstream PWC hits, momentum of the trigger track and vertex position (as calculated by the algorithm). This is shown on an L.E.D. display and is superimposed on to the main picture by means of mirrors. The information is very useful for a quick examination of an event. The film used is 70 mm monochrome roll film and the same roll is used for all three views (see section 3.1).

π⁻ (3.63)

π⁺ (0.37)

p̄ (1.57)

p (0.64)

p̄ (6.06)
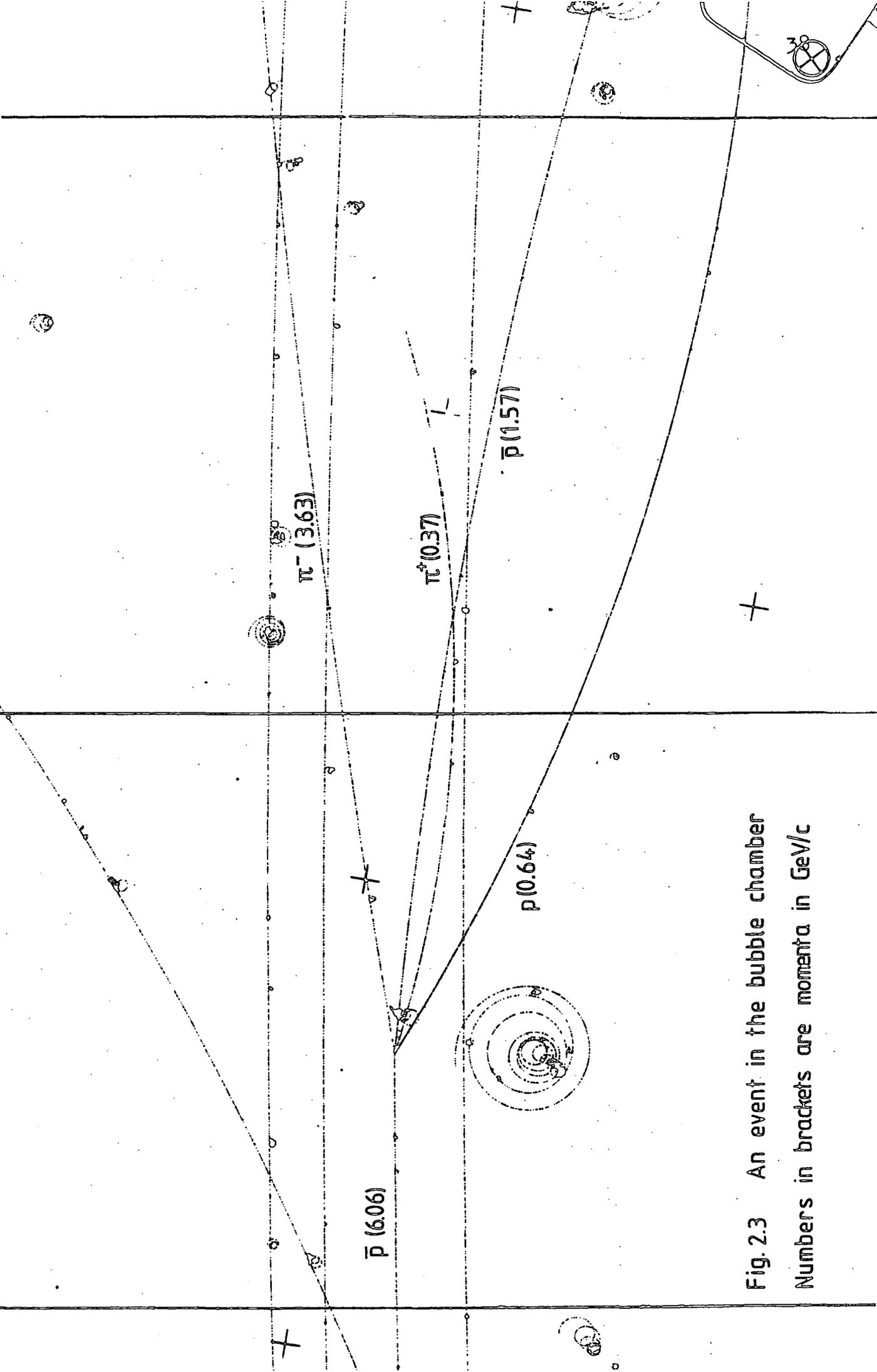
Fig. 2.3   An event in the bubble chamber

Numbers in brackets are momenta in GeV/c

It is wound on by a motor immediately after the flash, causing a camera dead-time of 330-500 ms. At frequent intervals (generally at the start of a new canister of film) a test strip was taken and inspected to check picture quality and algorithm performance.

2.2.2 Scintillation Counters and Beam Cerenkov

The upstream beam scintillation counter (S1), beam Cerenkov counter (CB), beam hodoscope (BH), and downstream beam veto counter (DV) are used in the fast trigger to define a "good" beam particle interacting somewhere in the system. S1 is the first counter intercepted by the beam and is placed between the last beam-line magnets (Q6 and D4). BH is a 4-counter hodoscope used, in this experiment, with the signals from each counter OR-ed together. The passage of a beam particle is thus defined by the signal $S1 \cdot BH$.

The beam Cerenkov counter CB is filled with Freon 12 at one atmosphere pressure and is used in the threshold mode: that is, with a beam of fixed momentum, pions, muons, and electrons produce light, while kaons and antiprotons do not. Thus a "good" beam track is defined by $S1.BH.\overline{CB}$, the only contamination coming from kaons (and a few pions from kaon decays).

The downstream beam veto counter DV is just behind Canute and is positioned to intercept all non-interacting beam particles. Thus, except for very small angle scatters (which are likely to be missed in scanning anyway) and a few events with a random track intersecting the veto counter, all interactions between BH and DV are signified by $\overline{DV}$; so the complete fast trigger is $S1.BH.\overline{CB}.\overline{DV}$.

2.2.3 Proportional Wire Chambers

The two upstream PWC's (P1 and P2) are used to provide positional information about the beam tracks. They each have a pair of sub-planes; one with vertical wires and one with horizontal wires. They are

designated Y1, Y2 and Z1, Z2 for chambers P1 and P2 respectively. The

notation Y or Z refers to the direction for which positional information

is given (thus, the Y-planes have horizontal wires). The wire spacing is

2.11 mm and the high voltage gap is 4.1 mm, operating at about 3kV. The

PWC deadtime is about 500 nsec.

The three downstream PWC's (called α, β, γ) are used for momentum

determinations of fast, forward particles and for estimating the position

of the interaction vertex. This is done both by the on-line algorithm

and by the off-line hybridisation program. The chambers are proportionately

larger the further downstream they are, so that roughly the same solid

angle is covered by each (∿ 0.25 sr). PWC α is actually mounted within an

insert box welded to the inside of the vacuum tank, so that it is as close

as possible to the bubble chamber. α and β are in the fringe field of the

bubble chamber magnet; whereas γ is in a region where the field is

practically zero (see fig. 2.4). The field strength over the area of the

PWC planes varies by no more than 1 to 2 Kgauss.

Each chamber contains three sub-planes with wires providing vertical,

diagonal, and horizontal coordinates which are referred to as Y, U, and

Z planes. The diagonal wires form a 3:4:5 triangle with the others (36.9°

to the horizontal) to simplify the fast integer arithmetic in the algorithm.

The sub-planes of each chamber are built as closely as possible together to

simplify wire-matching in track reconstruction. The spacing of α, β and γ

is chosen to be a simple ratio, viz. βγ : αβ = 2 : 1.

These downstream chambers have the same wire spacing as the upstream

ones, but the high voltage gap is rather more (6.4 mm) and they operate at

∿4kV. The PWC electronics is activated by a fast trigger to load the

signals from each channel (called "hits") into shift registers. If there

is a second fast trigger in the same beam spill, the hits from this are

stored in latches until the shift registers are cleared. No more than two

Field strength (kgauss) vs X (cm)
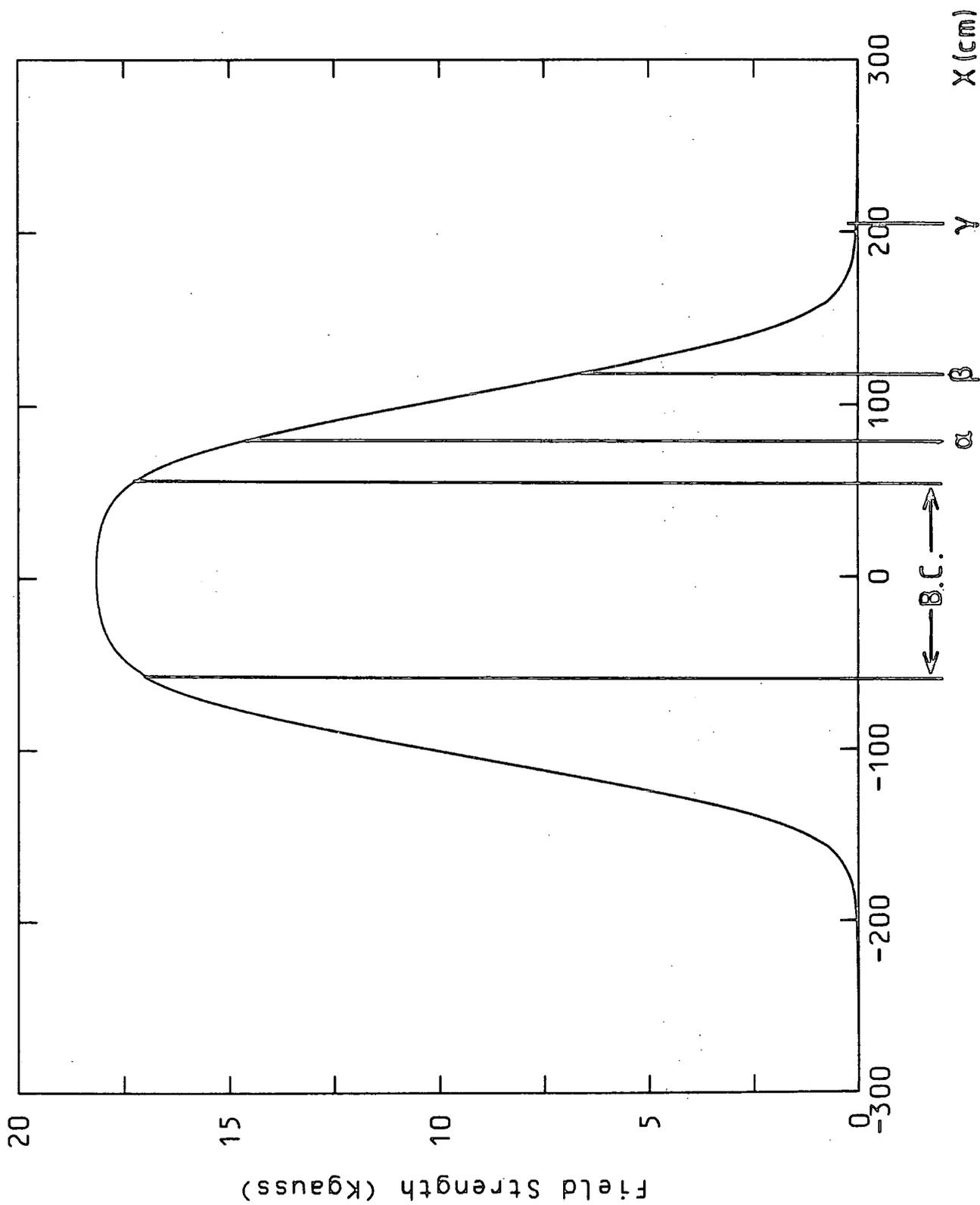
fast triggers are allowed in a beam pulse. After the beam spill, the data in the shift registers are strobed out at 10 MHz to digitizers in CAMAC crates attached to the computer. When this is completed, the results of the second trigger (if there is one) are loaded into the shift registers and strobed into the digitizers.

The information transmitted in this way to the computer are the wire numbers of each hit and the number of hits in each sub-plane. Typical efficiencies, defined as the fraction of tracks recognised by the computer as crossing a PWC sub-plane, are about 90 to 95% per plane.

2.2.4 Downstream Cerenkov Counter ("Canute")

Canute is an important element in the SHF - both for use in the trigger and for off-line particle identification of the fast, forward particles. It is a large aluminium pressure tank, cylindrical with a vertical axis (335 cm diameter and 406 cm high), and filled with a gas. The pressure was such that a pion above the threshold trigger momentum (defined in section 2.4.1) would produce Cerenkov radiation when passing through the gas, whereas protons and antiprotons would not.

The Cerenkov light is reflected by an array of twelve mirrors into respective light-collectors and phototubes. This results in signals proportional to the amount of light collected by each mirror cell which, after digitization, are read into the computer for every fast trigger.

A full description of the operation and use of Canute is given in sections 3.5.1 and 3.5.2.

2.2.5 On-line computer

The algorithm is executed by an on-line NOVA mini-computer, which also controls data acquisition. Magnetic tapes are written to record information used for off-line processing, viz. PWC hits, Cerenkov pulse heights, and results of computations by the algorithm.

Hardware

The central processor is a Data General Nova 849 with 48 kilowords

of 16-bit core memory. The peripherals are two disks, two tape drives,

a video terminal, a teletype, an electrostatic line printer, and two

CAMAC crates.

Software

In normal operation the computer services a "background" monitoring

program which is used for a variety of tasks e.g. displaying histograms

of any of the quantities collected by the foreground; displaying a

picture of the current event; changing the run parameters. This is

interrupted by a signal coming slightly before the beam pulse, and con-

trol is then given to the "foreground". The foreground program handles

all the time-critical tasks such as reading and recording the data from

a fast trigger, executing the algorithm, and writing data on to magnetic

tape. Various histogram tallies are updated, and then control is returned

to the background until the next beam pulse.

The data is divided by rolls, each roll containing about one

thousand pictures. At the end of every roll, the computer prints out a

summary of statistics for that roll. This includes such information as:

the number of fast triggers, the number of beam tracks, multiplicity

distributions and wire spectra for the PWC's. In this way, the performance

of the system was continuously monitored.

2.3   THE BEAM AND BEAMLINE

2.3.1   The Electron Beam

Electrons are injected into the SLAC linear accelerator and accelerated

along its 3050 metre length to a final energy of about 18 GeV. The

acceleration is by means of a travelling RF wave in the TM mode supplied

at a precise frequency of 2856 MHz. RF power is fed into the accelerator

cavity from 244 klystron amplifier tubes. The klystrons are pulsed at a
repetition rate of 60-360 Hz, each pulse lasting 1.6 µs. Thus the
electrons are bunched on two 'levels': beam pulses separated by ∿3-17 ms
and, within each pulse, electron bunches separated by the RF period 0.35 ns.
The beam current during a pulse is typically 30 mA. After acceleration,
the beam pulses are distributed between the various experimental stations.

2.3.2. The Antiproton Beam

Part of the electron beam is steered on to a beryllium target, a
thin pencil 30 cm long and 3 mm wide. The outgoing particles are then
directed along Beam Line 14, the layout and optics of which are shown in
Fig. 2.5. The purpose of the various components is to provide a well-
collimated, pure antiproton beam of well-defined momentum at the bubble
chamber.

The collimator C0 defines the beam aperture, whereas collimators C1
and C2, placed at the intermediate foci, define the momentum bite; C1 only
roughly, and C2 much more precisely. They were adjusted to give $\Delta P/P$ of
$\pm$ 1.5%.

The final quadrupole triplet Q 4.5, Q5, and Q6 are adjusted to give
a beam that is (i) as wide as possible in the vertical plane, so that
there is good separation of beam tracks in the pictures; and (ii)
parallel, to simplify wire matching in the upstream PWC's.

The RF separator (ref. 2.4) uses the collimator C2 as its mass slit.
Since the beam has RF structure, as explained in section 2.3.1, there is
only need for one deflector to achieve separation. The primary beam
occurs in 5 pS bunches (∿20° of phase) separated by 350 pS, within a
pulse length of 1.6 µS; the secondary beam also retains this structure,
resulting in bunches of particles travelling down the beam line. For
particles of a particular momentum, the velocity depends only on mass,

Fig. 2.5 Layout and optics of the beam line

Horizontal Plane

Vertical Plane

Beam Width

BC
D4
Q6
Q5
D3.1
Q4.5
C2
RF
D3.5
D3
Q4
Q3
D2
C1
D1
Q2
D0.5
Q1.5
Q1
C0

100 (metres)
90
80
70
60
50
40
30
20
10

llimator
ole magnet
adrupole magnet

45
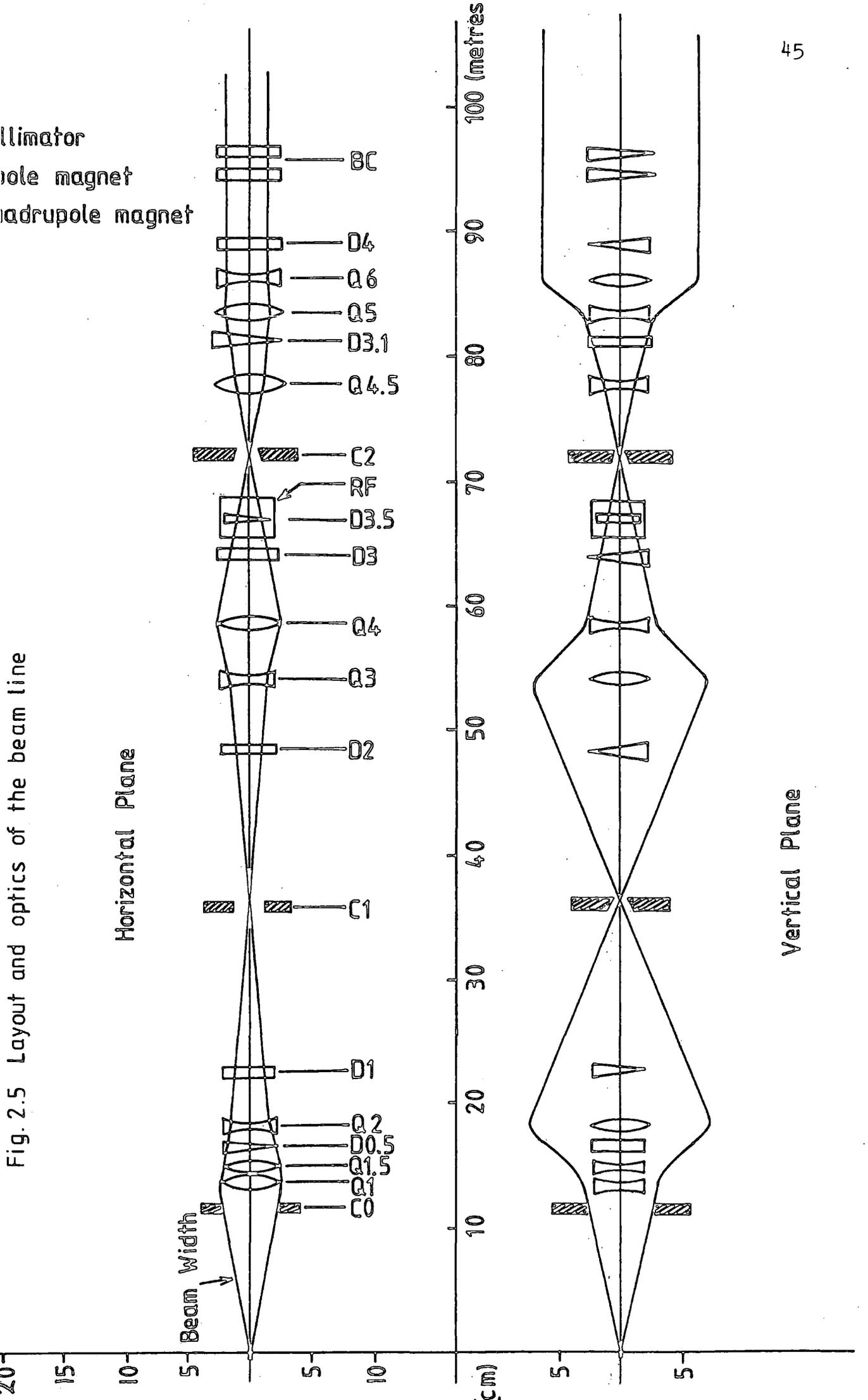
so that the bunches separate into mass bunches of the long lived hadrons: first pions, then kaons, and finally anti-protons. By appropriate choice of momentum and drift length L, the wanted particles can be arranged to be a half-integral number of cycles out of phase with the unwanted particles; thus wanted particles (i.e. anti-protons) may be deflected one way and unwanted particles (pions, kaons) the other way by applying a synchronised RF field (which is pulsed at the beam repetition rate). In principle, this method can only eliminate one type of particle, but at certain momenta the phasing can be such that both are eliminated efficiently. The phase difference between two particles of momentum p, mass m_1 and m_2 and velocity β_1 and β_2 is

$$\phi = \frac{2\pi L}{\lambda} \left(\frac{1}{\beta_1} - \frac{1}{\beta_2} \right) \qquad (c = 1)$$

$$\sim \frac{\pi L}{\lambda} \left[\frac{m_1^2 - m_2^2}{p^2} \right] \qquad \text{for } p \gg m$$

where L, the distance between target and RF separator, is 67 m and λ, the RF wavelength, is 10.5 cm.

The phase of the RF separator is adjusted such that antiprotons are deflected by a maximum in one direction i.e. the anti-protons arrive at the RFS just when the phase is a maximum. Thus the deflection angle of particle 2 relative to the anti-proton is

$$\theta = \frac{p_t}{P} (1 - \cos \phi)$$

where P_t is the maximum transverse momentum imparted to the beam.

Fig 2.6 shows θ as a function of p for $p_t = 25$ MeV/c.

Angular deflection in mrads vs Momentum in GeV/c
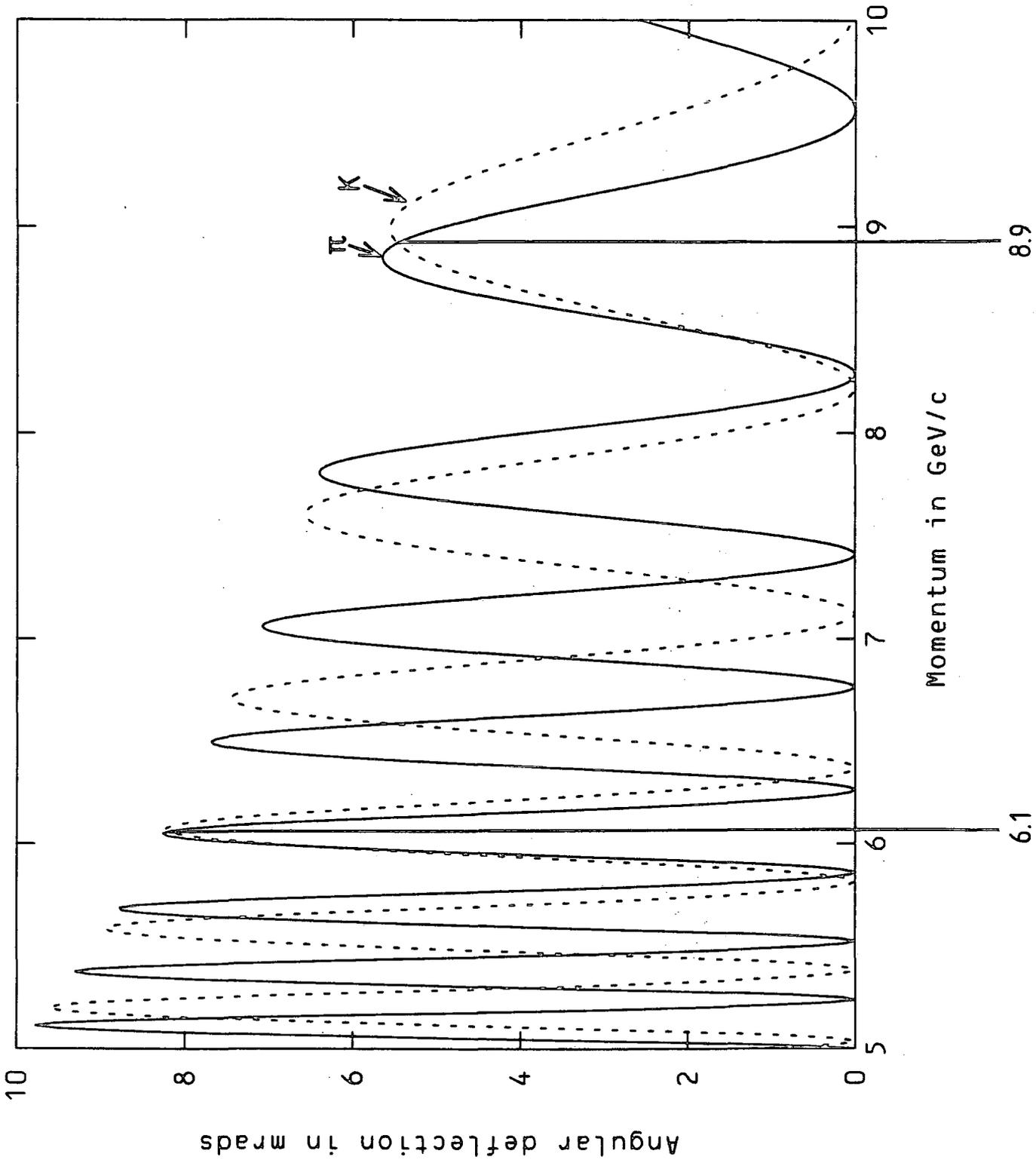
As can be seen, there are two momenta (6.1 and 8.9 GeV/c) where both pions and kaons are well separated from antiprotons. At 6.1 GeV/c, kaons are ahead of protons by 5½ cycles and pions are ahead of protons by 7½ cycles; at 8.9 GeV/c, kaons are ahead of protons by 2½ cycles and pions are ahead of protons by 3½ cycles. This is why a separated anti-proton beam is only available for the SHF at these two momenta.

2.3.3. Beam purity and yield

The secondary beam coming off the target consists mainly of pions, kaons, and antiprotons in the negatively charged component. The ratio of $\pi : K : \bar{p}$ at 6-10 GeV/c momentum, where the antiproton yield is a maximum, is about 250 : 5 : 1 . The beam purity is much improved after separation although, by the time the beam reaches the separator, there are a substantial number of muons from kaon and pion decays. At the SHF the average number of beam particles per pulse is about 6. The ratio of light particles (π, μ) to heavy particles (K, $\bar{p}$) was found to be about 1 : 1 from beam Cerenkov data. Of the light particles about 85% are muons (determined by counting the number of random events in the BC pictures); the remainder are assumed to be pions. The kaon contamination is more important since the beam Cerenkov does not distinguish these from antiprotons. A film scan for τ-decays[*] shows that kaon contamination is negligible ($\lesssim$ 0.2% at 6 GeV/c; $\lesssim$ 1% at 9 GeV/c). Thus there are about 3 antiprotons per pulse.

The various beamline elements were continuously monitored during the run, and were adjusted appropriately whenever the beam flux or ratio of $\bar{p}$ to π/μ became unacceptable. In particular, the RF phase needed frequent adjustment because the separator was very temperature sensitive.

[*] that is, K $\to$ 3π decays

2.4 THE TRIGGER

2.4.1. Definition of the Trigger for BC68

The trigger used in experiment BC68 is: record the event if there

is a fast, forward $\pi^{\pm}$, K^{+}, or proton coming from an antiproton inter-

action within the fiducial volume of the bubble chamber. 'Forward' means

within the solid angle defined by the downstream detectors (see

section 2.2.3); 'fast' means greater than a certain momentum (2.5 GeV/c

for a 6 GeV/c beam and 4.0 GeV/c for a 9 GeV/c beam). For the Phase I

9 GeV/c exposure, the Canute pressure was such that K^{-} particles of

momentum greater than 6.0 GeV/c could also trigger. The main purpose of

the trigger is simply to remove events with a forward anti-proton, these

being mainly elastic scatters and meson-exchange interactions.

2.4.2 Operation and timing of the trigger

The bubble chamber expansion system is operated at a rate synchronised

with the beam pulses i.e. so that there are an integral number of beam

pulses in one complete oscillation of the BC. The pressure curve and

timing are shown in fig. 2.7. The beam pulse enters the BC just before

the pressure reaches its minimum, when the liquid is at its most

sensitive. After each particle passes through the system, the fast trigger

responds in $\sim$ 20 ns if there is an antiproton interaction (defined by the

signal S1.BH.$\overline{CB}$.$\overline{DV}$ - see section 2.2.2.). If so, this initiates read-out

of the PWC's, during which time (180 ns) the counter electronics are

inhibited from producing another fast trigger. After this, they are

ready to receive a second fast trigger: however, as explained in sec. 2.2.3,

the PWC electronics will not accept more than two fast triggers per beam

pulse.

After the beam pulse has finished (1.6 μs) the data from the first

trigger is transferred to the computer in about 150 μs. The algorithm
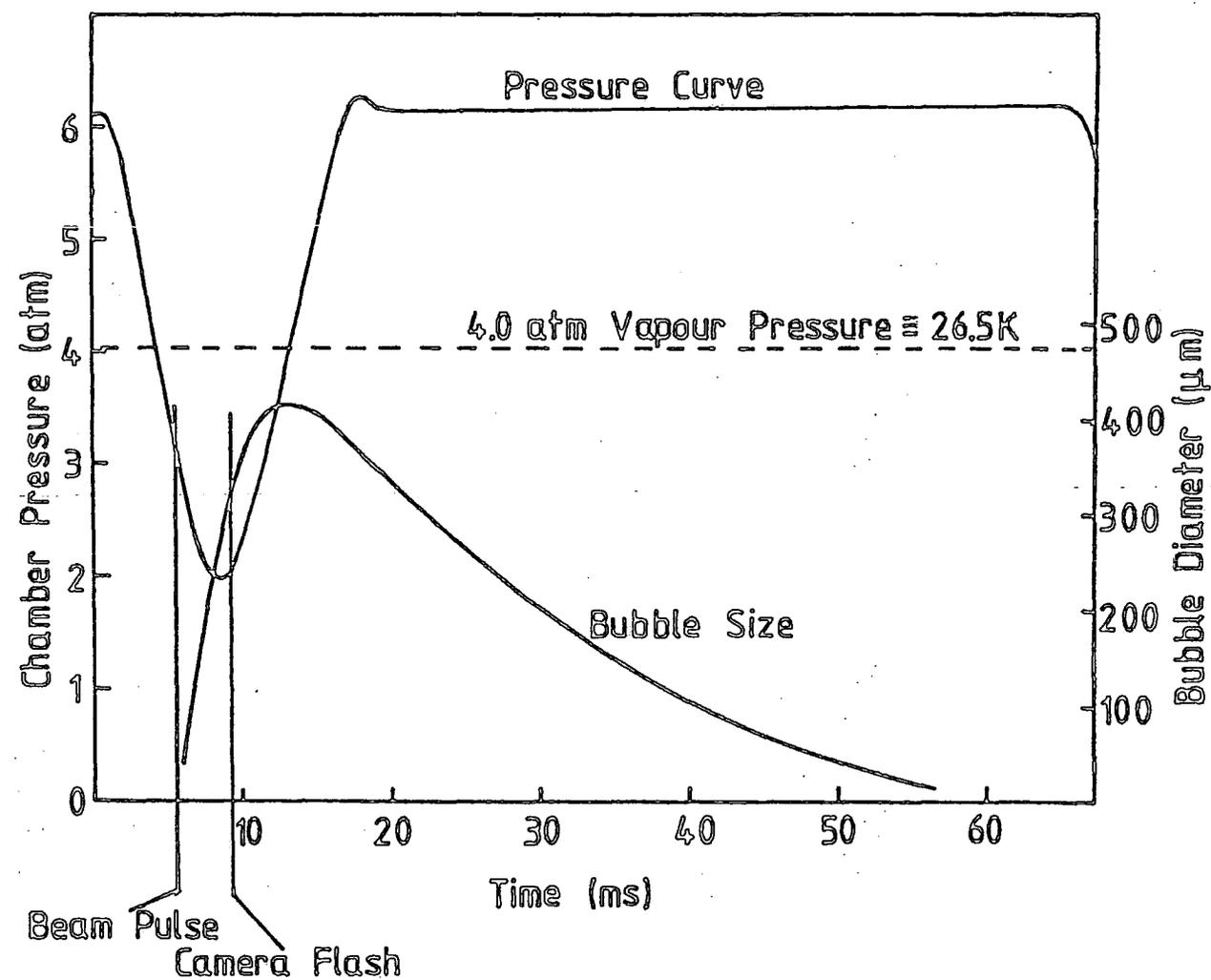
Fig. 2.7   Pressure Curve and Bubble Size During One Cycle
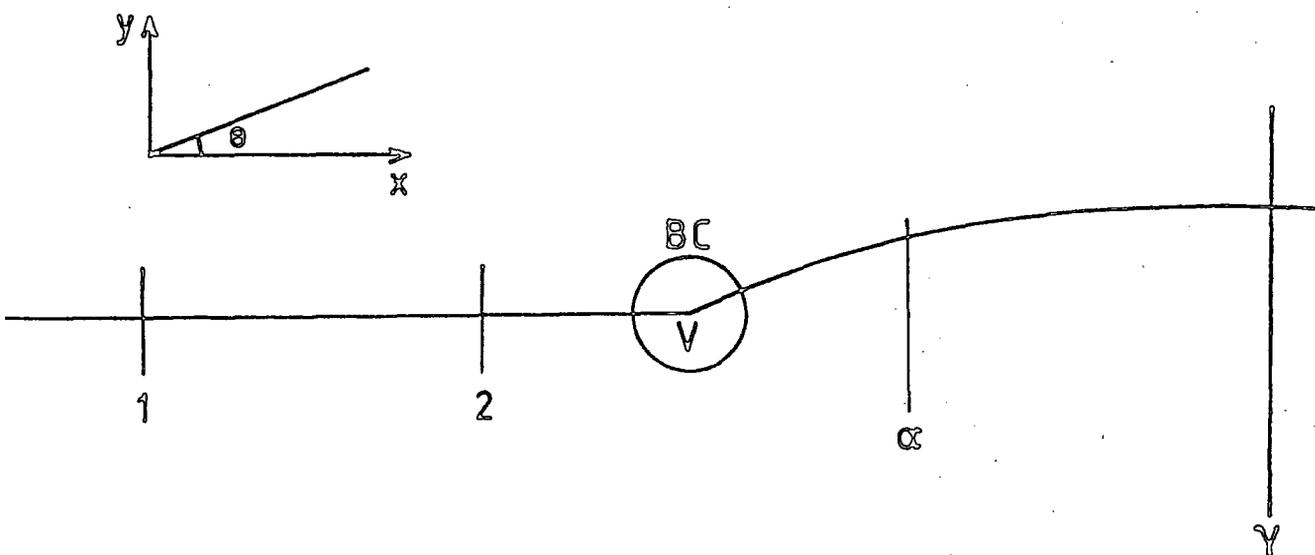
Fig. 2.8   Beam and Outgoing Track Passing Through the BC and PWC's

program is then automatically run, and takes typically 1-2 ms to decide whether or not to accept the event. If the event is successful, a signal is sent to flash the BC camera lights; if it is not successful, the data from the second trigger (if there is one) is read into the computer, and the algorithm is run again, and may also result in a camera trigger if there is enough time.

From the moment a beam particle passes through the bubble chamber, bubbles start to grow along its track. The bubbles grow as long as the liquid pressure is less than the equilibrium vapour pressure (at constant pressure, bubble radius $\propto \sqrt{time}$). After 3.5 ms the bubbles are about 300 μm in diameter, a size suitable for accurate measurement from a photograph. Therefore, the camera lights are flashed 3.5 ms after the beam pulse, and the algorithm must have finished in this time. A camera trigger also causes the digital and binary displays to be set on the film data box, and PWC and Cerenkov data to be written on to magnetic tape.

As the BC pressure increases beyond the vapour pressure, the bubbles are recompressed until they disappear. The whole cycle is then repeated at the next expansion.

2.4.3. The Algorithm

The algorithm is coded in NOVA assembler language using 16-bit integer arithmetic. The principles of operation are as follows (see fig. 2.8). In the Z-X plane, where tracks are straight, the beam track and outgoing track are projected to determine the X-coordinate of the vertex, X_v. After checking that X_v is inside the fiducial region, it is used together with the Y hits at PWC2 and two downstream PWC's to determine the momentum of the outgoing track (see appendix A for details). If the momentum is greater than the required threshold value and, for negative particles, the pulse height from Canute is sufficiently high, the event is accepted.

In detail, the steps executed by the BC68 algorithm are as follows (as used in phase I):

(1) Multiplicity cuts are made on the number of hits in the PWC sub-planes. No more than two hits in each sub-plane are allowed in PWC2, and no more than five hits in the downstream PWC's α, β, γ. If PWC2 was bad, it could be substituted by PWC1 with an appropriate offset.

(2) For each downstream PWC, matched points are found between the three sub-planes (Y, U, Z) to remove ambiguities in the association of Y and Z hits. This is done by looping through all combinations of hits and testing them against the "tie-up" relation

$$\left| 3Z + 4Y - 5U - K \right| \quad < \quad Tol$$

where K is a constant for the PWC and Tol is a tolerance (= 35/2 wire spacings). This relation follows from the wires in the sub-planes forming a 3 : 4 : 5 triangle. The values of K for α, β , and γ were determined during the calibration run (see appendix A).

(3) A pair of downstream PWC's is chosen for the vertex and trigger momentum calculation. The order of preference is (i) α γ , (ii) α β (iii) β γ, to favour the pair with largest track sagitta. Thus, pair α β would be chosen only if wire matching failed in γ ; and pair β γ would be chosen only if wire matching failed in α .

(4) A "software beam veto" is applied to remove any non-interacting beam tracks. The beam tracks found in PWC2 are projected into the downstream PWC's using the calibration constants, and the predictions are compared with the matched points already found. If they are consistent, the track is removed and the matched points deleted.

Then, for each pair of matched points, and for each beam track, the following loop is executed:

(5)   The vertex is calculated from the Z-plane information (see appendix A), and is checked to lie inside the fiducial region. If the dip is too small for an accurate calculation, the vertex is imposed (at $X_v = 0$ for very small dip; or at $X_v = +25$ cm or -25 cm for intermediate dip).

(6)   The momentum of the outgoing particle is calculated (appendix A) and checked to be within the momentum range of interest. The sign of the momentum indicates the sign of the charge of the particle.

(7)   For negatively charged particles the presence of light in Canute is checked; the total signal (CSUM) from all twelve cells must be greater than a certain threshold value. For positive charges this test is not applied, since protons are acceptable trigger particles.

(8)   Finally, using the calculated momentum, the track is projected into the PWC so far unused, and predictions are made for Y, U, and Z. Confirmation is required from at least two sub-planes.

All combinations of PWC2 and matched, α, β, γ hits are tested for a configuration satisfying the conditions in steps (5) to (8). The first positive result triggers the cameras. Rejection of all combinations means no picture is taken.

The main algorithm parameters for phase I are given in table 2.4.

TABLE 2·4 ALGORITHM PARAMETERS FOR A LARGE PART OF THE PHASE I DATA

Beam Momentum	Number of Rolls taken	Momentum limits (GeV/c)		Canute threshold (ADC units) -ve triggers only
		+ve triggers	-ve triggers	
9 GeV/c	15	$4 < p < 15$	$4 < p < 30$	CSUM > 500
"	92	"	"	CSUM > 90
6 GeV/c	170	$2.5 < p < 10$	$2.5 < p < 20$	CSUM > 170
"	39	"	"	CSUM > 40
"		$2.5 < p < 10$	$2.5 < p < 3.5$	CSUM > 40
	20	"	$3.5 < p < 4.5$	CSUM > 70
		"	$p > 4.5$	CSUM > 110

2.5 CHANGES MADE FOR PHASE II

2.5.1 Fast Trigger

Phase II was mainly a deuterium run, and since the cross-section for antiprotons in deuterium is about twice that in hydrogen, the losses due to the limit of two fast triggers per beam pulse would be considerable. Therefore a way was found of "tightening" the trigger so that there would be fewer fast triggers per beam track, without rejecting too many wanted events. This was done by including another PWC (called δ) in the system placed between PWC γ and Canute. PWC δ was not used in the normal "read-out" mode, but as a hodoscope: that is, the wires from the lower and upper half were separately gated together so that a fast signal could be obtained, indicating which half of the PWC a particle passed through.

Since most unwanted events have antiproton triggers, which curve upwards under the magnetic field, PWC δ was used in conjunction with Canute to veto these events. The fast trigger used in most of Phase II was

$$S1.BH.\overline{CB}.\overline{DV}.(\delta_L + CSUM)$$

where δ_L = hit in lower part of PWCδ and CSUM = total Canute pulse height > a discriminator threshold.

The boundary between the upper and lower halves of δ was just below the area crossed by beam particles. The only good events lost were kaon and proton triggers which missed δ_L. PWC δ was not used in the algorithm. This new fast trigger reduced the fast trigger rate by a factor of $\sim$ 2.3.

2.5.2 Camera Trigger

For most of phase II the algorithm was modified to make a more sophisticated test on the signals from Canute. A "fast" track found by the algorithm was projected to the Canute mirror plane, and the intercept was thus predicted. The photomultiplier pulse heights were then added only if the corresponding mirrors were within a certain distance of the track intercept. For negative particles this "local CSUM" was required to be greater than a certain level. In this way, negative particles which interact downstream of the BC and produce Cerenkov light in a different region of Canute would not trigger the cameras, whereas in phase I they did. The camera trigger rate was reduced by a factor of 0.75 and the number of wanted events per roll was therefore significantly improved.

As an additional precaution against triggering on antiprotons, some of the phase II data were taken with a "positive only" algorithm, i.e. all events with a negative triggering particle were rejected.

2.6 PERFORMANCE AND EFFICIENCY

Table 2.5 shows typical figures for trigger rates, beam yields, and number of pictures taken during the five stages of the experiment. In all about 1,086,000 pictures were taken in 116 days of running. From the fast

trigger rate, it is apparent that most beam pulses result in one or more interactions; but only a few per cent of these are accepted by the algorithm. So, in order to accumulate the same number of events of the kind with a fast, forward meson, an untriggered experiment taking pictures at the same rate would have taken 20 years - and a great deal longer than this to process the data! In general, the experiment ran smoothly, except for a serious leak in the chamber vacuum jacket during phase II.

TABLE 2.5   STATISTICS OBTAINED DURING EXPERIMENTAL RUNS

	Beam momentum (GeV/c)	6	9	9	6	9
	BC Liquid	H_2	H_2	H_2	D_2	D_2
	Phase	I	I	II	II	II
$\bar{p}$/beam pulse		1.8	2.6	2.4	2.4	2.0
$\bar{p}$/other beam particles		1.0	0.9	1.1	1.3	1.0
Fast triggers/$\bar{p}$		0.53	0.50	0.17	0.23	0.24
Fast triggers/beam pulse		0.98	1.30	0.41	0.55	0.47
$\bar{p}$/camera trigger		174	125	160	92	99
Camera triggers/fast triggers		0.009	0.016	0.037	0.047	0.042
Second triggers/first triggers		0.28	0.39	0.14	0.18	0.20
Number of pictures taken (thousands)		220	105	195	49	517

There are two kinds of inefficiency: the loss of good events, and the contamination of the data with unwanted events. These will now be considered in some detail. The figures given refer to phase I.

2.6.1 Losses

The various contributions to loss of good events are as follows:

(1) "Down-time" of the accelerator and hybrid facility due to faults. During phase I the system was operational for 78% of the time available.

(2) Poor beam flux due to bad steering, R.F. phase drift, "trip-offs" etc. Also, there was an unacceptably high proportion of electrons and photons in the beam, which had to be reduced by inserting a lead absorber in the beam. This reduced the beam flux further. The average flux obtained was 73% of that available with optimum tuning.

(3) Interactions of antiprotons in the beam Cerenkov and entrance windows of the BC. About 88% of antiprotons survive as far as the fiducial volume of the bubble chamber.

(4) Loss of second fast triggers due to fast electronics deadtime. About 9% of events were lost this way.

(5) Loss due to limit of two fast triggers per beam pulse. This caused 13% of events to be lost.

(6) Beam PWC's inefficiency, mainly because of deadtime. The efficiency factor for accepting beam tracks is 93%.

(7) Downstream PWC's inefficiency. In terms of the efficiency for an event to be accepted by the algorithm, the factor is 94%.

(8) Geometric acceptance of the S.H.F. This is dealt with fully in Chapter 4. The efficiency factor depends on the particular reaction being investigated.

(9) Camera deadtime. The resulting losses are 14%.

(10) Algorithm inefficiency, causing incorrect or inaccurate reconstruction of tracks. Also, there are losses due to multiplicity cuts, and the time limit for execution of the program. The efficiency is estimated to be 90%.

(11) Interactions or decays of triggering particles between the fiducial volume of the BC and Canute; hence failing in track reconstruction, or by no light in Canute. Efficiency factor = 0.84.

(12) Random tracks passing through the beam veto. About 7% of events are lost in this way.

Factors (4) and (5) were substantially improved in phase II. Otherwise, the inefficiencies are inherent in the apparatus, and can not easily be ameliorated.

2.6.2. Contamination

The main sources of contamination are:

(1) Events triggered by a beam particle interacting outside the fiducial volume of the BC or in the chamber walls, together with failed or inaccurate vertex reconstruction by the algorithm.

(2) Unwanted events with a fast, forward particle interacting or decaying downstream, and hence being accepted e.g. a fast antiproton interacting in the wall of Canute, producing pions which then give light.

(3) Delta rays from the triggering particles of unwanted events producing light in Canute.

(4) The wrong momentum or sign of the triggering particle is calculated by the algorithm.

Scanning results for 6 GeV/c H_2 data indicate that 59% of pictures have events in the fiducial volume with an outgoing particle of momentum >2GeV/c, and with a beam track agreeing with Y2 hits. Of these events, about 60% have an antiproton trigger, mainly because of (2) above. This was improved considerably in phase II by using a modified trigger.

Figures for the sensitivity (events per microbarn of cross-section) are given in Chapter 4.

CHAPTER 3

DATA PROCESSING

The data obtained in experiment BC68 consisted of a total of 1182

rolls of film with corresponding NOVA tapes of counter information. These

were distributed amongst the six collaborating laboratories as shown in

Table 3.1

TABLE 3.1 FILM DISTRIBUTION (Numbers of Rolls)

Beam MOM. BC Liquid Phase	6 GeV/c H_2 I	9 GeV/c H_2 I	9 GeV/c H_2 II	6 GeV/c D_2 II	9 GeV/c D_2 II	Total Rolls
IC	37	15	56	O	74	182
RL	36	28	49	O	85	198
Saclay	51	10	O	O	101	162
SLAC	99	31	110	25	171	436
Tohoku	14	21	O	28	116	179
Tufts	O	10	O	O	15	25
Total Rolls	237	115	215	53	562	1182

Each laboratory processed its portion of the film through the standard

sequence of scanning, measuring, and data reduction and produced a data

summary tape (DST). The DST's from the different laboratories were then

combined into a master DST on which physics analyses were made. The film

scanned and measured at Tufts, however, was analysed on the SLAC computer,

and was counted as SLAC data for DST purposes.

This chapter describes the data processing at the Rutherford Laboratory only, to which the author is affiliated for this experiment; however, the procedures at other laboratories differ only in detail e.g. method of 'choicing' fits. These details, where they affect physics results, are known and are accounted for.

The complete data processing chain at Rutherford Laboratory, from raw data to DST, is shown in Fig. 3.1. Each stage will now be described in detail.

3.1 SCANNING

The scanning of BC68 film is 'directed': that is, events are only recorded if it is possible for them to have triggered the camera. An event is required to have (i) a primary vertex in the fiducial volume, (ii) a track of an outgoing particle with sufficiently high momentum, and (iii) a beam track entering the fiducial region at the correct location. The last check is enabled by extracting from the NOVA tapes information on the hits in PWC Y2 for the appropriate frame and trigger. The wire numbers of the hits, with tolerances, are presented to the scanner in the form of a scan list. Also given on the scan list are locations of views 1 and 2 for a given view 3. This is necessary because all three views of a picture are contained on the same roll of film, separated by a number of frames, and the frame number is only given with view 3. (In fact, one scanning table was obtained which could project all three views together, but other tables had just one projector per film spool).

The scanning procedure is as follows:
1. On view 3, the scanner looks for events with beam tracks which cross a template in the regions given on the scan list. The template is calibrated for each table and is positioned between fiducials B and C (figure 3.2).
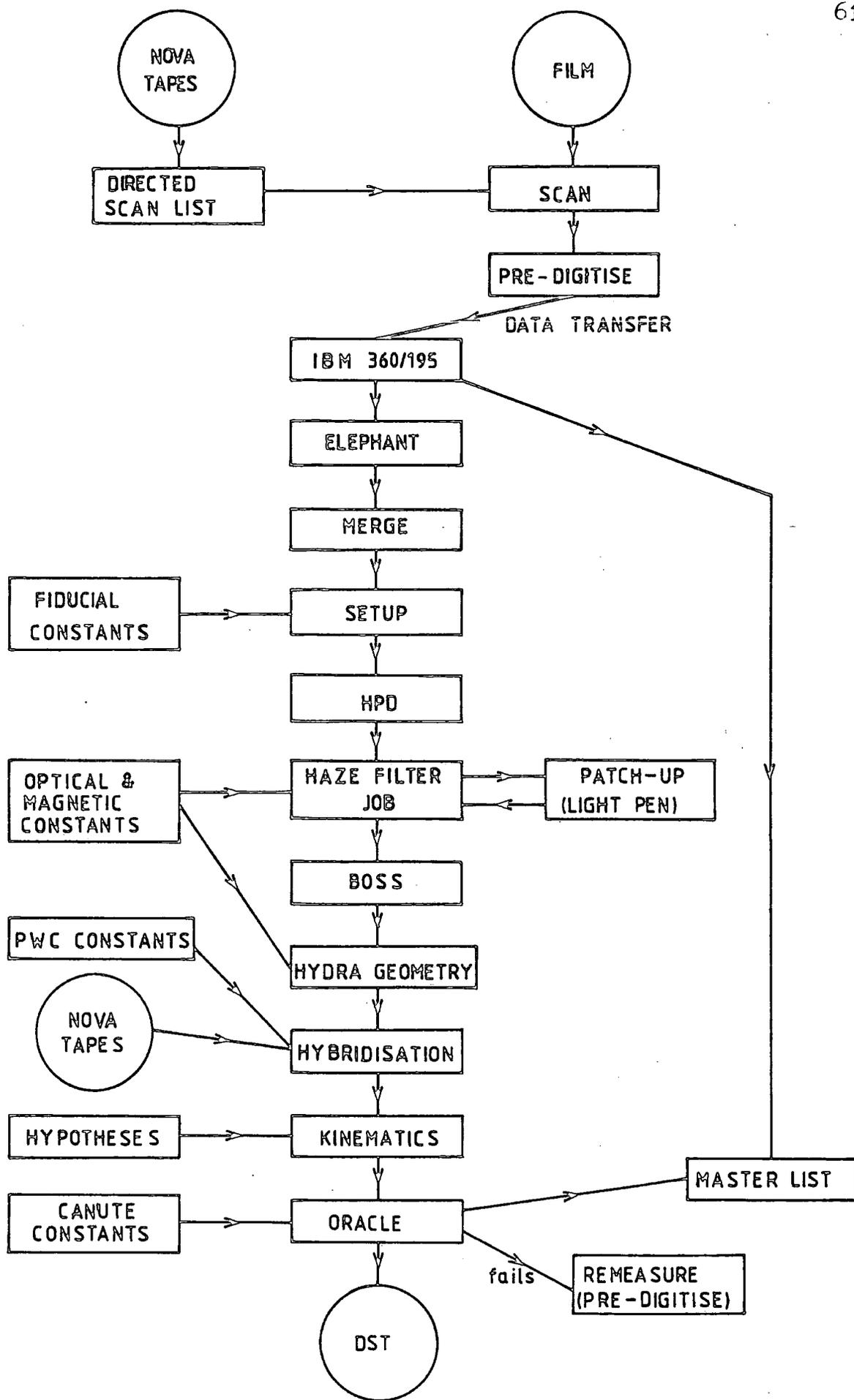
Fig. 3.1   Flow Diagram for Data Processing at RL.
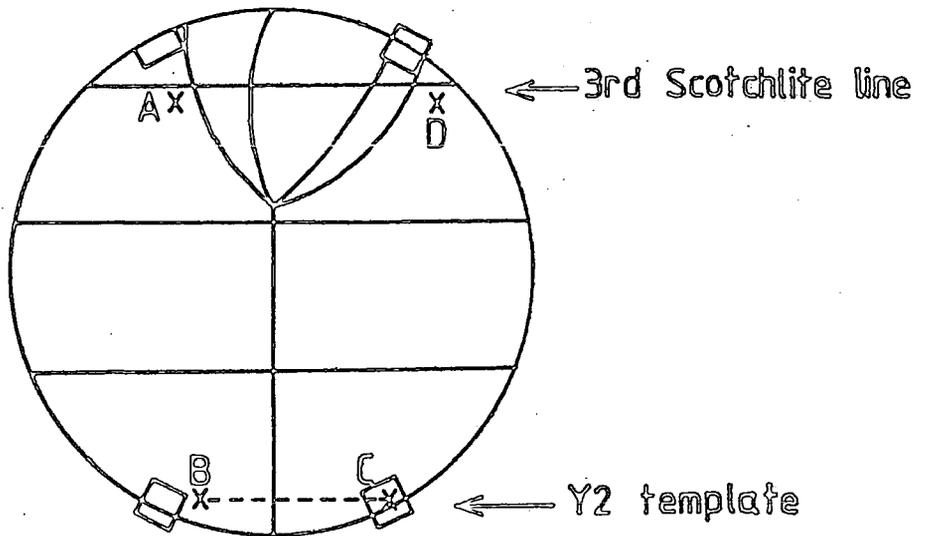
Fig. 3.2   View 3 - Features Used in Scanning

2. The primary vertex is checked to be inside the scanning region -
    defined to be between the line joining fiducials B and C and the third
    scotchlite line (see figure).

3. The scanner checks that there is at least one "fast" track from the
    event using a momentum template. The track must be straighter than
    the curve on the template (corresponding to momenta of 2.1 and 3.5
    GeV/c for 6 and 9 GeV/c beam momenta respectively). In fact, this
    test was found to reject so few events that it was omitted after the
    first few rolls.

4. View 2 is now selected to check that the view is good (i.e. well-
    illuminated, non-overlapping), and that the primary vertex is
    visible.

5. Step 4 is repeated for view 1.

6. If the event passes all these checks, it is now pre-digitised; if it
    fails, the scanner proceeds to the view 3 of the next event. In rare
    cases, there is more than one successful event on a frame.

Special scan codes are recorded for events with associated stopping protons;
$\pi-\mu-e$ decays; or "stars" ($\geqslant$ 3 prongs) from secondary neutron, antineutron,
or antiproton interactions.

3.2 MEASURING OF EVENTS

Film measurement was performed on an HPD automatic measuring machine.
Firstly however, each event had to be pre-digitised manually to help the
HPD program locate the tracks. This considerably improves the efficiency
of track identification.

3.2.1 Pre-digitising

This is carried out in conjunction with scanning; after a frame is
scanned on all three views, the event, if successful, is measured according
to the following sequence:

1. View 1. Measure two fiducials (C & A on fig. 3.2).

2. Measure vertex.

3. Measure all tracks (beam first); two points per track.

4. Repeat for view 2, and then for view 3.

Pre-digitising was performed on image plane digitisers (accuracy $\sim$ 50μm)
on-line to an IBM 1130 computer (or, for some processing, on-line to a
microprocessor interfaced with a VAX computer). At intervals, the data
was transferred to a disk on the Rutherford Laboratory IBM 360/195, on
which all subsequent computation was performed. Information on topology,
scan codes, and measurement history is stored on a Master List disk. The
data is then passed through a series of programs: ELEPHANT transforms table
co-ordinate measurements to the film plane by removing projection distor-
tions, and monitors the digitising; MERGE puts together complete rolls in
increasing frame number order; SETUP prepares input for the HPD.

3.2.2. HPD

The HPD (Hough-Powell Device) is an automatic film measuring machine which works on a flying spot technique. A laser beam is spread out so that the light falls on the length of a fixed glass fibre, acting as a cylindrical lens. Another fibre (one of eight fixed into a rotating disk) is moved close to the fixed fibre and is kept orthogonal to it. At the point of intersection a light spot is formed which is projected onto the film by one lens and onto a digitising grating by another lens. In the "normal scan", the spot ($\sim 3\mu$m diameter) scans across the film perpendicularly to the film edge, while the film moves through the machine along its length. A photomultiplier behind the film registers any marks on the film, the x co-ordinate of which is given by the film position and the y co-ordinate by the number of counts recorded by another photomultiplier behind the digitising grating.

In this way, the entire area of a frame is digitised. Six fiducial crosses are searched for, using the approximate positions passed through from SETUP, and those found (normally 4 or 5) are digitised accurately.

As well as the "normal scan", there is also an "abnormal scan" in which the light spot scans parallel to the film edge. This is necessary to obtain good accuracy on tracks which are at a small angle to the normal scan direction. Scan lines are spaced by 2 μm and a typical RMS error on a track is 2-3 μm on film (manual filmplane digitisers have track errors typically 5-6 μm).

Apart from accuracy and the speed of measurement (3-4 secs/frame) compared with a manual machine, the HPD also has the great advantage that it measures the relative bubble density of all tracks in an event. This provides information on the velocity of the particles by means of track ionisation, and hence is useful for selecting the correct mass fit (see section 3.5.3).

3.2.3 HAZE and PATCH-UP

The digitizings from the HPD are processed through a filter program HAZE which tries to identify tracks within roads. "Roads" are areas on the film in which a track should be found; they are obtained by a circle fit to the rough digitisings for each track and defining a band 400 μm wide centred on the track. The HPD digitisings within each road are grouped into "strings" of nearby points which lie (approximately) in a straight line. The strings are then connected together to form tracks, and these tracks are divided into a number of slices. Within each slice a master point is obtained by averaging all the digitisings of points forming the strings which belong to the track. These master points take the place of normal measured points from manual digitisers. There are 3 to 20 master points per track (typically 10), and once these are obtained the raw digitisings may be discarded.

It often happens that HAZE identifies the wrong track e.g. if there is a crossing track. For this reason, a simplified geometrical reconstruction program EDGEOM is run. The master points are reconstructed in space by combining the three views, and a mass-independent helix fit is made. If the points fail this reconstruction they are passed through a second filter program EDGING which makes another attempt at stringing and derives a new set of master points. Any problem tracks are sent for PATCH-UP.

The PATCH-UP system is a manually-assisted procedure for recovery of tracks failing the filter steps, or failing track matching; or generally for improving track digitising (e.g. if the residuals are too large). The digitisings of the tracks on each view are displayed on a video screen so that an operator, using a light-pen, can direct the on-line program to correct the track, or to only use part of the available track length. About 30% of events are patched up in this way. Patched and unpatched events are merged by program BOSS.

3.3 SPATIAL RECONSTRUCTION OF EVENTS

This section describes the procedure used to reconstruct the events in 3 dimensions and to derive momentum vectors for the charged particles. This was done using the HYDRA GEOMETRY program (ref. 3.1) incorporating a specially written hybridisation processor.

"Hybridisation" is the synthesis of film measurements with data from the proportional wire chambers. The purpose is to improve momentum accuracy of the beam and fast, outgoing particles (which have nearly straight tracks, and so are poorly measured in the bubble chamber), and to check that the events are wanted. Events are not wanted if (a) they are triggered by another event in the same beam pulse e.g. a beam particle interacting outside the fiducial region which has a Y2 hit close to the measured event; (b) the triggering particles interact or decay in the downstream part of the system e.g. an outgoing antiproton may interact, producing a pion which causes the trigger. These "antiproton triggers" are the largest contribution to the background.

3.3.1 Optical constants

To reconstruct events in the bubble chamber, the optical constants of the BC must be well known. The optical system is shown in figure 3.3 and a schematic view of the bubble chamber, looking towards the cameras along the z-axis, is shown in figure 3.4. The camera lenses form an equilateral triangle whose circumcentre lies on the z-axis (by definition). There are four sets of fiducial marks, 26 in all: 17 engraved crosses on the liquid side of the BC window; 3 stick-on "pasties" on the vacuum side of the BC window; 2 pasties on the piston; and 4 pasties on flanges welded to the chamber body. The window fiducials have been surveyed to an accuracy of 2μm for the engraved marks and 100 μm for the pasties. The piston fiducials have not been surveyed since they are in motion during picture taking, and they can only be used for point matching. The body fiducials have been
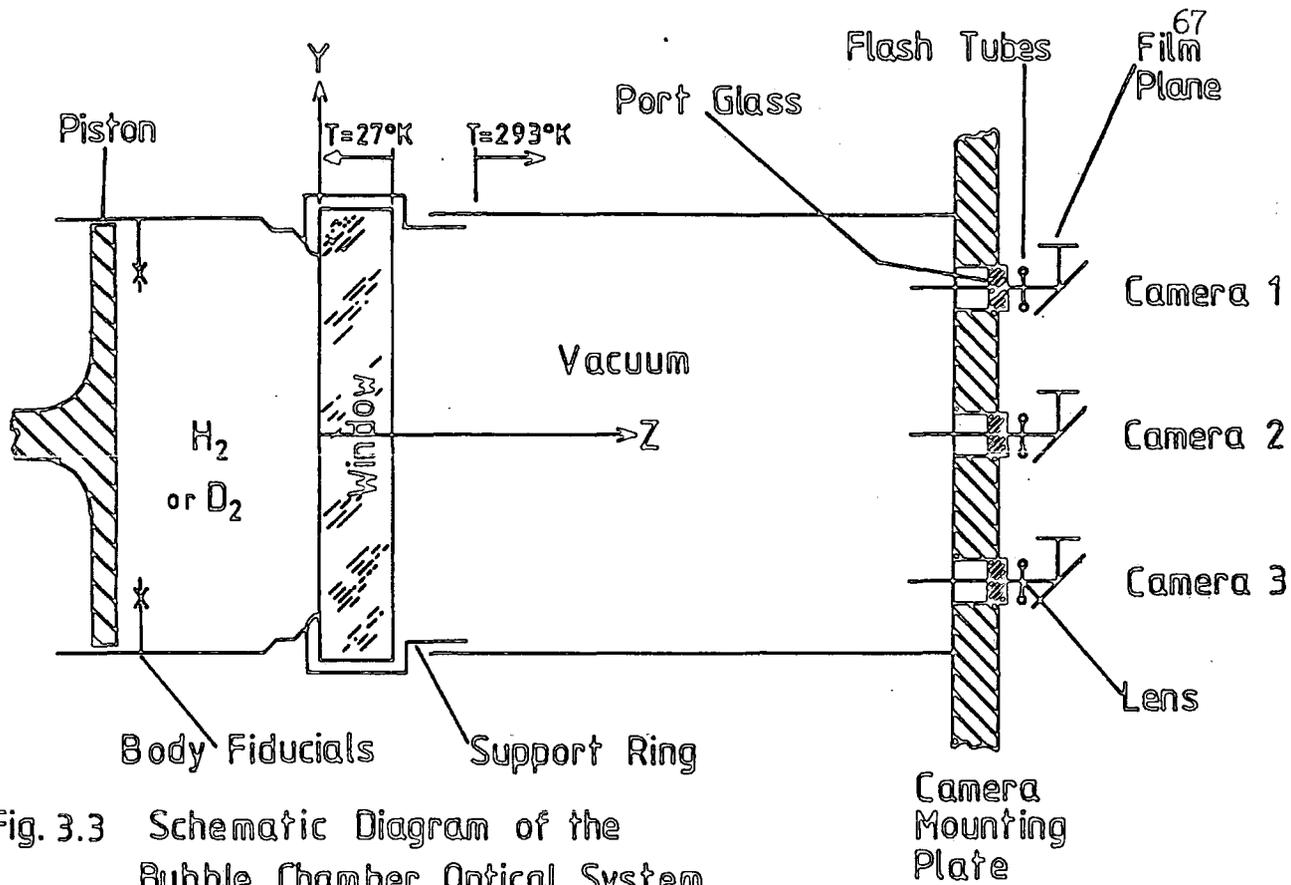
Fig. 3.3 Schematic Diagram of the Bubble Chamber Optical System

○ Camera with view number

⊕ Window fiducial - vacuum side

✛ Window fiducial - liquid side

⊕ Piston fiducial

⊗ Chamber body fiducial
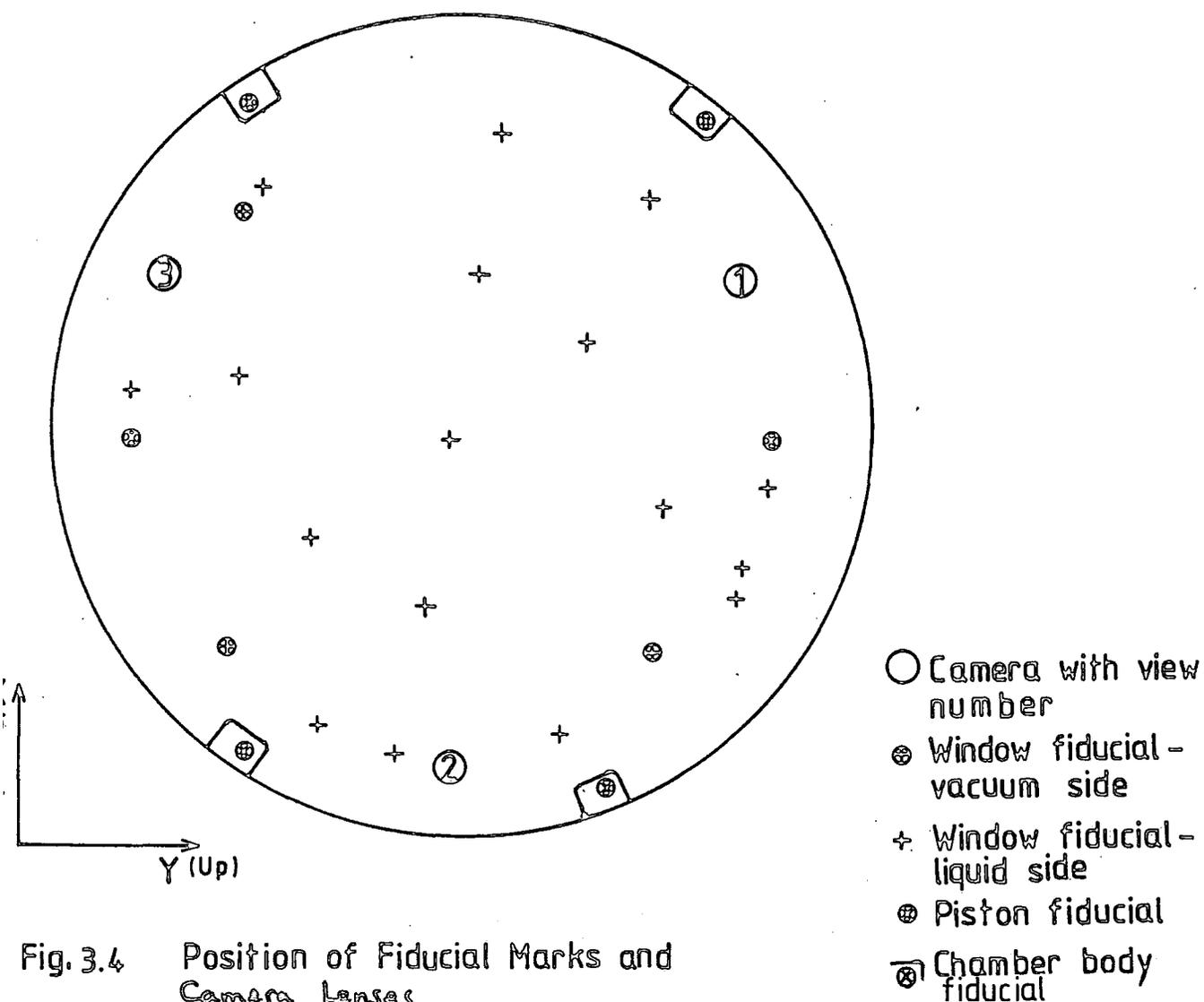
Fig. 3.4 Position of Fiducial Marks and Camera Lenses

measured in the x-y plane, but not in z, so only their separations can
be used.

In order to determine the fiducial coordinates relative to the
standard SHF axes, a short survey is made before each run with the
chamber filled. Two window fiducials are viewed through port-holes in
the camera plate, and they are measured relative to fixed points on
the plate. Then a linear transformation is made on all window fiducials
to the standard axes, taking account of the contraction factor in going
from room to liquid hydrogen temperature.

After the exposure, these survey positions are compared with film
measurements. For each run all fiducials were measured on three views
for 100 frames, using film-plane digitisers. Average values were found,
with r.m.s. deviations of $\sim$ 6 μm, and given as input data to a fitting
program AD, which performs the following steps:

1. Rays are traced from the survey fiducial positions to the film plane
   of each view, taking account of refraction in the liquid, window,
   and port glass, and of lens distortions. Thus, predicted film
   coordinates are obtained for each view.

2. By a least squares fit to these predictions, a linear transformation
   is made to the film measurements to bring them into a camera-based
   co-ordinate system.

3. Rays are then traced from the transformed film measurements back
   into the bubble chamber. The three rays corresponding to the same
   fiducial on each view form a closest point of intersection, which
   is compared to the survey position in three dimensions by a χ^2
   test. Typical spatial errors corresponding to a film setting error
   of 3 μm are: 30 μm in x and y and 150 μm in z.

The BC window angle, camera z-coordinates, and lens distortion coefficients are varied and steps 1 to 3 are repeated until a minimum χ^2 is obtained. These parameters and the predicted film fiducial co-ordinates found in step 1 are then passed to HYDRA GEOMETRY.

The beam momentum and track stretch functions derived using these titles were found to be sensitive to the type of lens distortion parametrisation used (see section 3.3.3). After many trials, it was found that the following parametrisation gave the best stretches and most consistent beam momenta, and is a fair representation of the kind of lens aberrations expected:

$$X^1 = (1 + \frac{D_3}{F} Y^2/X + \frac{D_5}{F^2} (X^2 + Y^2)) X$$

$$Y^1 = (1 + \frac{D_6}{F} X^2/Y + \frac{D_5}{F^2} (X^2 + Y^2)) Y$$

where X^1, Y^1 are ideal (i.e. undistorted) film co-ordinates and X, Y are real film co-ordinates.

F is the distance from the lens nodal point to the film plane.

Typical values for D_5 are 0.002, and for D_3 and D_6 -0.002. Other constants are given in table 3.2.

TABLE 3.2   PRINCIPAL OPTICAL CONSTANTS OF THE 1-METRE BUBBLE CHAMBER

	x	y	z	(cm)
Camera 1	20.003	34.646	213.16	
Camera 2	-40.005	0.	213.99	
Camera 3	20.003	-34.646	213.27	

Lens nodal point to film plane, F = 13.477 cm.
BC window thickness = 19.556 cm.
BC window refractive index = 1.520
Port glass thickness: View 1 = 3.228 cm. View 2 = 3.358 cm.
                                      View 3 = 3.505 cm.
Port glass refractive index = 1.46
Liquid refractive index : H_2 = 1.098, D_2 = 1.110

3.3.2 Geometrical Reconstruction in the Bubble Chamber

The HYDRA GEOMETRY program combines information from the three views to reconstruct events in three dimensions. A vertex is located by finding the nearest point of intersection of rays, traced from the film, corresponding to measurements of the same vertex on each view. Track reconstruction is more difficult since the points measured on different views do not correspond; therefore a preliminary fit is attempted by projecting the track in stages from the vertex outwards. Each track is fitted to a helix to determine the azimuthal angle (ϕ), the dip angle $(\lambda = \pi/2 - \text{polar}$ angle), and the radius of curvature at the vertex. Then, using a map of the magnetic field, the momentum (p) of the track is obtained. Corrections are made for loss of energy due to track ionisation which depends on the particle mass (heavier particles lose energy more quickly). Thus a mass-dependent fit is made for the three masses: pion, kaon, and proton. Often one or two of the masses do not fit, thus aiding particle identification. The momentum of a stopping particle is obtained from a range-momentum table, providing the end-point has been measured.

3.3.3 Beam constants and PWC offsets

From bubble chamber measurements alone, the spread in beam momenta is about $\pm$ 5%. Of this, only about $\pm$ 1% is the true width, the rest being measurement error. Clearly, the majority of beam momenta would be brought nearer to the true value by averaging the measured momenta with the nominal momentum; this is in fact done in the GEOMETRY program, a procedure known as "beam averaging". The two terms in the average are weighted by appropriate error matrices, the error on the nominal value being the best estimate of the true width of the distribution (given by the beam optics). Beam averaging improves the success rate of beam hydridisation, particularly for short tracks, but at the expense of

introducing a small bias for well-measured tracks. The "nominal"
beam p, λ, and ϕ at the plane X = O, together with distribution widths,
are the beam constants supplied to HYDRA GEOMETRY. Although known
approximately from beam line conditions, they are determined more
accurately from the data in the way described below.

The hybridisation procedure requires knowledge of the PWC offsets
(that is, the distances of the zero-wires from the X-axis) in order
that the beam and fast, outgoing particle tracks may be reconstructed
accurately. To determine the offsets, tracks are "swum" (i.e. the
paths of particles are traced through the magnetic field) from the BC
to the wire planes. Predicted wire hits are compared with actual hits
and the offsets are adjusted so that, on average, the differences centre
on zero. It should be stressed that this is necessary to eliminate
systematic bias in the momenta, whereas hybridisation is done to
improve individual measurements.

The track variables needed for the determination of these constants
were derived in three different ways from a sample of 4C fit events
with vertices in the range -15 to +20 cm (so as to avoid short tracks):
1. Using measured quantities for all tracks i.e. from unhybridised,
    un-beam-averaged geometrical reconstruction. The beam constants
    are simply the averages of all the beam track measurements.
2. Using measured quantities for outgoing tracks, and substituting
    for beam tracks the vector sum of outgoing measured momenta. Thus
    beam constants and upstream PWC offsets were derived using these
    substituted momenta.
3. Using kinematically fitted quantities for all tracks, on events
    which have passed through unhybridised, un-beam-averaged GEOMETRY.

Method 1 is the "natural" way which one would expect to be most

free of bias. However, it was found that the constants derived by

this method depended sensitively on the optical constants used by

GEOMETRY. The titles finally chosen were those obtained by method 2, as

these led to the best overall figures for beam momenta (consistency

with other laboratories), track stretches, and missing masses (see

section 3.6.2). The beam constants used at Rutherford Laboratory are

given in table 3.3. The angles λ and ϕ are defined in the normal way

with respect to the Cartesian axes, but with the direction of the beam

track reversed. The momentum widths are estimated by unfolding from

the observed distributions the known experimental errors, while the

widths of the angular distributions were taken to be the smallest

values obtained by any method.

TABLE 3.3. BEAM CONSTANTS USED AT RUTHERFORD LABORATORY

	$P \pm \sigma_p$ (GeV/c)	$\lambda \pm \sigma_\lambda$ (rads)	$\phi \pm \sigma_\phi$ (rads)
Phase I, 6 GeV/c, H_2	6.012 ± 0.100	-0.00040 ± 0.0017	3.14298 ± 0.0017
Phase I, 9 GeV/c, H_2	8.674 ± 0.150	-0.00021 ± 0.0013	3.11568 ± 0.0017
Phase II, 9 GeV/c, H_2	8.757 ± 0.150	-0.00027 ± 0.0013	3.11237 ± 0.0017
Phase II, 9 GeV/c, D_2	8.849 ± 0.150	0.00051 ± 0.0026	3.11531 ± 0.0033

A plot of the beam momentum obtained from 4C fits for the Phase I

data at 6 and 9 GeV/c is shown in fig. 3.5. Given on the figure are the

average momentum and width from fitted quantities, which are noticeably

different to the table values. Clearly, a bias is present and this was

investigated in considerable detail (e.g. by using different sets of

optical constants); however, as a later section shows, the quality of

fits was considered to be acceptable.

Fig. 3.5 Fitted Beam Momentum (6GeV Phase 1)
(4C Fits)

$<P> = 6.018$ GeV/c

$\Delta P = 0.059$ GeV/c

Momentum, GeV/c
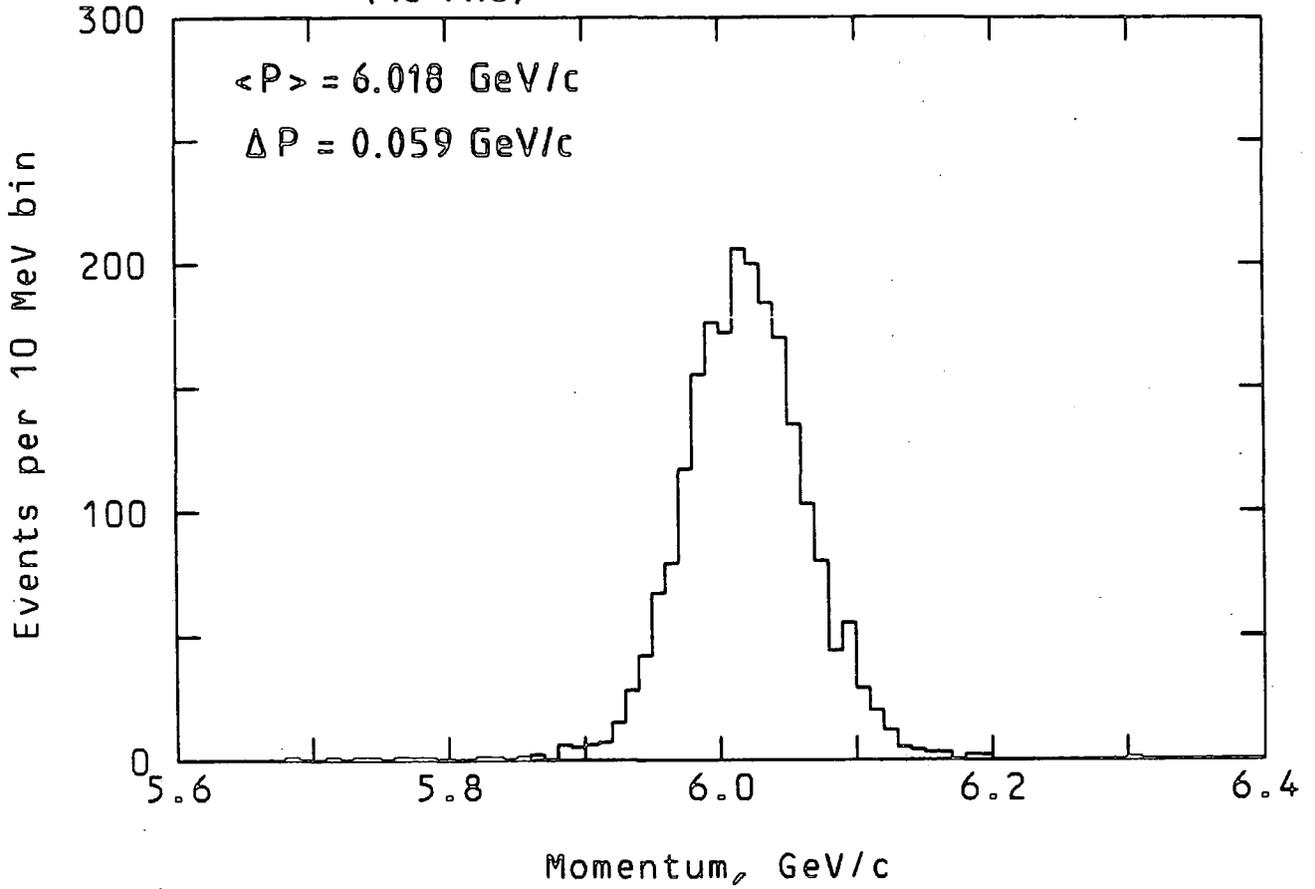
Fitted Beam Momentum (9GeV Phase 1)

$<P> = 8.767$ GeV/c

$\Delta P = 0.095$ GeV/c

Momentum, GeV/c
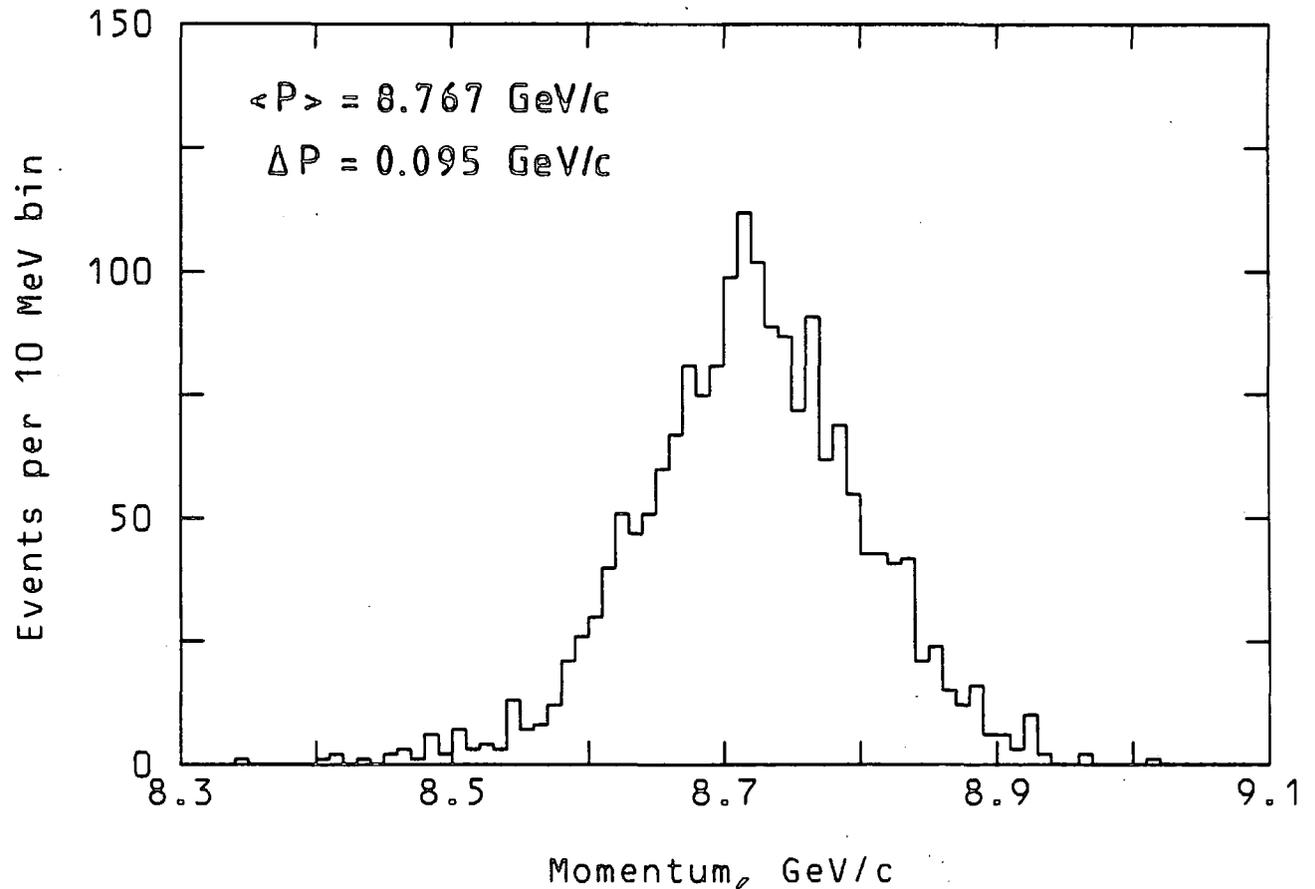
3.3.4 Hybridisation

Hybridisation is carried out on each event after they have passed through HYDRA GEOMETRY. The beam track and certain outgoing tracks are subjected to a hybrid fitting procedure. To be a candidate for this, an outgoing track must

(1)   have a good helix fit from GEOMETRY.

(2)   come from a primary or V^o vertex.

(3)   have a momentum greater than 2 GeV/c. Since this has an error the criterion used is $\frac{1}{p} - \delta(\frac{1}{p}) < \frac{1}{2 \text{ GeV/c}}$.

(4)   intersect all three downstream PWC's. To check this the track is swum using the mass-independent fit.

Predicted wire hits are calculated for the Y and Z planes, with a full error matrix deduced from the effect of multiple Coulomb scattering by material in the path of the particles. A similar procedure is followed for the beam track, using the upstream PWC's. The actual PWC data is then consulted (from the NOVA tape) to look for observed hits which match the predictions. To be a "good hit" the observed and predicted wire numbers must be within a certain tolerance (4 standard deviations, and not more than 12 x wires, where x is the co-ordinate of the plane in metres). If there is a good hit in the Y-plane but not in the Z-plane (or vice-versa), the observed U-plane hits are used to reconstruct the missing hit (downstream PWC's only).

A track is said to hybridise if

(1)   there are at least 3 planes with good hits,

(2)   at least one Y-plane has a good hit

(3)   probability of $\Delta\chi^2 > 0.001$, where $\Delta\chi^2$ is the change in χ^2 of the track fit as a result of hybridisation.

The χ^2 is composed of two contributions: a bubble chamber (BC) part, referring to co-ordinates of track points; and a PWC part, referring to wire hit positions. To obtain the improved (hybridised) track momentum vector, the χ^2 is minimised. Since the GEOMETRY program has already minimised an unhybridised χ^2, the BC track points need not be known, and the improved track vector is derived in terms of the PWC hits (with its associated error matrix), the matrix of derivatives of the hit positions with respect to track vector components, and the covariance matrix of the BC track vector. Corrections are made for the mass-dependent fits, using the derivatives.

The effectiveness of hybridisation is well illustrated on figure 3.6, which shows how the momentum error is substantially reduced by the process. About 85% of beam tracks hybridise and 75% of outgoing hybrid candidates are successful. In hydrogen at 6 GeV/c there is rarely more than one outgoing hybrid candidate, but at 9 GeV/c there are often two. Thus, about $\frac{2}{3}$ of events are fully hybridised at 6 GeV/c and slightly more at 9 GeV/c. This fraction is nearer to $\frac{1}{2}$ in deuterium, mainly because of secondary interactions in the liquid.

3.4 KINEMATIC FITTING OF HYPOTHESES

Once the momentum vectors of the charged particles have been obtained, an attempt can be made to determine their masses (m) and to identify any neutral particles present. This is done using the standard Rutherford Laboratory KINEMATICS program (ref. 3.2) which applies a number of different physical hypotheses of appropriate topology to each event. At the primary vertex the four constraint equations of energy-momentum conservation must be satisfied, to within a certain tolerance:

Fig. 3.6   Scatterplot illustrating the effect of hybridisation on the momentum error.

(6 GeV/c, Phase I)
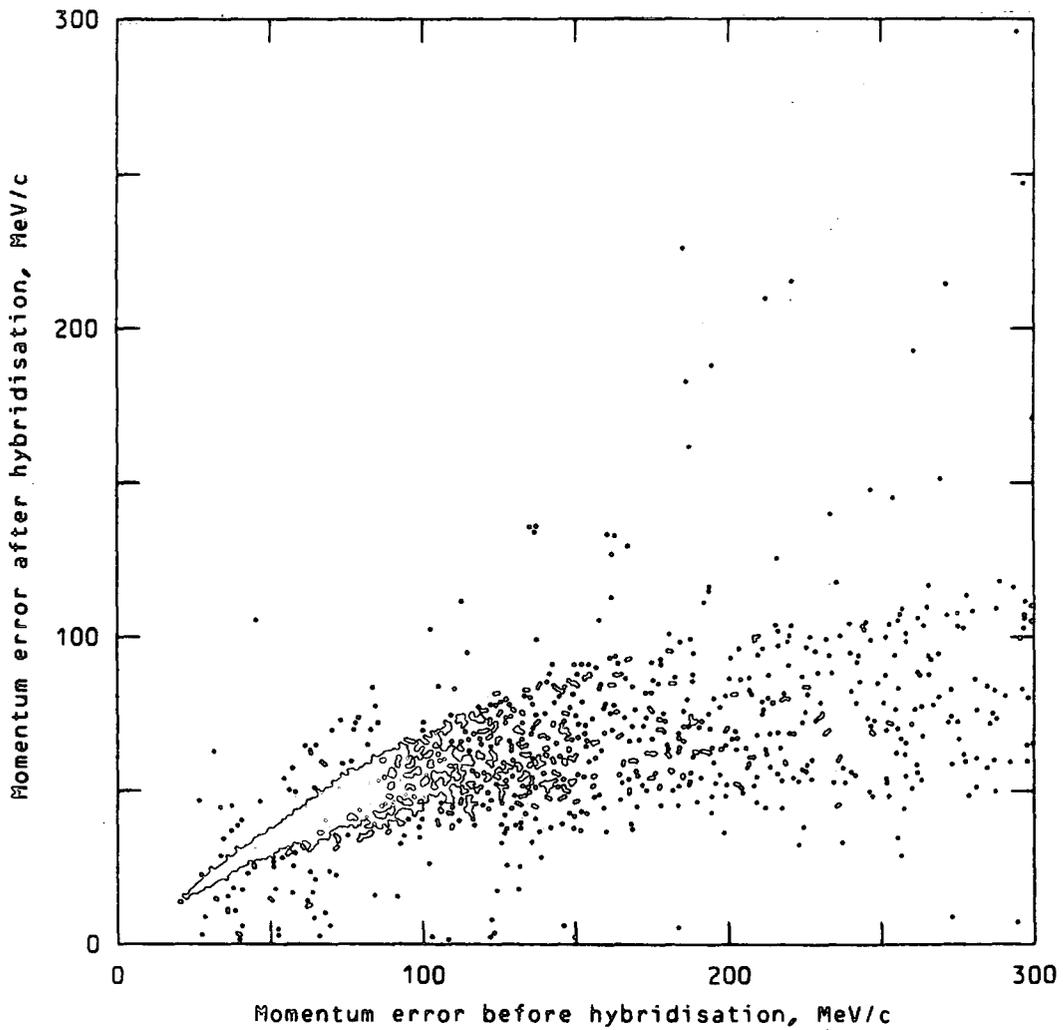
$$p_b \cos \lambda_b \cos \phi_b = \sum p_i \cos \lambda_i \cos \phi_i$$

$$p_b \cos \lambda_b \sin \phi_b = \sum p_i \cos \lambda_i \sin \phi_i$$

$$p_b \sin \lambda_b = \sum p_i \sin \lambda_i$$

$$\sqrt{p_b^2 + m_b^2} + m_t = \sum \left(\sqrt{p_i^2 + m_i^2} \right)$$

where the summation index i refers to all outgoing particles, subscript
b to the beam particle, and subscript t to the target particle. If
all particles in the hypothesis are charged and well measured, there
are four constraining equations and this is called a 4C fit. If, however,
there is one neutral particle in the final state of the hypothesis, three
quantities are unknown and so there is only one constraint (1C fit).
With more than one neutral particle the equations are unconstrained
(unless there are more vertices) and only a missing mass may be calculated
(no-fit). In this way a number of Kinematic hypotheses may be eliminated
and many events, notably 4C fits, have only one possible interpretation.
Also, for constrained fits, the accuracy of the momentum vectors is
improved by fitting.

At the energies used in this experiment there is a very large number
of possible hypotheses, which must be formatted in a special way for
KINEMATICS. For this reason a program HYPGEN was written for generating
hypotheses. For a given topology, the program loops through all combin-
ations of "stable" particles and checks every one against conservation
of charge, baryon number, strangeness, and energy. A priority was
assigned to each hypothesis based on its a-priori probability e.g.
hypotheses for single vertex topologies with final state strange
particles were given low priority. This priority was used in the choicing
procedure (section 3.5.4).

3.5   RESOLUTION OF KINEMATIC AMBIGUITIES (CHOICING)

After Kinematic fitting, certain hypotheses can be rejected on the

basis of low χ^2 probability, or a-priori knowledge of the "likeliness"

of a hypothesis compared to others.   Further selections may be made by

testing the particle mass assignments for consistency with measured

track ionisation (for slow particles) and Canute pulse heights (for fast

particles).   This is called "choicing" and is performed by the program

ORACLE, which also handles two other tasks: updating the Master List;

and writing the DST.   The Master List is a book-keeping system for record-

ing the current status of events in the analysis chain.   Events which fail

at various stages can be sent back for re-measure, which often successfully

rescues the events.   The DST (data summary tape) contains information on

the momentum vectors of particles, vertex positions, successful Kinematic

fits, and hybridisation status.   After combining DST's from the different

laboratories, the program SUMX is run in order to further the physics

analysis.

The remainder of this section gives details of the choicing procedure.

3.5.1   Canute characteristics

As well as being used in the trigger, the Cerenkov counter "Canute"

is useful for identifying any fast outgoing particles.   In order to do

this, the characteristics must be well known (ref. 3.3).

A cutaway drawing of Canute is shown in figure 3.7.   The pressure

tank is 335 cm in diameter and 406 cm high, and made of aluminium 1.9

cm thick.   To reduce particle interactions in the walls, entrance and

exit windows are provided with a thickness of 5.7 mm and covering an

area 102 cm wide by 204 cm high.   The tank is filled with Freon-12 at 1

to 4 atmospheres pressure, which has a refractive index n given by

$$n \; = \; 1 + \varepsilon$$

$$\text{where} \quad \varepsilon \; = \; 1.076 \times 10^{-3} \times P$$

and P is the pressure in atmospheres.
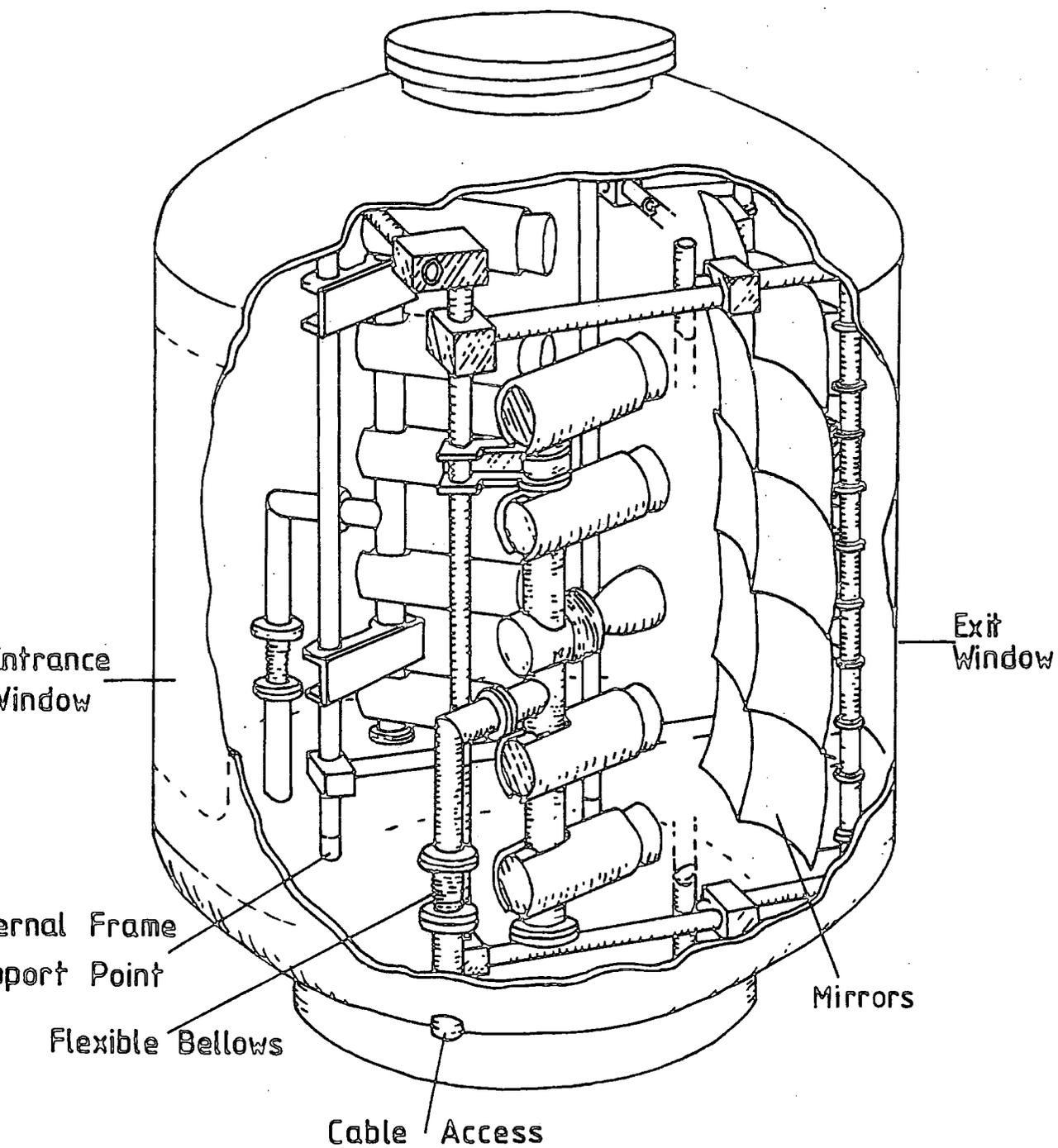
Fig. 3.7   Cutaway Drawing Of The Cerenkov Counter, CANUTE

Particles passing through the gas emit Cerenkov radiation if their velocity is greater than the threshold : $\beta > 1/n$. The light is reflected by an array of twelve mirrors (only ten are shown in the diagram) into photomultiplier tubes, guided by light-collecting cones. The signals from the phototubes are passed through ADC's (Analogue to Digital Converters) so that they can be read into the computer as pulse heights.

The choicing program ORACLE needs to know the predicted pulse heights in each mirror for the two mass hypotheses pion and kaon (the prediction for (anti-) protons is always zero). They are derived using the equations given in appendix B. The fractions of light in each mirror are found by swimming the outgoing hybridised tracks to the mirror plane (at $x = x_c$). It was found that, in order to get good agreement between predicted and observed pulse heights, it is necessary to fit x_c and the y and z positions of the mirror edges, and also the twelve gains A_i (the conversion factors from photoelectrons to ADC channels).

Gains

The phototube gains were adjusted before the run to be approximately the same, so that pulse heights could be usefully added. Using these nominal gains, a plot of predicted pulse height against observed pulse height was made for each mirror using a selection of events which gave a unique 4C fit identifying the fast outgoing particle as a pion (see fig. 3.8). A best straight line was drawn through the points, the gradient of which was the correction factor for the gain. Figure 3.9 is a histogram for these events of the quantity

$$S_{local} = \frac{\text{measured pulse height} - \text{predicted pulse height}}{\text{error in predicted pulse height}}$$

where pulse heights are summed over the mirrors predicted to be hit plus the adjacent mirrors ("local" sum). The histogram shows that the predictions

Fig. 3.8   Signal from pion tracks in mirror 2

6 GeV/c

Phase I data

Fig. 3.9   6 GeV/c

Phase I data
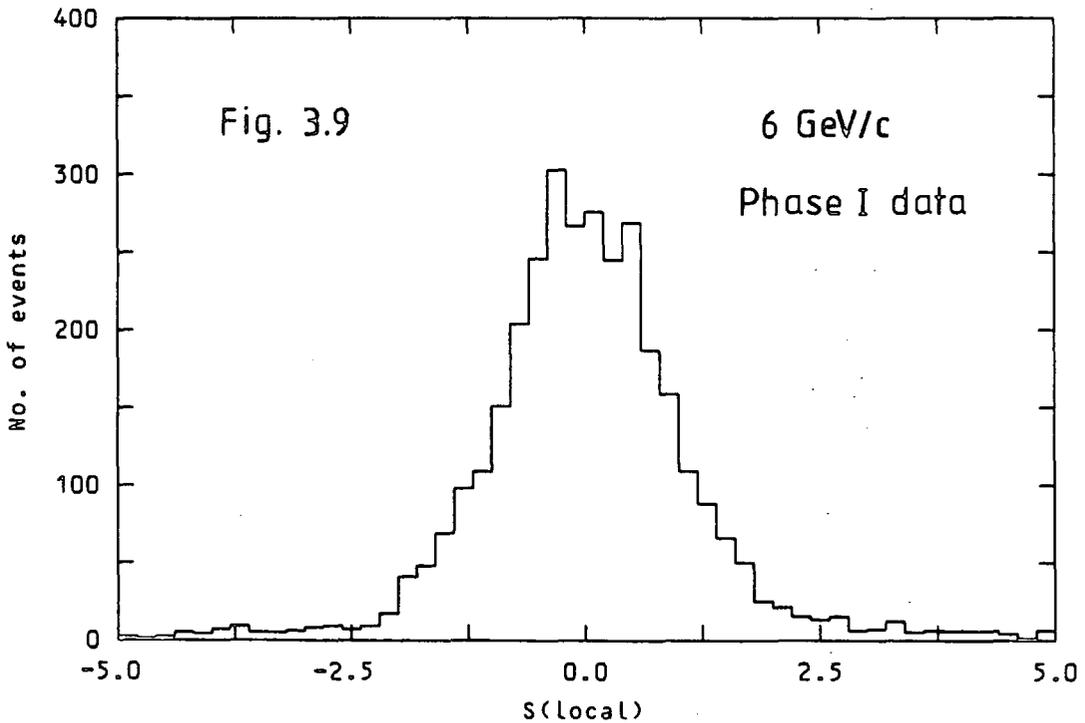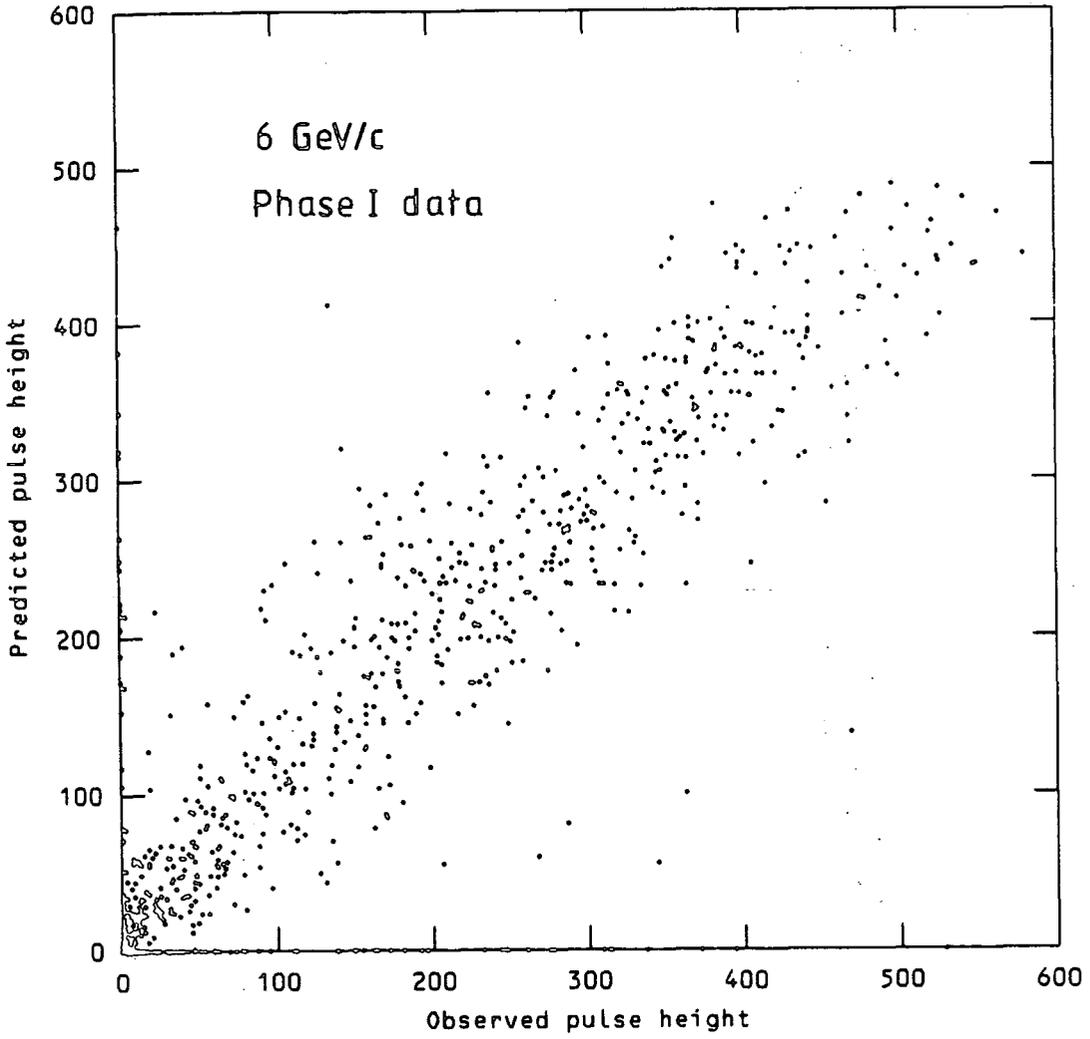
work well, the mean being 0.014 and the standard deviation 1.15, compared

with the ideal values of 0 and 1 respectively.

Mirror positions

The boundaries between adjacent mirrors were located by plotting an

asymmetry ratio r as a function of predicted track intercept. For example,

in the z direction the function plotted in fig. 3.10 is

$$r(z) = \frac{CR - CL}{CR + CL}$$

where CR = sum of observed pulse heights in right hand mirrors

and CL = sum of observed pulse heights in left hand mirrors

(corrected for gain variation from mirror to mirror). The boundary

between the right and left mirrors is thus seen to be at z = -25 cm from

where the curve crosses r = 0, which is in fact the nominal position.

Similar ratios were plotted for the five y-boundaries and, using the

constraint that the mirrors are all the same height (h), a fit was made

to determine the boundary locations and value of h. The number x_c was

then adjusted such that h derived in this way agreed with the known

height (= 55 cm). This is not accurately a realistic result, but it

corrects for simplifying assumptions about the geometry of the system

(e.g. neglecting differences in radiation length, angles of tracks,

angles and curvature of mirrors). Fitted values of x_c and gas conditions

are given in table 3.4.

Fig. 3.10

6 GeV/c Phase I data

r(Z)

Z of predicted track intercept (cm)

33

Fig. 3.11   Predicted numbers of photoelectrons as a
            function of momenta.

(a) 9 GeV/c H_2, phase I
   (i) π - meson
   (ii)   K - meson
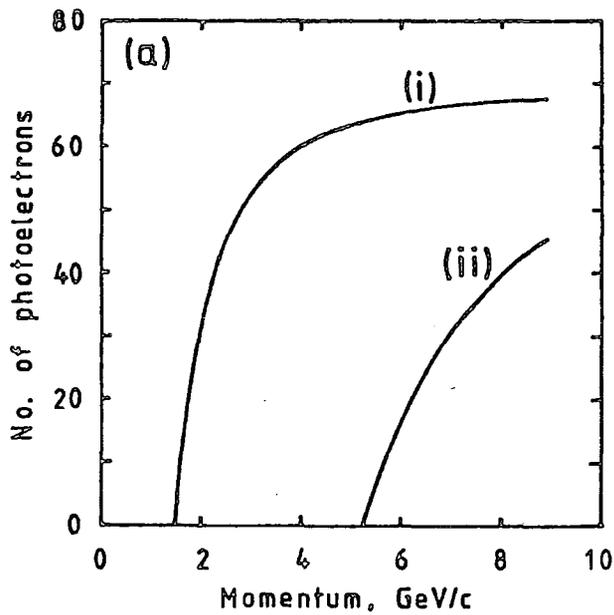
(b) 6 GeV/c H_2, phase I, π
   (i) P = 2.04 atm
   (ii) P = 1.36 atm
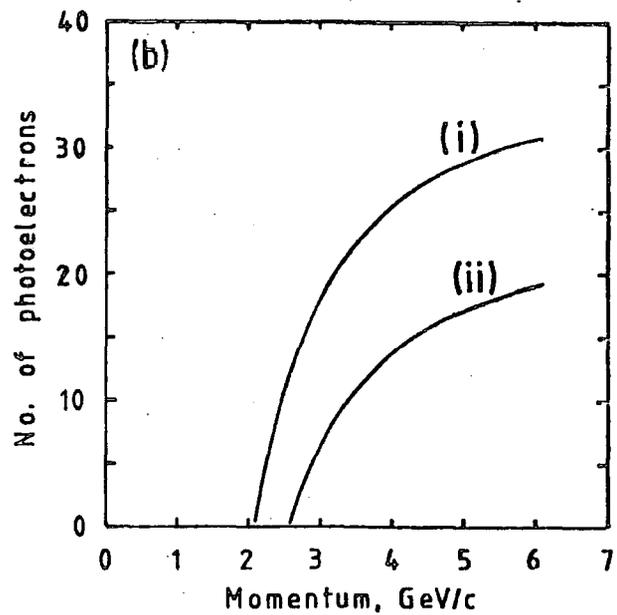
(c) 9 GeV/c, phase II, π
   (i) $H_2 + D_2$ first part
   (ii) D_2 second part
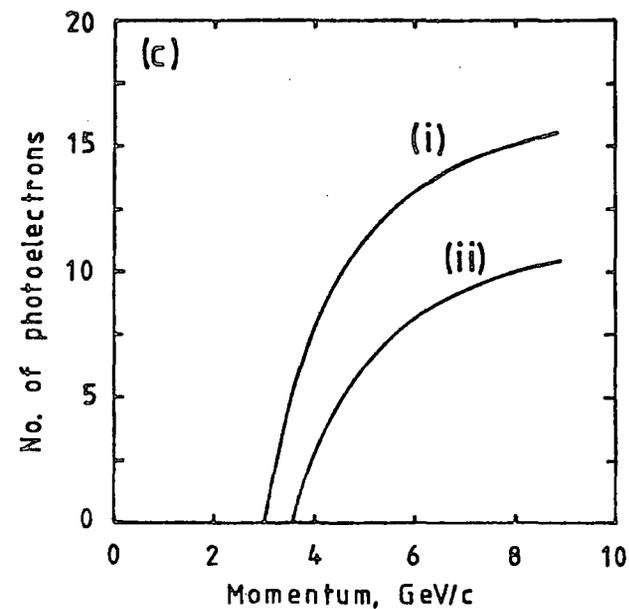
(d) 6 GeV/c D_2, π
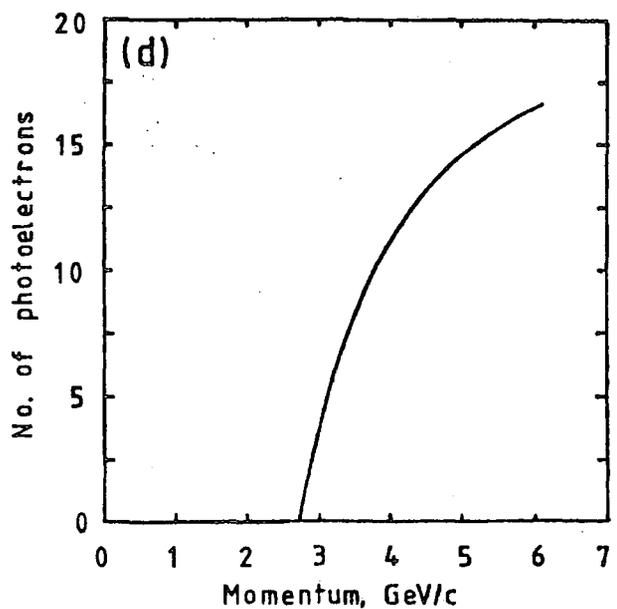
producing secondary pions; (c) by delta-ray production in the gas of Canute which, being very low in mass, are often above threshold. Hence, generally, antiprotons may be distinguished from pions as giving too little light or light in the wrong place; however, interacting pions produce a similar effect.

The test used at Rutherford laboratory for Phase I is:

1. events are excluded from the test if:-

    (a) there are no hybrid candidates (defined in section 3.3.4).

    (b) two or more tracks hit the same mirror

    (c) no tracks give predicted light for pion mass greater than a noise level (= 3 photoelectrons).

    (d) Canute conditions were not fixed or known accurately.

2. Pion mass test

    for mirrors which are predicted to receive light from a pion greater than the noise level (but excluding those which could receive light from other nearby tracks); reject if $S_i < -3.0$ for any of these mirrors. S_i = (measured pulse-height - predicted pulse-height)/error in predicted pulse-height for mirror i.

3. Kaon mass test

    for the same mirrors defined above, but excluding those for which both measured and predicted light for a kaon are less than the noise-level; reject if $|S_i| > 3$.

4. (Anti-)Proton Mass test

    for the principal mirror only (i.e. the one hit by the particle); reject if measured pulse height > 2 x noise level.

These tests are performed on each of the tracks designated "hybrid candidates" according to the mass assigned in the hypothesis (independent of charge), and if the assignment is rejected for any track, the hypothesis is rejected. It is possible for all three mass assignments

to be rejected for a given track; such events are mainly antiproton triggers and are rejected outright. A corresponding set of tests were devised for phase II.

The tests described above were arrived at after trying a number of different tests and measuring their performance by using a sample of unique 4C fit events. The identity of the triggering particle given by the 4C fit was assumed to be the true one, and events were divided into two categories: π triggers and p triggers. The latter includes proton and antiproton triggers, but are in practice overwhelmingly antiproton triggers. Kaon triggers are very rare and were not considered. The following figures of merit are useful (given for events with only one hybrid candidate): p = % of events which are π triggers (as given by 4C fit); u, usefulness = % of events for which Canute makes a decision (i.e. one of π or p trigger); Out of the selection of events for which Canute makes a decision we then define: c, contamination = % of events identified by Canute as π-triggers which are in fact p triggers, and l loss = % of π triggers which are identified by Canute as p triggers.

These figures are given in table 3.5 for each of the experimental runs:

TABLE 3.5   CANUTE CHOICING PERFORMANCE

	p	u	c	l	(%)
Phase I, 6 GeV, H_2	37	91	13	1	
Phase I, 9 GeV, H_2	24	73	21	3	
Phase II, 9 GeV, H_2	45	88	18	5	
Phase II, 9 GeV, D_2	75	79	10	13	

The following points should be noted: (a) the table does not give figures

for events with two hybrid candidates (e.g. one π and one $\bar{p}$) - at 9 GeV

these are very numerous; (b) the proportion of pion triggers is much

higher in Phase II as a result of the changes made to the algorithm;

(c) the actual contamination in a choiced sample of π-triggered events

will be much less than c, as it depends on the actual level of Kinematic

ambiguities and the effectiveness of other choicing methods (e.g.

ionisation). Similarly the actual losses of π-triggers will be less than l.

3.5.3. Use of Ionisation Information

It is well known that the bubble density of a track in a bubble

chamber produced by an ionising particle of mass m and momentum p is given

by

$$b = b_o \left(1 + \frac{m^2}{p^2}\right)$$

where b_o is the bubble density of a minimum ionising (β = 1) track. Thus

the relative bubble density of a track of known momentum can be predicted

for the three "stable" particle masses π, K, and p, and compared with the

observed bubble density. No manual judging was done in this experiment,

since the HPD was used. The filter program described in section 3.2.3

determines the number of "stringed" digitisings per slice from which

(correcting for the angle of the track from the view direction) the

bubble density on each view is calculated, normalised to the minimum

ionising tracks on that view (beam track and fast outgoing tracks).

It is very difficult to distinguish tracks reliably with a relative

bubble density of less than 1.45 on this film (the HPD can operate better

than this, but 1.45 is a more typical number with this film). Therefore,

if the predictions for pion and proton mass are within this factor no

choice is attempted (for non-dipping tracks, this corresponds to momenta

greater than 1.38 GeV/c). For tracks which pass this test, a simple

chi-squared is calculated for each mass assignment, comparing measured with predicted bubble densities. Mass assignments with a χ^2 greater than twice the minimum χ^2 are excluded, but there must be agreement on at least two views (or three views for highly dipping tracks). If any of the tracks identified in this way are inconsistent with the mass assigned in a Kinematic hypothesis, the hypothesis is rejected in choicing.

For a typical roll of 4C fits at 9 GeV (Phase I), out of all the tracks where an ionisation choice was possible, there were: 51% uniquely and correctly identified; 43% two-fold ambiguous (π/K or K/p); 3% three-fold ambiguous (π/ K/p); and 3% incorrectly identified.

3.5.4. Choicing Logic

The program ORACLE puts every event into one of four classes:

(A) Rejects - includes events that are not expected to be used for cross-section and normalisation purposes and are not remeasured.

(B) Remeasures - events with no hypotheses satisfying the necessary conditions for a successful interpretation of the measurements - perhaps due to bad measurements or an incorrect error structure.

(C) Unique - only one hypothesis satisfies all the tests; these are written to the DST.

(D) Ambiguous - more than one hypothesis satisfies the tests; these are written to the DST.

A flow chart showing the choicing logic used at Rutherford Laboratory is shown in figure 3.12. The following points need to be explained:

Fig. 3.12 Choicing Logic   90

Fig. 3.12 Choicing Logic
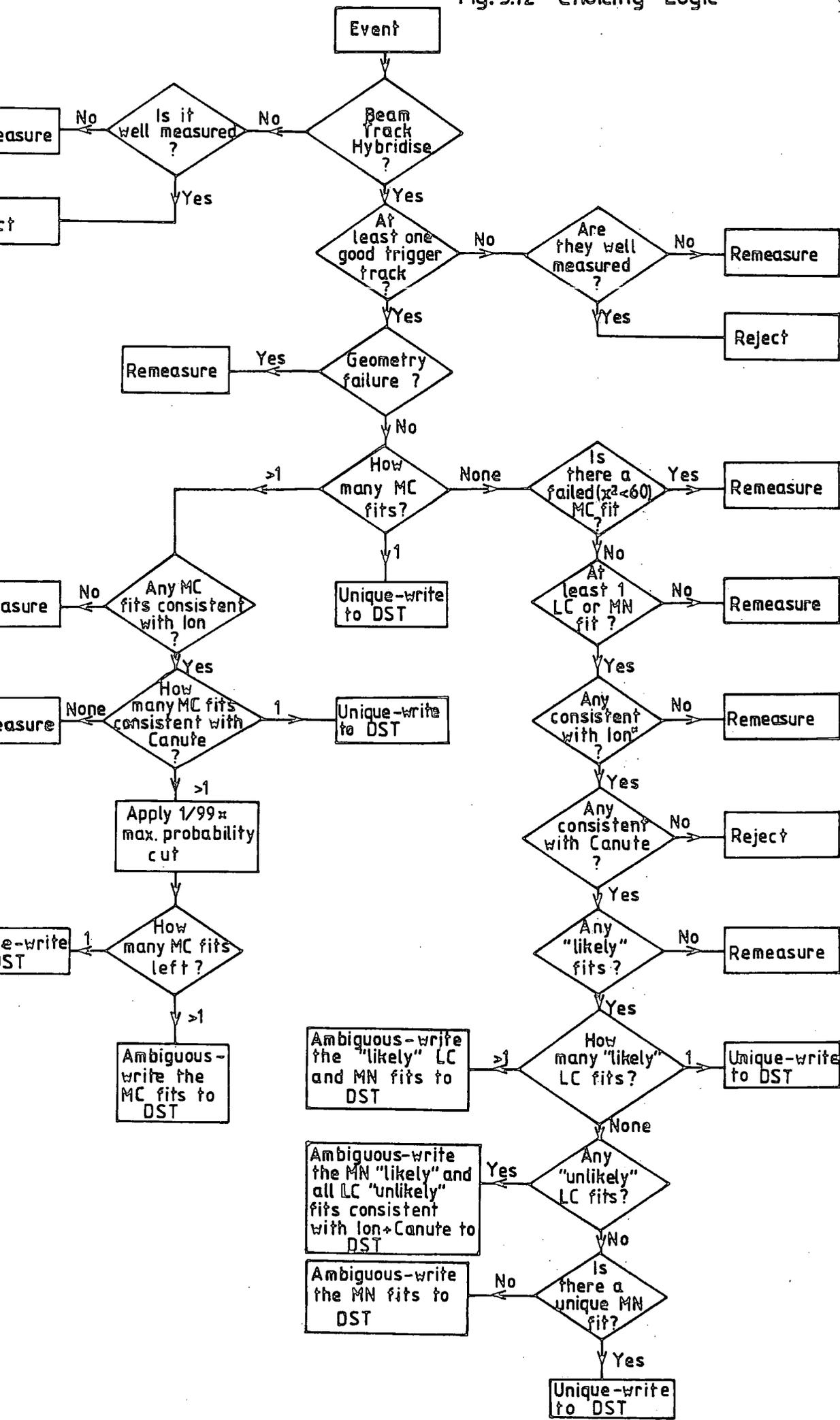
1. All "fits" i.e. Kinematic interpretations are divided into three

    categories:

    (a) MC – Multi-Constraint fits i.e. $\geqslant 3$ constraints with

    $$\chi^2\text{-probability} > 10^{-5};$$

    (b) LC – Low-constraint fits i.e. 1 or 2 constraints, with

    $$\chi^2\text{-probability} > 10^{-3};$$

    (c) MN – Multi-neutral interpretations (not really fits) where the

    missing mass is consistent with that of the expected missing

    neutral particle and at least one extra π^o.

2. The hypotheses which LC and MN fits satisfy are either "likely" or

    "unlikely", depending on their a-priori probability. This is a

    classification defined by the hypothesis generating program (sec. 3.4);

    a hypothesis is deemed "unlikely" if there are final state strange

    particles, but no $V^{\pm}$ or V^o in the topology e.g. $\bar{p}p \rightarrow 2\pi^+ \pi^- K^- K^o$.

    A hypothesis may also be unlikely if there is a small amount of phase

    space available to the final state particles:

3. A "well-measured" track is defined as one with an r.m.s. residual

    less than 7.5 μm on film.

4. A "good trigger track" is a well-measured, hybridised outgoing track

    with momentum above the trigger threshold (4.0 GeV/c for 9 GeV/c data

    and 2.5 GeV/c for 6 GeV/c data).

5. A "failed ($\chi^2 < 60$) MC fit" is one of too low χ^2-probability to be

    acceptable ($\chi^2 > 26 \equiv$ Prob (χ^2) $< 10^{-5}$), but not too low to be

    ignored. Such events are sent for remeasure.

6. The "$\frac{1}{99}$ x Max probability cut" is a selection to eliminate multi-

    constraint fits with a χ^2-probability less than $\frac{1}{99}$ x P_{max}, where

    P_{max} is the maximum χ^2-probability of the fits in the sample.

    ($\frac{1}{99}$ was chosen rather than 1% for computational reasons).

3.5.5. Throughput Statistics

With the choicing algorithm described above, events were analysed in detail for one roll in each batch of data. It was found that the number of events which could benefit by a manual "judging" on the scan table was only 2% for the 9 GeV Phase I data and 4% for the 6 GeV Phase I data. therefore, it was decided not to do any "judging" at Rutherford Laboratory.

Events falling in the "Remeasure" class were sent for a second measure, and were re-processed through the analysis chain, but with slightly different choicing logic (mainly to rescue events with genuine fits to "unlikely" hypotheses). The final throughput statistics for the hydrogen data after two measures (no third measure was made) are as follows:

TABLE 3.6   THROUGHPUT STATISTICS FOR THE HYDROGEN DATA

	6 GeV/c, phase I	9 GeV/c, phase I	9 GeV/c, phase II
DST	53%	46%	47%
Remeasure	12%	12%	13%
Reject	33%	40%	36%
Unmeasureable	2%	2%	4%

Of the events rejected, nearly all were because of failure to hybridise; about 36% had a beam track which did not hybridise, and 57% had no fast hybridised downstream track. Of the events needing a further remeasure, most failed in geometrical reconstruction or else had no Kinematic fit (MC, LC, or MN). A break-down of the DST events for one roll of 6 GeV/c (phase I) data is given in table 3.7. Most ambiguities are between LC

and MN fits, and these can often be resolved by physics selections in particular channels. Generally, the level of ambiguity is much lower than one would expect for a conventional bubble chamber experiment, mainly because of the use of Canute.

TABLE 3.7 AMBIGUITY LEVELS FOR ONE ROLL OF 6 GeV/c, H_2 DATA

	No. of Events	%
DST Unique	287	80
(i) Multi-constraint (MC)	63	18
(ii) Low-constraint (LC)	120	33
(iii) Multi-neutral (MN)	104	29
DST Ambiguous	73	20
(i) MC	1	0.3
(ii) LC (+MN) "likely"	21	6
(iii) MN "likely" + LC "unlikely"	40	11
(iv) MN "likely" only	11	3

3.6   MEASUREMENT ACCURACY AND QUALITY CONTROL

The accuracy of film measurement and reliability of the constants can be checked by a variety of methods to ensure that errors are acceptable and that there are no appreciable biases. This section describes the most useful and sensitive methods.

3.6.1   Helix fit residuals

The geometrical reconstruction program calculates for each track a helix fit residual. This is defined as the r.m.s. distance between the rays projected from the measured points on each view and the fitted helix, transformed to the film plane. The distribution of residuals for 6 GeV/c

hydrogen film is shown in figure 3.13(a) and (b) for the beam track and outgoing tracks respectively. For the beam track, the distribution peaks at 1.9 μm with a mean of 2.8 μm and with 3% greater than 7.5 μm. For outgoing tracks, the distribution peaks at 2.3 μm with a mean of 4.0 μm and with 9% greater than 7.5 μm. The source of the errors is a combination of four things: film measurement inaccuracy; errors in optical reconstruction; spiralling due to momentum loss; and multiple coulomb scattering. The last two effects are more appreciable for low momentum tracks, which is why the outgoing tracks have rather larger residuals than beam tracks. Thus, according to this check, the measurement accuracy and optical constants are good.

3.6.2 Stretches, Missing Masses, and Probability (χ^2) checks

The goodness of the Kinematic fit can be checked by three methods which are very sensitive to biases, and allow one to check the size of the errors. The first is to plot the distribution of the stretch function

$$\frac{F - U}{\sqrt{\sigma_u^2 - \sigma_F^2}}$$

for the three track variables $1/p$, λ, ϕ, where

F = fitted value (i.e. from a constrained Kinematic fit to a hypothesis).

U = unfitted value (i.e. measured value given by the geometrical reconstruction with a mass-dependent helix fit, and hybridised if appropriate).

σ_F = error on fitted value

σ_U = error on unfitted value.

This function has the property of being normally distributed with mean of zero and variance of 1.0, and any variation from this will result from

Fig. 3.13(a)   Beam tracks: 6 GeV/c Phase 1

No. of tracks

Helix fit residual (microns)
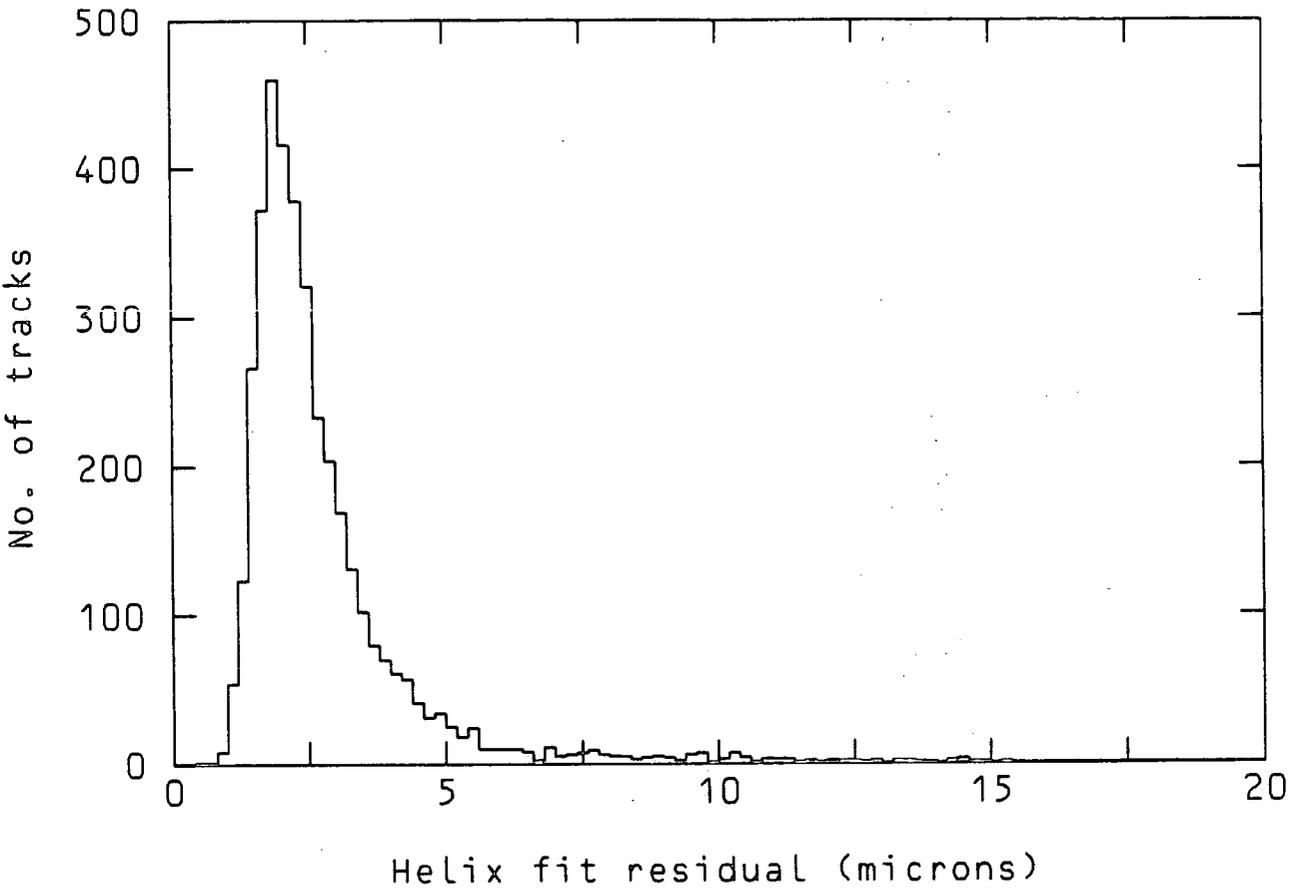
(b)   Outgoing tracks: 6 GeV/c Phase 1

Helix fit residual (microns)
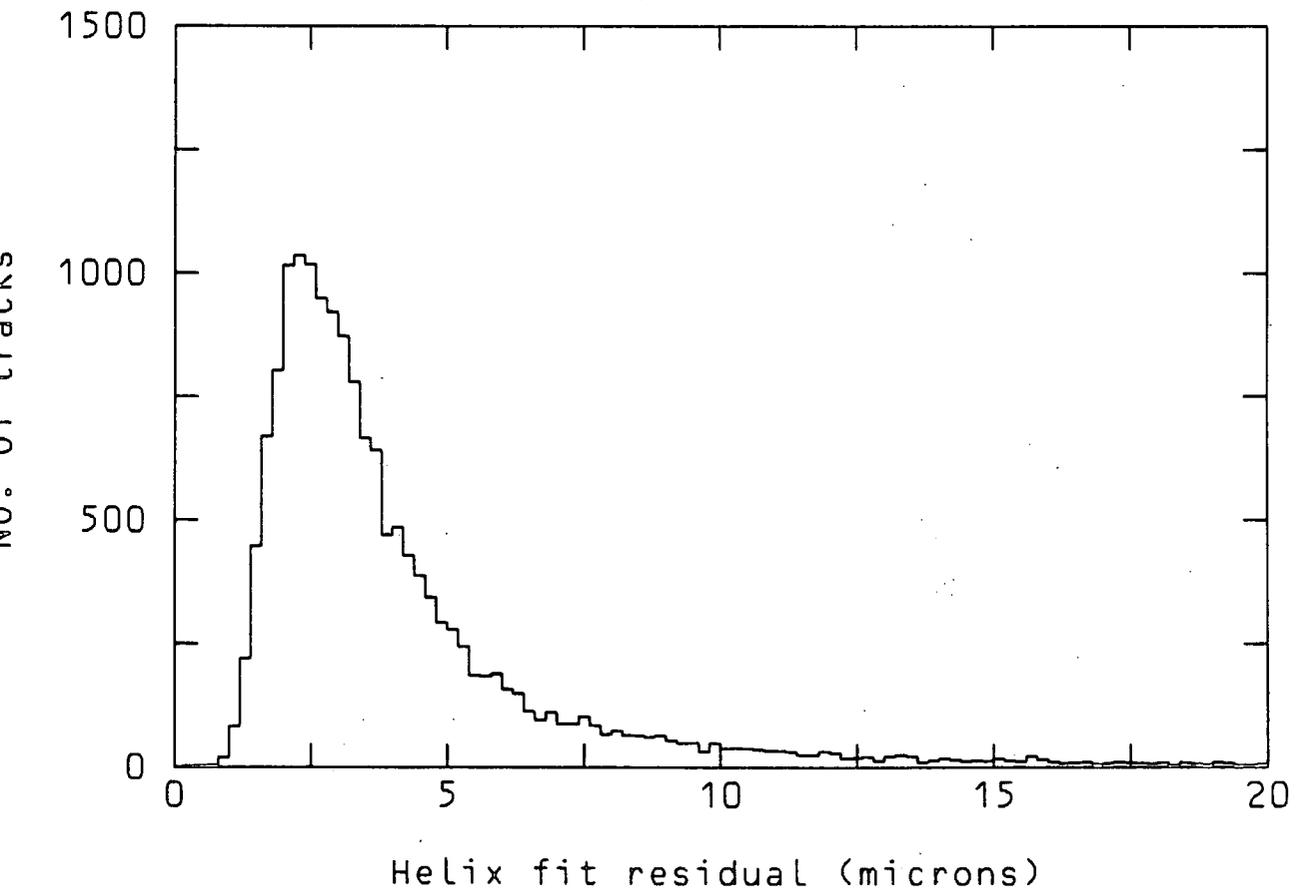
systematic errors. Figure 3.14 shows typical stretch distributions from

a sample of 4C fits (6 GeV Phase I data) for the beam tracks; and table

3.8 gives the means and standard deviations of the stretches for these

tracks and also for outgoing tracks, which are separated according to

the sign of their charge and their momenta ("fast" = above 2.5 GeV/c,

"slow" = below 2.5 GeV/c).

As can be seen, the stretch widths are all close to 1.0 showing that

the errors are scaled correctly, but the means are significantly different

from zero, indicating systematic errors. However, although these

systematic errors are significant compared with the random errors, they

are in magnitude very small and are only apparent because of the small

errors on the variables. The differences between the fitted and unfitted

values have means and widths as given in the table under the column "F-U".

It will be seen that the worst stretch means correspond to systematic

momentum errors of <0.5% and angular errors of ∿0.2 m rads. It is believed

that the cause of the systematic errors is an imperfect description of the

optical properties of the bubble chamber, thus it was found that the stretch

means depended sensitively on the type of lens distortion parametrisation

used, and the one finally chosen was that which gave best overall performance.

(see section 3.3.1).

The method of stretches is a very sensitive one for examining

systematic errors in the momentum vectors. However it is not obvious how

these errors are manifested in quantities of physics interest, such as

invariant masses. For this reason, a check is made on the missing mass to

the unfitted track vectors for events which give a 4C fit to the channel

$\bar{p}p \rightarrow \bar{p}p \pi^+ \pi^-$, which should be zero. Further checks are made by dropping

each final state particle in turn from the invariant mass combination,

which should then yield a missing mass equal to the known missing particle

Beam stretch distribution (6GeV Phase 1)
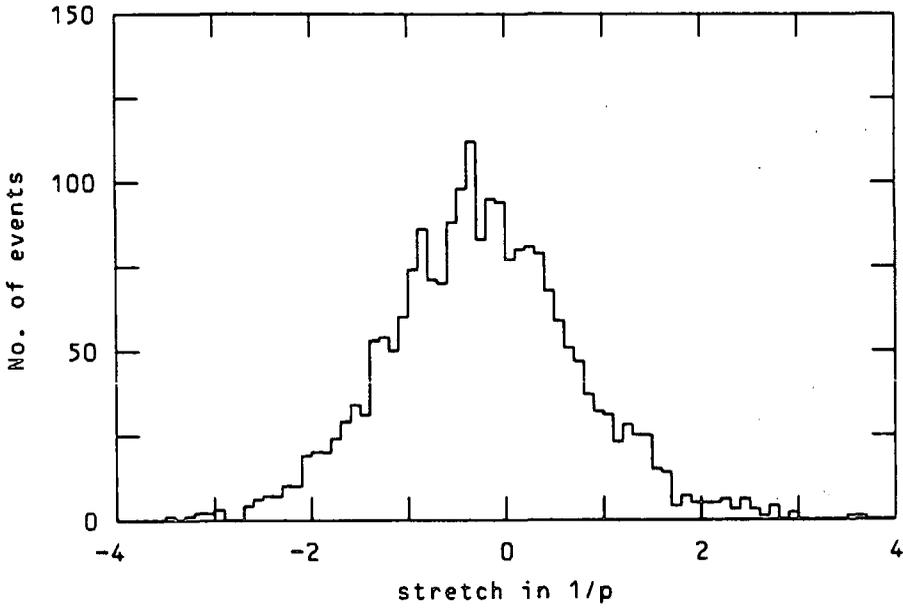
Fig. 3.14

Beam stretch distribution (6GeV Phase 1)
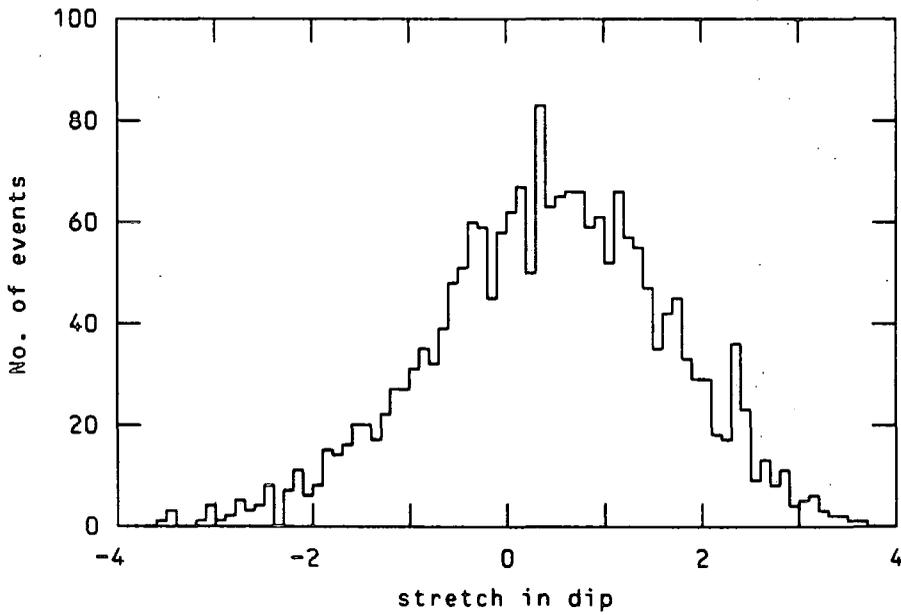
Beam stretch distribution (6GeV Phase 1)
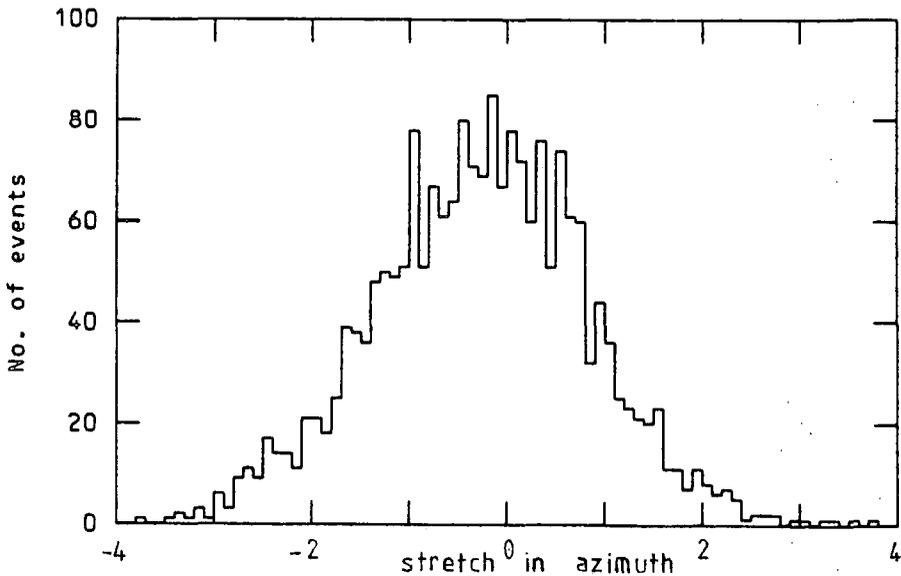
TABLE 3.8 COMPARISON OF FITTED AND UNFITTED TRACK VARIABLES

Track	Variable	Stretch Means	Stretch Widths	F-U in MeV* or mrads Mean	Width
Beam		-0.24	0.95	11	37
Slow +		0.11	1.03	-1.0	13
Slow -	$\frac{1}{P}$	0.02	1.01	-0.5	13
Fast +		0.40	1.03	-13	46
Fast -		0.07	0.96	-0.5	64
Beam		0.41	1.16	0.12	0.49
Slow +		-0.29	1.12	-0.33	1.52
Slow -	λ	-0.29	1.12	-0.25	1.14
Fast +		-0.34	1.13	-0.11	0.39
Fast -		-0.43	1.17	-0.17	0.47
Beam		-0.27	1.06	-0.03	0.17
Slow +		0.14	1.06	0.10	1.64
Slow -	ϕ	0.04	1.01	0.06	1.13
Fast +		0.47	1.04	0.15	0.39
Fast -		0.00	0.94	0.02	0.39

* Values are given for $P_F - P_U$, not $\frac{1}{P_F} - \frac{1}{P_U}$.

mass. The missing mass-squared distributions for these events (6 GeV, Phase I data) are shown in figure 3.15 and the means, widths, and errors on the means of the missing masses are given in Table 3.9.

TABLE 3.9 MISSING MASSES FOR $\bar{p}p \rightarrow \bar{p}p\,\pi^+\pi^-$ EVENTS

	True MM	Mean	Width	Error on Mean	Units
All particles included*	0	-870	3150	130	MeV^2
Proton excluded	938.3	933.3	79.8	3.3	
Antiproton excluded	938.3	940.5	36.7	1.5	MeV
Pion + excluded	139.6	137.9	162	6.7	
Pion - excluded	139.6	143.4	137	5.6	

* Missing Mass squared is given.

All particles included

Excluding proton

Excluding antiproton
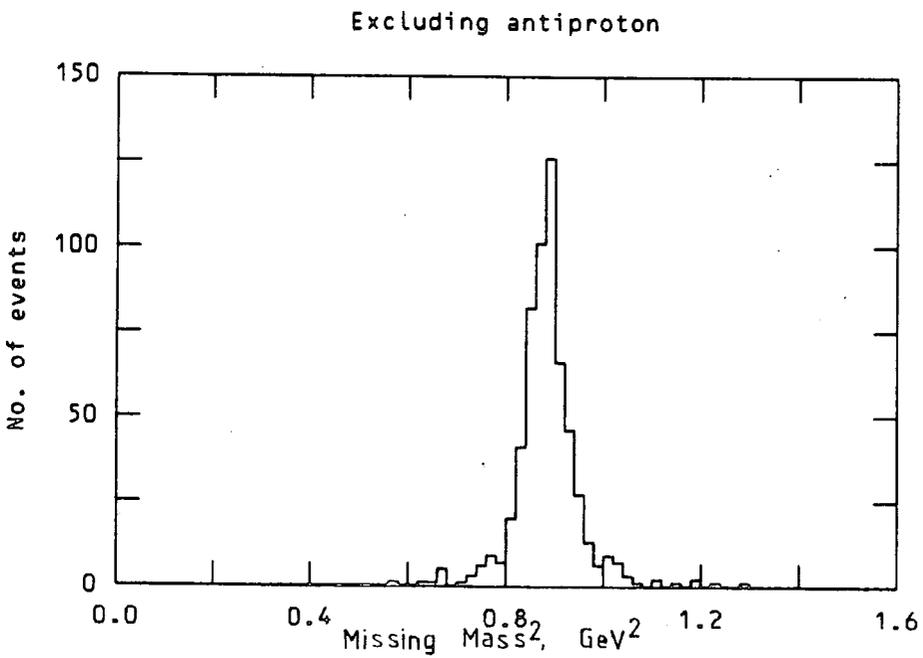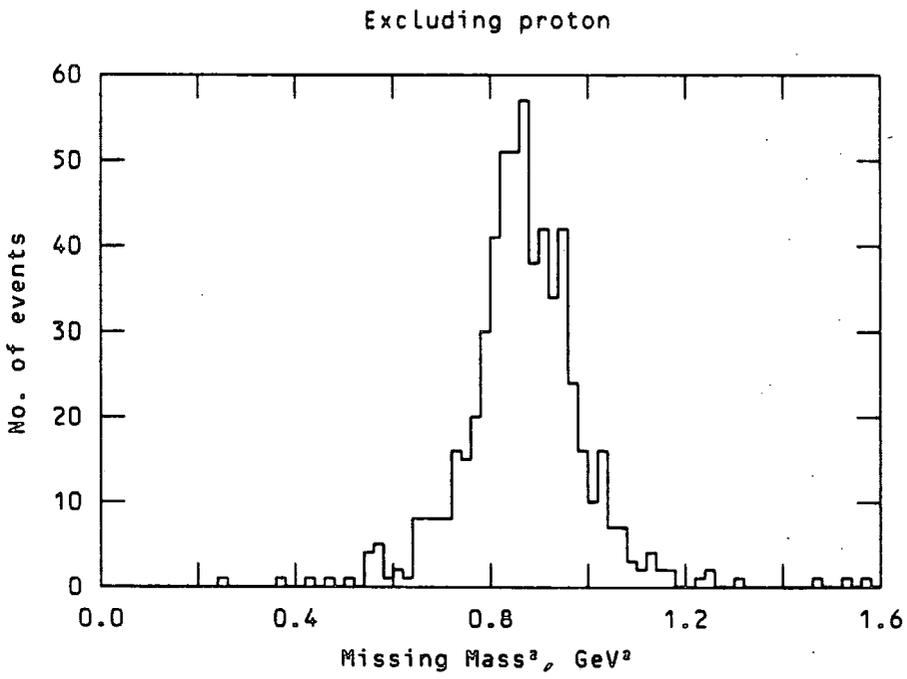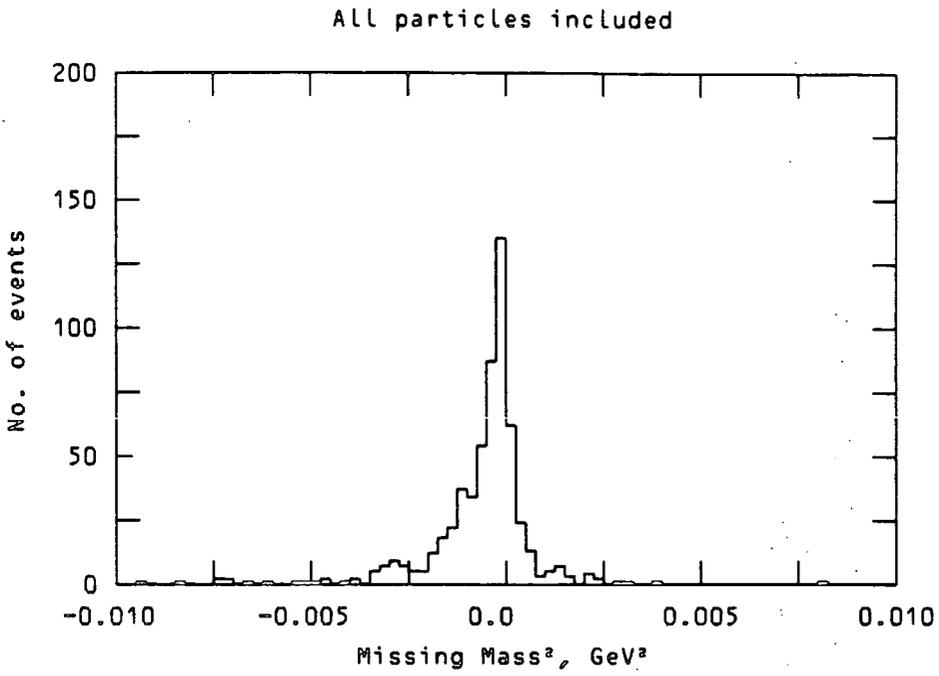
Fig. 3.15 Missing mass distributions for $\bar{p}p \to \bar{p}p\pi^+\pi^-$

Fig. 3.15 cont.

Excluding π+

Missing Mass², GeV²

Excluding π-
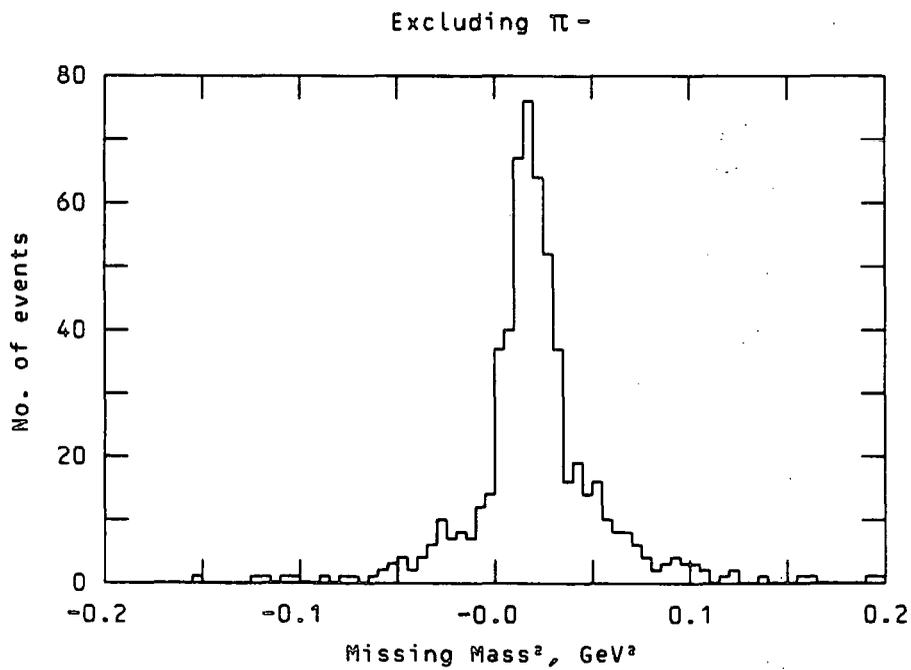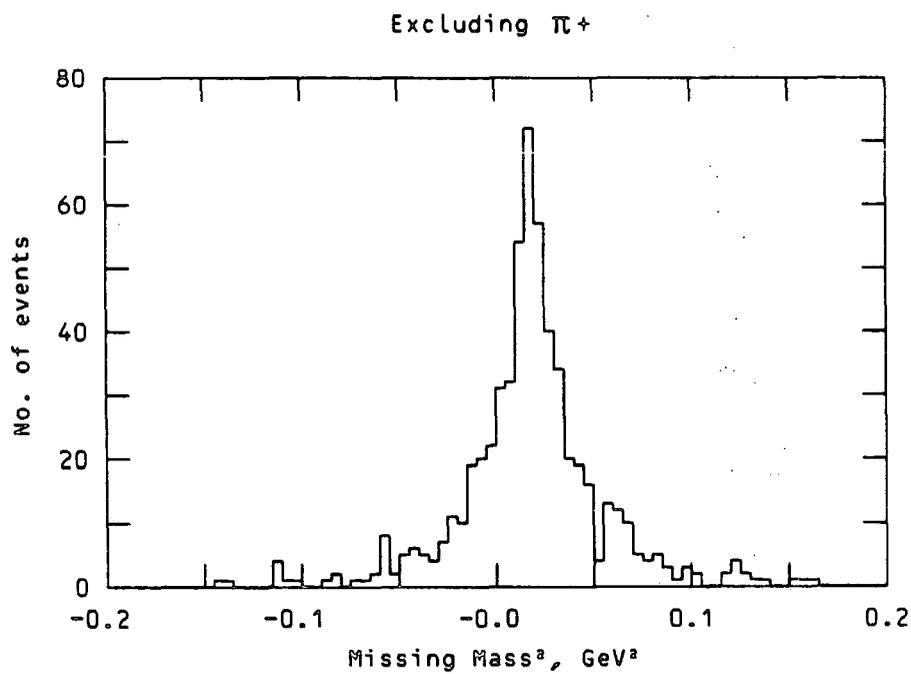
Missing Mass², GeV²

Though the overall missing mass squared is significantly non-zero, indicating a small systematic error, the missing particle masses are in excellent agreement with the known true masses. Since it is quantities of this kind that are of interest in this experiment, it is considered that the problem of errors is sufficiently dealt with.

The third method of checking Kinematic fits is from the distribution of the χ^2-probability (see figs. 3.16 (a) and (b)). It is well known that this distribution should be flat for a pure sample of genuine fits; if the errors used are too big or too small the plot will be sloping one way. The peak at low probability and the sharp peak in the first bin are due to events from other channels which accidently fit the channel giving the accepted fit, and also due to particularly bad measurements. This is worse for the 1C fits than for 4C fits because there are more ambiguities possible in the former. With the exception of this peak, the distributions are reasonably flat indicating the errors are scaled correctly.

Although this section has given examples only from the Rutherford lab. 6 GeV phase I data, comparable results are found for other batches of data and in other laboratories.

Fig. 3.16

(a) 4C Fits

(b) 1C Fits
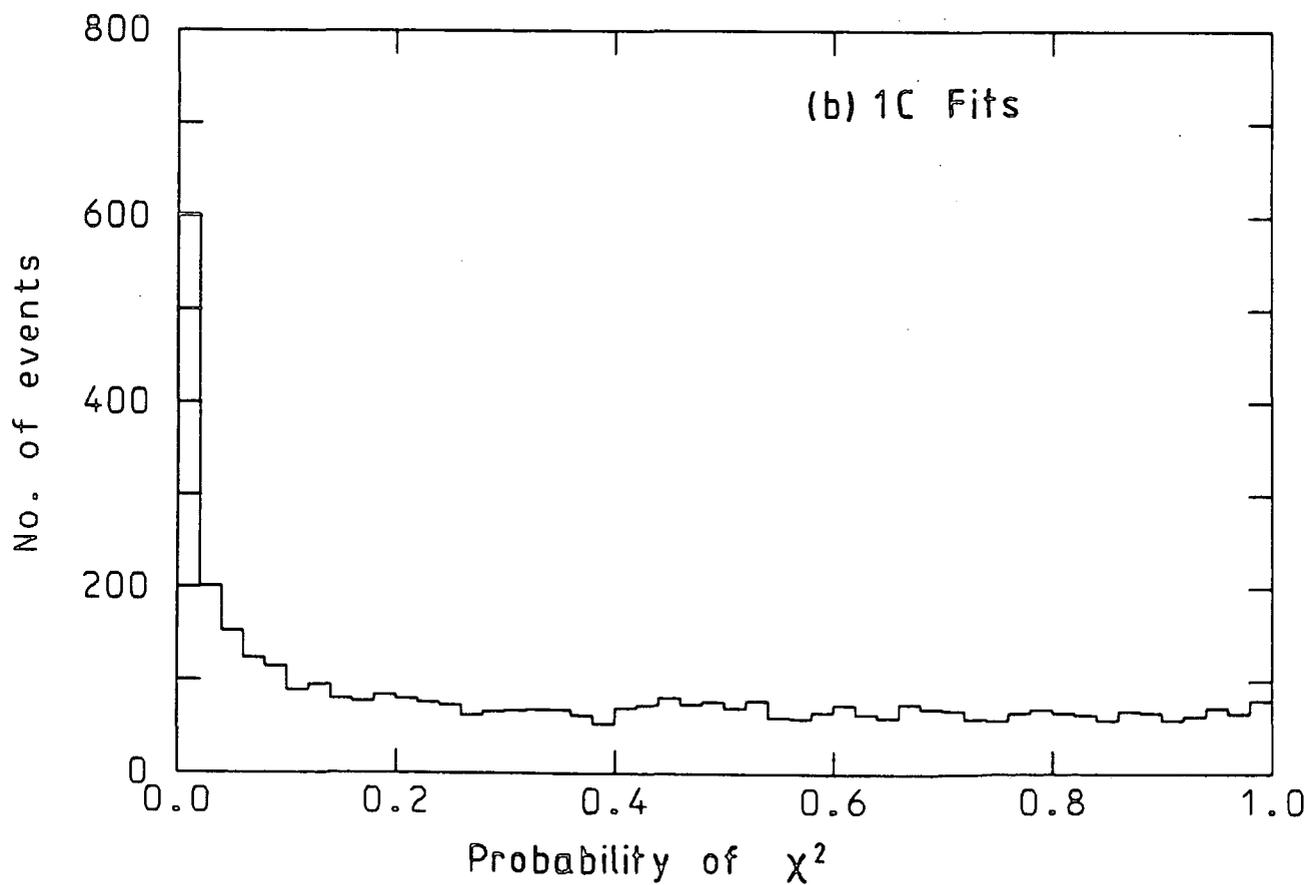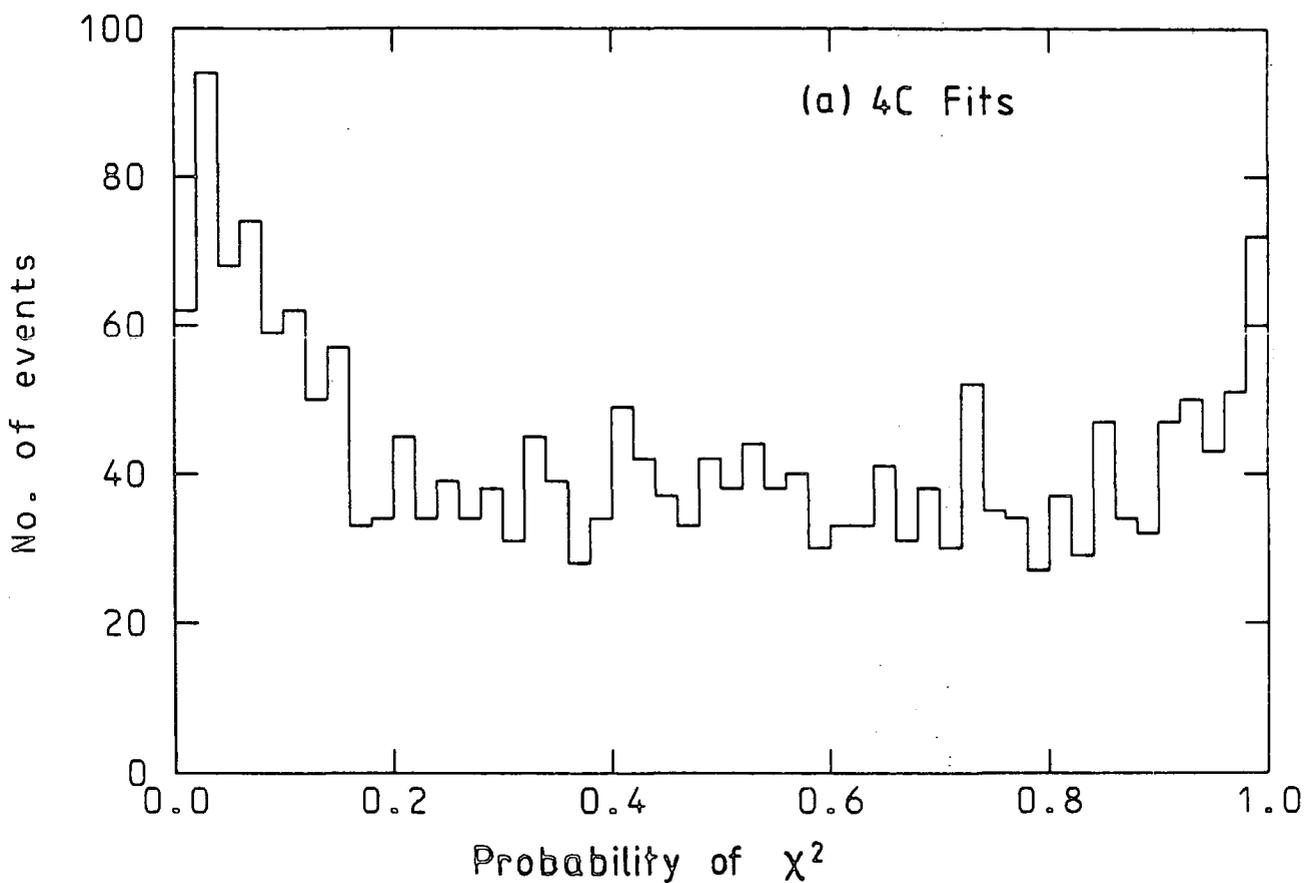
CHAPTER 4

ACCEPTANCE CONSIDERATIONS AND DETERMINATION
OF CROSS-SECTIONS

In any triggered experiment, the determination of cross-sections is
complicated by the acceptance, that is the probability that an event is
accepted by the trigger. These difficulties are dealt with in this
chapter. Two methods of normalisation are discussed, and the appropriate
choice of Kinematic variables is illustrated. Cross-sections are given
for inclusive processes $\bar{p}p \rightarrow \pi^{-} X$, and for certain multi-pion exclusive
processes. The inclusive data are fitted to the statistical thermo-
dynamic model of Hagedorn and Hoang, confirming expectations from
Feynman scaling. Only hydrogen data are used in this chapter.

4.1 ACCEPTANCE

The trigger used in this experiment selects a sample of events in
a certain region of phase space, in particular where there is a charged,
high momentum particle moving in roughly the same direction as the beam
particle. Nothing can therefore be said about events occuring outside
this region of phase space. Furthermore, within this region, an event
of a particular Kinematic configuration may not be accepted simply
because of its orientation about the beam direction or the position of
the interaction vertex. To obtain numbers which are experiment-independent,
it is clearly necessary to correct for such geometrical losses.

We define the acceptance A of an event as the probability that an
event of that particular Kinematic configuration will cause a trigger,
assuming no losses due to trigger inefficiency. It is derived by averag-
ing over the parameters which affect the acceptance, but are not
dependent on the physics of the interaction; namely, the vertex position,

the orientation about the beam direction (since the beam is unpolarised),
and statistical variations such as the Cerenkov pulse heights. Strictly,
the acceptance should include the trigger efficiency η which incorporates
the PWC efficiencies, algorithm efficiency, deadtime efficiencies etc.
(defined precisely later). However, to a good approximation, η will be
the same for every event so it is here removed as a separate factor.

Suppose we trigger on n events in a certain region of phase space.
Then the number N of events which we would have obtained had there been
no trigger is

$$N = \frac{1}{\eta} \sum_{i=1}^{n} \frac{1}{A_i} \qquad\qquad (4.1)$$

Thus, in order to obtain cross-sections and corrected plots (e.g. t-dis-
tributions, or angular distributions), the acceptance weights, $w_i = \frac{1}{A_i}$,
must be summed. Of course, the summation must only be over a region of
phase space where the acceptance is non-zero and, preferably high.

4.2   CALCULATION OF ACCEPTANCE

The acceptance was calculated for every event on the DST except
those with strange topologies or with unknown running conditions
(e.g. Canute pressure). Since the acceptance depends on the identity of
one or more forward particles, it was calculated for every Kinematic fit
allowed by the choicing tests.

A Monte Carlo method was used to choose the free parameters of the
event and to represent the geometry of the apparatus. For each event 25
trials were made, and for each trial the free parameters were chosen
randomly as follows:

(i)   The interaction vertex was chosen with x from an exponential
      distribution between -42 and +30 cm. The exponent used an

antiproton interaction length of 450 cm in liquid hydrogen (270 cm

in deuterium).

(ii)   The y and z of the vertex were chosen from gaussian distributions

with centres and widths taken from the observed distributions.

(iii) The orientation of the event was chosen from an isotropic angular

distribution around its beam track.

Outgoing tracks with momenta greater than 2 GeV/c were swum downstream,

and the Canute pulse heights were chosen for each mirror from gaussian dis-

tributions centred on the theoretical values. The geometry and logic of the

detectors were simulated both for the fast trigger and the camera trigger.

The momentum deduced by the algorithm was chosen from a gaussian distribu-

tion in $\frac{1}{p}$ centred on the actual track value, with a width corresponding to

the known resolution $(0.025 \ (GeV/c)^{-1})$.

The acceptance A of an event is given by

$$A = \frac{n_a}{n_t}$$

where n_a = number of trials accepted by the simulated trigger, n_t = number

of trials made (= 25, this being a number big enough to ensure reasonable

statistical accuracy without consuming excessive computation time). n_a

follows a binomial distribution of standard deviation $\sqrt{n_t \ A \ (1 - A)}$,

therefore

$$\delta A = \frac{1}{5} \ \sqrt{A(1 - A)}$$

Also, $w = \frac{1}{A}$ and $\delta w = \frac{w}{5} \ \sqrt{(w - 1)}$

Contours of acceptance as a function of momentum and angle (from the

beam direction) of the trigger track (lab. system) are shown in figures 4.1

and 4.2 for π^+ and π^- triggers separately. Here, "trigger track" refers

(a) Negative triggers, 6 GeV/c data
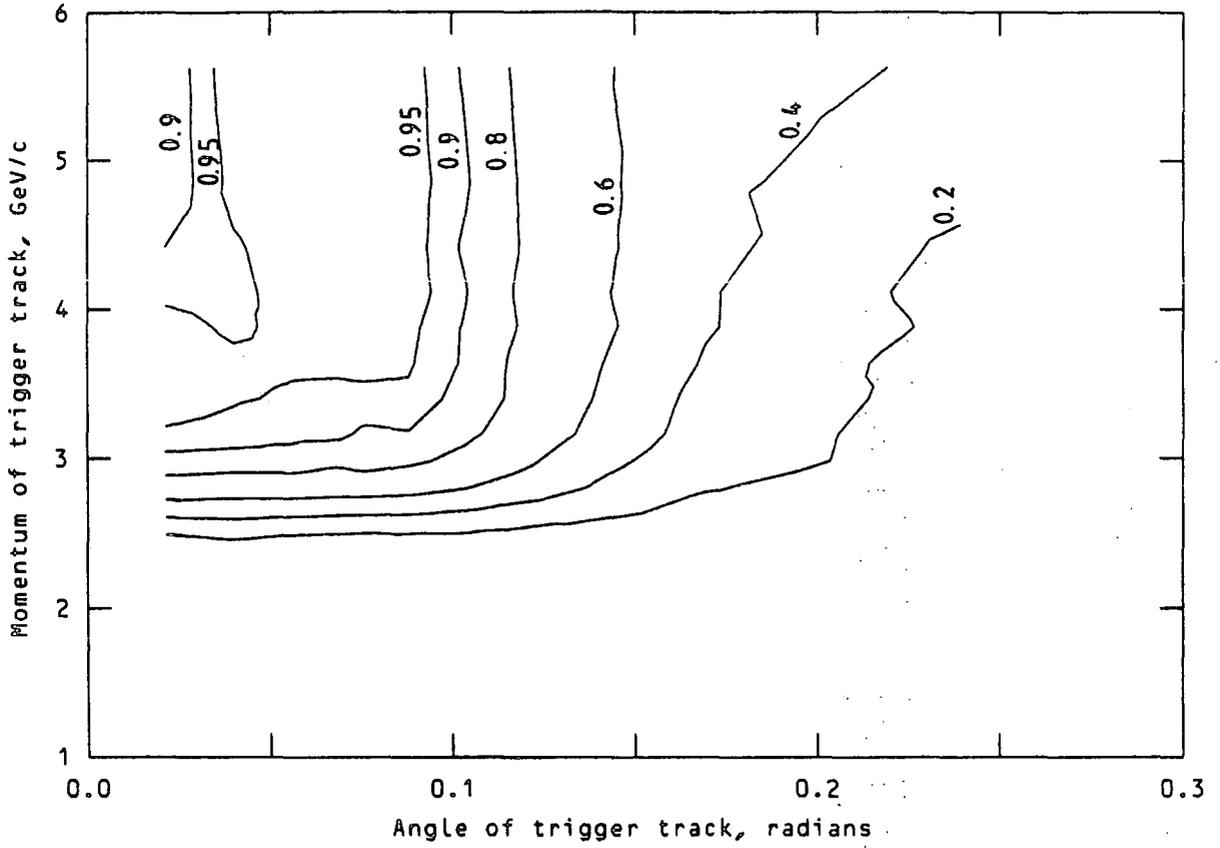
(b) Positive triggers, 6 GeV/c data
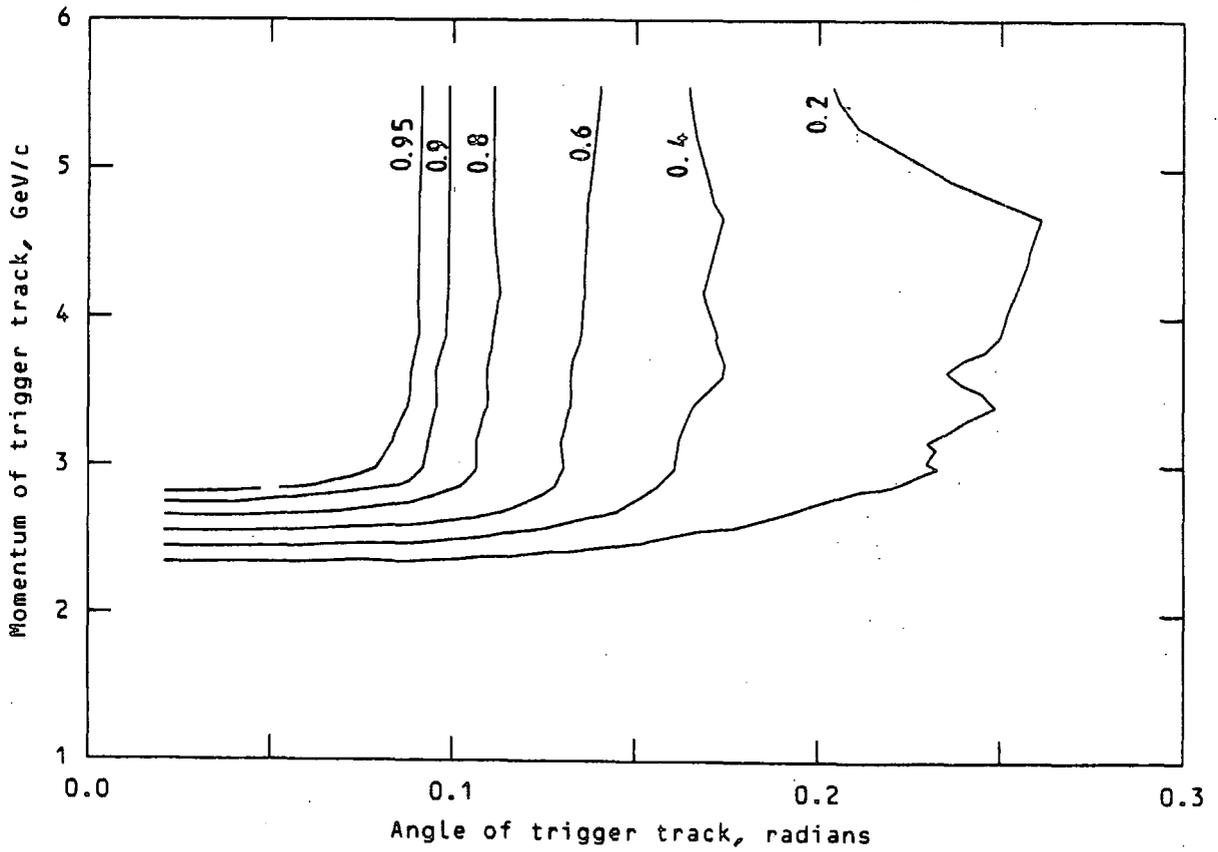
Fig. 4.1 Contours of acceptance

(a) Negative triggers, 9 GeV/c data
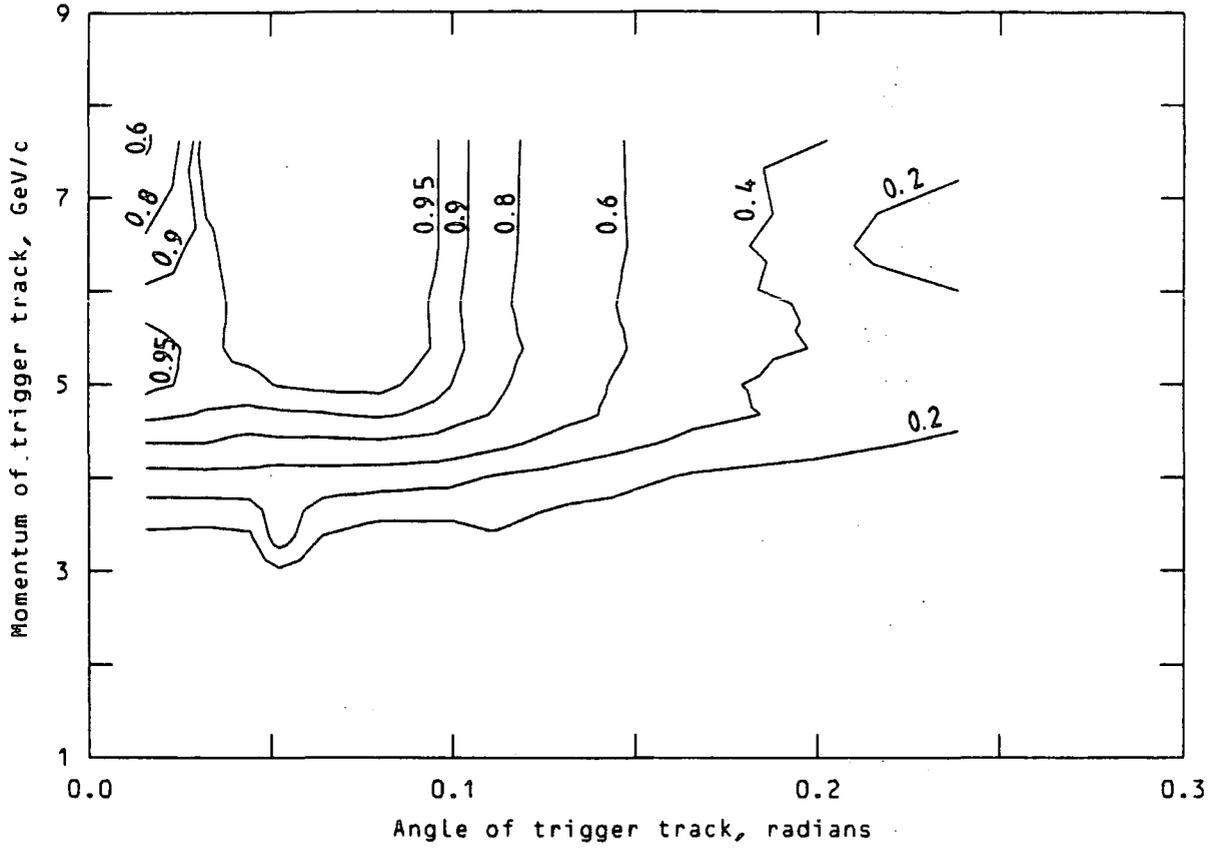
(b) Positive triggers, 9 GeV/c data
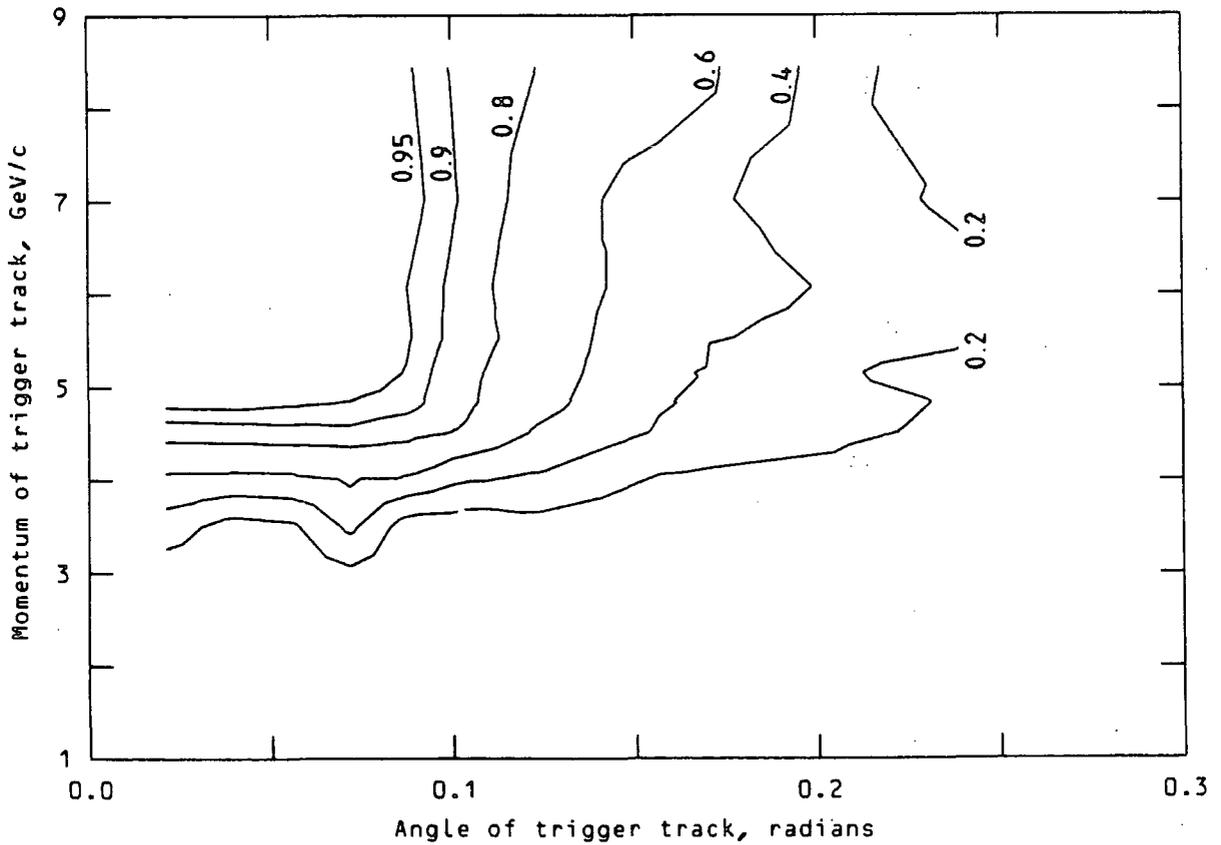
Fig. 4.2   Contours of acceptance

1C3

to the outgoing particle of highest momentum (excluding antiprotons);
there is normally a single particle that is above the trigger momentum,
but about 10% of events have two such particles, and both may contribute
to the acceptance. Apart from this complication, there is a good
correspondence between acceptance and the (p, θ) of the trigger track.
To take advantage of this correspondence, a look-up table has been con-
structed which gives the acceptance for a given trigger particle's
momentum, angle, and charge. This has been used for some purposes
(notably for Monte-Carlo events), but generally the individual event
acceptances are preferred and have been used where possible.

The contours show expected behaviour: the dip in acceptance at
high momentum and small angle for negative triggers is caused by the beam
veto; there is appreciable acceptance below the trigger momentum because
of algorithm inaccuracy; and the acceptance at large angles is higher for
positive triggers than for negative triggers - this is because no Canute
light is demanded from positive particles and so they can miss the mirror
plane more often and still be accepted.

The distributions of event acceptances are shown in figures 4.3 -
4.4. The peaks at high acceptance show clearly that the region of phase
space selected by the trigger contains an enhanced proportion of events
produced peripherally.

4.3 CROSS-SECTION NORMALISATION

The cross-section of a particular process k is given by

$$\sigma_k = \frac{N_I}{N_B \rho L}$$

where N_I is the number of interactions of process k occurring in
fiducial length L, N_B is the number of beam tracks, and ρ is the number
of target nuclei per unit volume.

Fig. 4.3 Distribution of acceptance (6 GeV/c)

Fig. 4.4 Distribution of acceptance (9 GeV/c)
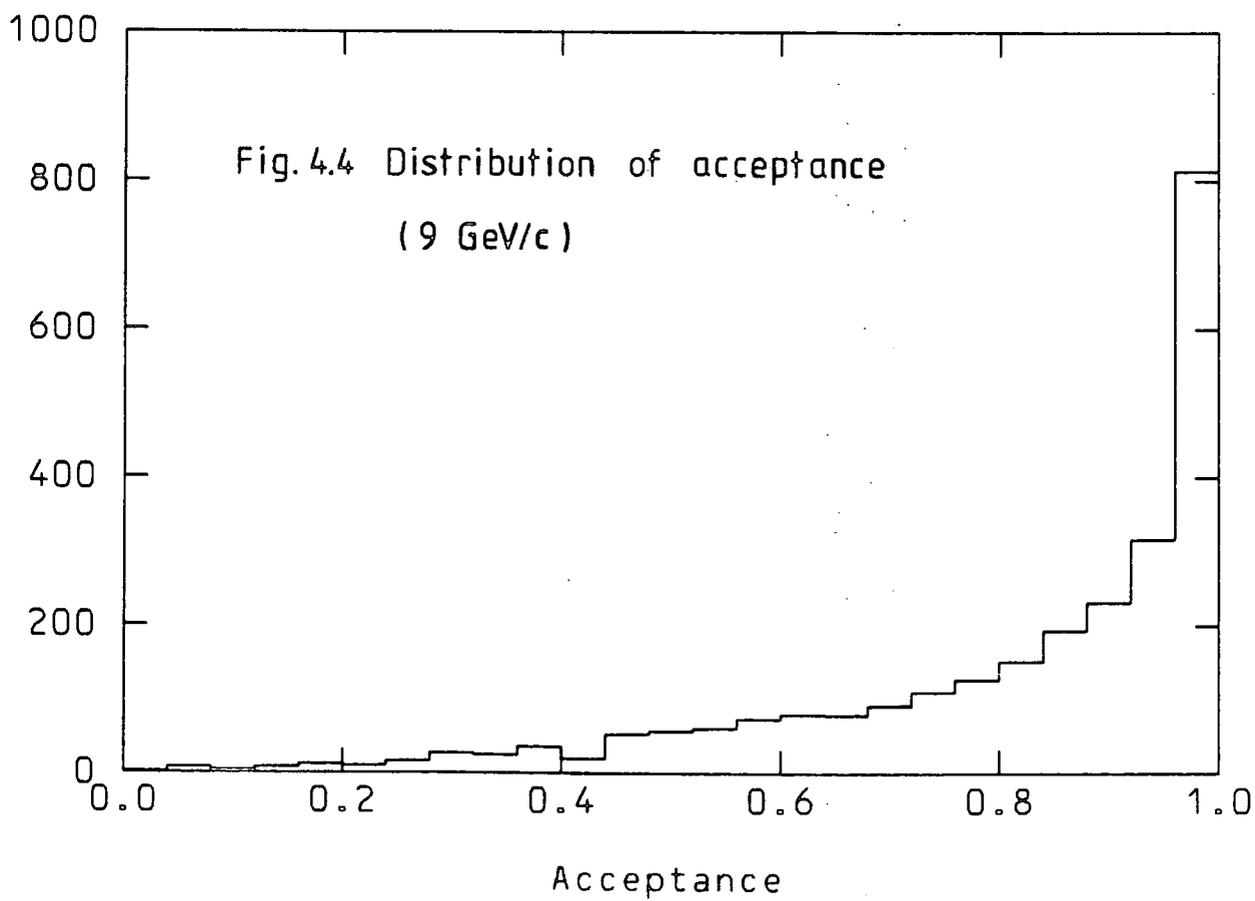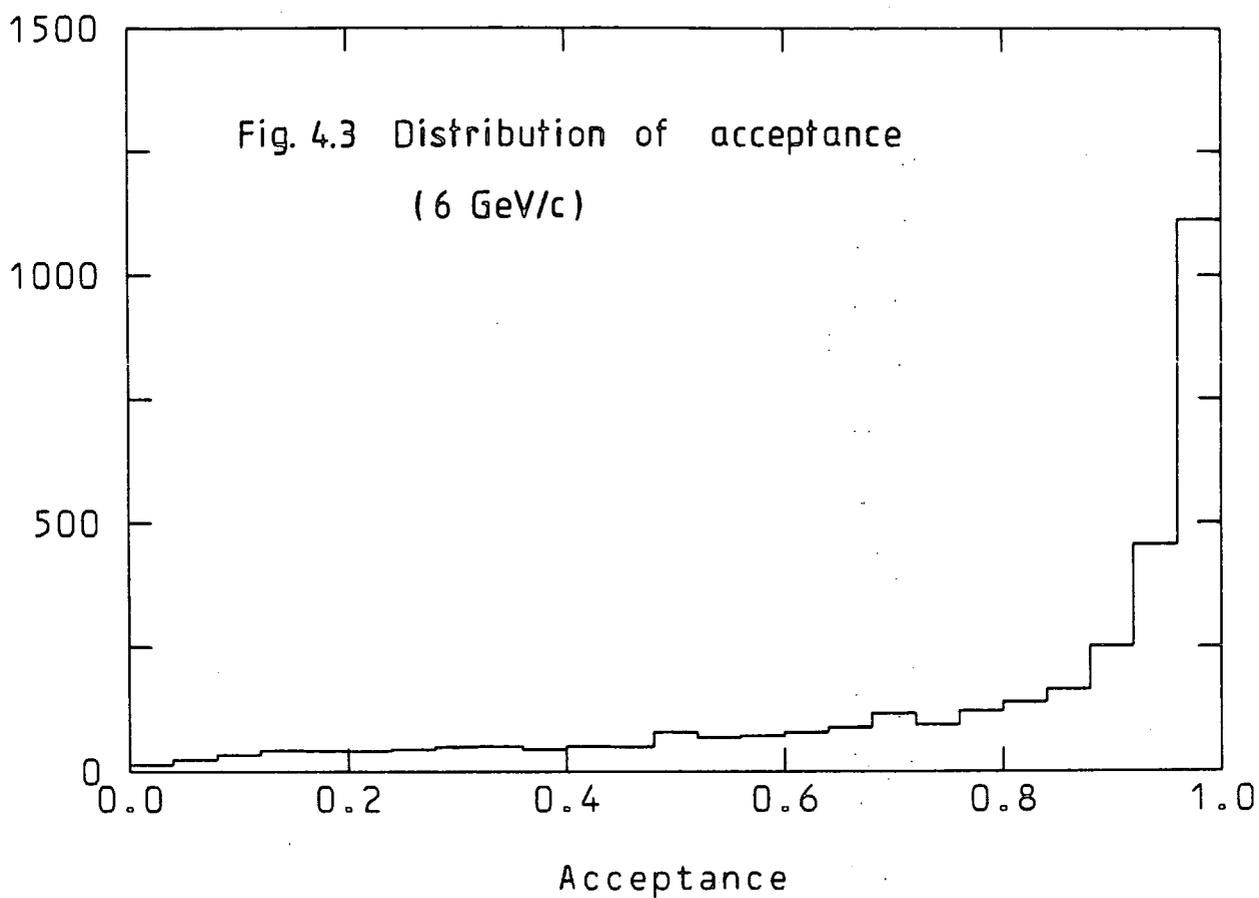
Since we do not observe all N_I interactions that occur, because of the trigger, the total cross-sections cannot be found in this experiment. However, we can find the cross-sections in a region of phase space where the acceptance is non-zero, referred to as the "partial cross-sections" in this work. Then, the number N_I is given by equation 4.1. However, since we only count events which are included on the DST, the equation must be modified thus:

$$N_I \quad = \quad \frac{1}{\epsilon e \eta} \sum_{}^{n} \frac{1}{A_i}$$

where n is now the number of events on the DST within our chosen Kinematic cuts. ϵ, e, and η are three efficiency factors.

η = trigger efficiency i.e. probability than an event is accepted by the trigger, not including the geometrical/Kinematical factors which are accounted for in the acceptance;

e = scanning efficiency i.e. probability that an event on film is detected in the scan. Since the scanning is directed by PWC data, e is nearly 100% and it is only necessary to correct for losses of frames occurring at the ends of rolls or due to film processing.

ϵ = throughput efficiency i.e. probability that a good scanned event passes the measuring and analysis up to the DST. This is rather low (typically 50%), mainly because of hybridisation failures. The measuring and geometrical reconstruction efficiency depend on the number of tracks, and so ϵ is topology-dependent.

Two methods of cross-section normalisation are now described:

(i) an absolute method i.e. counting the number of beam tracks and correcting for the losses described above;

(ii) normalising to cross-sections for certain processes obtained by other experiments at comparable beam momenta.

4.3.1 Normalisation by the absolute method

The number of beam antiprotons passing through the bubble chamber (N_B) is counted by the signal $S1.BH.\overline{CB}$ and is recorded on the NOVA tapes. However, this must be corrected for losses due to beam interactions between the upstream detectors and the interaction vertex (mainly interactions in the walls of the bubble chamber).

The main difficulty in finding N_I is determining accurately the trigger efficiency η. If a good event is the first event in that beam spill, it will be accepted with some efficiency η_{T1} which depends mainly on the PWC efficiencies; however, if that same event were the second one in the beam spill, it would be less likely to be accepted owing to the algorithm execution time limit; furthermore, if the event were the third (or more) in the spill, it could not be accepted at all (see section 2.2.3). To circumvent this problem, a method has been devised (ref. 4.1) using only events which were the first fast triggers in the beam spill (T1). It can then be shown that

$$N_I = \frac{1}{\varepsilon \, e \, \eta_{T1}} \cdot \frac{N_T}{N_S} \cdot \sum_{T1} \frac{1}{A_i}$$

where the summation is over events on the DST which were the first events in the beam spills, and which satisfy the Kinematic selection;

and N_T = total number of fast triggers i.e. count of the signal $S1.BH.\,\overline{CB}.\overline{DV}$

N_S = number of beam spills which have one or more fast triggers. All this information is recorded on the NOVA tapes.

To determine η_{T1} the following factors need to be accounted for:

(a) PWC efficiencies

(b) trigger particles interacting before detection

(c) algorithm efficiency, including multiplicity cuts.

This work is being done elsewhere in the collaboration, and it is intended that any published cross-sections will be normalised in this way. Preliminary results (given in section 4.3.3) are in broad agreement with normalisation from other data, which will now be described.

4.3.2 Normalisation to other experimental data

If the partial cross-section, within specified Kinematic cuts, is known for a certain process k, the cross-section for any other process X is given by

$$\sigma_x = \frac{N_I^x}{N_I^k} \sigma_k = \frac{\sum_x w_i}{\sum_k w_i} \cdot \frac{\varepsilon_k}{\varepsilon_x} \sigma_k \qquad (4.2)$$

where the sum of weights w_i (acceptance weight x ambiguity weight) are taken over the Kinematic regions included in the respective cross-sections. This method has the great advantage that the trigger efficiency cancels out and need not be known (since it is channel-independent); so also does the scanning efficiency. Furthermore, the throughput efficiencies are simply topology-dependent and so need not be know if channels x and k are the same topology (the throughput efficiency may in principle be channel-dependent, but this should be a second order effect).

Since the normalisation cross-sections are for a restricted region of phase space, their determination requires access to the DST's of other experiments. We have used the CERN-Prague data (ref. 4.2) for 5.68 GeV/c $\bar{p}p$ interactions to normalise our 6 GeV/c data; and the Liverpool data (ref. 4.3) for 9.1 GeV/c $\bar{p}p$ interactions to normalise our 9 GeV/c data. No suitable data is available to normalise the deuterium cross-sections.

Before giving details of this method, which was used to normalise all cross-sections given in this thesis, two variants are described for completeness. They both give comparable results to the above method.

(i) Rather than comparing the number of events in the other experiment with the sum of acceptance weights (w_i) for our experiment, we can compare the number of events in our experiment with the sum of acceptances (A_i) for the other experiment. This method has been tried, but it requires calculating the acceptances of events in the other data that they would have in our experiment. Since the run conditions changed many times, this can only be done approximately.

(ii) Using the CERN-Prague inclusive data for $\bar{p}p \rightarrow \pi^{\pm} X^{\mp}$, a fit was made to the differential cross-section using an empirical formula. To smooth out statistical fluctuations, Monte Carlo events were generated with a distribution determined by the fit, normalised to the cross-section, and weighted by the acceptance A_i (assumed to be purely geometrical). This method was used to obtain a preliminary figure for the sensitivity (0.12 events/μb/roll).

4.3.3. Selections used to define event sample

The channels chosen for normalisation were the 4C channels with the highest cross-sections, namely:

at 6 GeV/c   = 4π, $\bar{p}p2\pi$

at 9 GeV/c   = 4π, $\bar{p}p2\pi$, 6π, $\bar{p}p4\pi$, 8π

(At 6 GeV/c only 4 prong data was available). The $\bar{p}p$ elastic channel could not be used, since all such events are background and their acceptance is not well known.

Kinematic cuts were applied to the CERN-Prague and Liverpool data to select a region of phase space with good acceptance; this required defining a "trigger particle" which was taken to be the outgoing particle of highest momentum (not including antiprotons). The cuts were applied to the momentum (p) and angle from the beam track (θ) of the trigger particle, in the laboratory system, as follows:

(1)   p >   2.79 GeV/c   (6 GeV/c data)

or   p >   4.38 GeV/c   (9 GeV/c data)

(2)   θ <   0.15 radians

With these cuts, there is no acceptance less than 0.2 and the average

acceptance weight is $\overset{\sim}{}$1.1. A further selection was made on 4 prongs to

reduce ambiguities: at least one negative particle must be less than

2 GeV/c (so that it could be identified by ionisation choicing).

The partial cross-section of a particular channel and particular

trigger charge is given by

$$\sigma_S \;=\; \frac{N_S}{N_T} \; \sigma_T$$

where σ_T is the published cross-section for that channel (refs. 4.4 and

4.5), N_T is the total number of events of that channel on the CERN-Prague

or Liverpool DST, and N_S the selected number of events of the required

trigger charge. Appropriate corrections (generally very small) were made

for ambiguities by using ambiguity weights.

The cross-sections were thus obtained at 5.68 and 9.1 GeV/c. The

cross-sections at our beam momenta of 6.05 and 8.81 GeV/c were then

derived for 4-prongs by linear interpolation (the form of the interpolation

is not critical as the beam momenta are very close to those of the

normalisation data). The 6 and 8 prong cross-sections were scaled in

proportion to the 4 prong values. The momentum corrected, partial cross-

sections are given in table 4.1 (a). Here, a negative trigger refers to a

π^-, whereas a positive trigger refers to a π^+ or a proton. The errors

quoted are purely statistical; that is, they are derived from the Poisson

error on N_S, any other source of error being much smaller than this.

For comparison, the cross-sections obtained by the absolute method are given in table 4.1(b), with the same selections as above.

(a) Normalised using CERN-Prague (6 GeV/c) and Liverpool (9 GeV/c) data

Trigger Charge	Channel $\bar{p}p \rightarrow$	Partial cross-section (µb)	
		6 GeV/c	9 GeV/c
−	4π	41.0 ± 3.5	21.0 ± 4.5
−	$\bar{p}p$ 2π	30.0 ± 3.0	16.6 ± 3.9
+	4π	23.6 ± 2.7	7.8 ± 2.6
+	$\bar{p}p$ 2π	38.6 ± 3.3	32.4 ± 5.5

(b) Normalised by the absolute method (preliminary results)

Trigger Charge	Channel $\bar{p}p \rightarrow$	Partial cross-section (µb)	
		6 GeV/c	9 GeV/c
−	4π	43.3 ± 5.3	17.0 ± 2.4
−	$\bar{p}p$ 2π	28.4 ± 4.3	10.7 ± 1.9
+	4π	15.9 ± 3.3	9.8 ± 1.8
+	$\bar{p}p$ 2π	33.3 ± 4.7	23.8 ± 2.8

TABLE 4.1 PARTIAL CROSS-SECTIONS USED FOR NORMALISATION (WITH SELECTIONS AS DEFINED IN THE TEXT)

The two sets of results are consistent within errors, although there is a trend for the cross-sections given by the absolute method to be smaller than those from other data. Since the numbers given in Table 4.1(b) are preliminary, the values in (a) were used for normalisation in this thesis.

4.3.4   Sensitivity of the Hydrogen data

A useful quantity in evaluating cross-sections is the "sensitivity",
that is the number of events in a data sample equivalent to one microbarn
of cross-section.   Equation 4.2 may be rewritten

$$\sigma_x = \frac{\sum\limits_x w_i}{\epsilon_x S} \quad , \qquad S = \frac{\sum\limits_k w_i}{\epsilon_k \sigma_k}$$

where   S   is the ultimate sensitivity, that is the sensitivity that
would be obtained with perfect throughput efficiency.   A more useful
figure is the topological sensitivity S_T:

$$\sigma_x = \frac{\sum\limits_x w_i}{S_T} \quad , \qquad S_T = \frac{\epsilon_{T_k} \sum w_i}{\epsilon_k \ \sigma_k}$$

where X is any channel with topology T.   If the normalisation channel   k
has the same topology, the throughput efficiencies need not be known;
the topological sensitivities thus obtained (using the January 1981 DST)
are given in tables 4.2 (6 GeV/c) and 4.3 (9 GeV/c, phases I and II).
The few ambiguous events are weighted according to the number of 4C fits
(an arbitrary, but reasonable way), so that the overall expression for
w_i is

$$w_i = \frac{1}{\text{no. of 4C fits x acceptance}}$$

A cut in chi-squared probability of 1% was used for unique and ambiguous
events.   The summation is then over the same selection of events, and with
the same definition of trigger particle, as was used to determine the
partial cross-sections.   The error on the sum of weights is purely statistical:

$$\text{If} \quad n \quad = \quad \sum w_i$$

$$\text{then} \quad (\delta n)^2 \quad = \quad \sum (w_i^2)$$

The sensitivities are shown for each channel separately to show they are consistent, and then combined to give a better estimate. Similarly (at 6 GeV/c) the sensitivities for + and - triggers are shown separately and combined, since they should be the same. However at 9 GeV/c, part of the data was taken with an algorithm which only accepts positive triggers (" + only"), as opposed to the normal algortihm ("+/-"). Thus sensitivities can only be combined from data taken with the +/- algorithm. The overall sensitivity for positive triggers is then the sum of the "+/-" sensitivity and the "+ only" sensitivity.

To find the sensitivities at 6 GeV/c for channels other than 4 prongs, the relative throughput efficiencies must be known. The throughput efficiency of topology k is, by definition.

$$\epsilon_k \quad = \quad \frac{N_{DST}^k}{N_S^k}$$

where N_{DST}^k is the number of events on the DST of topology k, and N_S^k is the number of good scanned events of topology k. This number is corrected for background; that is the number of frames which accidently have an event in the directed scan region not associated with the trigger. The proportion of background events depends (linearly) on the size of the directed scan width and is therefore somewhat laboratory-dependent. At Rutherford Laboratory, it has been determined to be typically 6-10% (depending on beam momentum and topology). The numbers N_S^k are not yet known for other laboratories; however, assuming random distribution of film, we can write:

$$\frac{\varepsilon_T}{\varepsilon_k} = \frac{N^T_{DST}}{N^k_{DST}} \div \frac{N^T_S}{N^k_S} \sim \frac{N^T_{DST}}{N^k_{DST}} \div \left[\frac{N^T_S}{N^k_S} \right]_{RL}$$

where the subscript RL refers to Rutherford Lab. data only. These numbers are given in table 4.4, where the topology classification follows the normal European convention (e.g. topology 400 = simple 4 prong). However, see next section, point (3).

Using the ratio of throughput efficiencies, the sensitivities for 2, 6 and 8 prongs at 6 GeV/c and 2 prongs at 9 GeV/c were determined in terms of the 4 prong sensitivities. Finally, the 6 and 8 prong sensitivities at 9 GeV/c were also calculated by this method (not given in tables) and found to be consistent with the direct method, with generally smaller errors. Therefore a weighted average was taken for these results. These averages and the other figures are summarised in table 4.5, and apply to the January 1981 version of the DST.

4.3.5 Errors in the sensitivity and determination of overall sensitivity

As stated above, the random errors given in the tables for the sensitivity are dominated completely by the statistical errors on the number of events in the normalisation data. There are, however, a number of possible sources of systematic errors:

(1) Systematic errors in the published cross-sections for the normalisation channels. These are unknown and assumed to be small.

(2) Systematic errors in the acceptances. These are assumed to be small, and are very likely to cancel out in the determination of cross-sections.

(3) Systematic errors in the relative throughput efficiencies.

TABLE 4.2   SENSITIVITY OF THE 6 GeV/c HYDROGEN DATA

4 prongs

Trigger Charge	Channel	Number of events	Sum of Weights	Partial Cross Section (μb)	Topological Sensitivity ev/μb
−	4π	902	1005.0 $\pm$ 33.5	41.0 $\pm$ 3.5	24.5 $\pm$2.2
−	$\bar{p}p\ 2\pi$	484	538.3 $\pm$24.5	30.0 $\pm$3.0	17.9 $\pm$2.0
−	4π + $\bar{p}p\ 2\pi$	1386	1543.3 $\pm$41.5	71.0 $\pm$4.6	21.7 $\pm$1.8
+	4π	406	460.0 $\pm$22.8	23.6 $\pm$2.7	19.5 $\pm$2.5
+	$\bar{p}p\ 2\pi$	658	748.0 $\pm$29.2	38.6 $\pm$3.3	19.4 $\pm$1.8
+	4π + $\bar{p}p\ 2\pi$	1064	1208.0 $\pm$37.0	62.2 $\pm$4.3	19.4 $\pm$1.5
+ and −	4π + $\bar{p}p\ 2\pi$	2450	2751.3 $\pm$55.6	133.2 $\pm$6.3	20.7 $\pm$1.1

TABLE 4.3   SENSITIVITY OF THE 9 GeV/c HYDROGEN DATA (PHASE I & II)

4 prongs

Trigger Charge and Algorithm	Channel	Number of Events	Sum of Weights	Partial Cross Section (μb)	Topological Sensitivity ev/μb
–	4π	583	640.9 $^{+}_{-}$26.5	21.0 $^{+}_{-}$4.5	30.5 $^{+}_{-}$6.7
–	p̄p 2π	354	394.9 $^{+}_{-}$21.0	16.6 $^{+}_{-}$3.9	23.8 $^{+}_{-}$5.7
–	4π + p̄p 2π	937	1035.8 $^{+}_{-}$33.8	37.6 $^{+}_{-}$6.0	27.5 $^{+}_{-}$4.4
+ +/– alg.	4π	271	300.5 $^{+}_{-}$18.3	7.8 $^{+}_{-}$2.6	38.5 $^{+}_{-}$13.0
+ +/– alg.	p̄p 2π	818	942.6 $^{+}_{-}$33.0	32.4 $^{+}_{-}$5.5	29.1 $^{+}_{-}$5.0
+ +/– alg.	4π + p̄p 2π	1089	1243.1 $^{+}_{-}$37.7	40.2 $^{+}_{-}$6.1	30.9 $^{+}_{-}$4.8
+ + only alg.	4π	9	9.4 $^{+}_{-}$3.1	7.8 $^{+}_{-}$2.6	1.2 $^{+}_{-}$0.6
+ + only alg.	p̄p 2π	53	60.3 $^{+}_{-}$8.3	32.4 $^{+}_{-}$5.5	1.9 $^{+}_{-}$0.4
+ + only alg	4π + p̄p 2π	62	69.7 $^{+}_{-}$8.9	40.2 $^{+}_{-}$6.1	1.7 $^{+}_{-}$0.3
+ and – +/– alg.	4π + p̄p 2π	2026	2278.9 $^{+}_{-}$50.6	77.8 $^{+}_{-}$8.6	29.3 $^{+}_{-}$3.3

TABLE 4.3 (Cont.) SENSITIVITY OF THE 9 GeV/c HYDROGEN DATA (PHASE I & II)

6 and 8 prongs

Trigger Charge and Algorithm	Channel	Number of events	Sum of Weights	Partial Cross Section (μb)	Topological Sensitivity ev/μb
−	6π + $\bar{p}p\ 4\pi$	920	1055.6 $^+_-34.8$	42.7 $^+_-7.3$	24.7 $^+_-4.3$
+ +/− alg.	6π + $\bar{p}p\ 4\pi$	510	584.5 $^+_-25.9$	27.9 $^+_-6.2$	20.9 $^+_-4.7$
+ + only alg.	6π + $\bar{p}p\ 4\pi$	24	25.7 $^+_-5.2$	27.9 $^+_-6.2$	0.9 $^+_-0.3$
+ and − +/− alg.	6π + $\bar{p}p\ 4\pi$	1430	1640.1 $^+_-43.4$	70.6 $^+_-9.6$	23.2 $^+_-3.2$
−	8π	140	162.4 $^+_-13.7$	6.6 $^+_-3.3$	24.6 $^+_-12.5$
+ +/− alg.	8π	83	97.5 $^+_-10.7$	7.3 $^+_-3.7$	13.4 $^+_-6.9$
+ + only alg.	8π	7	7.9 $^+_-3.0$	7.3 $^+_-3.7$	1.1 $^+_-0.7$
+ and − +/− alg.	8π	223	259.9 $^+_-17.4$	13.9 $^+_-5.0$	18.7 $^+_-6.8$

TABLE 4.4   NUMBERS OF EVENTS SCANNED (RL) AND ON DST
(ALL LABS) BY TOPOLOGY

(a)

6 GeV H_2 T =	200	400	600	800
N^T_{DST}	34800	35721	12156	716
$\left[N^T_S\right]_{RL}$	9150	8911	3272	270
$\varepsilon_T/\varepsilon_{400}$	0.95	–	0.93	0.66

(b)

9 GeV H_2 T =	200	400	600	800
N_{DST}	35001	41293	15702	1798
$\left[N^T_S\right]_{RL}$	15980	18313	7750	1178
$\varepsilon_T/\varepsilon_{400}$	0.97	–	0.90	0.68

TABLE 4.5   BEST ESTIMATES OF SENSITIVITY, BY TOPOLOGY

Sensitivity, ev/μb		200	400	600	800
6 GeV H_2		19.7 $^{+}_{-}$1.0	20.7 $^{+}_{-}$1.1	19.3 $^{+}_{-}$1.0	13.7 $^{+}_{-}$0.7
9 GeV H_2	$-$ Trigger	28.4 $^{+}_{-}$3.2	29.3 $^{+}_{-}$3.3	24.9 $^{+}_{-}$2.2	19.8 $^{+}_{-}$2.0
	$+$ Trigger	30.1 $^{+}_{-}$3.2	31.0 $^{+}_{-}$3.3	26.1 $^{+}_{-}$2.2	21.0 $^{+}_{-}$2.0

We have determined the relative throughput efficiencies of one

topology to another for data from all trigger types. However, most

results are presented in this thesis for pion triggers, since proton

and kaon triggers are very few in number, and antiproton triggers have

an indeterminate acceptance (most of these will have been accepted by

an associated, lower momentum pion producing light in Canute). Since

pion triggers have a much higher hybridisation efficiency than antiproton

triggers, this method is only valid if the fraction of pion triggers is

topology-independent. This is true to a reasonable extent, and is con-

firmed by the agreement between the two methods of determining the 6-prong

and 8-prong sensitivities at 9 GeV/c.

The throughput efficiencies for Rutherford Lab. (all triggers) and

fractions (f_T) of events of each topology (all laboratories) are:

Topology	6 GeV/c		9 GeV/c	
	ϵ_{RL}	f_T	ϵ_{RL}	f_T
200	0.60	0.42	0.52	0.37
400	0.60	0.43	0.47	0.44
600	0.56	0.14	0.36	0.17
800	0.37	0.01	0.23	0.02

Strange topologies form only 2- 3% of the data.

The overall sensitivity (S_o) for data of all topologies (T) is

given by

$$\frac{1}{S_o} = \sum_T \frac{f_T}{S_T}$$

However, to determine inclusive cross-sections (see section 4.5), the

triggering particle must be identified by Canute (since not all events

have unique fits), and only a fraction F of the data could be used for

this purpose because of incomplete information on the DST. The

"inclusive sensitivity" is therefore

$$S_{inc} = F \, S_o$$

and the numbers obtained are:

	S_o	F	S_{inc} (ev/μb)
6 GeV/c	20.0	0.76	15.3
9 GeV/c, - triggers	27.9	0.92	25.8
9 GeV/c, + triggers	29.5		27.3

4.4 CROSS SECTIONS

4.4.1 Choice of Kinematic variables and Kinematic region

The Kinematic region of the partial cross-sections used for the normalisation was defined in terms of momentum (P) and angle (θ) of the "triggering particle" in the laboratory system. It is preferable, however, to use variables with a more general physical interpretation. There are two pairs of variables normally used:

(1) Four-momentum transfer squared, -t and recoil mass, m_x.

(2) Transverse momentum, P_t and longitudinal momentum, P_L^* (in the centre-of-momentum system, denoted *).

The dimensionless variables Feynman x or rapidity, y are often used in place of P_L^*. For the inclusive process $\bar{p}p \rightarrow \pi^{\frac{+}{-}} x^{\frac{-}{+}}$, the variables used refer to the charged pion of highest momentum. The minimum recoil mass is then the pion mass.

Figures 4.5 and 4.6 show the plots of m_x^2 against t (Chew-Low plots) at 6 and 9 GeV/c respectively, with contours of P and θ for certain values. The region of best acceptance is at high t (that is, small momentum transfer) and low recoil mass. Also shown are experimental

$\bar{p}p \rightarrow \pi X$, 6 GeV/c
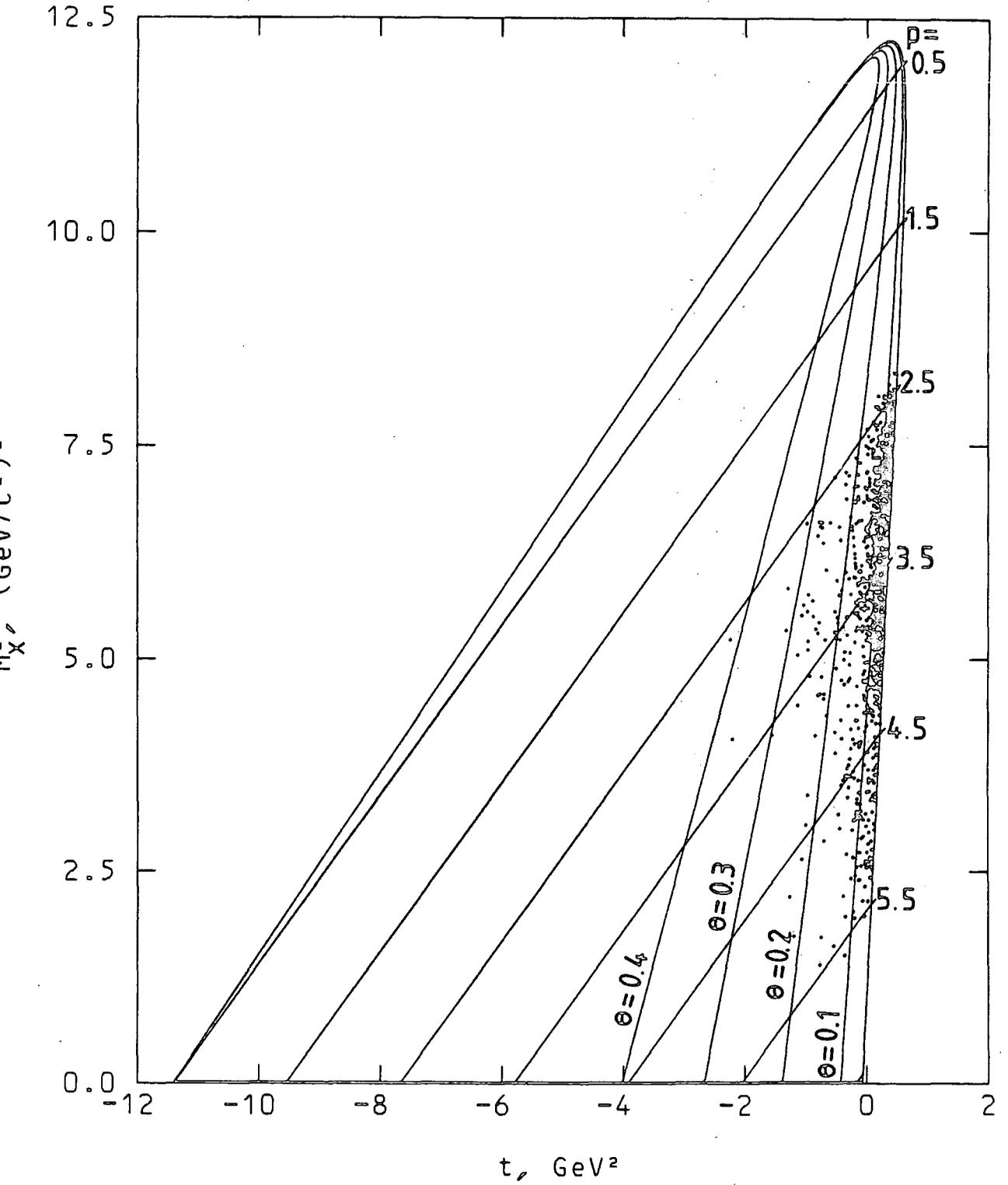
Fig. 4.5   Chew-Low plot

$\bar{p}p \to \pi X$, 9 GeV/c
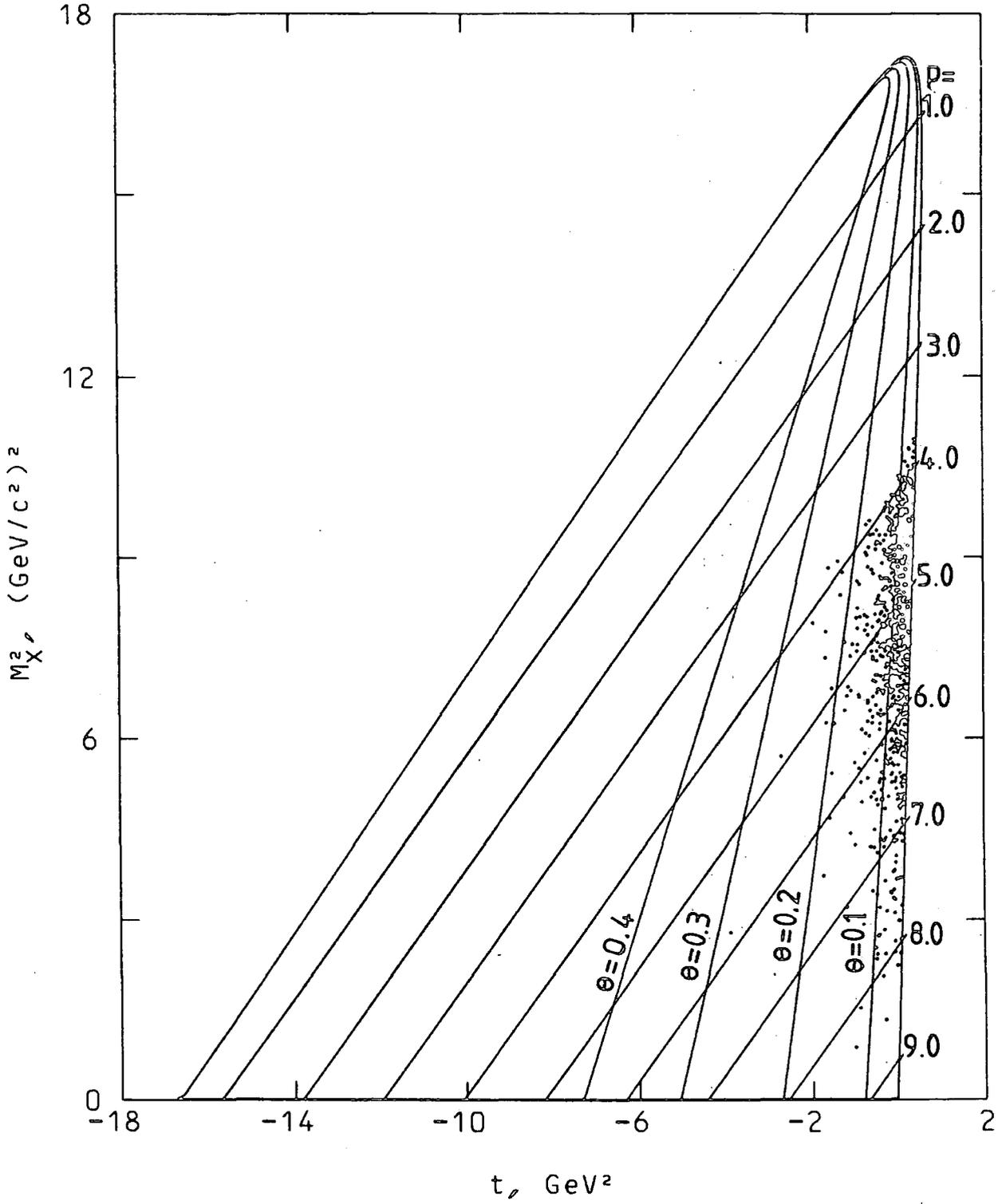
Fig. 4.6   Chew-Low plot

points for 1000 events, which cluster at high t (small θ) because of the peripheral nature of most interactions. Therefore, the angular limitation on acceptance is not severe and few events are lost this way. However, the momentum cut clearly removes a large number of events, and there are none with recoil mass greater than 2.9 (3.3) GeV/c^2 at 6(9) GeV/c beam momentum.

The upper bound on t (i.e. θ = 0) increases slowly with M_x up to a certain mass well above the acceptance threshold. Therefore, there is a small range of t at the upper limit where the acceptance is zero. This illustrates the conclusion reached by other authors (e.g. ref. 4.6) that t is not a good variable to define the leading pion for an inter-action of the type $\bar{p}p \to \pi X$.

Turning to the second pair of variables, we note that the scaling variable, Feynman x, and the transverse momentum are commonly used in the literature for inclusive processes. x is defined as

$$x = \frac{p_L^*}{p^*_{(max)}} \qquad \text{where} \quad p^*_{(max)} = \sqrt{\frac{s}{4} - M_\pi^2} \qquad \text{is the}$$

maximum momentum in the CMS, corresponding to a pion recoiling against another pion, with total CMS energy $\sqrt{s}$. x and p_t are the variables used here for defining cross-sections (rapidity is simply related to x and could equally well have been used).

Figures 4.7 and 4.8 show the plots of x against p_t^2 (the square of p_t is used because the phase space element is proportional to d p_t^2). Again, 1000 experimental points are shown, which cluster at low p_t^2 where the acceptance is good. The momentum cut restricts most events to the region x > 0.37 (0.42) at 6 (9) GeV/c beam momentum, though this depends on p_t^2.

$\bar{p}p \rightarrow \pi X$, 6 GeV/c
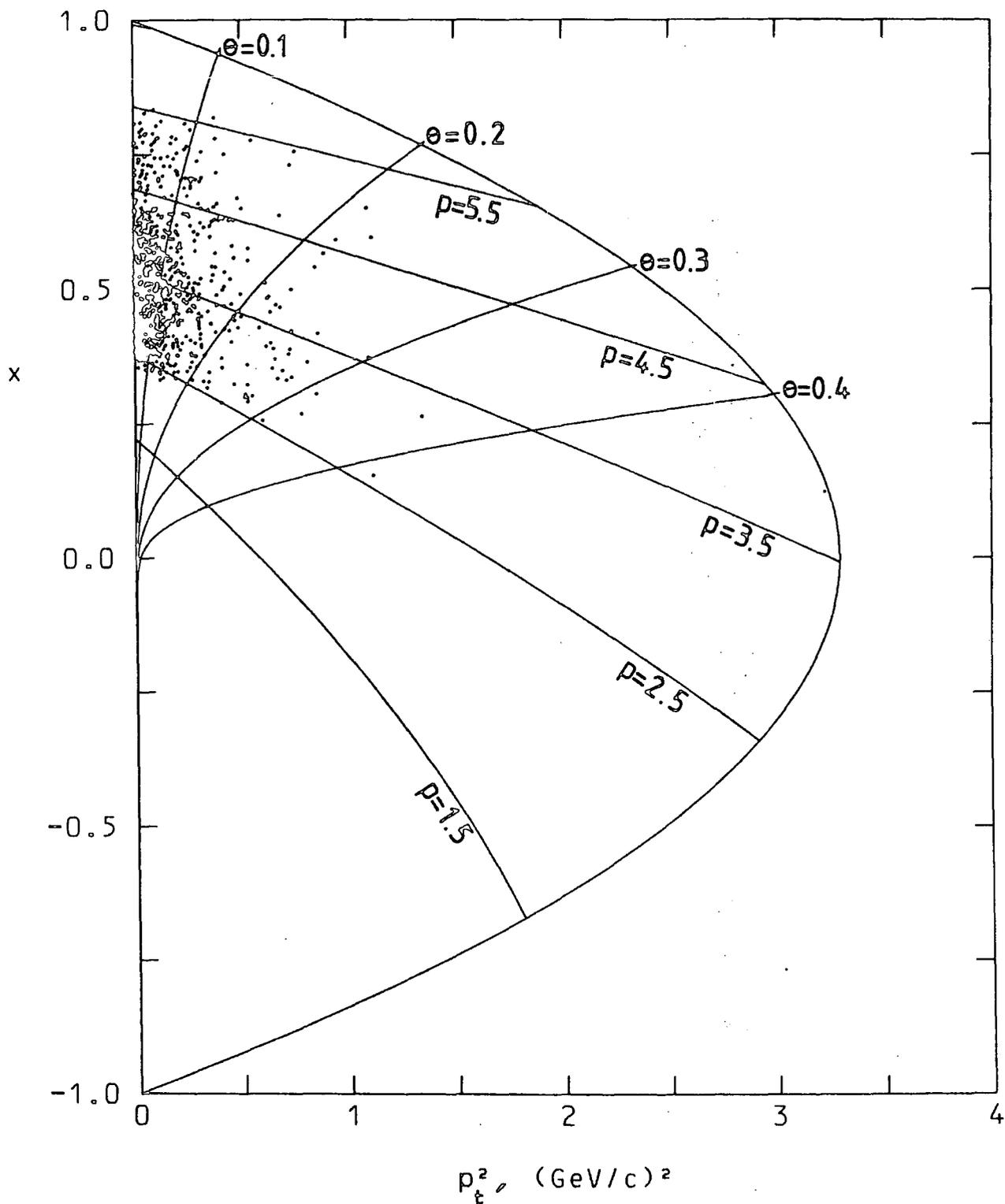
Fig. 4.7   Plot of Feynman x against p_t^2

$\bar{p}p \to \pi X$, 9 GeV/c
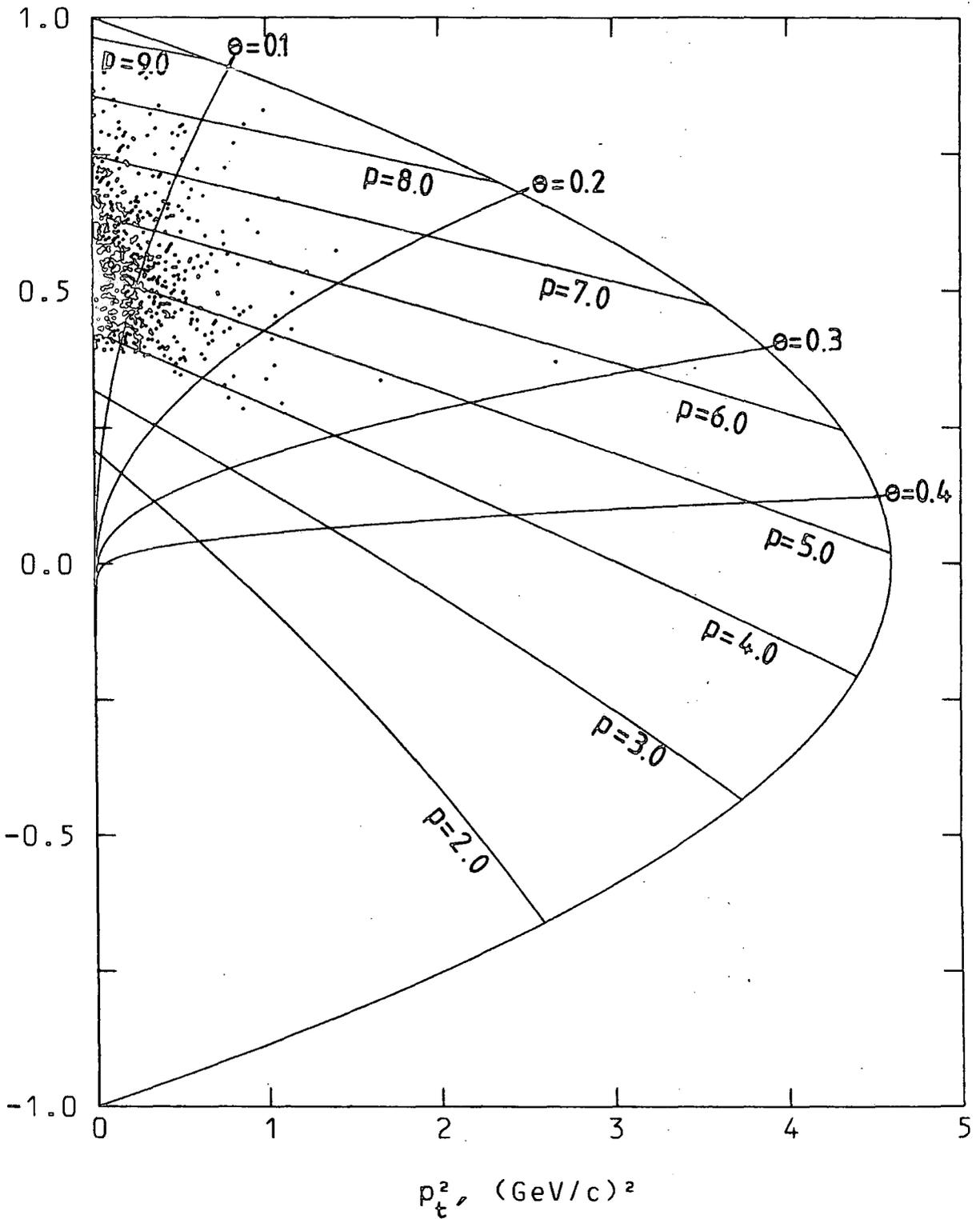
Fig. 4.8 Plot of Feynman x against p_t^2

Cross sections are given for the Kinematic region

p > 2.5 GeV/c   θ < 0.2 rads   (6 GeV/c)

p > 4.0 GeV/c   θ < 0.2 rads   (9 GeV/c)

where the acceptance is good (generally greater than 0.4). This is

somewhat wider than the region defined for normalisation (section 4.3.3),

and few accepted events are outside of this region.

4.4.2 Inclusive Double-Differential Cross-sections

Inclusive cross-section data is of interest in fitting various

theoretical models such as the quark recombination model (this has been

done in ref. 4.7). In this thesis, a simple fit is made to the modified

statistical thermodynamic model of Hagedorn and Hoang. Inclusive cross-

sections have been found for the reactions

$$\bar{p}p \rightarrow \pi^- X^+$$
$$\text{and } \bar{p}p \rightarrow \pi^+ X^-$$
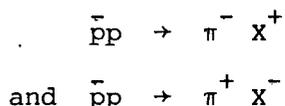
where X represents all other secondary particles. Previous results for

these processes have been given by the Liverpool collaboration at 4.6

and 9.1 GeV/c in the proton fragmentation region (ref. 4.8) and at

12 GeV/c (ref. 4.9); and by the Cern-Prague collaboration at 5.7 GeV/c

(ref. 4.10). However, this data is sparse, particularly in the region

of high Feynman x where the present experiment makes a valuable

contribution.

Identification of the pion was made by means of the downstream

Cerenkov detector, Canute. Where two or more identical particles were

above the trigger momentum, the one of highest momentum was taken. No

Kinematic fit information is used, as this would bias the throughput

efficiency in favour of constrained fits. As mentioned in section 4.3.5,

Canute information was not available for a certain fraction of the data,

and the inclusive sensitivity was appropriately modified. Where Canute

information was available, the identification procedure was as described

in section 3.5.2. There still remained about 6 - 10% of events

unidentified. These are mainly events with (a) particles of too low

momentum, so that pion-produced light is comparable to the noise level;

or (b) two or more tracks intercepting the same mirror; or (c) all three

mass assignments rejected, probably because of a downstream interaction,

decay, or delta-ray. These unidentified events were accepted as pion

triggers, but given an ambiquity weight in proportion to the fraction of

known pion triggers of that charge. These fractions were determined

from uniquely identified events which gave the following fractions of

each trigger type:

Trigger:	π^-	π^+	$K^-/\bar{p}$	K^+/p
6 GeV/c	0.46	0.22	0.29	0.03
9 GeV/c	0.50	0.22	0.25	0.03

The total numbers of events with a pion trigger (unique and ambiguous)

used for the determination of inclusive cross-sections are:

Trigger	π^-	π^+
6 GeV/c	30061	15768
9 GeV/c	46041	19534

About 30% of these events do not have an individual (fit-dependent)

acceptance calculation (as described in section 4.2), either because there

are no fits, or the only fits present are inconsistent with Canute in

identifying the trigger particle. Also, there is no acceptance calculation

for events with strange topologies, or indeterminate algorithm conditions.

These events are given an acceptance from a look-up table for single

pion triggers of given laboratory momentum and angle which, though

approximate, is known to be reasonably consistent with the fit-dependent

method.

A certain number of misidentifications is inevitable, and is

apparent in the momentum distribution of triggering particles identified

as pions (not shown). A peak is seen near to the beam momentum, indicating

that these events are really antiproton triggers from low angle elastic

scatters. Since the number of pion triggers at such a high momentum is

very small, such events were only accepted if the momentum was less than

5.56 GeV/c or 8.46 GeV/c for the 6 or 9 GeV/c data respectively.

The event weights (acceptance weight x ambiguity weight) of the

good events were summed in bins of Feynman x (bin width 0.01) and p_t^2

(bin width 0.1 $(GeV/c)^2$). Then, bins adjacent in x were added together

until the sum exceeded a minimum value required for statistical accuracy,

but only over the range of x and p_t^2 where the acceptance is good.

These summed weights were then divided by the inclusive sensitivity (see

section 4.3.5) and by the bin widths. This yielded, for each bin, the

value of

$$F(x, p_t^2) = \left[\int_{\Delta p_t^2} \int_{\Delta x} \frac{d^2\sigma}{dx \, dp_t^2} \, dx \, dp_t^2 \right] / (\Delta p_t^2 \, \Delta x)$$

which is the average of $\dfrac{d^2\sigma}{dx \, dp_t^2}$ over that bin.

$F(x, p_t^2)$ as a function of x is shown on figures 4.9 and 4.10 for 4

or 5 ranges of p_t^2 at 6 GeV/c and 9 GeV/c respectively. The errors

shown are statistical, and do not include the overall normalisation

Fig. 4.9(a) Differential cross-section,
$\bar{p}p \rightarrow \pi^- X$, 6 GeV/c
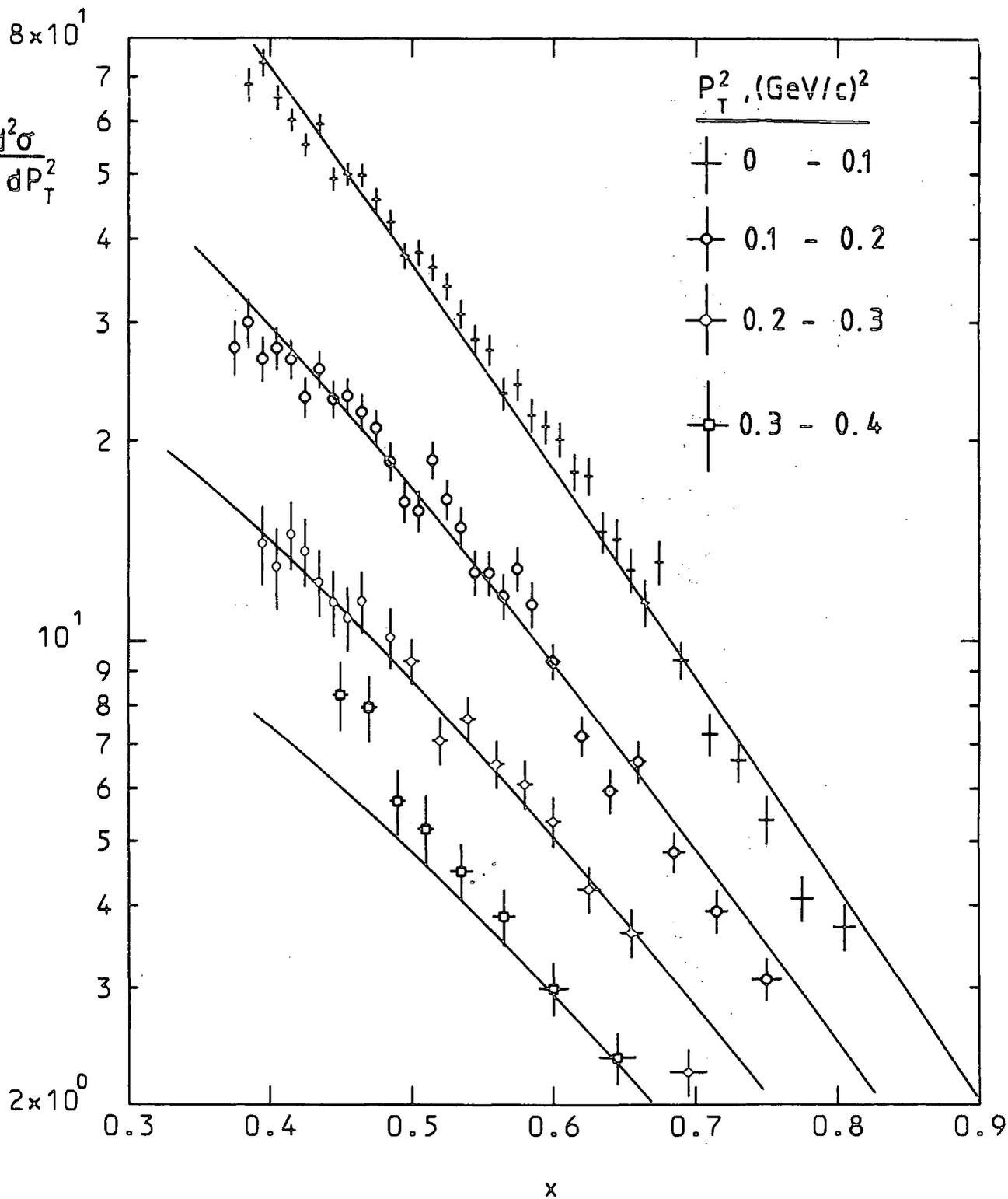
The curves are fits to the two-parameter modified Bose distribution.

Fig. 4.9 (b) Differential cross-section,
$\bar{p}p \rightarrow \pi^+ X$, 6 GeV/c
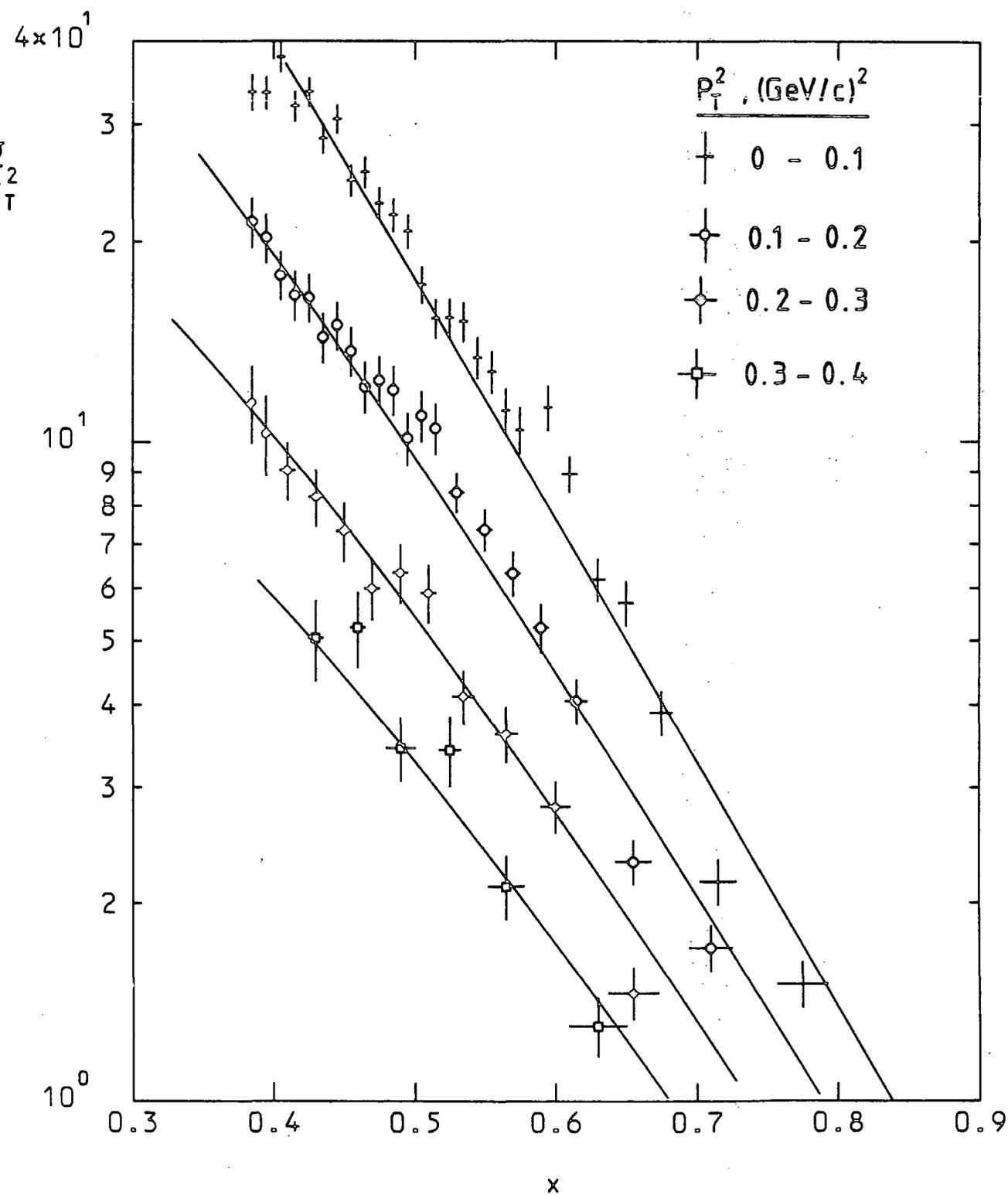
Fig. 4.10(a) Differential cross-section,

$\bar{p}p \rightarrow \pi^- X$, 9 GeV/c

Fig. 4.10 (b) Differential cross-section,
$\bar{p}p \to \pi^+ X$, 9 GeV/c
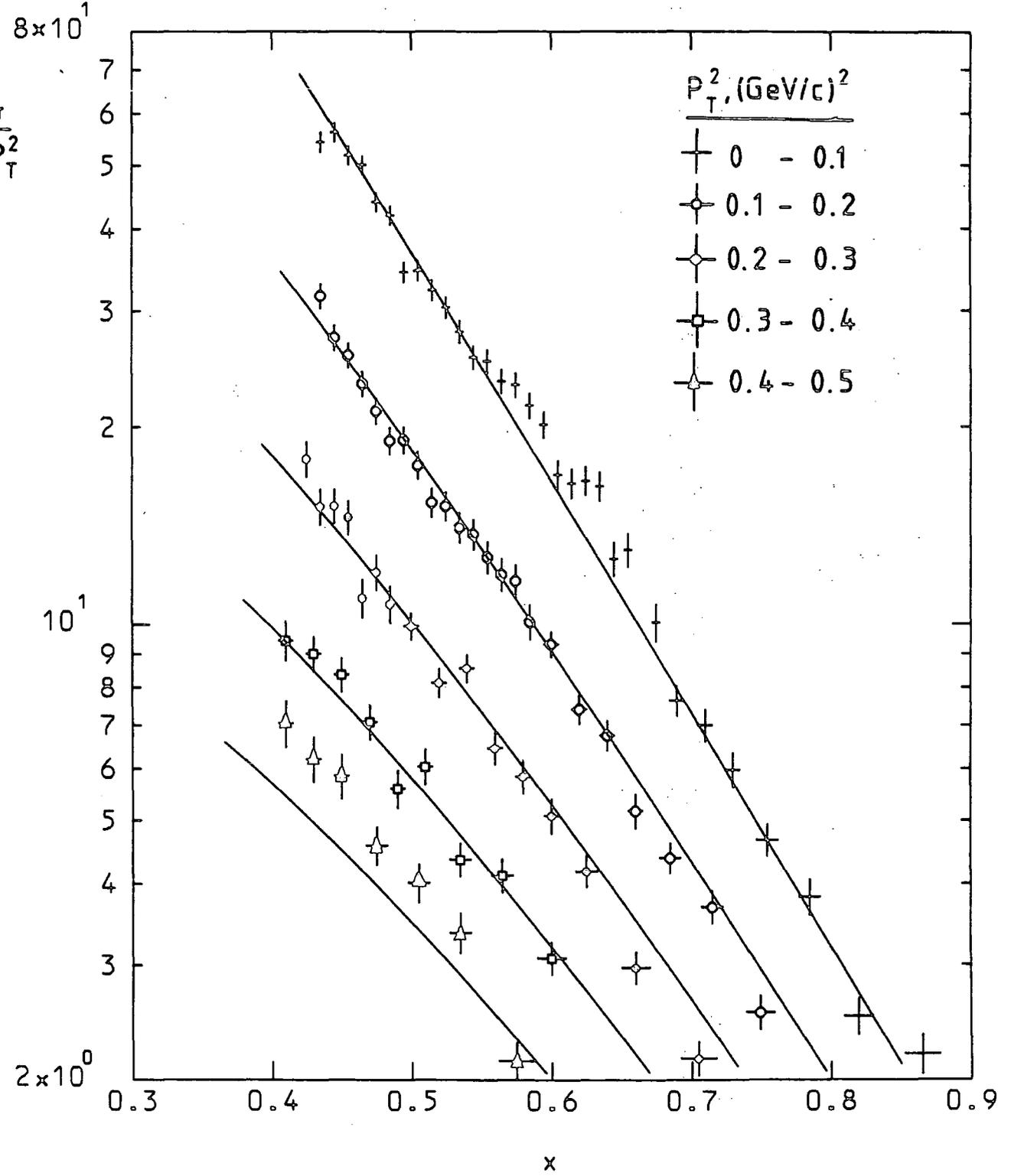
Fig. 4.10 (b) Differential cross-section,

$\bar{p}p \rightarrow \pi^+ X$, 9 GeV/c
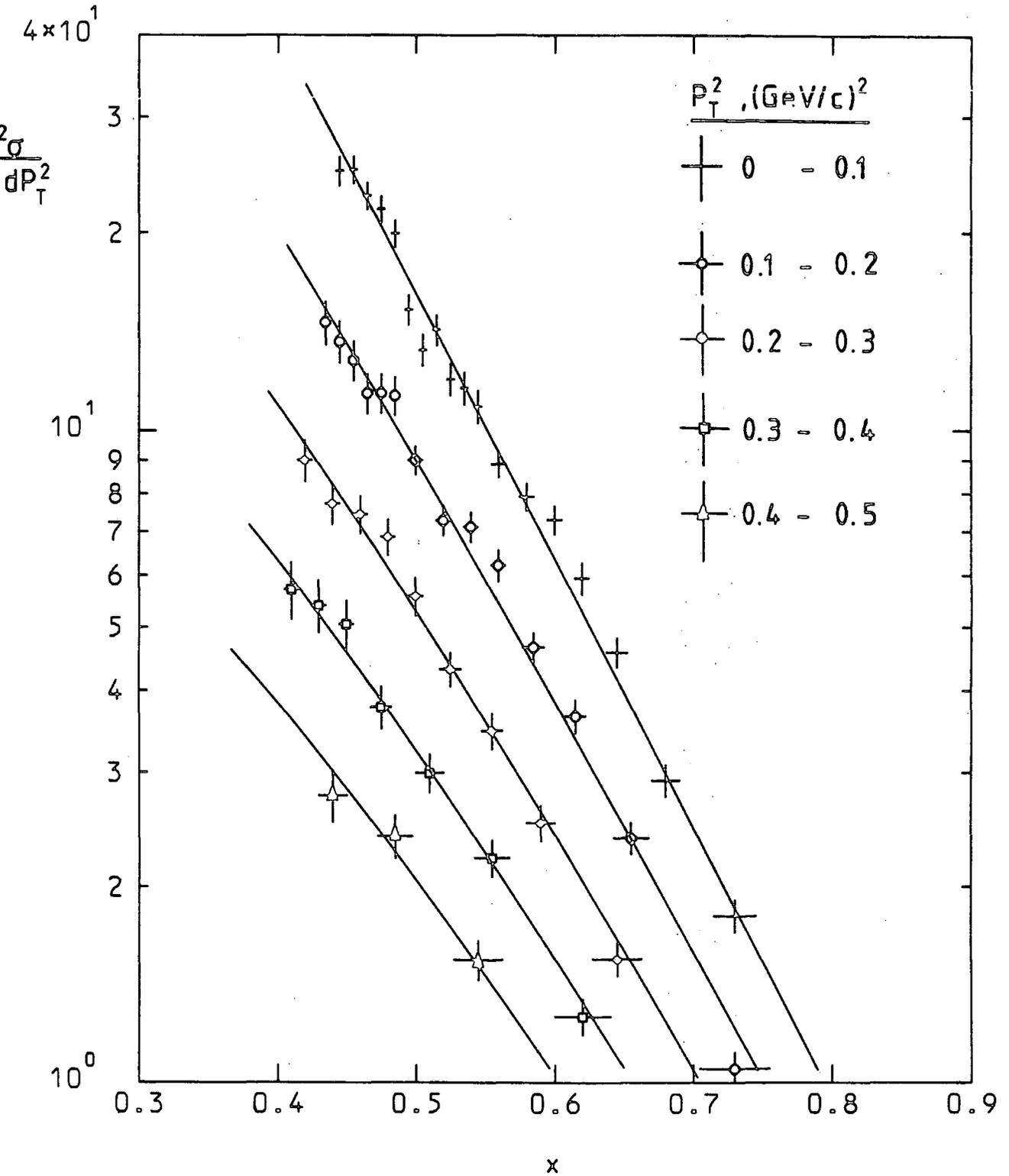
uncertainty (horizontal error bars represent $\pm \frac{1}{4}$ bin width). These
results are preliminary, especially regarding the normalisation.
Possible sources of errors are:

(a) Uncertainty in the sensitivities (see section 4.3.5); This
should be improved when the absolute normalisation is completed.

(b) The assignemnt of ambiguity weights is only approximate; however,
as indicated above, this affects no more than 10% of the data.

(c) Approximate acceptance weights used for $\sim$30% of the events. This
will be improved by use of a more precise, refined acceptance
table.

(d) Systematic errors in Canute identification. This has been con-
sidered in Chapter 3 in some detail.

(e) Treatment of multi-neutral events. It is assumed that these events
have the same throughput efficiency as constrained fits. This is
approximately true, but is somewhat laboratory-dependent, and
should be improved on subsequent DST's.

The normalisation has an estimated error of not more than $\pm$ 30%
at 6 GeV/c and $\pm$ 40% at 9 GeV/c, corresponding to the worst case of all
errors affecting the normalisation in the same sense. Comparisons with
previous data have been made, but are made difficult by different ranges
of p_t being used. Using the results in ref. 4.8 for the negative x
region, taken as appropriate in the positive x region of the charge
conjugate channel, the normalisation and slope of the differential
cross-section are consistent with our data.

4.4.3 Fits to the inclusive cross-sections

In the statistical thermodynamic model of Hagedorn (ref. 4.11) the distribution of transverse momentum is derived from the Bose distribution

$$\frac{d^2\sigma}{dp_L dp_t^2} \sim \frac{1}{\exp(E/T) - 1} \qquad (4.3)$$

where E is the total energy of the boson (in our case, pion), and

$$E = \sqrt{p_t^2 + p_L^2 + m^2} \qquad \text{(all quantities in C.M. System)}$$

and T is the "effective temperature". Neglecting the rest mass m, this yields the Hagedorn distribution for transverse momentum,

$$\frac{d\sigma}{dp_t} \sim p_t^{3/2} \exp(-p_{t/T})$$

which has been experimentally confirmed for πp and pp collisions. Furthermore, this gives for the average p_t

$$<p_t> = \frac{5}{2} T$$

and the observation that $<p_t>$ approaches an asymptotic limit at high energies (s → ∞) is well described by the "highest temperature" T_o ($\sim$ 0.160 GeV) which Hagedorn obtains from his model.

However, as pointed out by Hoang (ref. 4.12), the distribution (4.3) does not adequately describe the longitudinal momentum distribution. In particular, the ratio of the average p_t to that of p_L (for p_L > 0) is predicted to be a constant whereas, experimentally, $<p_L>$ increases with total energy. Asymptotically, Feynman scaling predicts

$$<p_L> \propto \sqrt{s}$$

To avoid this problem, Hoang has modified the distribution (4.3) thus

$$\frac{d^2\sigma}{dp_L dp_t^2} \sim \frac{1}{\exp(\varepsilon/_T) - 1}$$

where $\quad \varepsilon = \sqrt{p_t^2 + \lambda^2 p_L^2 + m^2}$ $\hspace{3cm}$ (4.4)

and λ is a dimensionless parameter. This does not affect the form of the p_t distribution, while for p_L it gives (asymptotically)

$$\langle p_L \rangle \sim T/\lambda$$

so, to satisfy the scaling law, we require

$$\lambda \sim \frac{1}{\sqrt{s}}$$

or, equivalently,

$$\lambda\, p_{max} \to \text{const. as } S \to \infty$$

where p_{max} is the maximum of the c.m. momentum of the secondary meson. This property has been investigated by Hoang (ref. 4.13) for p-p collisions at various energies. Here, the product $\lambda\, p_{max}$ was found to reach a limiting value of 1.86 ± 0.06 GeV/c above incident lab momenta of 20 GeV/c, and there were indications of a trend that $\lambda(\pi^+) < \lambda(\pi^-)$. Also, the temperature parameter T was found to be less for π^+ than for π^-. This is in accordance with the property of leading particles to have the largest p_L and (often) the smallest p_t which, for p-p collisions, are more likely to be π^+ than π^-.

However, in $\bar{p}p$ collisions, the leading particle is more likely to

be a π^-, so we would expect to observe the reverse behaviour. Hoang et al

(ref, 4.14) have fitted the parameters λ and T for forward and back-

ward inclusive π^+ production in $\bar{p}p$ collisions at 2.32 GeV/c. Since, by

charge conjugation invariance, the cross-section for backward π^+ produc-

tion is the same as forward π^- production, we can compare the values of

the parameters for π^+ and π^- in the forward region as shown in table 4.6.

Also shown in this table are fits to the $\bar{p}p$ data from the current

experiment to the same two-parameter distribution (equation 4.4).

The fitted curves are shown on figures 4.9 and 4.10, and were obtained by

minimising a χ^2 function constructed from all the data points shown on

each graph, separately for π^+ and π^- triggers and for the two incident

momenta.

.LE 4.6. FITS TO THE TWO-PARAMETER MODIFIED BOSE DISTRIBUTION FOR $\bar{p}p \rightarrow \pi^{\pm} X$
THE FORWARD $\pi^{\pm}$ REGION

		T(GeV)	λ	λp_{max} (GeV/c)	χ^2/NDF
.32 GeV/c*	π^-	0.128 ± 0.001	0.875 ± 0.003	1.111 ± 0.003	2.76
	π^+	0.125 ± 0.001	0.943 ± 0.001	1.198 ± 0.001	1.79
GeV/c	π^-	0.117 ± 0.002	0.501 ± 0.008	0.907 ± 0.015	2.33
	π^+	0.125 ± 0.003	0.617 ± 0.015	1.119 ± 0.028	2.95
GeV/c	π^-	0.119 ± 0.002	0.482 ± 0.008	1.035 ± 0.017	3.00
	π^+	0.123 ± 0.003	0.570 ± 0.011	1.223 ± 0.024	1.50

alues from ref. 4.14 (Hoang). Figures for forward π^- are inferred from fits to

ackward π^+ given in this reference.

The temperature T is seen to be about the same for secondary π^+ and π^- (if anything, $T(\pi^+) > T(\pi^-)$, as expected from above arguments), though T does not vary monotonically with CM energy. The parameter λ is clearly greater for π^+ than for π^-, and decreases with CM energy, as expected; however, $\lambda\, p_{max}$ is evidently not in the asymptotic region. Any interpretation of these numbers should take into account two points:

(1) The energies considered are well below those where scaling is applicable; however, it is in the higher energy scaling region where the thermodynamic model is least expected to describe well the longitudinal momentum distribution, since dynamical processes are more dominant.

(2) No single distribution of the form of equation (4.4) can possibly describe well both the forward and backward region of inclusive $\pi^{\pm}$ production at high energies, where the "leading particle" effect becomes significant. Indeed, a striking feature of the graphs 4.9 and 4.10 is that π^- cross-sections are about twice as big as π^+ cross-sections in the forward region, and this will be reflected in the forward-backward asymmetry by charge conjugation.

These are obvious shortcomings of the model; nevertheless the parameters T and λ are convenient ways of describing inclusive processes, and fits at higher energies would be interesting. Recent results at 12 GeV/c (ref. 4.15) give a temperature parameter (unmodified thermodynamic form), in the central region , of 111 ± 2 MeV.

The inclusive cross-section data from this experiment has also been fitted to a phenomenological expression, in terms of the invariant double-differential inclusive cross-section:

$$\frac{2\,E^*}{\pi\sqrt{s}}\ \frac{d^2\sigma}{dx\,dp_t^2} = A/\exp\,(b_1\,x + b_2\,x^2 + c_1 p_t + c_2 p_t^2 + d\,x\,p_t^2) \qquad (4.5)$$

Fitted values of the six parameters are given in table 4.7. It is emphasised that theabove expression should not be extended beyond the range of x and p_t^2 used in the fit (that is, the range of values plotted on the graphs 4.9 and 4.10).

TABLE 4.7   FITS TO THE PHENOMENOLOGICAL EXPRESSION (4.5) (see text) FOR $pp \rightarrow \pi^{\pm}$ X IN THE FORWARD $\pi^{\pm}$ REGION

	6 GeV/c		9 GeV/c	
	π^-	π^+	π^-	π^+
A	15.4	11.1	17.9	19.5
b_1	- 3.48	- 2.47	- 2.37	- 0.82
b_2	7.79	8.25	6.93	7.64
c_1	2.84	1.44	1.96	1.73
c_2	3.40	4.54	2.38	5.10
d	- 2.08	- 2.42	1.43	- 4.78
χ^2/NDF	1.12	1.63	1.90	1.67

4.4.4 Exclusive processes

A primary advantage of an experiment using a hybrid system is that accurate Kinematic fit information is available for many final state channels, at a statistical level normally unobtainable in a conventional bubble chamber experiment. This is especially true in this experiment of annihilation channels, since the trigger enhances the proportion of baryon-exchange processes. The drawback is that data are only obtained in a particular Kinematic region, so complete channel cross-sections can not be obtained. However, many processes which are good candidates for baryonium production are very likely to be selected by the trigger, so

cross-section limits can be usefully given. In this section, a graphical

way of presenting differential cross-sections is shown.

The numbers of fits for the common final state channels are given

in table 4.8. This excludes antiproton triggered events (so, for

example, the elastic channel is conspicuously absent), and is a count of

the "best fit" for each event; that is, the fit firstly of highest

number of constraints, and secondly of highest χ^2-probability. Multineutral

channels are not included here.

TABLE 4.8   NUMBERS OF "BEST FITS" ON THE JANUARY '81 DST (H_2 data only)

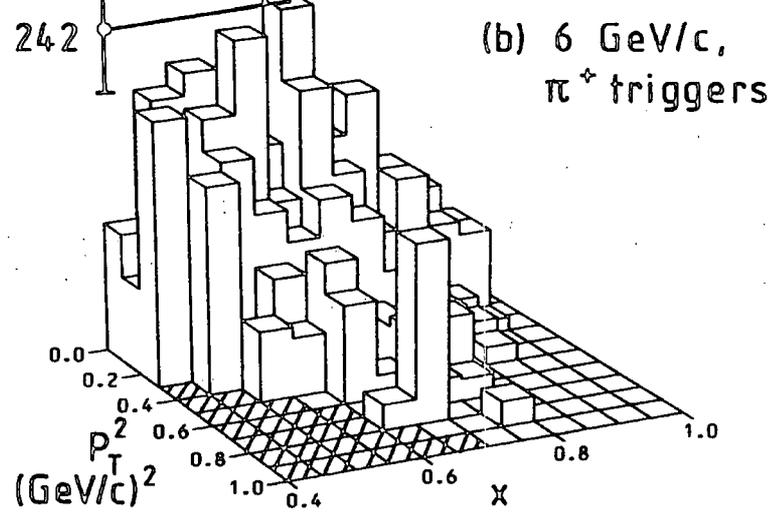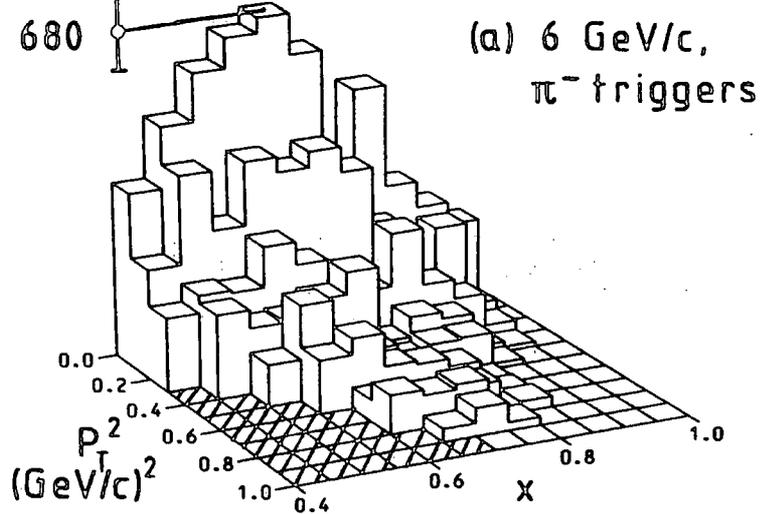| Channel	6 GeV/c	9 GeV/c
$\pi^+ \pi^-$	28	23
$\pi^+ \pi^- \pi^o$	712	802
$2\pi^+ 2\pi^-$	1712	1168
$2\pi^+ 2\pi^- \pi^o$	8279	6868
$3\pi^+ 3\pi^-$	1953	1760
$3\pi^+ 3\pi^- \pi^o$	5131	5901
$4\pi^+ 4\pi^-$	196	342
$4\pi^+ 4\pi^- \pi^o$	333	814
$\bar{p}p\pi^+ \pi^-$	2296	3508
$\bar{p}p\pi^+ \pi^- \pi^o$	739	1456
$\bar{p}n\pi^+$	2022	2078
$\bar{p}n\, 2\pi^+ \pi^-$	353	1551
$\bar{p}n\, \pi^-$	3960	5116
$\bar{p}n\, 2\pi^- \pi^+$	833	2215
$K^+ K^- \pi^+ \pi^-$	282	218
$K^+ K^- \pi^+ \pi^- \pi^o$	1466	1797
$K^+ K^- 2\pi^+ 2\pi^-$	214	246
$K^+ K^- 2\pi^+ 2\pi^- \pi^o$	500	1350
$K^+ K^o 2\pi^- \pi^+$	1170	712
$K^+ K^o 3\pi^- 2\pi^+$	283	305
$K^- K^o 2\pi^+ \pi^-$	1009	612
$K^- K^o 3\pi^+ 2\pi^-$	292	295

Double-differential cross-sections have been determined for the
four, five, six, and seven-pion final states, as a function of Feynman x
and p_t^2 of one of the pions (where two or more identical particles are
above the trigger momentum, the one of highest momentum is taken). The
results are displayed in figures 4.11 - 4.14. The height of a pillar
represents the average of $d^2\sigma/dx\ dp_t^2$ over that bin. The range of x
is limited to 0.4 - 1.0, below which the acceptance is zero, or too small
to give reliable results. This is also true in part of the region above
x = 0.4, shown as shaded areas in the figures. At 6 GeV/c this is due to
the cut on laboratory angle of the triggering particle (0.2 radians).
At 9 GeV/c there are two small shaded regions; the one in the foreground
is due to the angle cut (0.2 radians) and the one in the background is
due to the momentum cut (4.0 GeV/c).

On each diagram the height of the highest pillar is shown, in
$\mu b/(GeV/c)^2$, with an error bar representing the statistical error on
that number. Table 4.9 gives the summed cross-sections over the accepted
regions shown in the diagrams.

TABLE 4.9   PARTIAL CROSS-SECTIONS FOR THE FOUR, FIVE, SIX, AND SEVEN
            PION FINAL STATES (IN μb).

Trigger:	6 GeV/c		9 GeV/c	
	π^-	π^+	π^-	π^+
4π	63.6 ± 1.5	26.2 ± 0.6	31.3 ± 0.9	10.8 ± 0.3
5π	288 ± 3	141 ± 2	173 ± 3	77 ± 2
6π	61 ± 1.4	39 ± 0.9	48 ± 1.1	24 ± 0.6
7π	171 ± 2	100 ± 2	161 ± 2	84 ± 1

Fig. 4.11 Differential Cross-sections for $\bar{p}p \rightarrow 2\pi^+ 2\pi^-$

(a) 6 GeV/c, π^- triggers

(b) 6 GeV/c, π^+ triggers

(c) 9 GeV/c, π^- triggers

(d) 9 GeV/c, π^+ triggers

4 π

Fig. 4.12 Differential Cross-sections for $\bar{p}p \rightarrow 2\pi^+ 2\pi^- \pi^0$

(a) 6 GeV/c, π^- triggers

(b) 6 GeV/c, π^+ triggers

(c) 9 GeV/c, π^- triggers

(d) 9 GeV/c, π^+ triggers

5π

4226

2420

2020

991

P_T^2

$(GeV/c)^2$

X

(a) 6 GeV/c, π^- triggers

1556

(b) 6 GeV/c, π^+ triggers
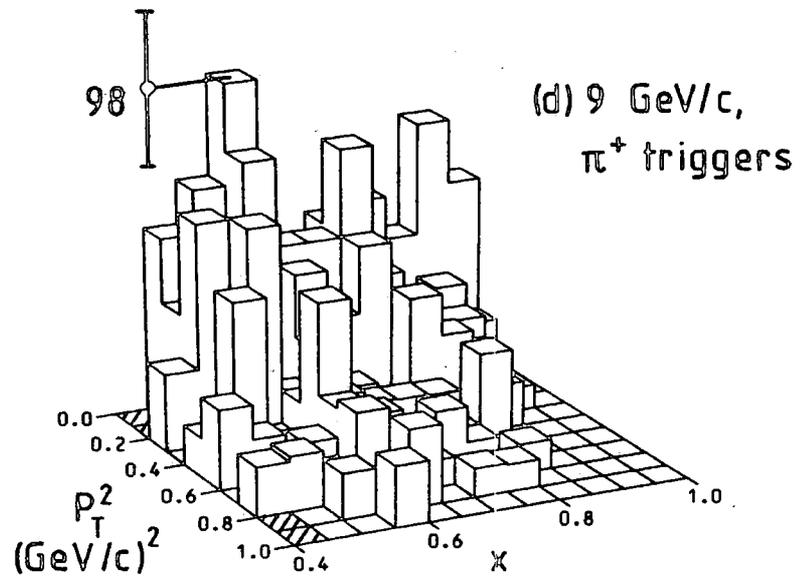
983

6π

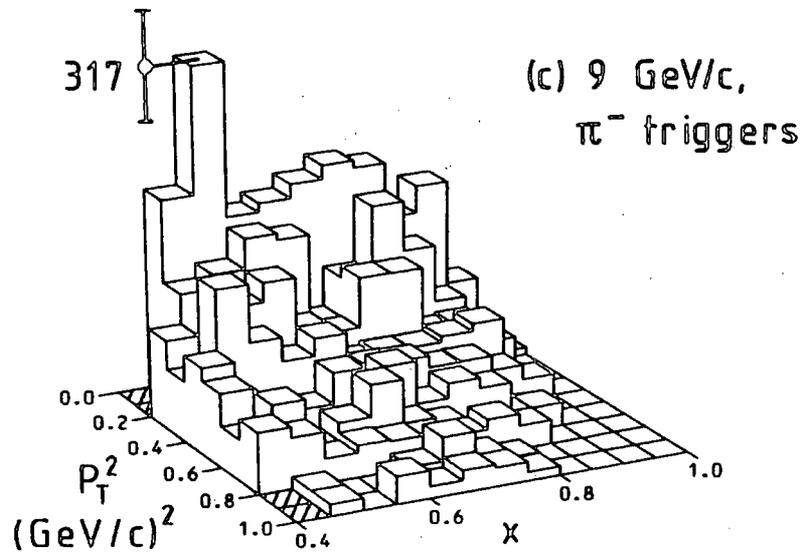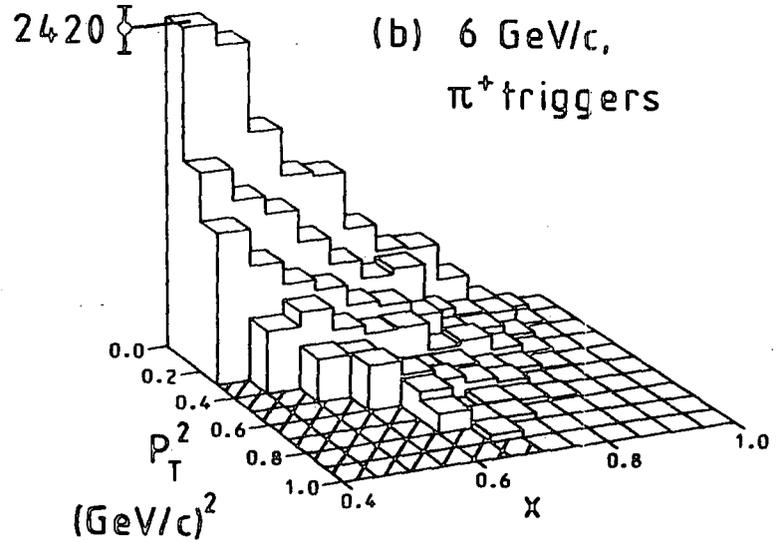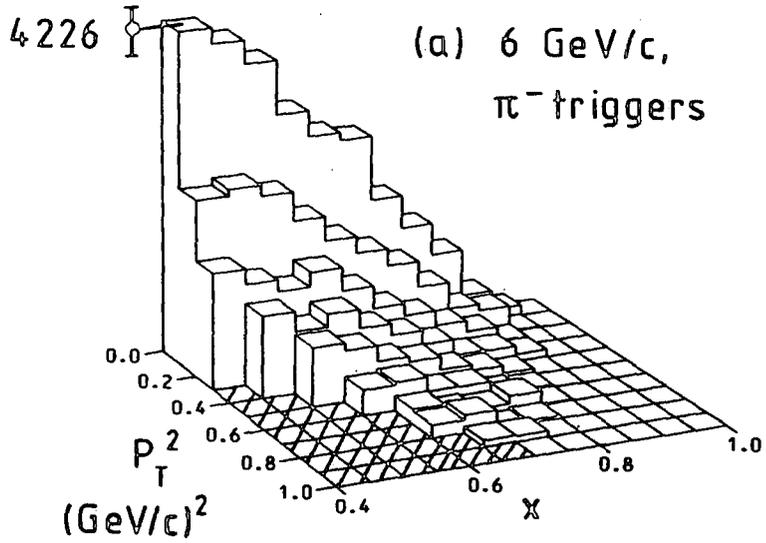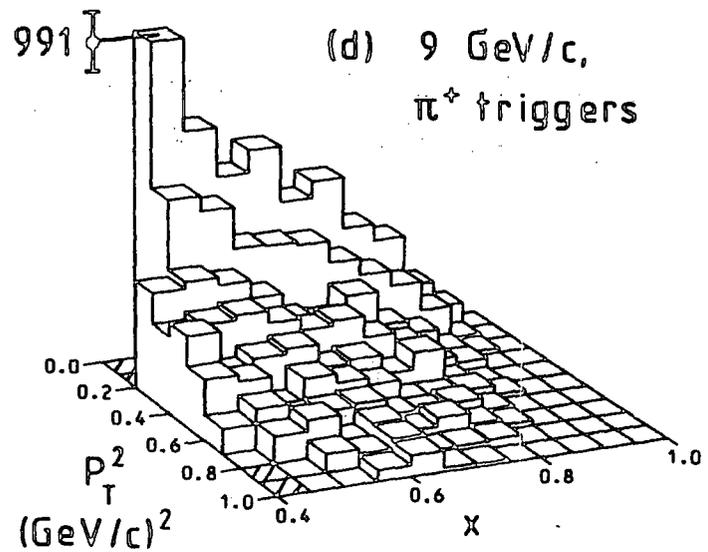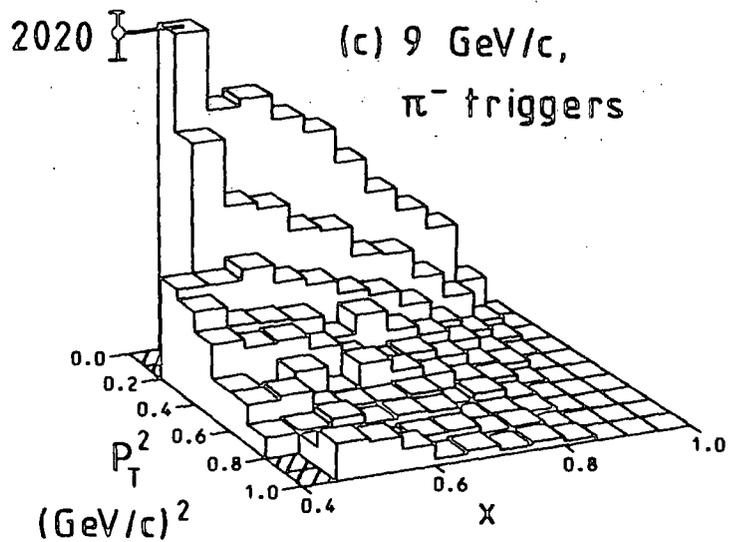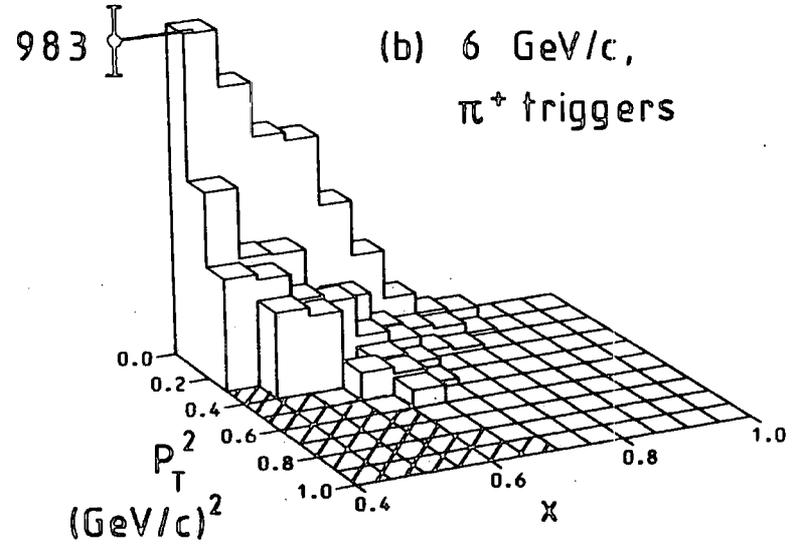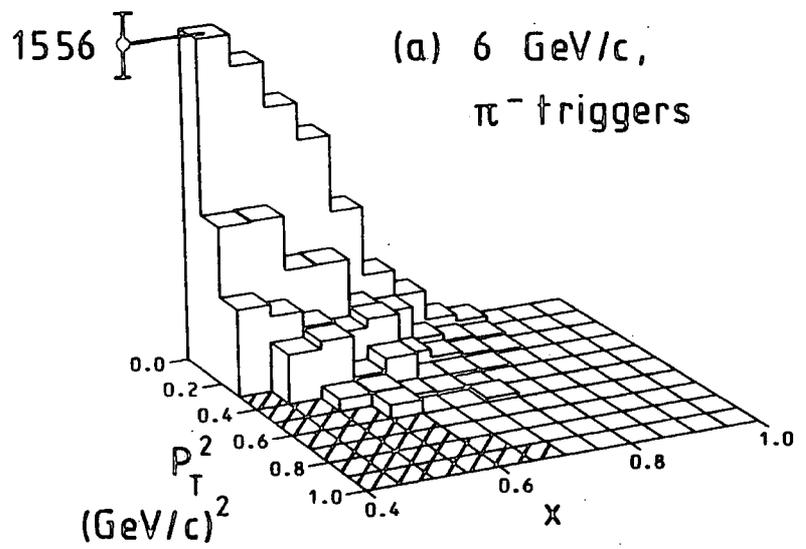(c) 9 GeV/c, π^- triggers

1073

(d) 9 GeV/c, π^+ triggers

436
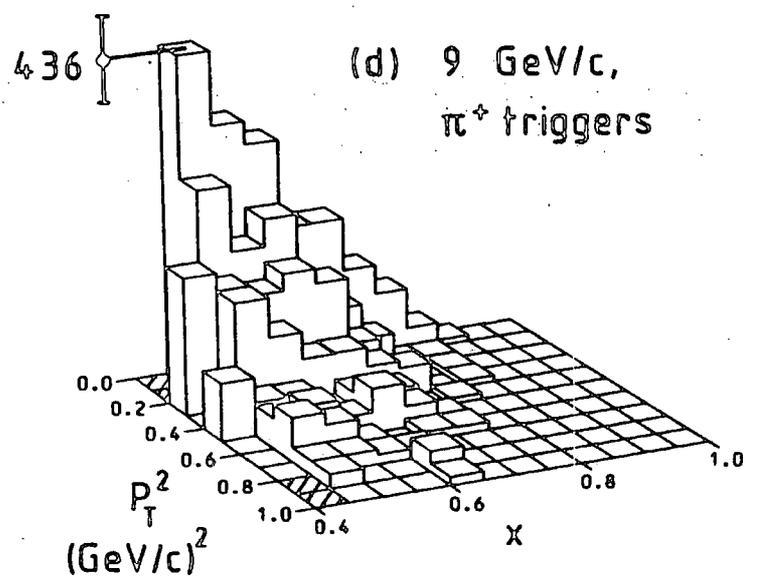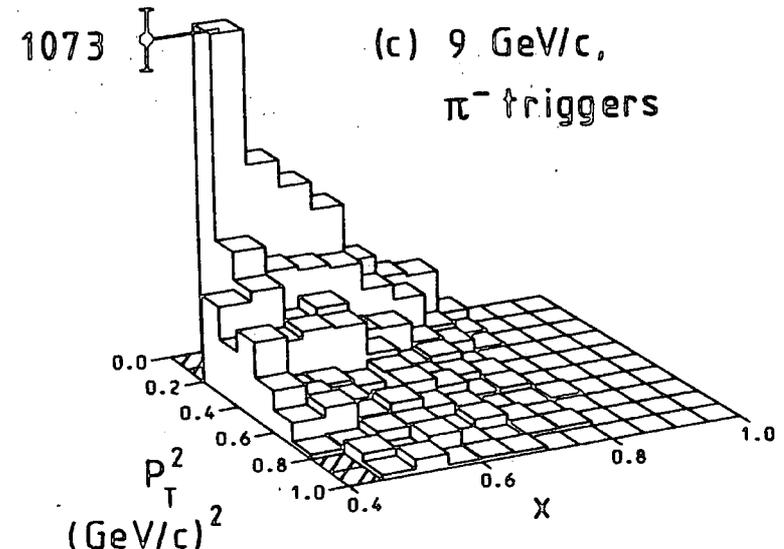
Fig. 4.14 Differential Cross-section for $\bar{p}p \rightarrow 3\pi^+3\pi^-\pi^0$

(a) 6 GeV/c, π^- triggers

(b) 6 GeV/c, π^+ triggers

(c) 9 GeV/c, π^- triggers

(d) 9 GeV/c, π^+ triggers

7π
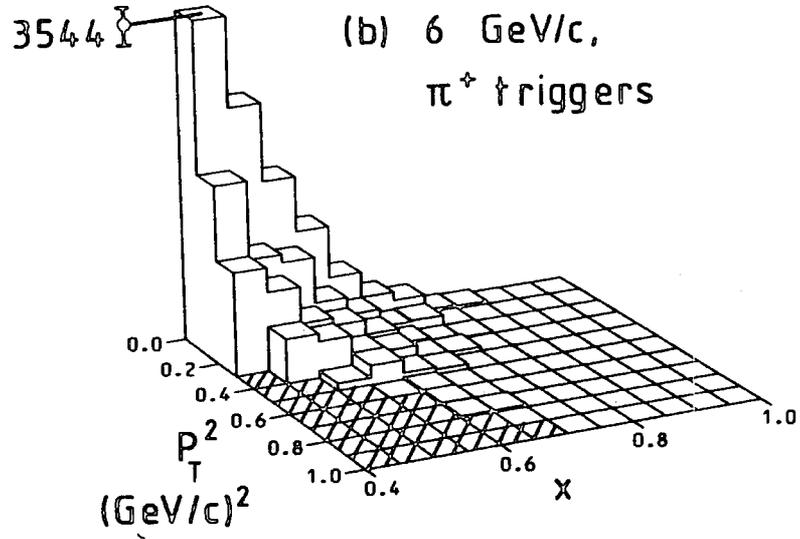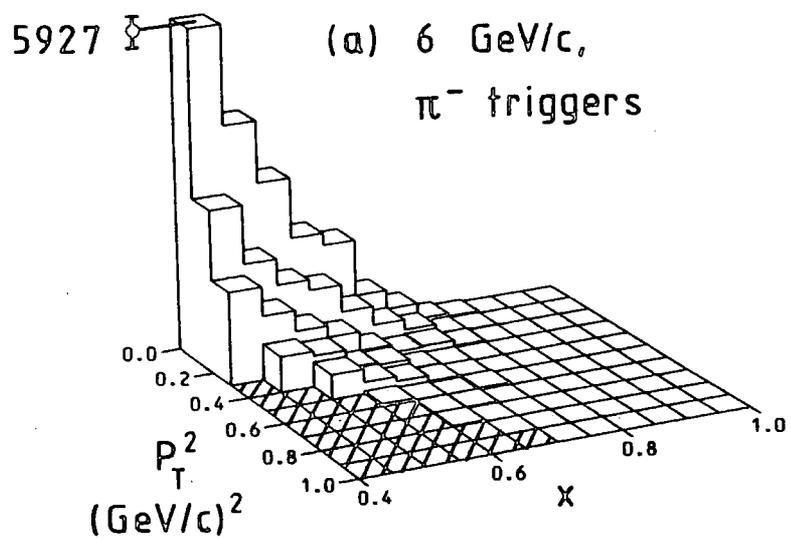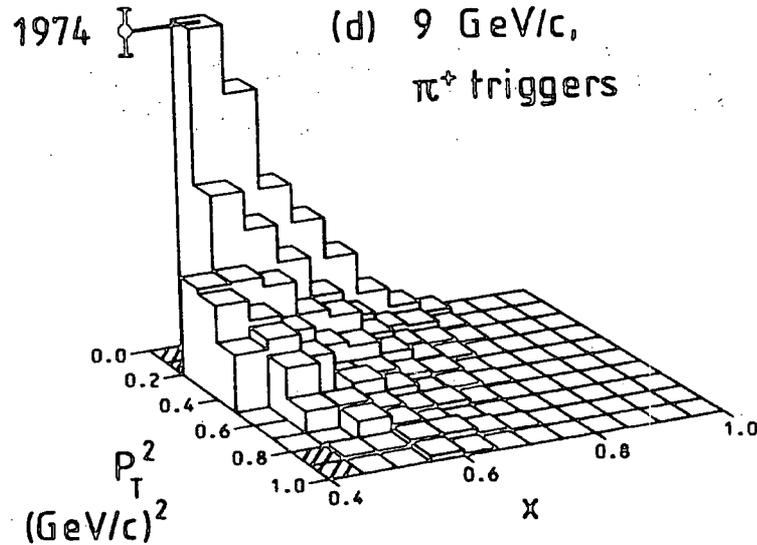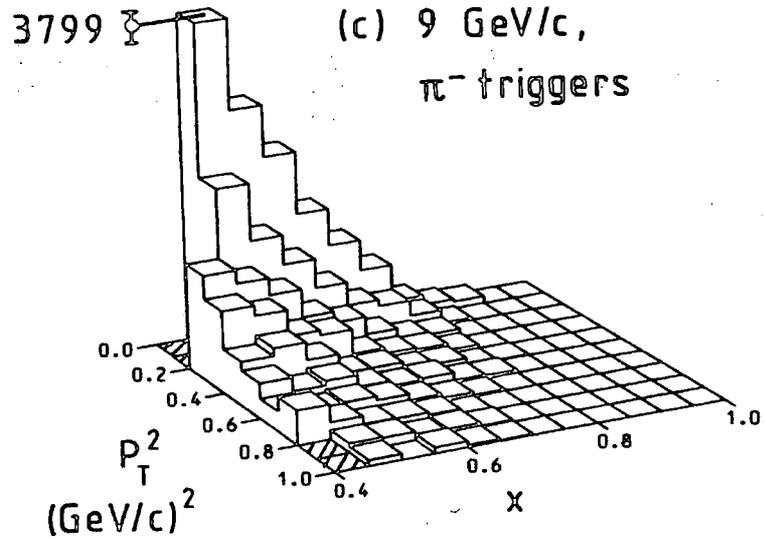
To give some idea of the acceptance restriction, the cross-sections
given for the 4π final state are 0.66 and 0.84 of the estimated total
cross-section (from averaging results of other experiments) at 6 and
9 GeV/c respectively. Errors given are statistical only; the uncertainty
in normalisation is not included. The highest level of ambiguities is
for the five pion final state (6% at 9 GeV/c), and is negligible for the
4C fits. Ambiguous fits are weighted in inverse proportion to the number
of ambiguities.

The heights of the highest peaks and the partial cross-sections show
the following trends: (i) the cross-sections for triggering on negative
pions are larger than for triggering on positive pions by a factor of
about two. This illustrates the leading particle effect (that is, the
tendency for fast, forward particles to preserve the charge of the beam
particle); (ii) the cross-sections at 9 GeV/c are typically half those
at 6 GeV/c. This is in accordance with the usual behaviour of annihilation
cross-sections to fall off rapidly with energy (typically as s^{-3});
(iii) the cross-sections for final states including a neutral pion are
considerably higher than the corresponding states without the neutral
pion. Although the comparison is complicated by the selection of a
restricted Kinematic region (especially as for many body final states a
large fraction of the cross-section is for $x < 0.4$), nevertheless the
trend is clear. This effect has been noted previously (e.g. ref. 4.16)
and is understandable in terms of the multiperipheral model with nucleon
exchange. In this model, the charge of an outgoing π^+ or π^- has to
alternate along the multiperipheral chain, whereas a π^o can be placed
anywhere in the chain, thus allowing more degrees of freedom for final
states with a π^o, and hence (intuitively) a greater cross-section.

Other observations from figs. 4.11 - 4.14 are: (a) the differential
cross-sections fall off rapidly with p_t^2, in the way characteristic of

most hadronic processes; and (b) in the four pion final state, the differential cross-section reaches a peak as x increases, and then falls to zero at high x. In the 5π, 6π, and 7π distributions, the peaks appear to lie below x = 0.4.

In summary, the differential cross-section distributions show the expected behaviour for multi-pion annihilations. Although the trigger acceptance complicates comparison with other data, the number of events is higher than any previous experiment at comparable beam momenta. Theoretical models may be used and fitted to a large part of the channel cross-section. This is done for the four pion final state in the next chapter.

CHAPTER 5

THE FOUR PION FINAL STATE

5.1   ANNIHILATIONS

In hadronic physics, annihilations are processes in which a
baryon and an anti-baryon interact but produce no final state baryons.
Such processes are not well understood theoretically and the subject of
annihilation mechanisms is one of considerable interest.

The main characteristics of annihilations, compared with non-
annihilations, are :

(a) Rapidly falling cross-section with beam momentum.

(b) Higher multiplicities at the same centre-of-momentum.
energy, even after allowing for annihilation of the leading anti-baryon
and baryon.

(c) Larger average transverse momentum of outgoing particles,
indicating a more central process.

(d) More copious production of resonances and kaons. This is
likely to be merely a result of the increase in available energy from the
annihilation of the massive particles.

(e) A pronounced "leading particle" effect ; that is, the tendency
for an outgoing meson to follow the direction of the baryon or anti-
baryon of the same charge. This is indicative of a baryon exchange
mechanism.

5.1.1 Models of Annihilations

There are three basic kinds of model for annihilation processes :
(a) Quark Models - These attempt to describe the mechanism in terms of
constituent quarks. Recent developments have produced a number of such
models (ref. 5.1). In the Quark Re-arrangement model (ref 5.2) the

quarks are simply re-grouped to form mesons. This is represented as in

figure 5.1(a), where the quark lines are shown as emitting mesons. In

the Quark Fusion model, the quarks and antiquarks fuse together to

produce mesons, and they may be either sea or valence quarks. The Quark

Recombination model (ref 5.3) incorporates both these ideas, and allows

for the combination of a valence quark and a sea antiquark from the same

hadron, thus explaining the leading particle effect. Finally, the Quark

Fragmentation model considers annihilations as three $q\bar{q}$ jets converting

into hadrons in a way analogous to $e^+ e^-$ jets. These models have been

tested with varying degrees of success, but no single model can account

for all the data at all energies.

(b) <u>Exchange Models</u> – Since Regge theory has been highly successful in

describing most high energy hadronic processes, it is natural to try

applying it to annihilations. Goldberg (ref. 5.4) has used a simple multi-

Regge model and has predicted cross-section variation and multiplicities.

This assumes baryon exchange with many meson vertices (see figure 5.1(b)).

(c) <u>Statistical Models</u> – It is known that, at low energies, annihilations

are dominated by phase space. This leads to the picture of the formation

of a single "cluster" or "fireball" which subsequently decays in a random

manner. The statistical bootstrap model (mentioned in the previous chapter)

has been applied to annihilations (e.g. ref 5.5), with considerable success

at very low energies. In the model of Orfanidis and Rittenberg (O.R.),

there are the additional postulates that the fireball undergoes a linear

chain of decays (fig 5.1(c)), and that the fireball can never be doubly

charged (ref 5.6).

The O.R. model has been compared to the Goldberg model in fits to annihila-

tion data by the Liverpool-Stockholm Collaboration (ref 5.7). They find that the

$\bar{p}$ $\left\{\begin{array}{l}\bar{q}\\\bar{q}\\\bar{q}\end{array}\right.$ — — M_1 (a)

— M_2

— M_3

p $\left\{\begin{array}{l}q\\q\\q\end{array}\right.$ — — M_4

— M_5

$\bar{p}$ ——————— M_1 (b)

M_2

M_3

M_4

p ——————— M_5

$\bar{p} \longrightarrow\!\!\!\!\!> \quad <\!\!\!\!\!\longrightarrow p$ (c)

M_5

M_1 $\quad$ M_2 $\quad$ M_3 $\quad$ M_4
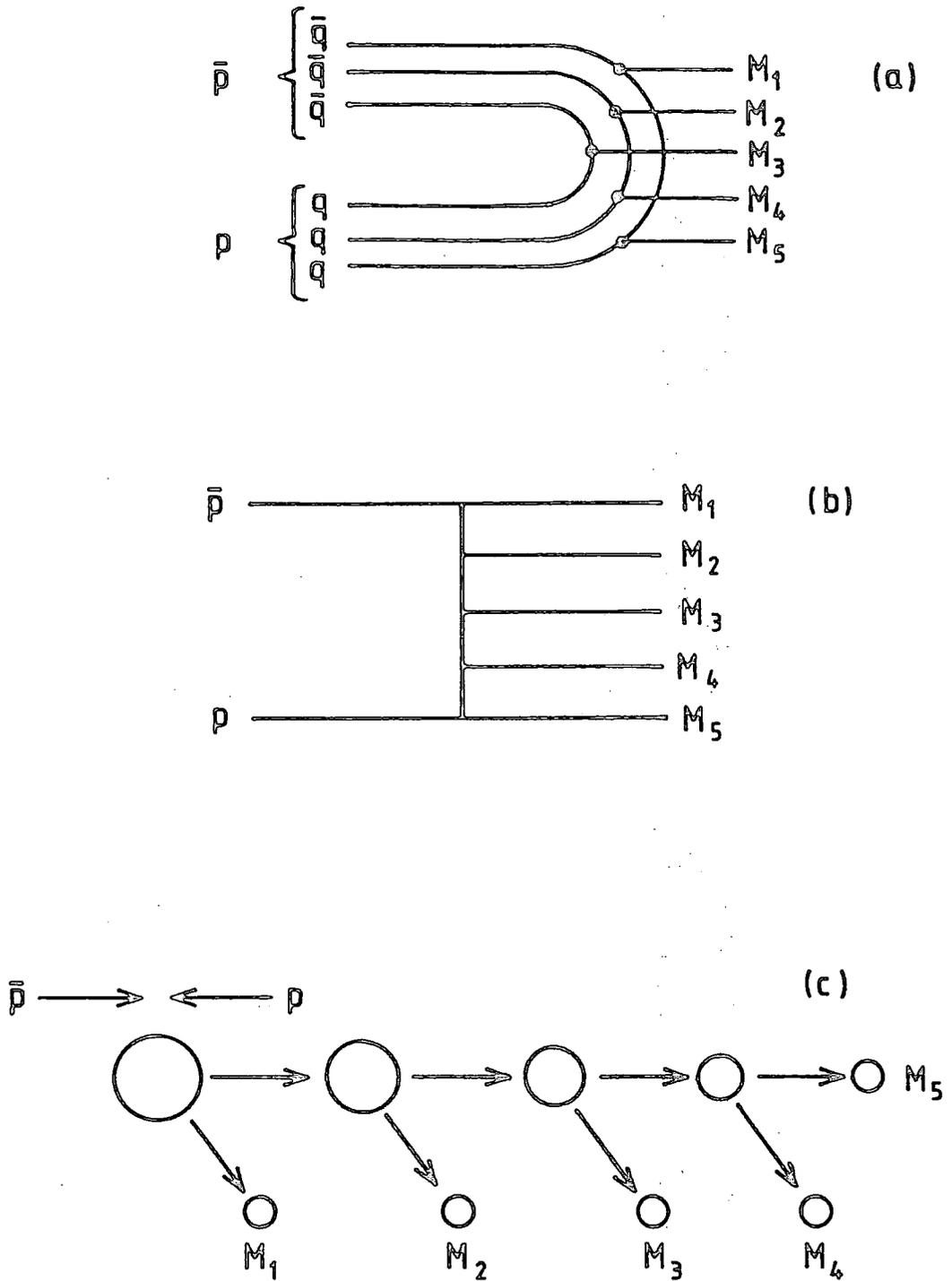
Fig. 5.1 Models of Annihilation: $\bar{p}p \rightarrow$ mesons

(a) Quark Rearrangement model

(b) Multi-Regge model

(c) Decaying Fireball model

Goldberg model of Regge exchange only gives reasonable fits at high

energies, while the O.R. fireball model describes the data better at low

energies (less than ∿ 10 GeV/c). A phenomenological model (C.L.A) which

interpolates smoothly between a low energy statistical amplitude and a

high energy multi-Regge amplitude has been proposed by Chan, Loskiewicz

and Allison (Ref. 5.8).

A serious deficiency of these models is that they do not take

into account resonance production, which is known to be dominant in

annihilations. Clearly, the annihilation process is a highly complex one,

and there is no single model yet that describes all the data well.

5.1.2 Is Annihilation Central or Peripheral ?

A simple hypothesis is that the difference between $\bar{p}p$ and pp

cross-sections is made up solely by the additional annihilation channels

in $\bar{p}p$, and this is known to work well for the total cross-sections at a

wide range of energies. It is also known (see e.g. Ref. 5.9) that the

total cross-section difference is sharply peripheral. If the hypothesis

were strictly applicable at each impact parameter separately, this would

imply that annihilations are also peripheral. There are severe experimental

difficulties in determining impact parameters for annihilation reactions ;

however, some attempts have been made to calculate lower bounds on the

average impact parameter (b_L). Warren et al (Ref. 5.10) find that b_L is

higher than for pure phase space, but lower than for non-annihilation events,

which conflicts with the above hypothesis. A similar conclusion is reached

by Braun et al (Ref. 5.11) who also give evidence that the variation of b_L

really does reflect the variation in actual impact parameter. However, a

recent analysis at 8.8 GeV/c (Ref. 5.12) is inconclusive concerning the

behaviour of b_L.

Another parameter indicating the degree of peripherality is the

average transverse momentum $<P_T>$ of outgoing particles. A highly peripheral

process would be expected to have a low $<P_T>$; and it is known that, for non-annihilation processes, $<P_T>$ reaches an asymptotic limit of ~ 0.35 GeV/c at high energies. In contrast, $\bar{p}p$ annihilations have consistently higher values of $<P_T>$ than for non-annihilations and show no obvious tendency to reach an asymptotic limit (at least up to 9 GeV/c) (see Ref. 5.12 and 5.13). In conclusion, the present evidence is that annihilations are more peripheral than phase space, but not as peripheral as non-annihilations. This could be a characteristic of baryon exchange, and does not necessarily indicate a dominant statistical component in annihilations.

5.2   SUMMARY OF PREVIOUS WORK ON THE REACTION $\bar{p}p \rightarrow 2\pi^+ 2\pi^-$

The simplest exclusive annihilation channel for which we have good statistics in the present experiment is the reaction $\bar{p}p \rightarrow$ four charged pions. This also has the advantage of being a 4C fit, so ambiguities are negligible. This reaction has been investigated in a number of previous experiments, mostly at lower beam momenta (Refs. 5.14 - 5.39). At high momenta there is a serious lack of statistics, which is where the present experiment makes a valuable contribution ; Atherton et al (Ref.5.15) have 577 events at 5.7 GeV/c (we have about three times this number at 6.05 GeV/c); Warren et al (Ref.5.19) have 60 events at 9.1 GeV/c (we have about 20 times this number at 8.8 GeV/c).

5.2.1 Effective Mass Plots

The two-body $\pi^+ \pi^-$ effective mass plots show abundant resonance production in all experiments. The ρ-meson is very strong, and so is the f-meson when well above threshold. There is also some production of the g-meson in the higher energy experiments. Breit-Wigner fits to these resonances reveal the following :-

(a) there is a dip in the higher energy data between the ρ and f peaks that falls significantly below the fitted curve. Atherton et al (Ref.5.15)

have attempted to explain this in terms of interference from an s-wave amplitude, without much success. As yet, there is no satisfactory explanation for this effect, and it indicates a complex production mechanism.

(b) The fitted central mass of the ρ-meson is commonly found to be in the range 740-755 MeV, considerably lower than the currently accepted value of 776 ± 3 MeV (from ref. 5.40). Fields and Singer (ref. 5.41) have noted that this can be explained in terms of the decaying fireball model as an apparent mass shift produced by restrictions on available energy from decay transitions. Alternatively, it could be the result of interference with a coherent background, and hence connected with observation (a).

(c) ρ-ω interference has been reported by a number of high statistics experiments (refs. 5.30, 5.33, 5.36, 5.37). This is manifested as a slight enhancement in the $\pi^+\pi^-$ effective mass near the ω^o mass. The effect on the apparent ρ mass would be a small shift to a higher value, and so does not explain observation (b).

The three-body $\pi^+\pi^-\pi^+$ effective mass plots show substantial $A_2^\pm$ production in most of the low energy experiments. There is also a tentative claim for A_1^+ production by Donald et al (ref. 5.16). However, in the higher energy experiments there are no significant signals, and distributions are generally consistent with phase space.

5.2.2. Cross-section Variation

The channel cross-section for $\bar{p}p \rightarrow 2\pi^+ 2\pi^-$ as a function of antiproton momentum is shown in figure 5.2 (a). Atherton et al (ref. 5.15) find a reasonable fit to the parametrisation.

$$\sigma = K s^{-\alpha} \qquad (s = \text{c.m.s. energy squared})$$

with $K = 326 \pm 37$ mb and $\alpha = 3.01 \pm 0.07$. Using this fit, the predicted cross-sections at our energies (s = 13.2 GeV^2 and 18.5 GeV^2) are 137 ± 29 μb and 50 ± 12 μb respectively. Since the four pion final state is dominated by resonance production, it is also of interest to give the cross-sections
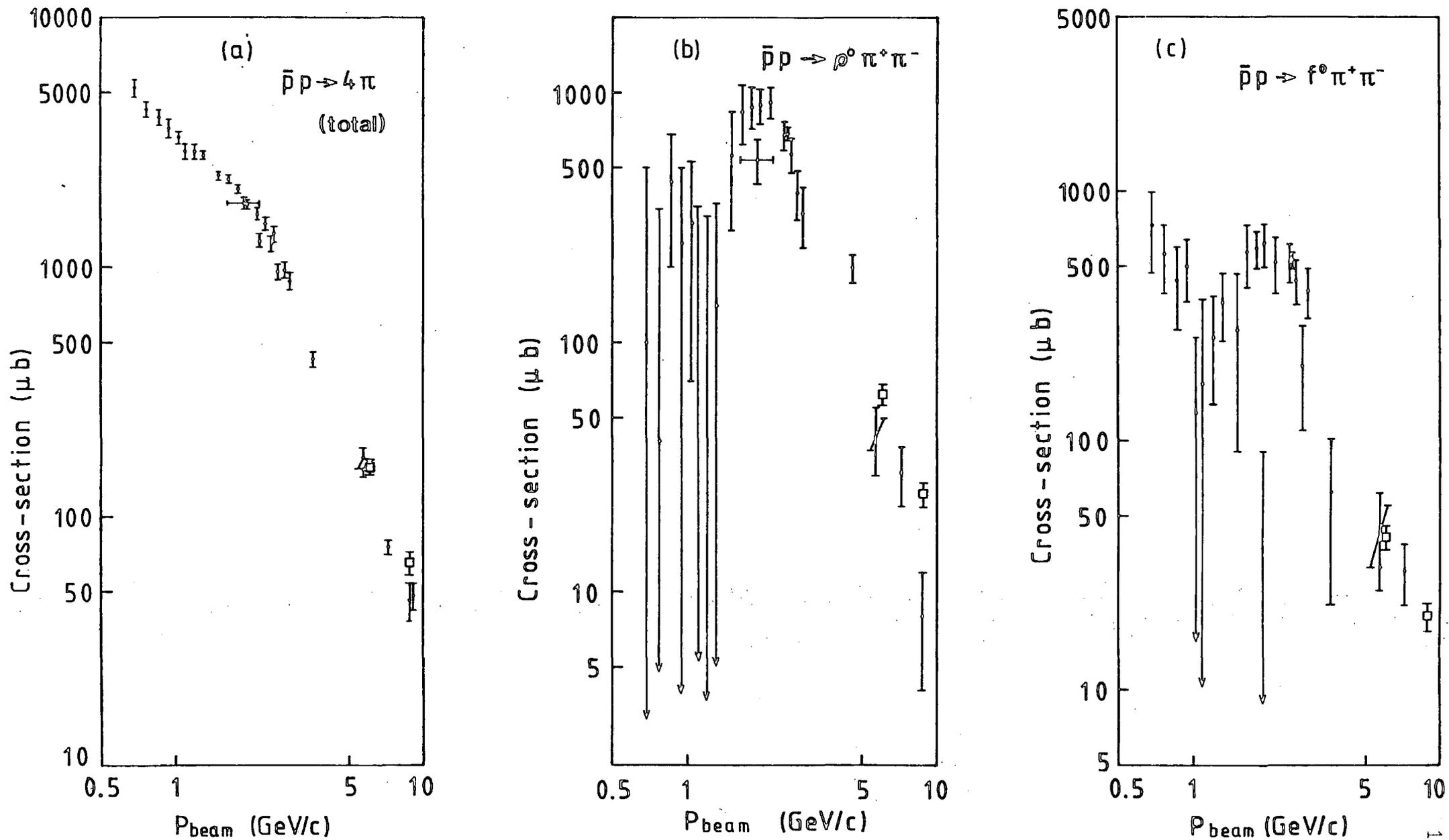
Fig. 5.2   Cross-sections for $\bar{p}p \to 4\pi$ and intermediate channels making up this final state.
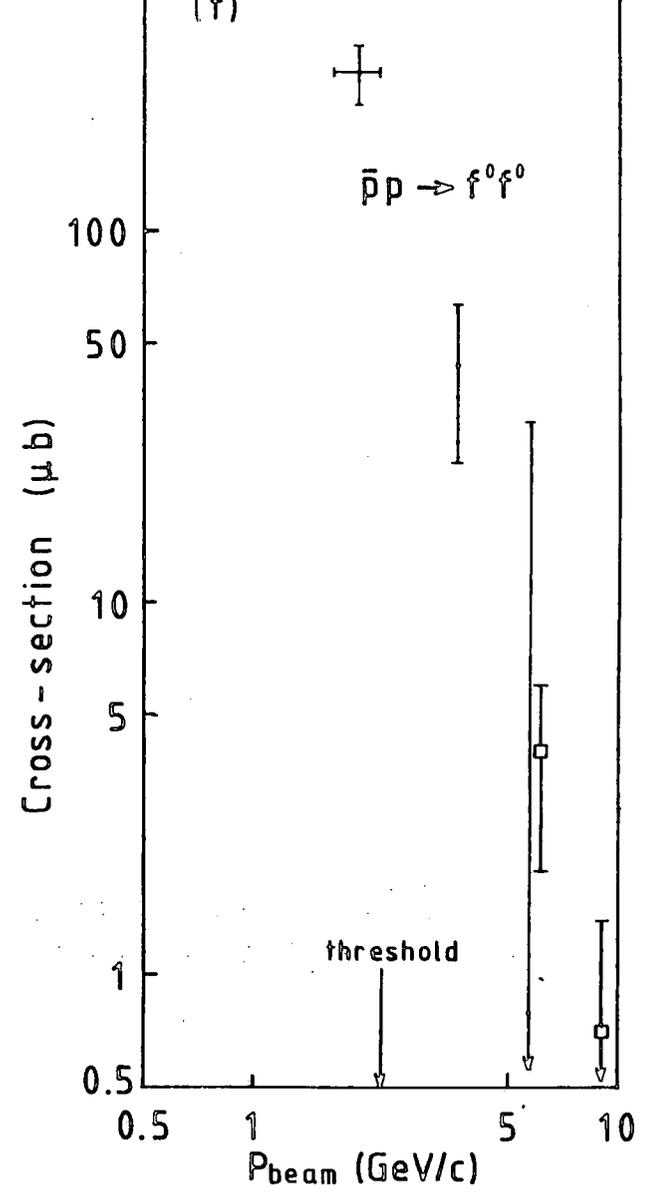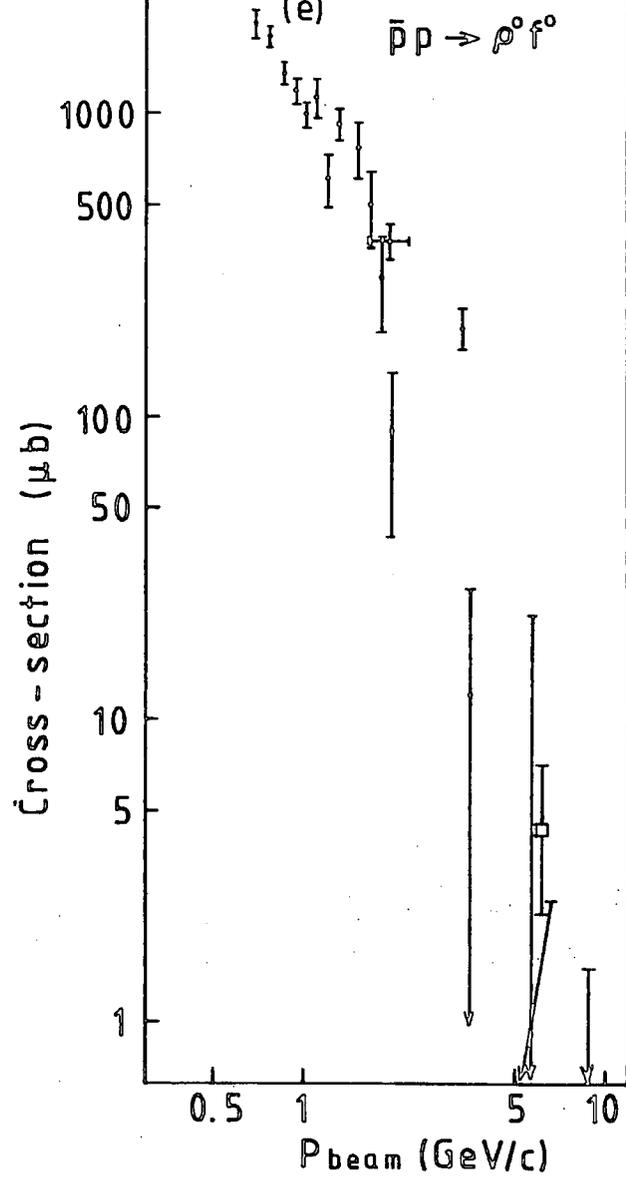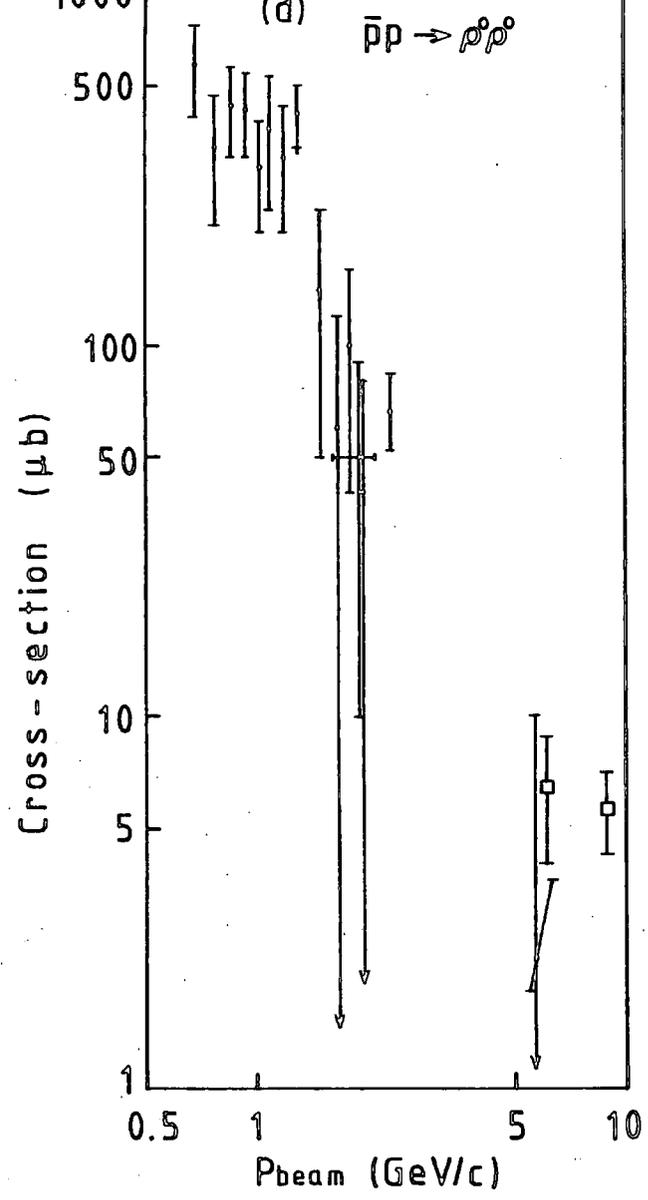
Fig. 5.2 (cont.)

for the main quasi two-body and three-body processes which contribute to this channel:-

$$\bar{p} \, p \;\rightarrow\; \rho^o \pi^+ \pi^- \quad \text{(fig. 5.2(b))}$$

$$\bar{p} \, p \;\rightarrow\; f^o \pi^+ \pi^- \quad \text{(fig. 5.2(c))}$$

$$\bar{p} \, p \;\rightarrow\; \rho^o \rho^o \quad \text{(fig. 5.2(d))}$$

$$\bar{p} \, p \;\rightarrow\; \rho^o f^o \quad \text{(fig. 5.2(e))}$$

$$\bar{p} \, p \;\rightarrow\; f^o f^o \quad \text{(fig. 5.2(f))}$$

The cross-sections given are for resonance decays to $\pi^+ \pi^-$ only. These have been obtained in the analysis of a number of experiments, mostly using a maximum likelihood technique. For all the processes, the cross-section falls very rapidly with incident momentum, and the data above 5 GeV/c are sparse, with large errors. In particular, the rates for associated production ($\rho\rho$, ρf, ff) above 5 GeV/c are consistent with zero. The cross-section for direct four pion production (that is, with no intermediate resonances) is not shown, but is generally fitted to be a small fraction of the total; the channel clearly proceeds overwhelmingly via resonance production.

5.2.3. Production and Decay Angular Distributions

The c.m. angular distribution of pions relative to the incident (anti) proton shows an increasingly peripheral behaviour as beam momentum increases. That is, at low momenta (e.g. $\sim$ 1 GeV/c, ref. 5.32) the distributions are nearly isotropic, while at higher momenta (e.g. 3.6 GeV/c, ref. 5.22) there is a pronounced forward peak (relative to the incident particle of the same sign), and a smaller backward peak. The production angular distribution of ρ^o and f^o mesons show a similar effect, except that the forward and backward peaks are equal, as required by C-invariance. This indicates a baryon exchange mechanism.

The so-called Goldhaber effect has been observed in the four pion final state by a number of experiments (refs. 5.34, 5.31, 5.17, 5.22, 5.28). This is the tendency for the opening angle to be smaller between like-charged than between unlike-charged pions. The effect seems to be most pronounced at low beam momenta where the correlations are fairly well described by considering resonance production and Bose symmetrisation. However, such explanations have been only partially successful when applied to higher energies, and the effect is still not well understood (ref. 5.42)

The resonance decay angular distributions are less well determined, but the available evidence from other experiments is that they are not very far from isotropic, which would indicate an almost unpolarised resonance (at least for the ρ^0). The density matrix elements determined by three different experiments are given in table 5.1 (referred to as d_{mm} to avoid confusion with the ρ-meson).

Table 5.1 : Density Matrix Elements for the ρ-meson
in the four-pion final state

P_{beam} (GeV/c) (Ref.)	Final State	d_{oo}	d_{1-1}	Re d_{10}
0.94 (Ref. 5.32)	$\rho^0 \pi^+ \pi^-$	0.25 ± 0.02	0.03 ± 0.02	-0.01 ± 0.04
	$\rho^0 f^0$	0.28 ± 0.05	0.02 ± 0.05	0.12 ± 0.12
1.26 - 1.65 (ref. 5.36)	$\rho^0 \pi^+ \pi^-$	0.2 ± 0.02	0.02 ± 0.02	0.01 ± 0.01
5.7 (ref. 5.14)	$\rho^0 \pi^+ \pi^-$	0.67 ± 0.25	-	-

5.2.4 Models of the four pion final state

Since the most obvious feature of the four pion final state is resonance production, a number of efforts have been made to describe the amplitude by a linear combination of various Breit-Wigner terms, with appropriate Bose-symmetrisation. The amplitude is then fitted to the data by a maximum

likelihood technique. This approach has been very successful at low energies where the peripheral nature of the reaction is not too significant. Some authors have tried adding the Breit-Wigner terms both coherently and incoherently and found that the fit is not very sensitive to this choice (though a slight preference for incoherent addition is indicated).

Ranft (ref. 5.25) has applied the C.L.A. model (mentioned in section 5.1.1) to the four pion final state at 5.7 GeV/c. The model describes the data quite well, especially after the introduction of resonances in quasi-three-body processes. The C.L.A. model is also tested by Frodesen et al (ref. 5.26) in comparison with two other multi-Regge models: a model by Plahte and Roberts where the resonances are accounted for by the inclusion of phases in the amplitude; and a model by Roberts which also has factors of the form e^{bt} in the amplitude.

Both of these models predict too much resonance signal, though the angular and t-distributions fit very well (especially the Roberts version where the amplitude has factors of the form e^{bt}).

De La Vaissiere (ref. 5.21) has achieved very successful fits to the C.L.A. model by introducing the fractions of resonance production as extra parameters, and assuming that the resonances are coupled to the exchanged baryon with the same intensity as pions. (However, in a later work (ref.5.23) it was claimed that the model could only be satisfactorily extended to higher multiplicities and different energies if one included production of an s-wave resonance of mass ∿650 MeV.) Further investigations of the production mechanism at 3.6 GeV/c have been made (ref. 5.24) by applying rapidity selections and examining mass plots. The conclusions are that: in quasi-two-body processes, the ρ^o is produced mainly peripherally, the f^o and g^o less so; while in quasi-three-body processes, the ρ^o appears to be produced mainly centrally, and the f^o even more centrally.

The Liverpool collaboration has put forward a model based on the observed leading particle effect (refs. 5.18 and 5.19). By separating out the leading pion, they find that this pion is rarely involved in resonance production, whereas the other three pions often are. The proposed model is of a single pion recoiling against a loosely bound cluster of three pions, which in turn decays to a pion and a resonance in the ρ, f, g sequence. This cluster is found to have weak internal directional properties and is hence reasonably described by phase space. The leading pion is sometimes the 'wrong' sign with respect to the incoming (anti) proton at that vertex, which gives rise to the backward peak in the angular distribution. This suggests that Δ^{++} exchange contributes significantly, in which case one would expect it to become more dominant at higher energies (because of the higher intercept of the Δ trajectory compared with the nucleon trajectory). However, ref. 5.18 points out that the backward peak may be purely a Kinematic effect.

A parametrisation for the differential cross-section is given in terms of the four-momentum transfer squared (t) and the recoil mass (M) (ref.5.19):

$$\frac{d\sigma}{dt} \propto \int F(t,M^2)\ dM^2 \left[\text{LIPS}\ (M \to 3\pi) \right]$$

where $F(t,M^2) = \left[0.75\ e^{2.2t} + 0.25\ e^{2.2\ u} \right] e^{-0.5M^2}$

The second term represents u-channel exchanges. The numbers in this expression are claimed to be valid at three different energies (2.5, 4.6, and 9.1 GeV/c), and also for the channel $\bar{p}p \to 3\pi^+ 3\pi^-$. This parametrisation reproduces satisfactorily several features of the data.

For completeness, two more models will be briefly mentioned. Stenbacka et al (ref. 5.20) have modified the statistical model of Orfanidis and Rittenberg to take into account resonance production. Fractions of resonance production, charge distributions, and multiplicities are predicted and are

found to be broadly in agreement with data, although there are some discrepancies. Finally, a quark model has been applied to the $\rho^0 \pi^+ \pi^-$ final state by Apeldoorn et al (ref. 5.38). The peripheral nature of the interaction is qualitatively described by the model of Eylon and Harari in which the mesons are emitted from one, two or three quark lines ; however, the more specific quark rearrangement model favours emission from all three quark lines, leading to isotropic angular distributions, which is inconsistent with data.

In conclusion, a variety of different models have been invoked to describe annihilation into four charged pions and the situation is rather confused. However, some features are persistent : abundant resonance production and a leading particle effect becoming more pronounced at higher energies. It is likely that a number of different mechanisms all contribute to the channel ; nonetheless one would expect a Regge exchange model to dominate at the energies of the present experiment, and this is pursued in section 5.4.

5.3 ANALYSIS OF THE PRESENT EXPERIMENT

As mentioned in the last section, the number of events in the four pion final state obtained in this experiment is far greater than in any previous experiment at comparable energies. This is somewhat disadvantaged by the selection imposed by the trigger which makes, for example, the angular distributions difficult to interpret. However, the kinematics of this channel is such that only about 40% of events are outside the accepted region of phase space, so most of the features of the reaction can be investigated, provided they are interpreted with caution. A very few events have ambiguous kinematic fits ; in this analysis, such ambiguities are neglected (that is, no ambiguity weight is used).

5.3.1 Effective Mass Plots

The two-body $\pi^+\pi^-$ effective mass distributions are shown in figure 5.3 (no acceptance correction has been applied here). The dashed curves represent the background, fitted by the phase space distribution multiplied by a third order polynomial. The solid lines are Breit-Wigner functions for the ρ, f, and g mesons, added incoherently to the background. The Breit-Wigner function used is

$$\text{B.W.} \propto \frac{m}{q} \frac{m\Gamma(m)}{(m_o^2 - m^2)^2 + m_o^2 \Gamma^2(m)}$$

where

$$\Gamma(m) = \Gamma_o \left(\frac{q}{q_o}\right)^{2\ell+1} \frac{m_o}{m} \cdot \frac{D_\ell(m_o)}{D_\ell(m)}$$

and $D_\ell(m) = 1 + (qr)^2$ for the ρ-meson

$D_\ell(m) = 9 + 3(qr)^2 + (qr)^4$ for the f-meson

$D_\ell(m) = 1$ for the g-meson

with $r = 3.5 \text{ GeV}^{-1}$.

Here, m is the effective mass and q is the pion momentum in the rest frame of the dipion, m_o and q_o being the corresponding values at the central resonance mass. $\Gamma(m)$ is the energy-dependent width taking into account centrifugal barrier effects, which depend on the resonance spin ℓ (ref. 5.43). The inclusion of the factors D_ℓ is a refinement which has been successfully used before, the main effect being to attenuate the tails at the high mass
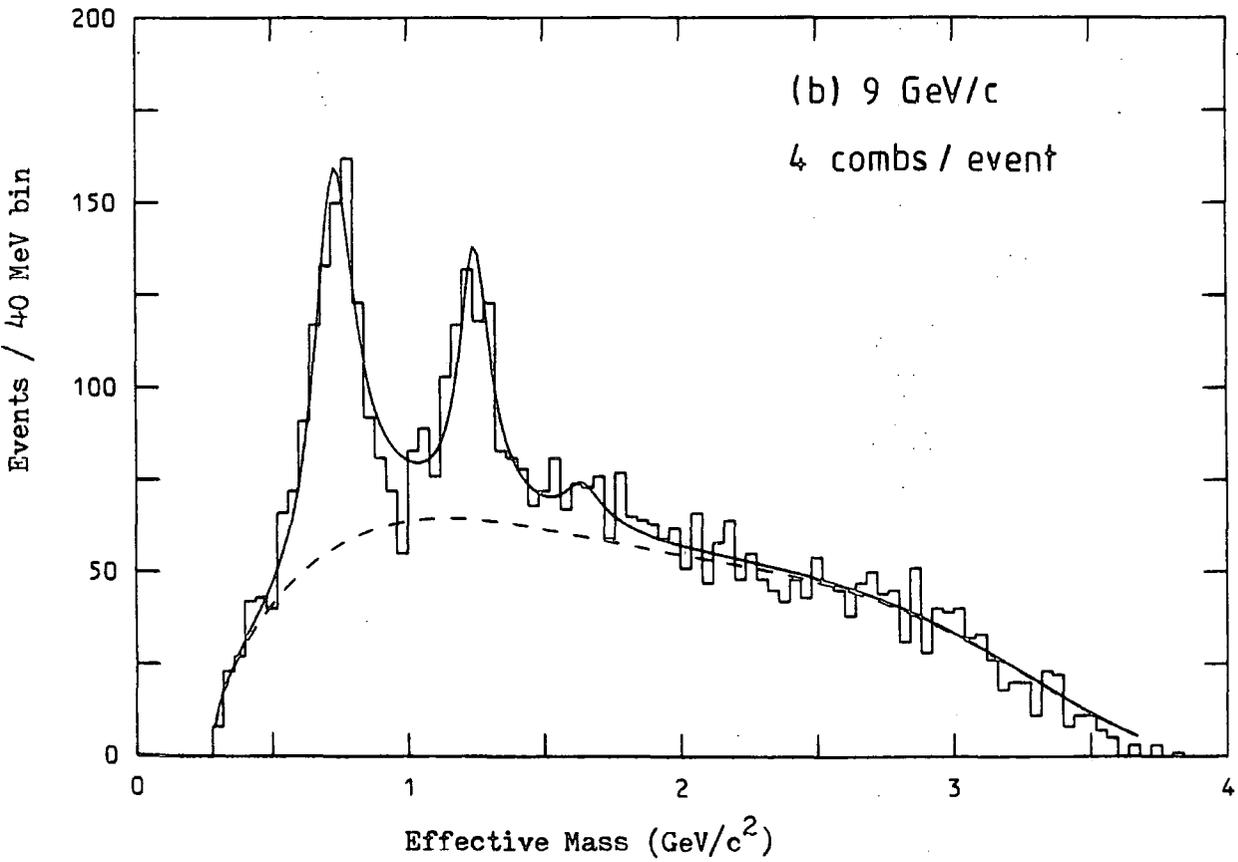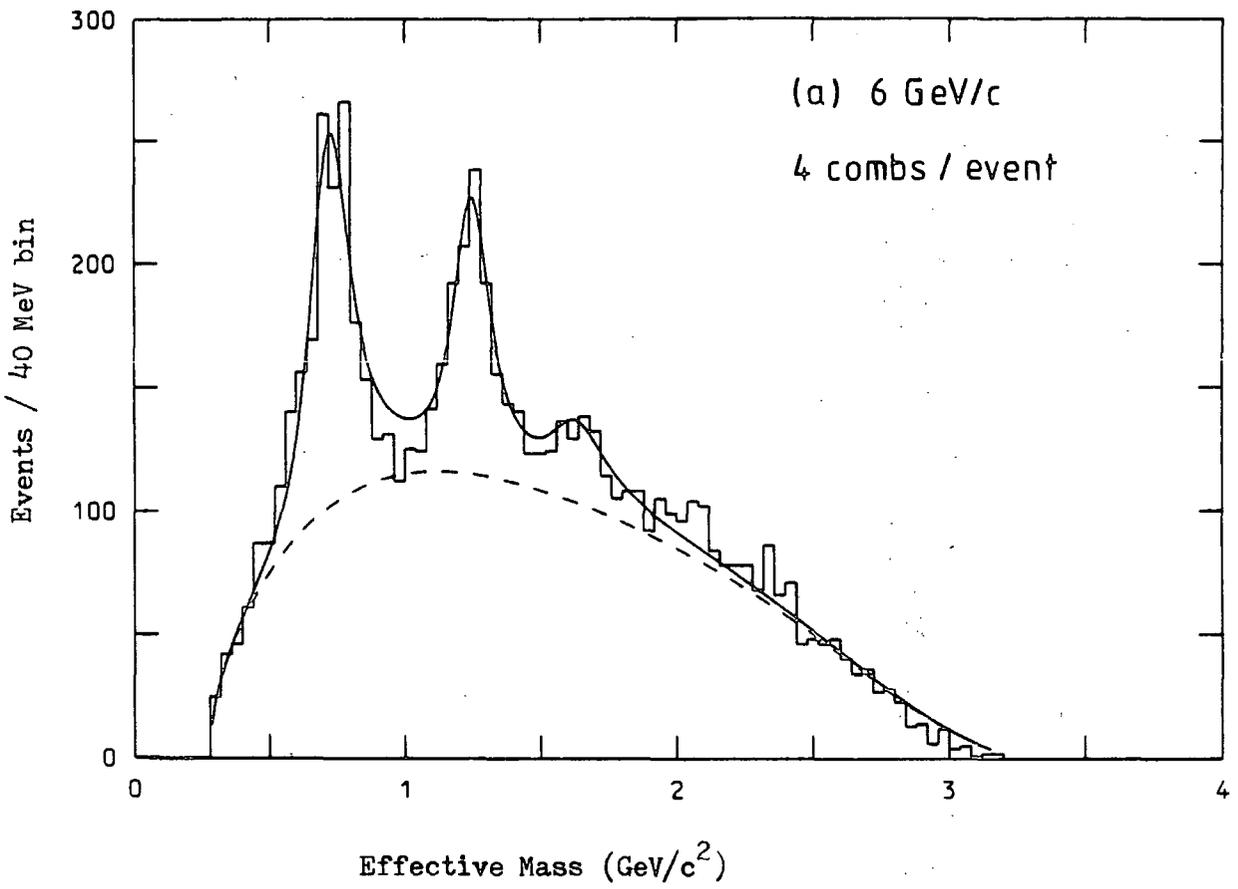
Fig. 5.3 Effective Mass Distributions of $\pi^+ \pi^-$

end of the distribution (though here the factor was not used for the

g-meson).

The fits are quite good except in the region between the ρ and

f where there is clearly a dip (3 standard deviations significance at

6 GeV/c), as noted in other experiments (see last section). Fits were

made by varying the masses, widths, and fractions of each resonance

and minimising the χ^2 of the distribution, giving the results shown in

table 5.2.

Table 5.2

		ρ	f	g
6 GeV/c	Mass (MeV/c^2)	722 ± 14	1248 ± 11	1661 ± 11
	Width (MeV/c^2)	155 ± 37	132 ± 22	280 ± 40
	No./Event	0.51 ± 0.09	0.32 ± 0.14	0.14 ± 0.02
	χ^2/d.f. = 90.6/72			
9 GeV/c	Mass (MeV/c^2)	731 ± 8	1247 ± 6	1653 ± 5
	Width (MeV/c^2)	176 ± 46	133 ± 27	185 ± 15
	No./Event	0.53 ± 0.13	0.28 ± 0.11	0.06 ± 0.02
	χ^2/d.f. = 92.3/85			

The fitted ρ mass is somewhat lower than that found by other experi-

ments (typically 745 MeV/c^2), and it seems unlikely that this is a purely

statistical effect as it is observed at both energies. We have confidence

in the normalisation of Kinematic fits as, for example, the fitted ω mass

in 1C fits is within an MeV of the accepted value, and we are here dealing

with 4C fits. The low mass obtained for the ρ could be a manifestation of

the trigger selection; though not by a direct Kinematic selection, as this

should be taken into account by the background curve, but by a more subtle

dynamical selection e.g. it is possible that the events selected are favourably those with a production mechanism that involves interference of the resonance with the background, as speculated in section 5.2.1. The f and g masses are consistent with other experimental data.

The sum of the number of ρ, f, and g mesons produced per event is very nearly one, which indicates that (assuming associated production to be a small contribution) nearly every event proceeds via intermediate resonance production.

The three-body effective mass distributions are shown in figure 5.4. No significant structure is apparent, showing that there is little or no production of resonances with negative G-parity in this channel at high energies. This confirms the trend noted in section 5.2.1.

5.3.2. <u>Van Hove Analysis</u>

A well known technique for separating events according to their position in longitudinal phase space is that of Van Hove (ref. 5.44). The success of this method depends on the process being essentially peripheral, as described by the multiperipheral Regge model; that is, the ordering of the particles in longitudinal momentum should roughly represent the order in which they appear on the multiperipheral chain. Thus, different sub-processes of the n-body final state occupy different regions in the n-1 dimensional longitudinal phase space, showing which subprocesses are dominant. In practise, the ordering of particles is somewhat mixed up, especially if there are intermediate resonances; nevertheless, the Van Hove analysis has often proved useful.

The simplicity of this procedure depends on the characteristics of the interaction being described in terms of the longitudinal momenta only. The transverse momenta are assumed to be small and largely independent of the reaction dynamics. In the case of the channel $\bar{p}\, p \rightarrow 2\pi^+\, 2\pi^-$ the
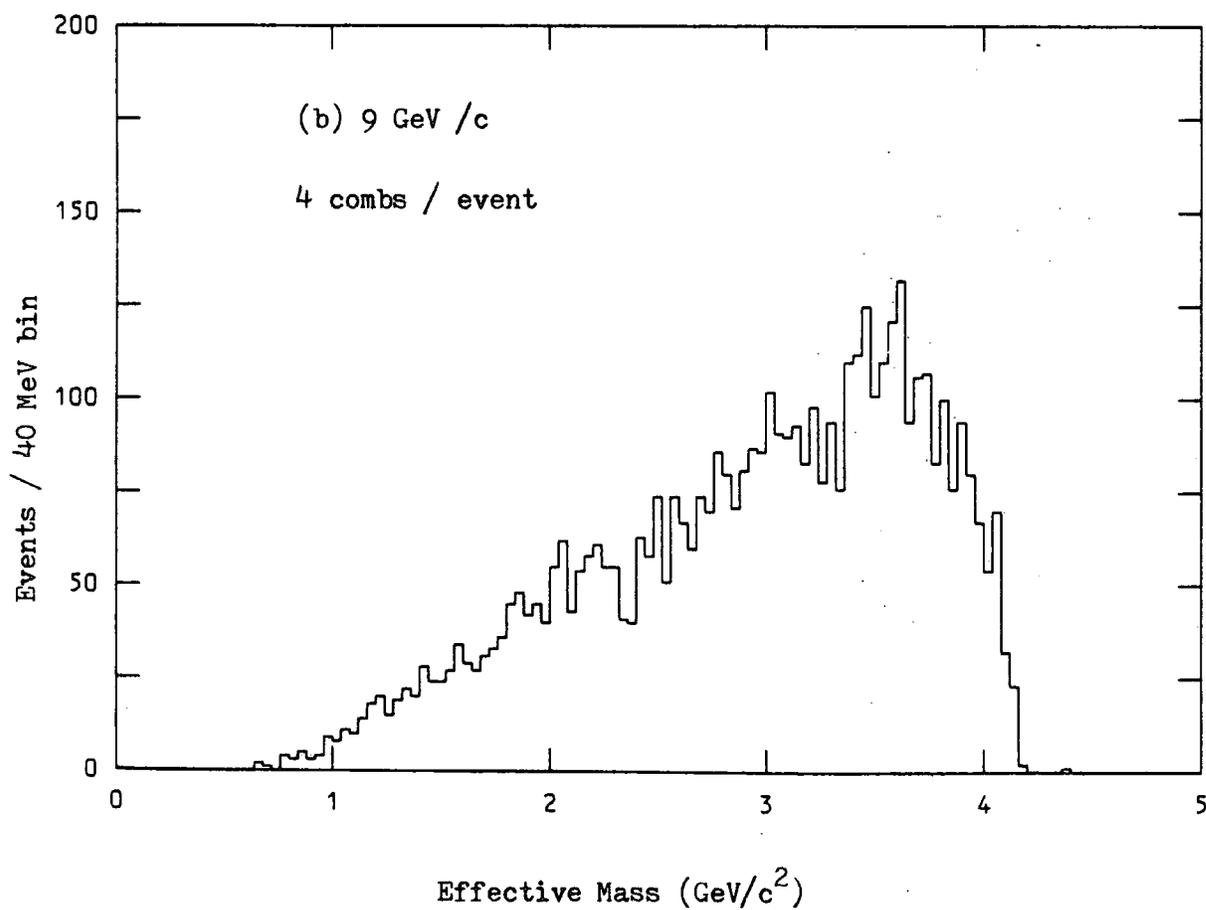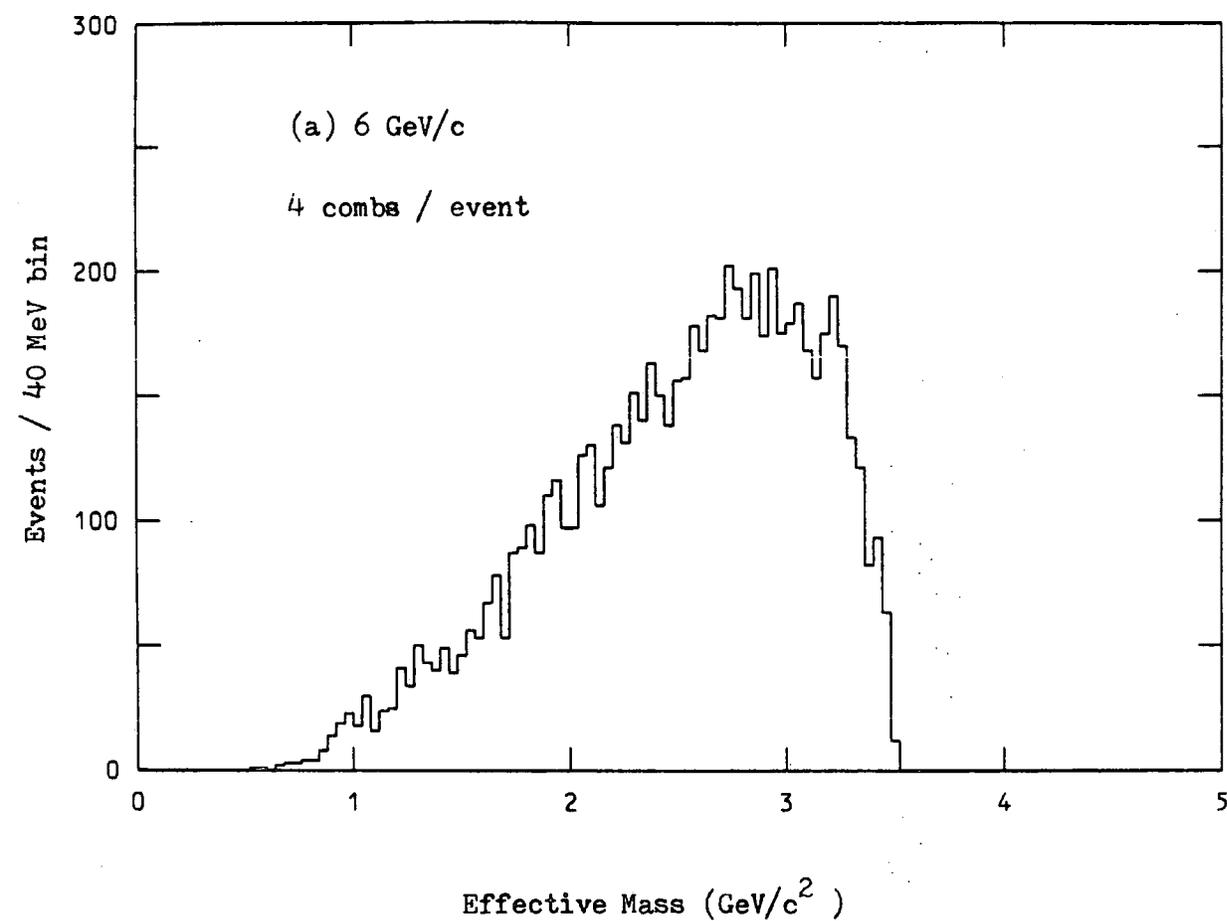
Fig. 5.4 Effective Mass Distributions of $\pi^{\pm}\pi^{+}\pi^{-}$

transverse momenta are somewhat larger than for non-annihilation channels;
however, the process is still sufficiently peripheral for the Van Hove
analysis to be of use. This is illustrated in figure 5.5 which shows the
distributions of R/R_{max} for the four-pion final state. Here, R is the
radius of the event in longitudinal phase space.

$$R = \sqrt{\frac{3}{4} \left(P_L^2 (1) + P_L^2 (2) + P_L^2 (3) + P_L^2 (4) \right)}$$

and R_{max} is the largest kinematically allowed value of R at the same
Van Hove angles (see ref. 5.45). For a purely peripheral event in which
all transverse momenta are zero, R/R_{max} is one. Also shown in fig. 5.5
are curves showing the distributions for acceptance corrected phase space
(obtained by generating a large number of four-pion Monte Carlo events),
and for a typical non-annihilation channel ($\bar{p}p \rightarrow \bar{p}p \pi^+ \pi^-$). The distri-
bution for real four-pion events is clearly much more peripheral than
phase space, though not quite as peripheral, and notably broader than,
the non-annihilation events.

In the Van Hove analysis, longitudinal phase space is divided into
sectors, each corresponding to a particular ordering of longitudinal
momenta. In the four-pion final state, there are 24 sectors; however two
pairs of particles are indistinguishable, so there are only 6 distinguish-
able sectors:-

(1)   (2)   (3)
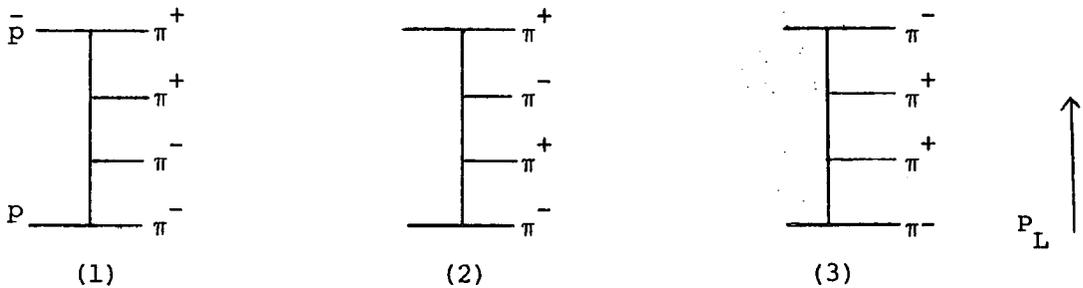
Fig. 5.5 R/R$_{max}$ Distributions for $\bar{p}p \rightarrow 4\pi$ (histograms);
Also shown are curves representing Phase Space and the channel $\bar{p}p \rightarrow \bar{p}p\pi^+\pi^-$
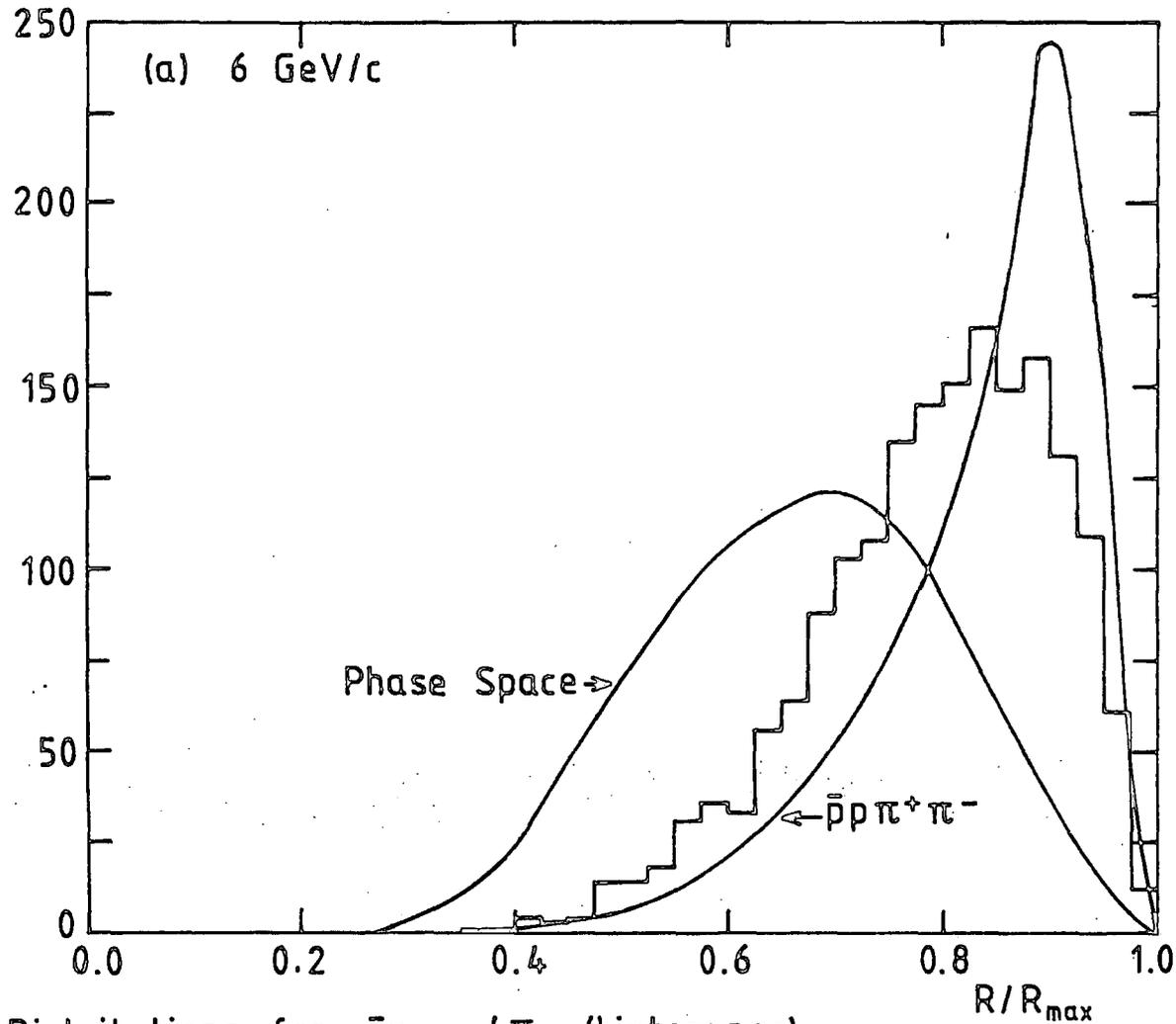
(b) 9 GeV/c

$\bar{p} p \pi^+ \pi^-$

Phase Space $\longrightarrow$

R/R_{max}

Fig. 5.5(cont.)

(4) π^+, π^-, π^-, π^+ (5) π^-, π^+, π^-, π^+ (6) π^-, π^-, π^+, π^+
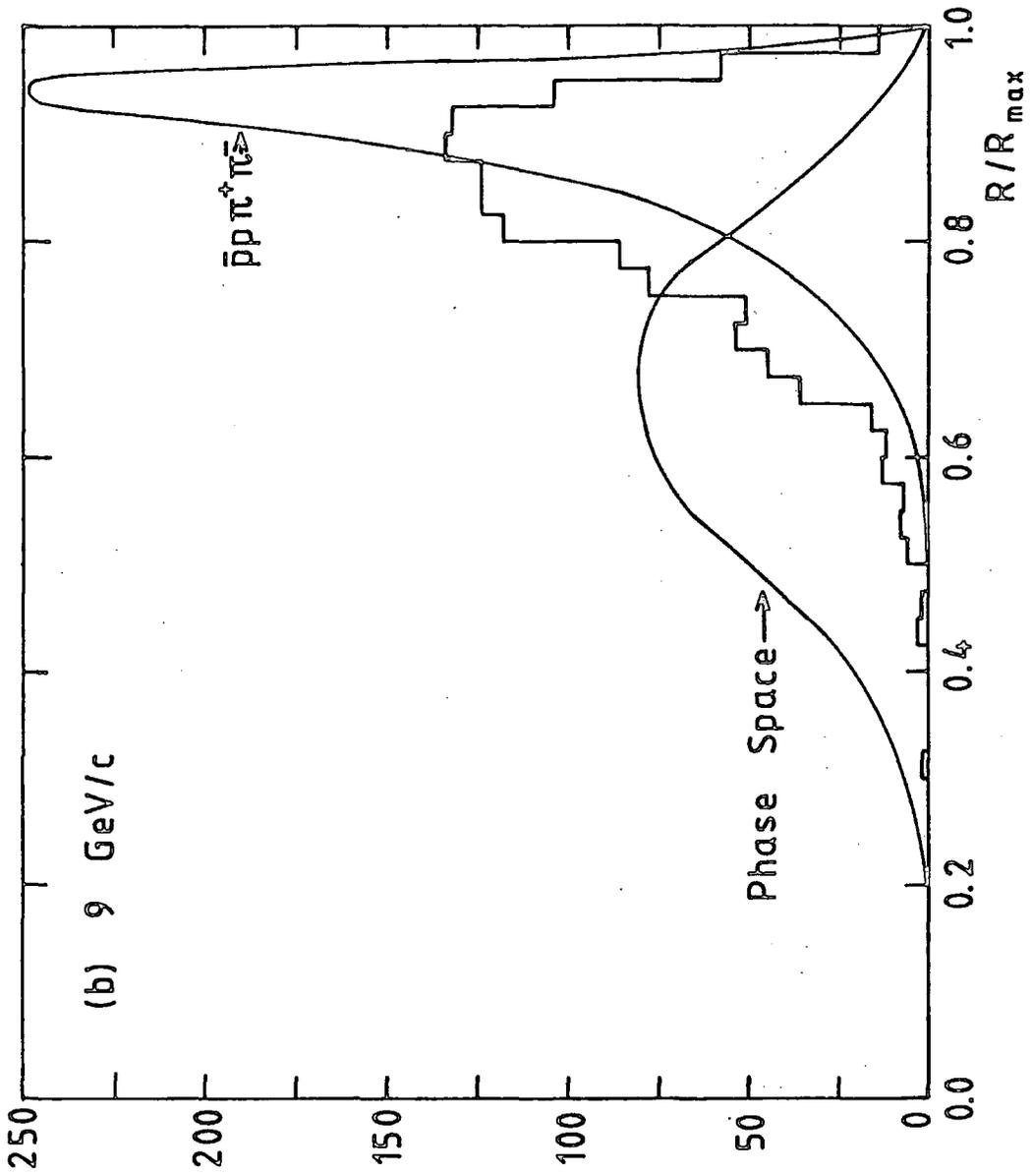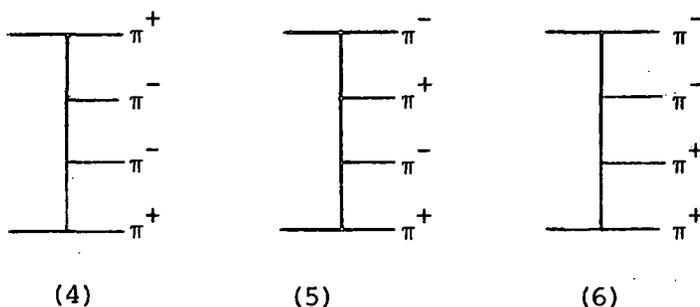
These are drawn as multiperipheral exchange diagrams, but they are strictly

schematic representations of the ordering in longitudinal momenta.

Each event has been allocated to its appropriate sector and the $\pi^+ \pi^-$

effective mass plots repeated for each sector separately (fig. 5.6). Pions

of the same charge are distinguished by subscripts f for the one of greater

longitudinal momentum ("fast") and s for the one of smaller longitudinal

momentum ("slow"). Plots for the 6 GeV/c data only are shown here. For

this data, table 5.3 gives the number of events in each sector and the

corresponding number of accepted phase space events (normalised to the same

total number).

Table 5.3. Population of Events in the Van Hove Sectors - 6 GeV/c

Sector	1	2	3	4	5	6	Total
Real Events	101	170	319	254	389	562	1795
acc. phase space	328	323	279	315	276	274	1795

The following observations are made:

(a) Some sectors are much more heavily populated than others. In

particular, sectors with negative pions of high P_L and positive

pions of low P_L are more populated, thus illustrating the lead-

ing particle effect. Sectors (3) and (4) should be equally

populated, by charge conjugation.

Fig. 5.6 Effective Mass Plots in each of
the Van Hove sectors, as defined in the
text. The inset diagrams show the ordering
of pions in each sector, the circled pair
being the ones included in the mass combination.

Fig. 5.6   Effective Mass (GeV/c²)

Sector 4

Sector 5

Sector 6

$\pi_f^+ \pi_f^-$

$\pi_f^+ \pi_s^-$

$\pi_s^+ \pi_f^-$

$\pi_s^+ \pi_s^-$

Fig. 5.6 (cont.)

Effective Mass (GeV/c²)

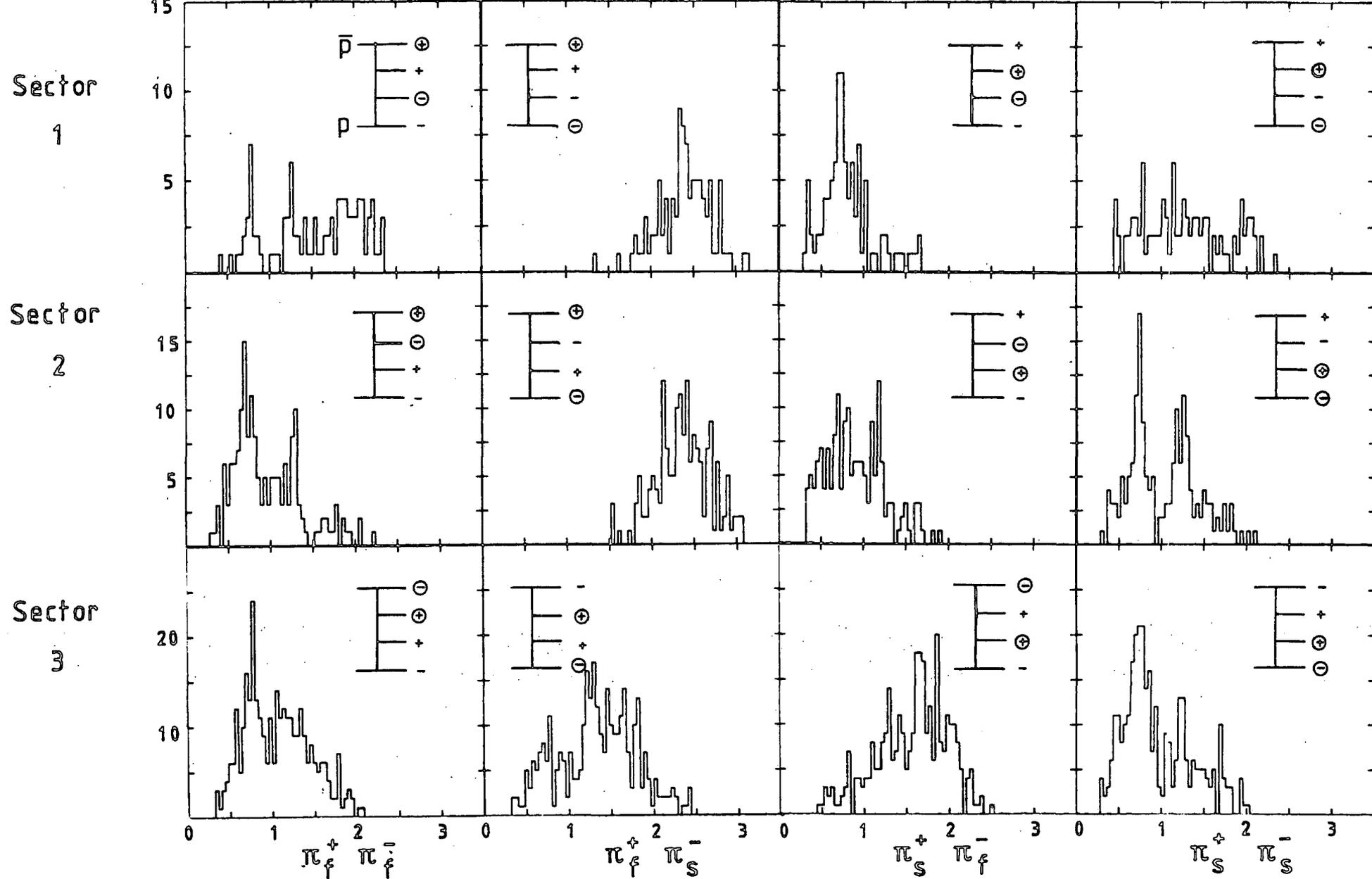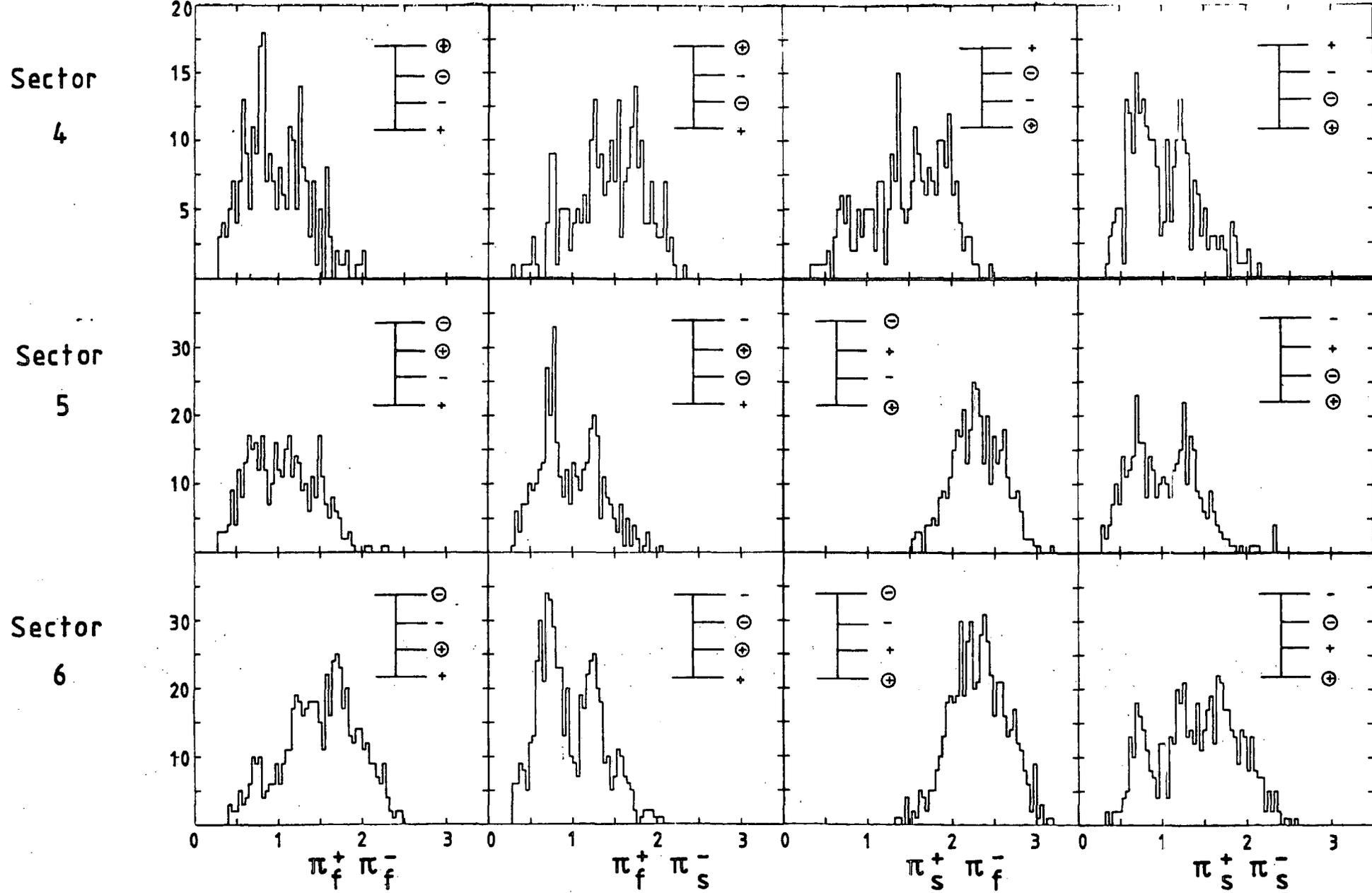(b) Acceptance does not play an important part in determining the populations of sectors.

(c) Strong ρ and f signals are present in $\pi_f^+ \pi_s^{--}$ in sectors (5) and (6), indicating central resonance production.

(d) Central ρ (but not f) is present in $\pi_s^+ \pi_f^-$ in sector (1), which is likely to proceed via Δ^{++} exchange. Since this is the least populated sector, it is deduced that Δ^{++} exchange is small.

(e) Strong ρ and f signals are also clear in $\pi_s^+ \pi_s^-$ in sections (5) and (6) (though on a large background in the latter sector). This is consistent with the leading pion model; that is, a leading π^- plus a three-pion cluster which decays to a resonance and a π^+. Such a model could also account for observation (c).

(f) Very strong ρ and f peaks are seen in both $\pi_f^+ \pi_f^-$ and $\pi_s^+ \pi_s^-$ in sectors (2), (3) and (4). This indicates associated production of resonances, as is also clear from the Goldhaber plot (fig. 5.7), which includes only events in these three sectors.

Similar observations are made at 9 GeV/c. The situation is summarised in figure 5.8 (a) - (d) along with suggested quasi-two and quasi-three body interpretations. At this stage, these are only tentative, as there is sure to be some mixing up in the ordering of pions from resonance decays (see fig. 5.8(e)). Also, it is difficult to distinguish between the leading pion and the central resonance models in this analysis. Finally, the selections imposed by the trigger should be taken into account (e.g. whether it is necessary to include a leading π^+ model). These considerations are dealt with in the remainder of this chapter, where a model is tested by a maximum likelihood technique.
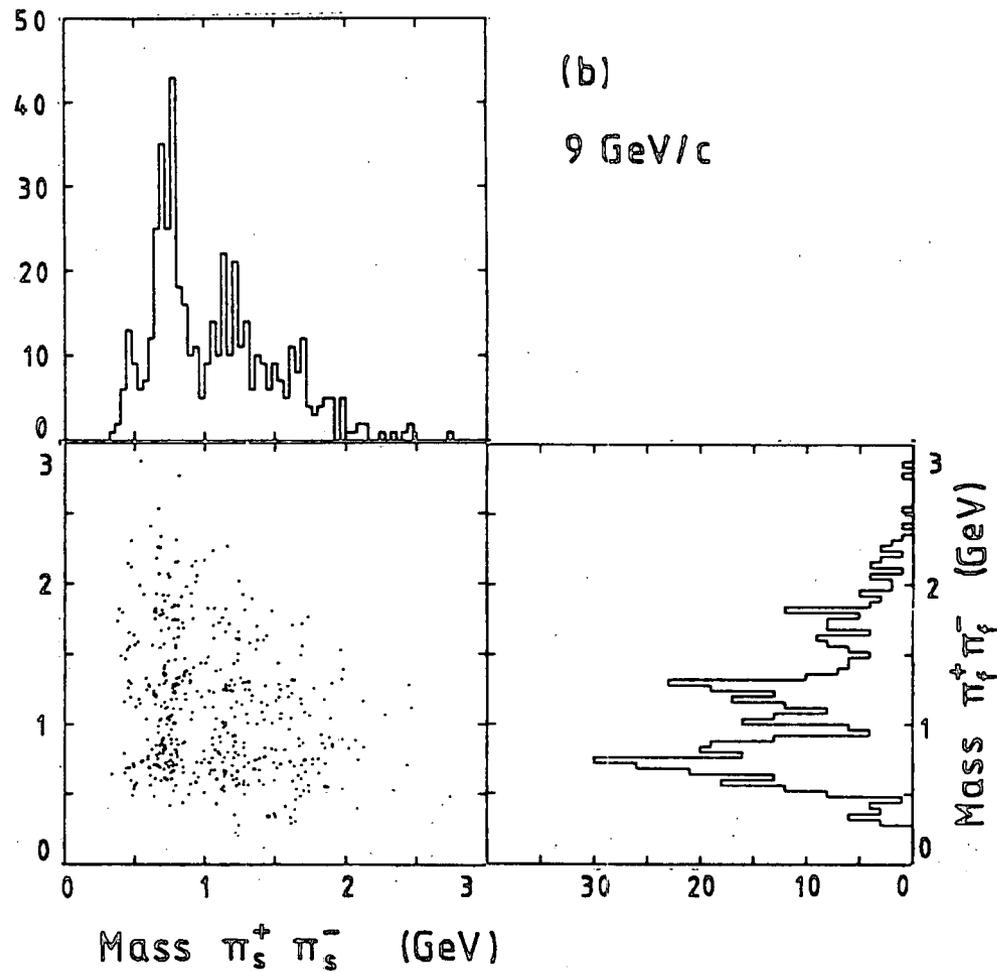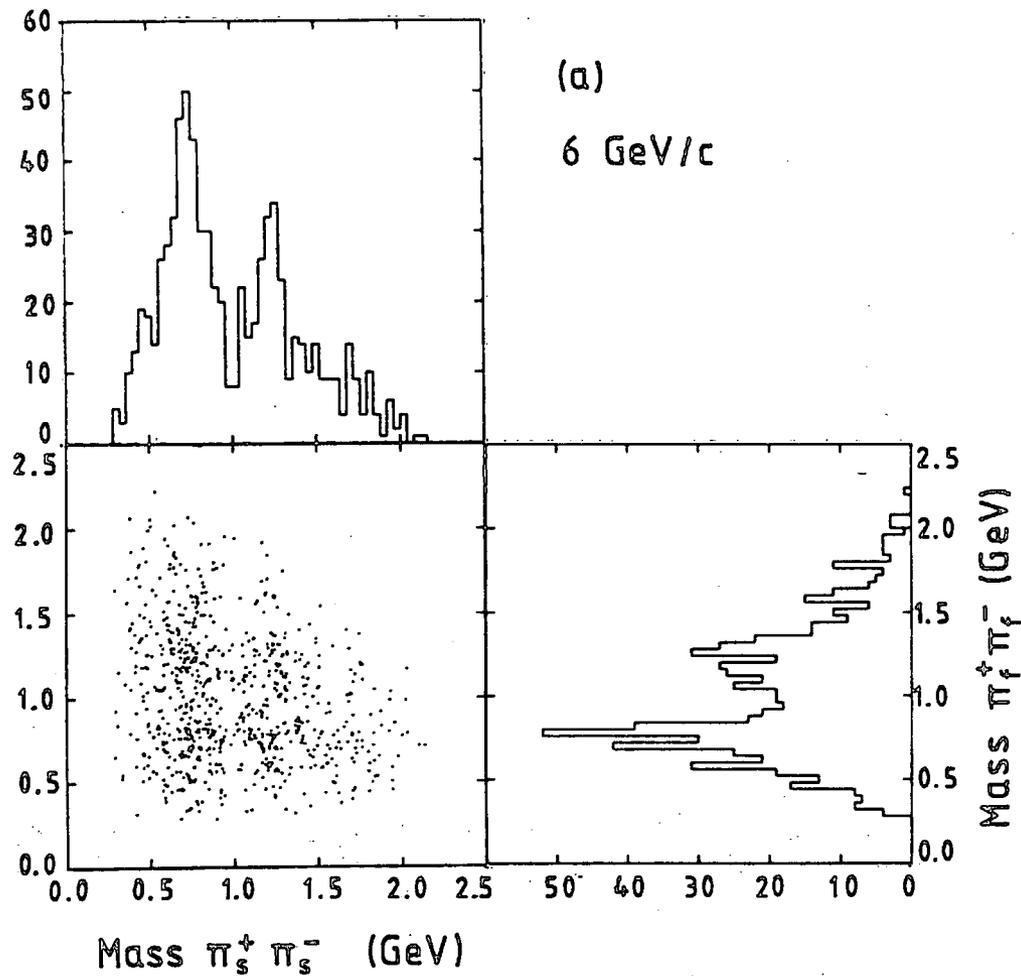
Fig. 5.7   Goldhaber plots for $\bar{p}p \rightarrow 4\pi$ in   selected   Van   Hove   sectors.

5.4 A SIMPLE PHENOMENOLOGICAL MODEL AND ITS FITTING TO THE DATA

In the overview of section 5.2, the multi-Regge model emerged as the most successful model to describe high energy data, provided it was extended to allow for resonance formation. This, together with the successful application of the Van Hove analysis, naturally leads one to postulate exchange diagrams of the type shown in fig. 5.8. Here, a quantitative model is proposed; however, the dynamics are represented by simple phenomenological terms, rather than formally Reggeised expressions.

5.4.1 Description of the Model

The following assumptions are made:-

(a) The channel proceeds predominantly by intermediate resonance production.

(b) Double charge exchange (Δ^{++}) is neglected, as the previous evidence show the contribution to be small (albeit non-zero).

(c) No correlations between vertices.

(d) The peripherality is represented by factors exp (bt) in the amplitudes, where t is the four-momentum transfer squared from the beam or target to the outgoing particle at that vertex.

(e) The resonance decay angular distributions are expressed in terms of density matrix elements, assuming all off-diagonal elements to be zero (this is supported by the evidence of table 5.1).

(f) The resonance masses are distributed according to a Breit-Wigner form, using central masses and widths obtained by an independent fit (see section 5.3.1.). g-meson production is neglected.

(g) Amplitudes are added incoherently. This has been found satis-factory in previous experiments at lower energies (see section 5.2.4).

(a) Central resonance with Δ^{++} exchange.

(b) Central resonance   (neutral exchange).

(c) Leading π^-.   (d) Associated production.

(e) Example of ordering mix-up.

(1) to (6) are Van Hove sectors, as defined in the text.
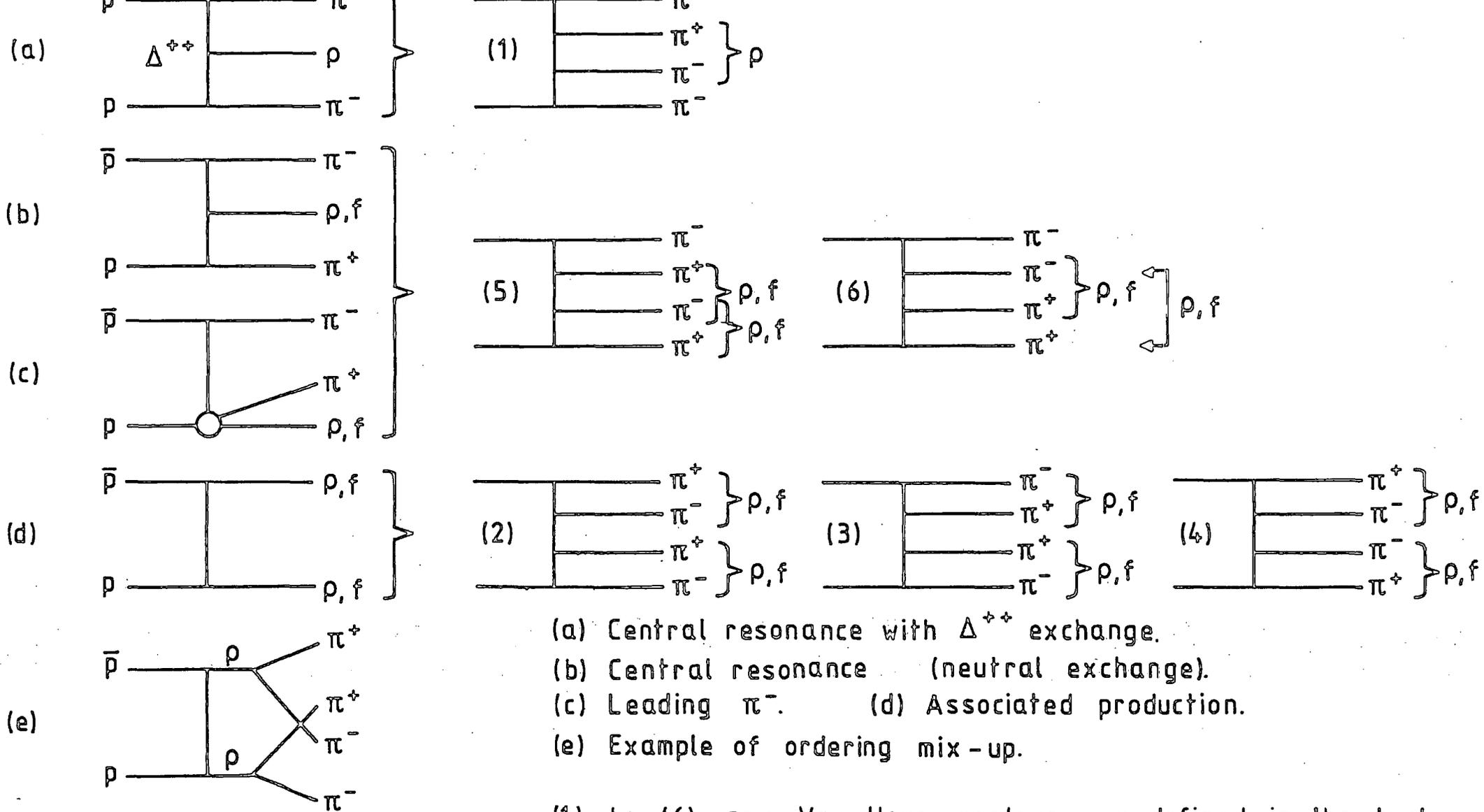
Fig. 5.8   Interpretation of Resonance Production in Each Van Hove Sector.

The four contributions to the model are:

1. <u>Uncorrelated 4π (U)</u>. This is where the four pions are simply distributed according to phase space (fig. 5.9(a)). This is not likely as an actual physical process, but if assumption (a) is true, the precise form of the distribution should be unimportant.

2. <u>Associated Production (AP)</u> This describes the processes

$$\bar{p}p \rightarrow \rho^0 \rho^0$$
$$\rightarrow \rho^0 f$$
$$\rightarrow ff$$
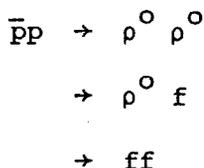
as shown in fig. 5.9 (b) - (e). A single Regge exchange is assumed, leading to peripherality at both vertices.

3. <u>Leading Pion (LP)</u> In this model there is a Regge exchange at one vertex and an off-mass-shell "core" annihilation at the other, always giving one resonance (fig. 5.9 (f) to (i)). The reactions described are

$$\bar{p}p \rightarrow \rho^0 \pi^+ \pi^-$$
$$\rightarrow f \pi^+ \pi^-$$
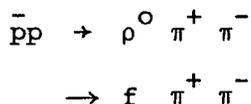
4. <u>Double Peripheral (DP)</u> This is an alternative to the L.P. model and describes the same reactions. There is a double-Regge exchange, giving peripherality at the top and bottom vertices (fig. 5.9 (j) to (o)). The Van Hove analysis suggests that the diagram with central resonance production dominates, but the other two must be included since they are related by isospin (as explained in the next section).

The squares of the amplitudes are then written down for each of these diagrams and added linearly. For example, diagram (b) contains such terms as

$$BW (\rho_1) \ BW (\rho_4) \ e^{bt_1} \ W(\rho_1) \ W(\rho_4)$$
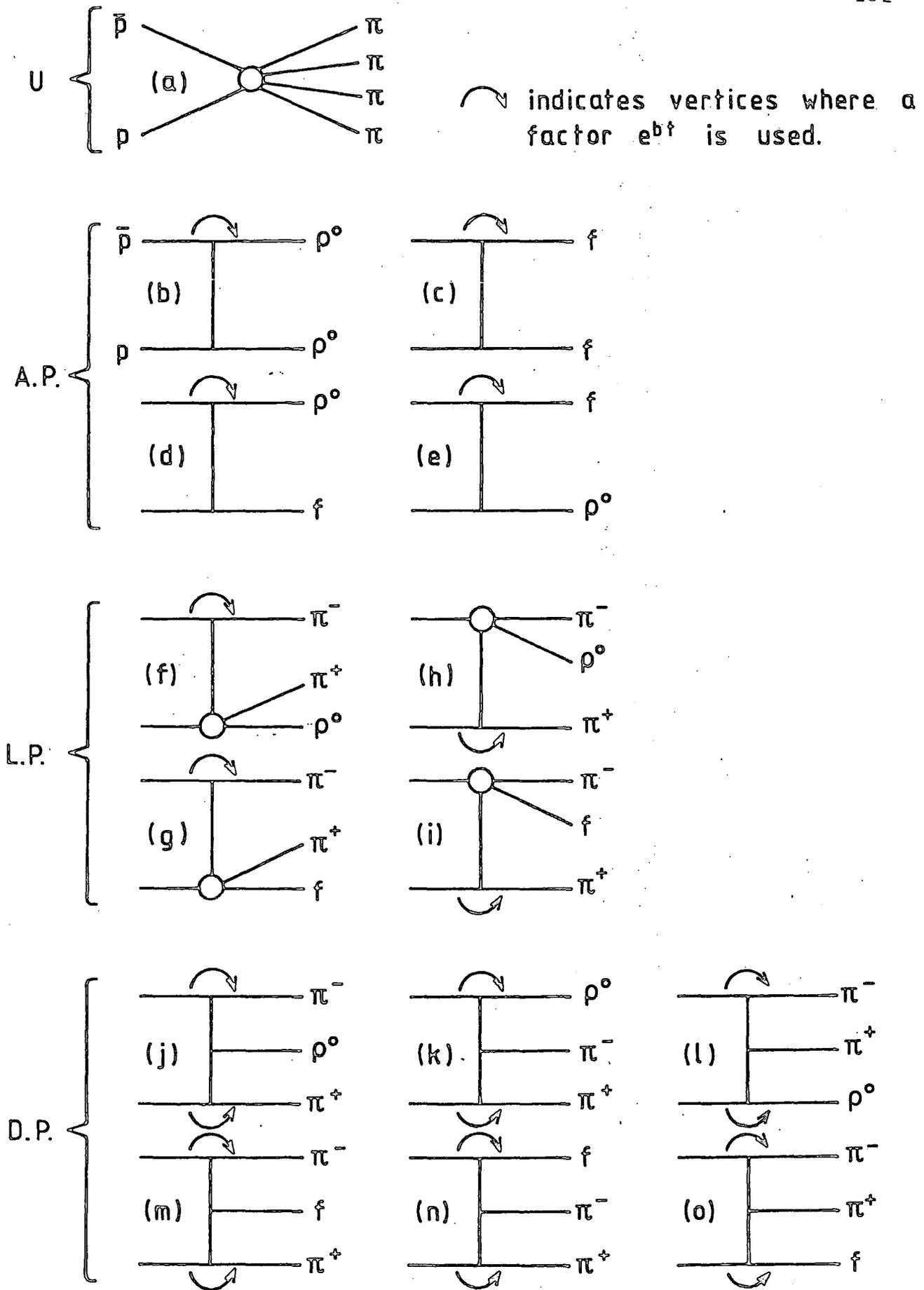
Fig. 5.9   Diagrams Contributing To The Model For

$\bar{p}p \rightarrow 4\pi$

where BW(ρ) is the Breit-Wigner factor for one of the dipion ($\pi^+ \pi^-$) com-
binations at the central mass of the ρ, and W (ρ) is its decay angular
distribution. The full expressions are detailed in Appendix C. They
are symmetrised so that interchanging any two identical particles does
not change the value of the amplitude. The contributions are combined
with their corresponding fractions, to make an overall amplitude for each
of the two cases:-

$$\text{Model I} : \quad U + A P + L P$$
$$\text{Model II} : \quad U + A P + D P$$

5.4.2 Maximum Likelihood Fit

Fitting data to a theoretical amplitude by the method of Maximum
Likelihood is a well tried technique. However, the restriction imposed by
experimental acceptance means that the phase space integrals can not be
calculated analytically. Furthermore, if amplitude-dependent parameters
are to be fitted (such as the slope parameters, b), the phase space integrals
must be evaluated at each iteration. A method for dealing with this using
Monte-Carlo generated events is described in Appendix C. The demands on
computing time are such that further simplifying assumptions must be made:-

(i) Only two slope parameters are fitted in any one fit; one for
associated production, b_{AP}; and one for either leading pion, b_{LP},
or double peripheral, b_{DP}, whichever is being fitted.

(ii) Four density matrices are fitted: one for the ρ and one for the
f, for each of the cases AP and LP/DP. Since all off-diagonal
elements are assumed to be zero, trace, parity, and Hermiticity
conditions reduce the number of free parameters to one for the ρ
density matrix, and two for the f.

(iii)   The fractions of processes related by charge conjugation are

constrained by equation C.9, so that two charge conjugate

events are given the same amplitude in their appropriate parts

of phase space. This ensures that the fractions in the whole

of phase space are equal. The processes thus related are:

(d) and (e); (f) and (h); (g) and (i); (k) and (l); (n) and (o).

(iv)   The three DP processes (j), (k) and (l) are also assumed to be

related by equation C.9, and similarly for (m), (n) and (o).

This is based on factorising the $\rho\,\pi\,\pi$ amplitude into the

three vertex coupling factors for each diagram:

$$T \;=\; T_1\,T_2\,T_3$$

with

$$T_1 = A_{NN\rho}^{-} \quad C.G._1$$

$$T_2 = A_{NN\pi}^{-} \quad C.G._2$$

$$T_3 = A_{NN\pi}^{-} \quad C.G._3$$

where N is the exchanged nucleon, A the charge independent

part of the coupling amplitude, and CG. the appropriate isospin

Clebsch-Gordon coefficient for the particular charge states of

each diagram. The product of the three factors turns out to be

the same for each of the three related processes. However,

unlike the charge conjugate processes, the fractions for centrally

produced resonance in the whole of phase space are not the same

as for the diagrams with a resonance at the top or bottom vertices,

but are considerably larger. This is because the amplitude

weights phase space in a different way (if the resonance had

zero width, the boundaries of phase space would be different for

the three diagrams).

(v) To simplify the Breit Wigner formula, the $D_\ell(m)$ factors mentioned in section 5.3 were dropped. This did not affect the quality of fit noticeably, nor the values of any of the fitted parameters except the fraction of uncorrelated 4π which was noticeably smaller without the $D_\ell(m)$ factors. This is simply because less background is needed to fit the high mass region of the effective mass plots. Since there was no serious attempt to model the non-resonant contribution, this was considered a reasonable simplification.

The maximum likelihood fit was performed using the minimisation program MINUI (ref. 5.46). Events were selected in a well defined region of phase space:-

6 GeV/c   p > 2.6 GeV/c,   θ < 0.22 rads   1721 events

9 GeV/c   p > 4.1 GeV/c,   θ < 0.20 rads   1190 events

p and θ being the laboratory momentum and angle of the fastest pion. The fractions of processes were normalised by a comparable number of phase space "events" with the same selections. These were generated by the Monte Carlo program FOWL (ref. 5.47), which also enable an extrapolation of the model to the whole of phase space (see appendix C).

To test the goodness of fit, histograms of certain quantitites were made and compared with the predictions of the models by generating a large number of Monte-Carlo events, weighted by amplitude weight and acceptance weight, and drawing smooth curves through the resulting plots (normalised to the number of real events). An overall χ^2 per degree of freedom was then evaluated for each of the two models. The variables histogrammed are (four combinations each):

> two-body effective masses
>
> t from beam (target) to π^- (π^+)
>
> t from beam to dipions ($\pi^+ \pi^-$)
>
> polar decay angles
>
> azimuthal decay angles

These are defined precisely in appendix C as they are used in the amplitude expressions. A selection of the histograms is shown in figs. 5.10 to 5.12 (6 GeV/c only).

5.4.3 Results and Discussion

Table 5.4 (a) and (b) gives the results of the fit outlined above for models I and II at 6 and 9 GeV/c. The errors on parameters were determined by varying each parameter in turn such that the log likelihood decreased by 0.5. As many of the parameters are strongly correlated, these uncertainties are only a rough guide.

The symbols d_{mn} are density matrix elements (normally called ρ_{mn} but here this would be confusing because of the ρ-meson). The agreement between the 6 GeV/c and 9 GeV/c results is very good, indicating that the figures are well reproducible. The density matrix for the ρ-meson is assumed to be the same for $\rho\rho$ and ρf, but the numbers obtained will be more applicable to $\rho\rho$ since this constitutes the greater fraction. The value of d_{oo} in this case is about 0.6, while the only previous number (see table 5.1) is 0.28 for $\rho^o f$ at a much lower energy. This suggests that the assumption may not be a good one, so it is fortunate that the fraction of $\rho^o f$ is very small. Since the fraction of ff is also very small, hot much credence can be given to the values of d_{11} and d_{22} in this case.

The density matrices obtained for $\rho\pi\pi$ and $f\pi\pi$ are far more reliable, as these two processes make up 60 to 80% of the channel. The results from both models agree, giving d_{oo} = 0.24 for $\rho\pi\pi$, in concordance with the
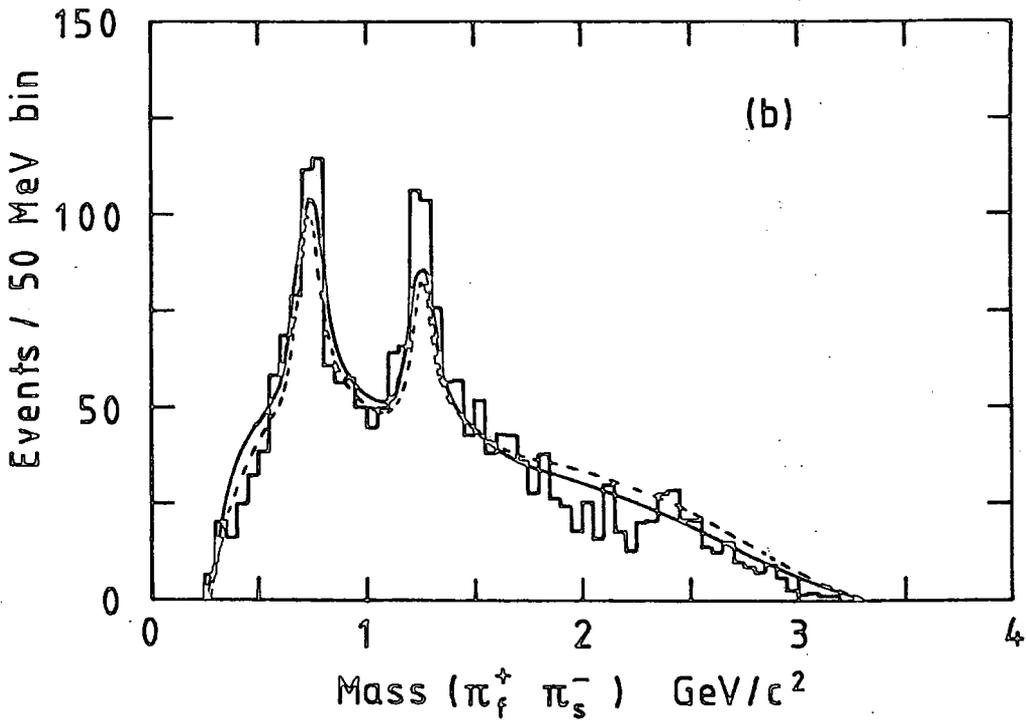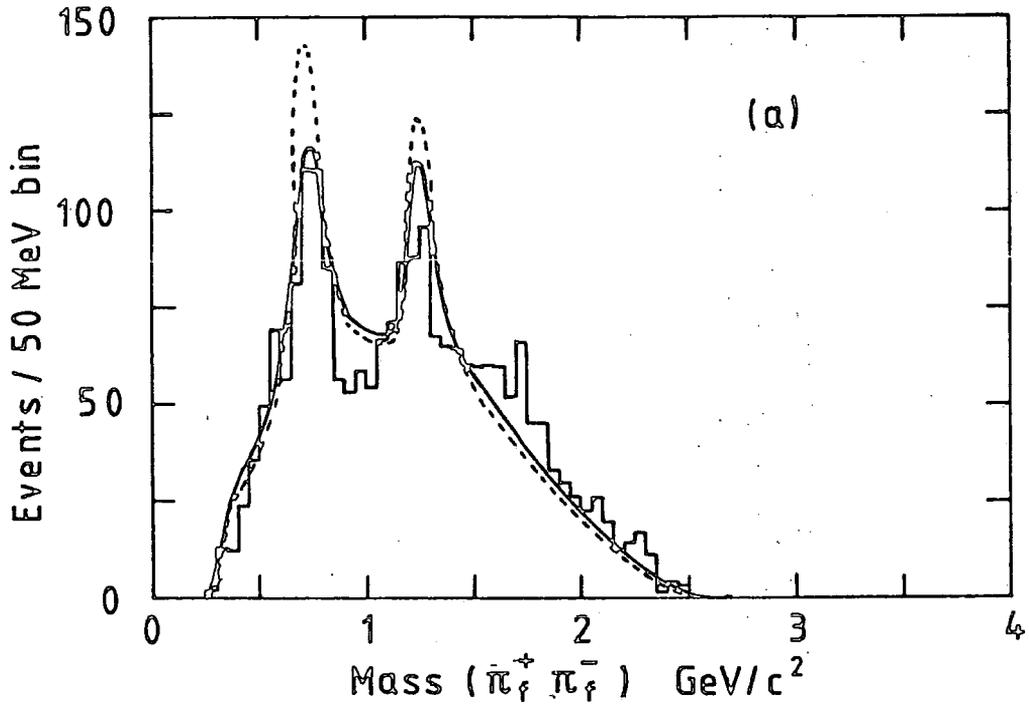
Fig. 5.10 Comparison of Models With Data (6 GeV / c): Mass plots.

```
--------    Model I    U + AP + LP
            Model II   U + AP + DP
```
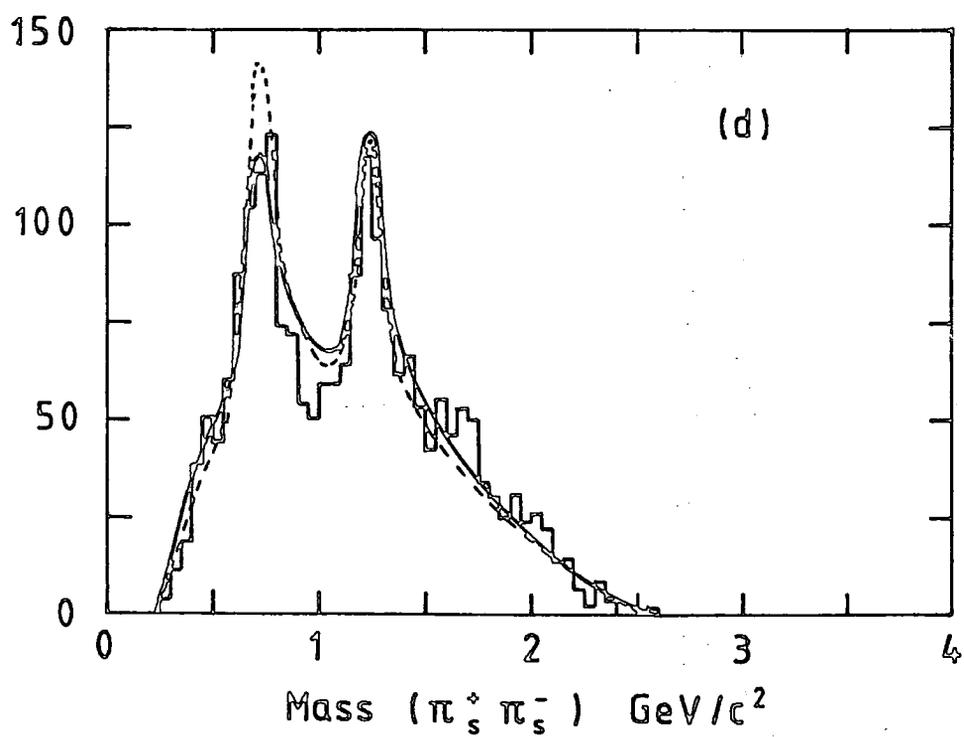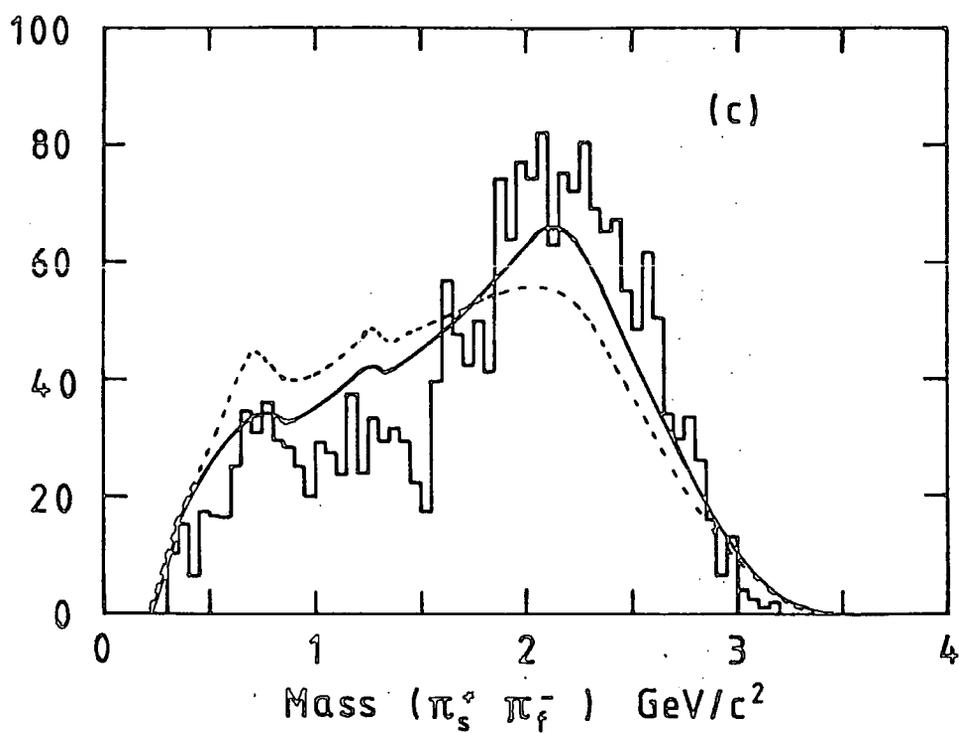
Fig. 5.10 (cont.)
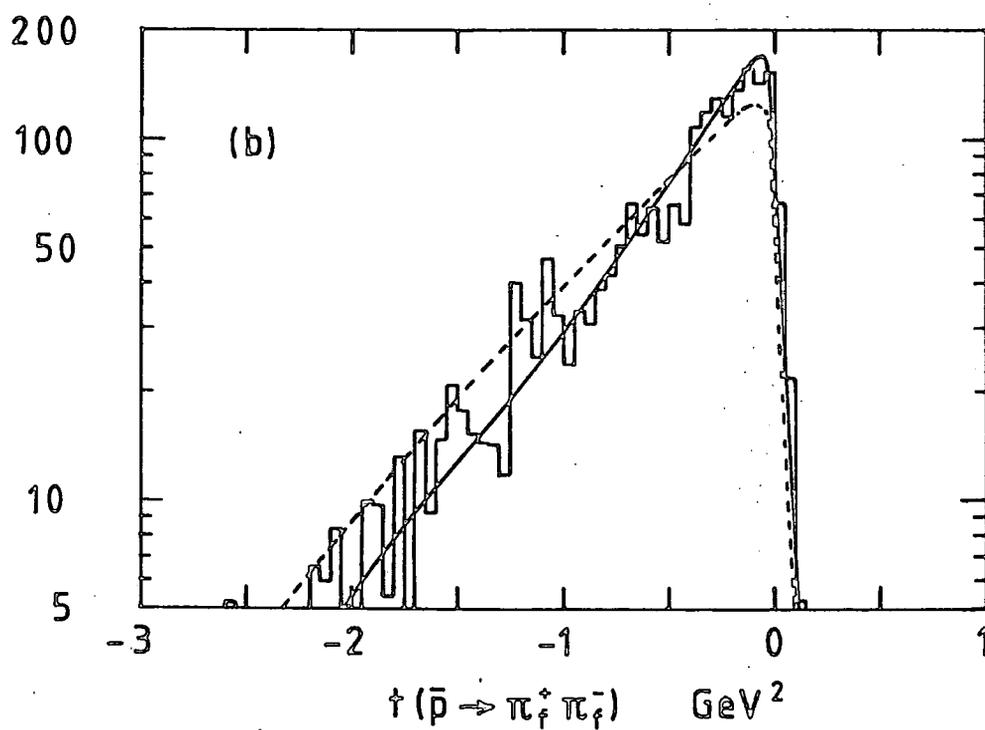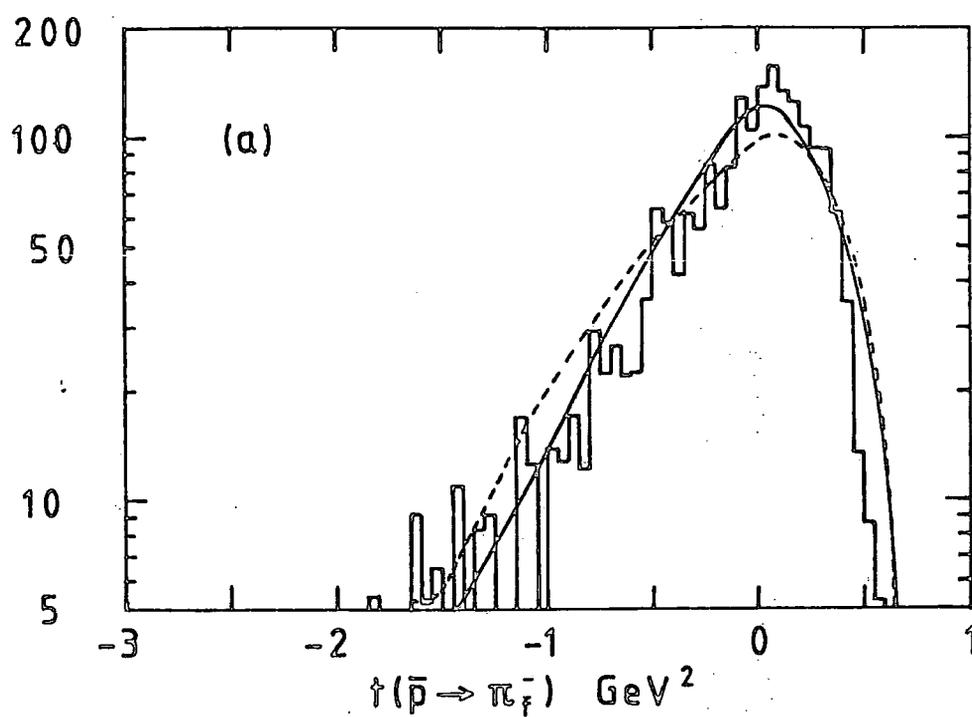
Fig. 5.11   Comparison of Models With Data (6 GeV/c):
             t - distributions
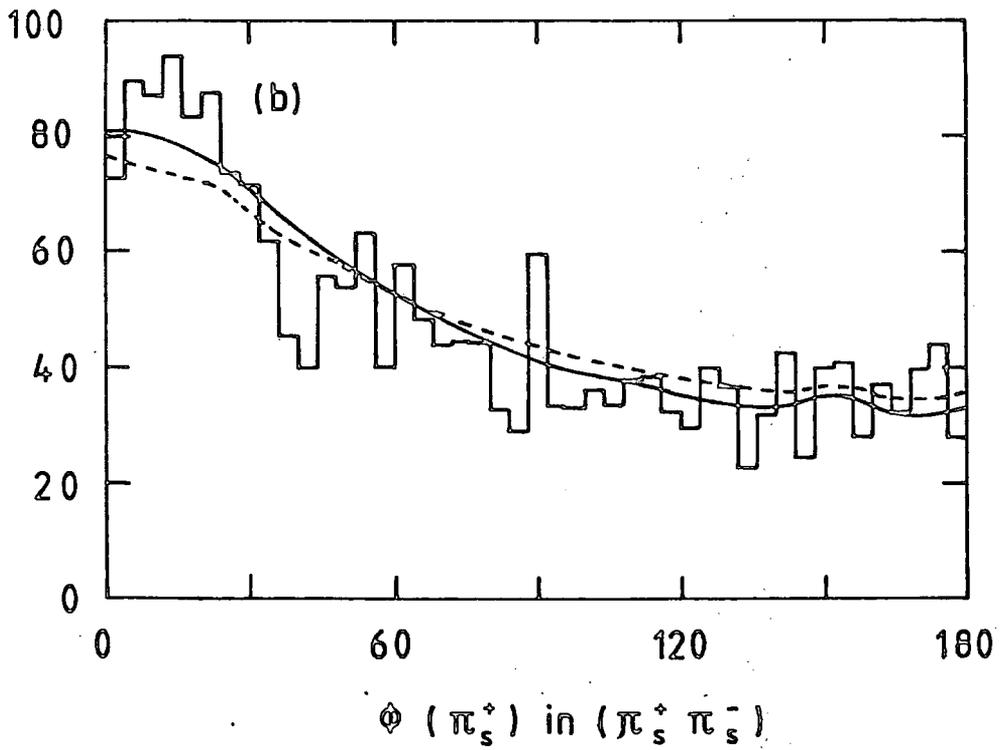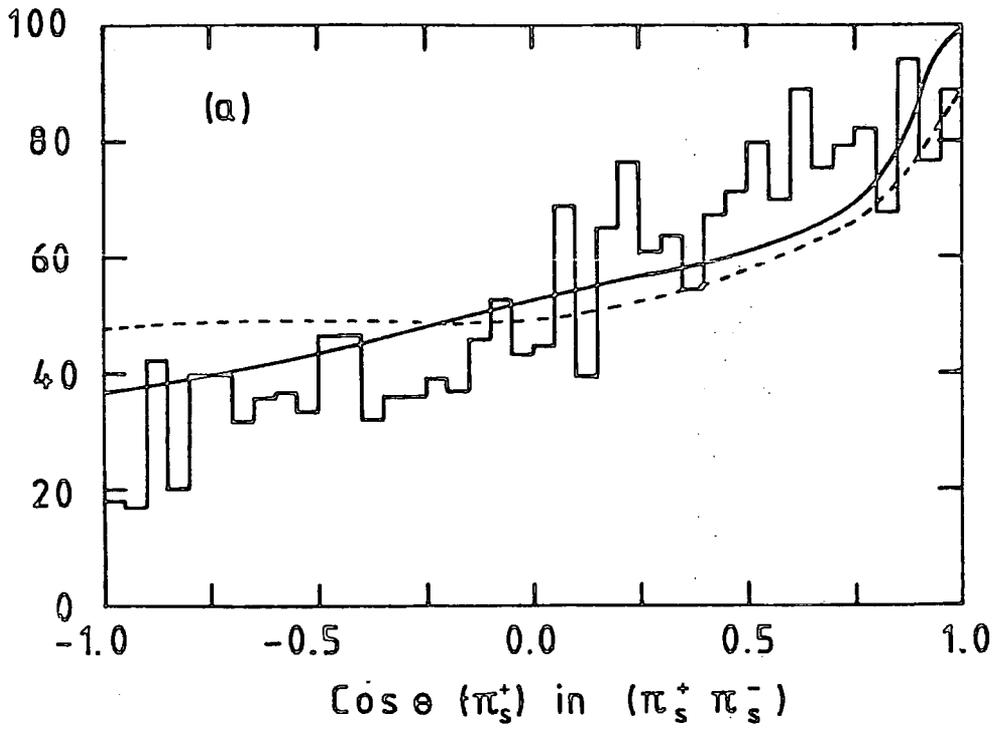
Fig. 5.12   Comparison of   Models With Data (6 GeV/c):
Angular   distributions

		6 GeV/c	9 GeV/c
U	fraction of (a)	0.088 ± 0.030	0.075 ± 0.030
AP	fraction of (b)	0.157 ± 0.017	0.237 ± 0.020
	fraction of (c)	0.039 ± 0.015	0.029 ± 0.015
	fraction of (d)	0.045 ± 0.015	0.032 ± 0.015
	fraction of (e)	0.040 ± 0.015	0.032 ± 0.015
	b_{AP}	3.0	3.0
	d_{11} (ρ-meson)	0.21 ± 0.05	0.22 ± 0.04
	d_{11} (f-meson)	0.41 ± 0.10	0.40 ± 0.10
	d_{22} (f-meson)	0.08 ± 0.10	0.02 ± 0.10
LP	fraction of (f)	0.194 ± 0.015	0.144 ± 0.015
	fraction of (g)	0.127 ± 0.015	0.140 ± 0.015
	fraction of (h)	0.185 ± 0.015	0.155 ± 0.015
	fraction of (i)	0.125 ± 0.015	0.157 ± 0.015
	b_{LP}	3.0	3.0
	d_{11} (ρ-meson)	0.38 ± 0.04	0.38 ± 0.04
	d_{11} (f-meson)	0.14 ± 0.06	0.21 ± 0.06
	d_{22} (f-meson)	0.21 ± 0.06	0.19 ± 0.06
	χ^2/df	2.436	2.675

Table 5.4 (a) Results of the fit to Model I

The letters in brackets refer to the diagrams of fig. 5.9

		6 GeV/c	9 GeV/c
U	Fraction of (a)	0.122 ± 0.030	0.099 ± 0.030
AP	fraction of (b)	0.053 ± 0.020	0.109 ± 0.022
	fraction of (c)	0.029 ± 0.015	0.015 ± 0.015
	fraction of (d)	0.018 ± 0.015	0.005 ± 0.010
	fraction of (e)	0.015 ± 0.015	0.005 ± 0.010
	b_{AP}	3.08 ± 0.25	3.63 ± 0.20
	d_{11} (ρ-meson)	0.15 ± 0.08	0.19 ± 0.08
	d_{11} (f-meson)	0.32 ± 0.10	0.43 ± 0.10
	d_{22} (f-meson)	0.18 ± 0.10	0.03 ± 0.10
DP	fraction of (j)	0.245 ± 0.018	0.249 ± 0.018
	fraction of (k)	0.106 ± 0.010	0.085 ± 0.010
	fraction of (l)	0.109 ± 0.010	0.085 ± 0.010
	fraction of (m)	0.170 ± 0.018	0.217 ± 0.020
	fraction of (n)	0.062 ± 0.010	0.067 ± 0.010
	fraction of (o)	0.069 ± 0.010	0.065 ± 0.010
	b_{DP}	2.16 ± 0.15	1.75 ± 0.10
	d_{11} (ρ-meson)	0.37 ± 0.04	0.40 ± 0.04
	d_{11} (f-meson)	0.11 ± 0.05	0.21 ± 0.05
	d_{22} (f-meson)	0.25 ± 0.05	0.22 ± 0.05
	χ^2/df	1.584	1.463

Table 5.4 (b) Results of the fit to Model II

Process		6 GeV/c		9 GeV/c	
		Model I	Model II	Model I	Model II
U.4π	(a)	0.130 $\pm$ 0.045	0.245 $\pm$ 0.045	0.116 $\pm$ 0.045	0.210 $\pm$ 0.045
$\rho\rho$	(b)	0.092 $\pm$ 0.010	0.041 $\pm$ 0.015	0.140 $\pm$ 0.013	0.088 $\pm$ 0.020
ff	(c)	0.024 $\pm$ 0.010	0.025 $\pm$ 0.013	0.016 $\pm$ 0.008	0.011 $\pm$ 0.010
ρf	(d)	0.025 $\pm$ 0.010	0.014 $\pm$ 0.010	0.018 $\pm$ 0.010	0.004 $\pm$ 0.010
	(e)	0.025 $\pm$ 0.010	0.014 $\pm$ 0.010	0.018 $\pm$ 0.010	0.004 $\pm$ 0.010
$\rho\pi\pi$	(f)	0.211 $\pm$ 0.017	–	0.172 $\pm$ 0.017	
f$\pi\pi$	(g)	0.141 $\pm$ 0.017	–	0.174 $\pm$ 0.017	–
$\rho\pi\pi$	(h)	0.211 $\pm$ 0.017	–	0.172 $\pm$ 0.017	–
f$\pi\pi$	(i)	0.141 $\pm$ 0.017	–	0.174 $\pm$ 0.017	–
$\rho\pi\pi$	(j)	–	0.211 $\pm$ 0.015	–	0.233 $\pm$ 0.015
	(k)	–	0.089 $\pm$ 0.008	–	0.073 $\pm$ 0.008
	(l)	–	0.089 $\pm$ 0.008	–	0.073 $\pm$ 0.008
	(m)	–	0.155 $\pm$ 0.015	–	0.195 $\pm$ 0.015
f$\pi\pi$	(n)	–	0.054 $\pm$ 0.008	–	0.055 $\pm$ 0.008
	(o)	–	0.054 $\pm$ 0.008	–	0.055 $\pm$ 0.008
N^W		4433	3260	2679	1956

Table 5.5 Predicted fractions and numbers of events in the whole of phase space

(μb)	6 GeV/c	9 GeV/c
Model I	214 $\pm$ 12	90 $\pm$ 10
Model II	157 $\pm$ 9	65 $\pm$ 7
Other Experiments	137 $\pm$ 29	50 $\pm$ 12

Table 5.6   Predicted Total cross-section for $\bar{p}p \to 2\pi^+ 2\pi^-$

Process	6 GeV/c		9 GeV/c	
	fraction	Cross-Sec.	fraction	Cross-Sec.
$\rho^0\rho^0$	0.041 $\pm$ 0.015	6.4 $\pm$ 2.4	0.088 $\pm$ 0.020	5.7 $\pm$ 1.4
$\rho^0 f$	0.028 $\pm$ 0.014	4.4 $\pm$ 2.2	0.008 $\pm$ 0.014	0.5 $\pm$ 0.9
ff	0.025 $\pm$ 0.013	3.9 $\pm$ 2.0	0.011 $\pm$ 0.010	0.7 $\pm$ 0.7
$\rho^0 \pi^+ \pi^-$	0.399 $\pm$ 0.019	62.6 $\pm$ 4.7	0.379 $\pm$ 0.019	24.6 $\pm$ 2.9
$f \pi^+ \pi^-$	0.263 $\pm$ 0.019	41.3 $\pm$ 3.8	0.305 $\pm$ 0.019	19.8 $\pm$ 2.5

Table 5.7   Fractions and cross-sections (μb) of the intermediate channels in the four pion final state, as predicted by Model II

previous estimates given in table 5.1 (the high value at 5.7 GeV/c has such a large error that it is preferable to assume that the density matrix elements do not depend much on beam momentum). The diagonal elements for $\rho\pi\pi$ and $f\pi\pi$ are consistent with being all equal, within errors, implying an unpolarised resonance. However, the trend from the present fit is for the higher helicity states to be more populated in the ρ, and less popu- lated in the f, as this is seen at both 6 and 9 GeV/c.

The azimuthal angular distributions are very well described by the models (one of these is shown in fig. 5.12 (b)), hence justifying the assumption that the off-diagonal density matrix elements may be neglected (that is, they are near to zero).

The slope parameters b were not fitted in Model I, but were fixed at a constant value 3.0, this being about the value expected for baryon exchange processes. This is because, when they were allowed to vary freely, the fit converged with unrealistic values of b (at 6 GeV/c, b_{AP} = 10.8 and b_{LP} = 2.06), which was considered to be a mathematical peculiarity of the likelihood function for this model. The values obtained by the fit for model II are, in contrast, quite reasonable. They compare well with the value of 2.2 obtained by Warren et al (see section 5.2.4.) for the slopes of the t and u distributions.

Turning now to the histograms of figs. 5.10 to 5.12, it is clear that the data is much better described by Model II than by Model I. This is confirmed by all the other histograms, at 6 and 9 GeV/c, as is indicated by the χ^2/d.f. given in table 5.4. It should be added that the curves obtained by using fitted values of b in Model I are somewhat closer to the data but still not as good as Model II. All the histograms are fitted very well by Model II except perhaps some of the effective mass plots (which are reasonable, considering the model does not account for g-meson production). Most notable is the $\pi_s^+ \pi_f^-$ distribution which has a high

mass peak not completely reproduced by the models (model I is especially poor here).

A similar effect has been observed by Rhines (ref. 5.39) at 2.32 GeV/c; an enhancement was seen in the mass of $\pi^+ \pi^-$ recoiling against the ρ^o in the high mass region of the spectrum (around 1.7 GeV/c^2). Rhines also reports a similar enhancement in the mass of $\pi^+ \pi^-$ recoiling against the ω^o in the five pion final state. Although the peak in the 2.32 GeV/c experiment is at about the g-meson mass, the decay angular distribution and width of the "resonance" was found to be inconsistent with the g. For the reaction $\bar{p}p \rightarrow \omega^o \pi^+ \pi^-$ a mechanism was suggested (see also ref. 5.48) in which the pions were produced peripherally and the ω^o centrally, akin to the DP (double peripheral) model proposed here. It is worth noting that this mass enhancement could be (at least qualitatively) explained as a manifestation of the Goldhaber effect mentioned in section 5.2.3.

Referring again to table 5.4, the fraction of process U (uncorrelated production of four pions) is given as 8 to 12% which is small enough to justify assumption (a) of section 5.4.1. The fractions of associated production (AP) are about as expected, except the fraction of $\rho^o \rho^o$ at 9 GeV/c which seems rather high (in both models). The fractions of $\rho^o \pi^+ \pi^-$ and $f \pi^+ \pi^-$ are all greater in the DP model than in the LP model. In the latter (leading pion model), it is interesting to note that the trigger selection has not significantly altered the relative proportion of charge conjugate contributions (a small or negative t does not necessarily imply a good acceptance, as pointed out in chapter 4). In the DP model, the higher fraction of the process with a central resonance emerges directly from the model and is therefore seen to be a Kinematic feature.

Table 5.5. gives the results of extrapolating the models to the whole of phase space, hence giving more useful fractions (called a_k^w in Appendix C). Unfortunately, the fraction of process U then goes up to

over 20% for model II, so the numbers must be used with caution. For this process, 33% of the events are within the region of phase space used in the fit (this is the fraction B_k given by equation C.10 of appendix C). For the LP model B_k = 44%; while for the AP and DP models B_k = 75 to 90%, so for these the extrapolation is more reliable.

The projected total number of events $\overset{N^W}{\wedge}$ enables a determination of the cross-section for the four pion final state (table 5.6), using the sensitivities given in chapter 4. The figures given for other experiments are those mentioned in section 5.2.2. The cross-sections obtained by model I are too large, showing again the superiority of the DP model over the LP model. For model II the cross-sections for each of the contributing processes are tabulated in table 5.7 and displayed, together with the total cross-section predictions, in fig. 5.2. Except for a trend for the cross-sections to be slightly higher than other data, the agreement is very good, giving some useful results in an energy region where other data is sparse.

In conclusion the results of this analysis favour a mechanism in which the majority of events in the four pion final state proceed via a double-Regge exchange with a preference for a centrally produced resonance. This is in support of the work of de la Vaissiere (see section 5.2.4), while the leading pion model of Liverpool does not fit the data at all well, in the way formulated here.

Suggested refinements of the model are inclusion of g-meson production, and a contribution with double charge exchange. It would also be valuable to investigate the five pion final state in a similar way, this being eased by the narrowness of the ω^o signal.

CHAPTER 6

SEARCH FOR NARROW MESON STATES

This chapter gives the results of a search for narrow states produced
in $\bar{p}p$ and $\bar{p}d$ interactions at 6 and 9 GeV/c, in particular, the states of
baryonium introduced in Chapter 1. An extensive search has been made in
inclusive channels and in a large number of exclusive processes. Although
this is completed, further work is continuing at the time of writing
(April 1982) on, for example, upper cross-section limits, and to investigate
particular effects in more detail. This study is intended to be the subject
of a forthcoming publication.

6.1 INCLUSIVELY PRODUCED STATES

As explained in Chapter 1, there are theoretical reasons for expecting
exotic meson states to appear as narrow enhancements in effective mass
spectra, and a number of such effects have been seen in other experiments.
One would expect baryonium to be produced in a baryon exchange reaction of
the kind represented in Fig 6.1, where X is produced inclusively together
with a fast pion at the top vertex. Here, X is a baryonium state which may
decay either directly into final state particles including a nucleon and
anti-nucleon, or via cascade into lower lying baryonium states which finally
decay into $N\bar{N}$. If such states are narrow, they should therefore appear as
enhancements in the recoil mass spectrum m(X), or in m ($N\bar{N}$). This search
will also be sensitive to narrow states coupling to purely mesonic final
states (in the annihilation channels).

6.1.1 Inclusive Mass Distributions

Events are assigned to the reaction

$$\bar{p} N \rightarrow \pi^{\pm} X$$
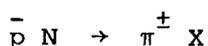
by selecting those with (a) a constrained kinematic fit, and (b) at least

Fig. 6.1
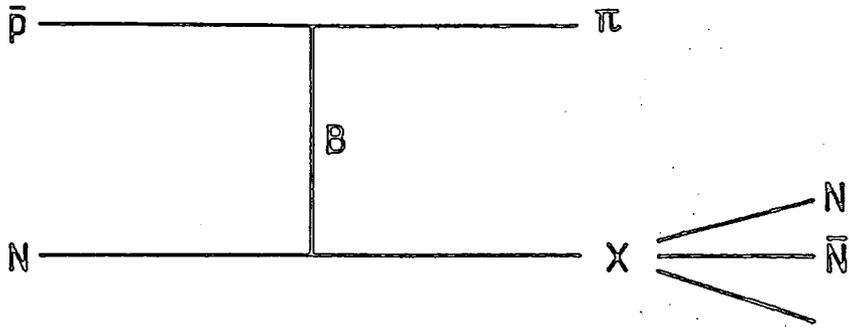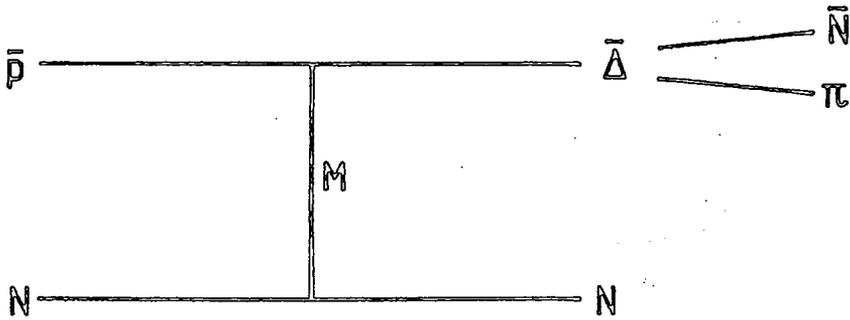
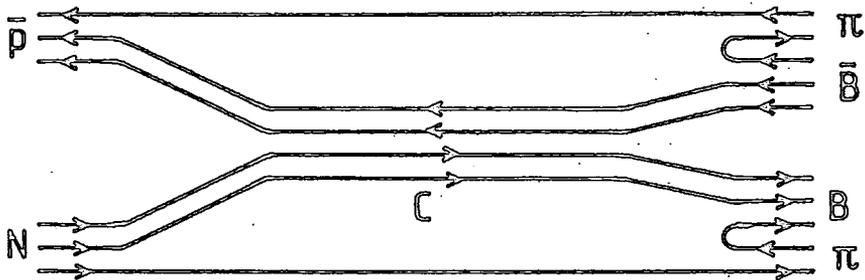Fig. 6.2

Fig. 6.3

Fig. 6.1   Feynman diagram showing production of
            baryonium via baryon-exchange.

Fig. 6.2   Feynman diagram showing a non-annihilation
            reaction proceeding via meson-exchange.

Fig. 6.3   Quark-line diagram showing central
            production of a four-quark state.

one charged outgoing pion above the trigger momentum. In rare cases where there is more than one 'fast' pion of the same charge, the fastest pion is taken as the one against which X recoils. Multi-neutral events are not included, because the resolution for these channels is considerably worse than for constrained fits, so the samples are not truly "inclusive".

The distributions of m(X) for all such events are shown (Ref 6.1) in histograms (a) of Figures 6.4 and 6.5 for π^- and π^+ triggers respectively (hydrogen data at 6 GeV/c only). Since the particles involved in the reaction are all identified, the data can be separated into annihilation (no nucleon or anti-nucleon in the final state) and non-annihilation reactions. Histograms (b) and (c) are the recoil mass distributions for the annihilation processes with an odd and even number of pions respectively (including the triggering pion).

For the non-annihilation channels the M(X) distributions are shown in histograms (d) and m($N\overline{N}$) in (f). This data suffers greatly from background contributions due to diffractive or meson exchange processes, such as that depicted in Fig 6.2. In order to reduce this background, a selection is made requiring the nucleon to have greater laboratory momentum than the anti-nucleon. This should remove half of the true baryonium events, while virtually eliminating background of the kind shown in Fig 6.2. The resulting recoil mass distributions are shown in histograms (e), and the $N\overline{N}$ mass in (g).

None of the histograms in Figures 6.4 and 6.5 show any outstanding narrow peaks ; however, the statistical significance of any peak can only be quantitatively judged when the background is reasonably well determined. The solid curve on each histogram represents a Legendre polynomial distribution of sufficiently high order to give a reasonably good fit to the data. With these background curves, no narrow enhancements are observed beyond the 5.0 standard deviation level in any of the inclusive distributions shown. The 9 GeV/c hydrogen data and the deuterium data have also been investigated in this way,

Fitted curve

Acceptance
(first R.H. scale)

3 S.D. Cross-section
limit (μb)
(second R.H. scale)
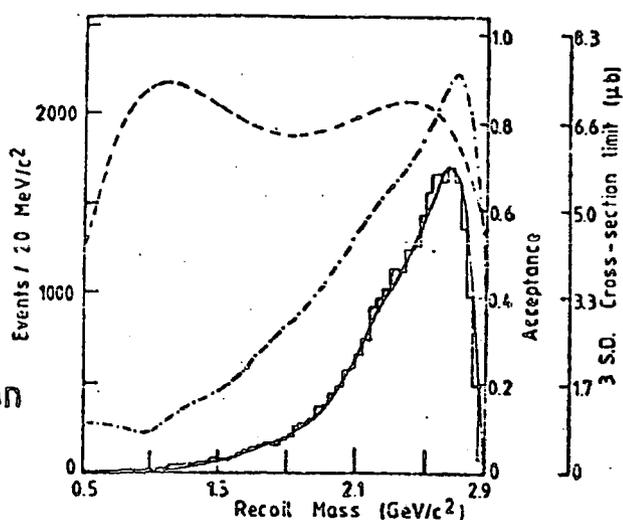
(a) All events.
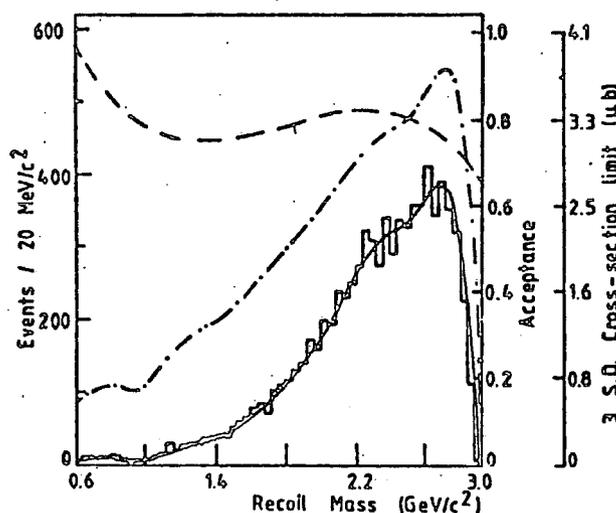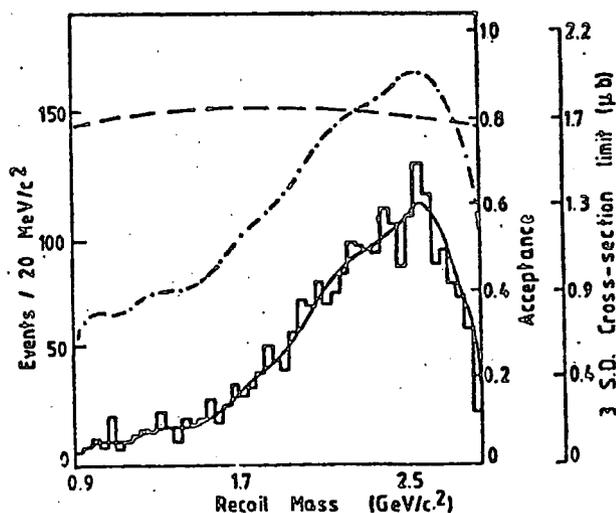
(b) Odd number of pions only.   (c) Even number of pions only.

Fig. 6.4   Recoil mass distributions from fast π⁻,
6 GeV/c   data.

(d) Events including N$\bar{\text{N}}$.

(e) Events including N$\bar{\text{N}}$, selecting mom.(N) > mom.($\bar{\text{N}}$)

(f) N$\bar{\text{N}}$ mass for events including N$\bar{\text{N}}$.

(g) N$\bar{\text{N}}$ mass for events including N$\bar{\text{N}}$, selecting mom.(N) > mom.($\bar{\text{N}}$).

Fig. 6.4 continued.
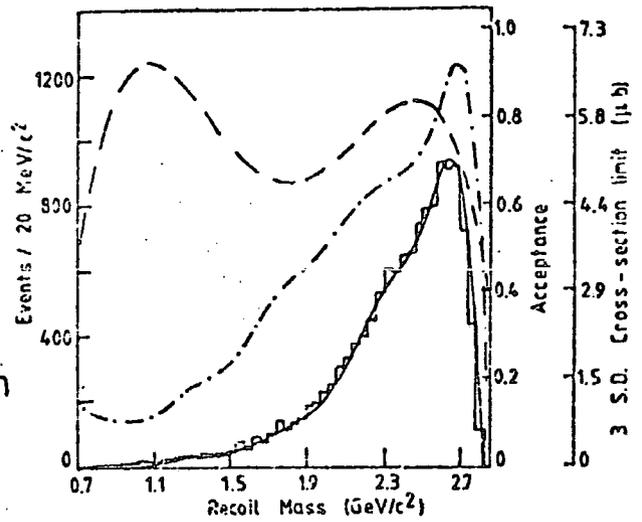
(a) All events.

(b) Odd number of pions only.   (c) Even number of pions only

Fig. 6.5   Recoil mass distributions from fast π^+, 6 GeV/c data.
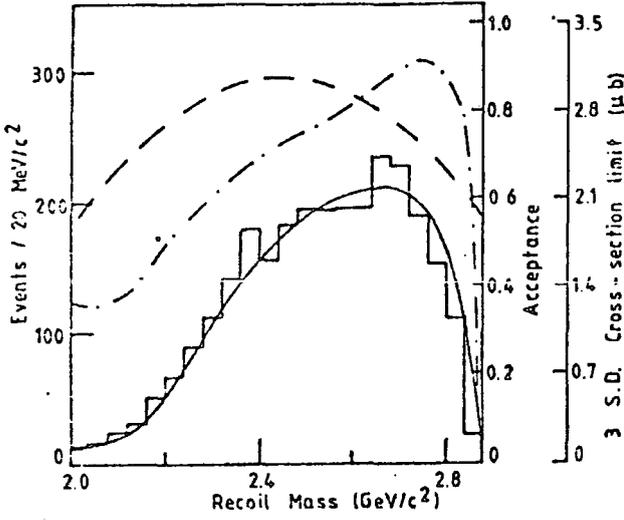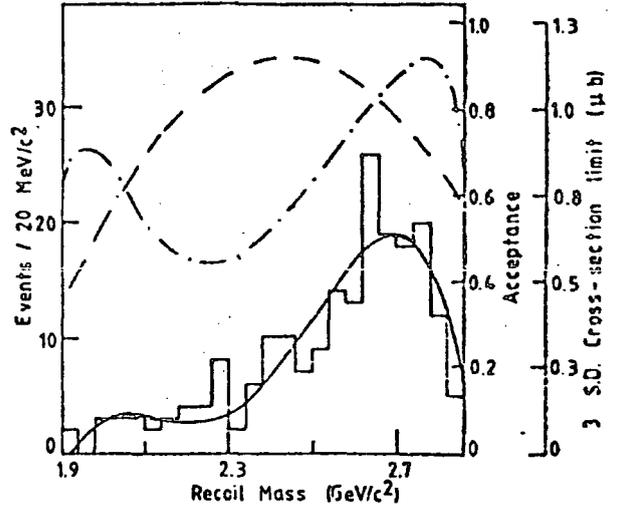
(d) Events including $N\bar{N}$.

(e) Events including $N\bar{N}$, selecting mom.(N) > mom.($\bar{N}$).
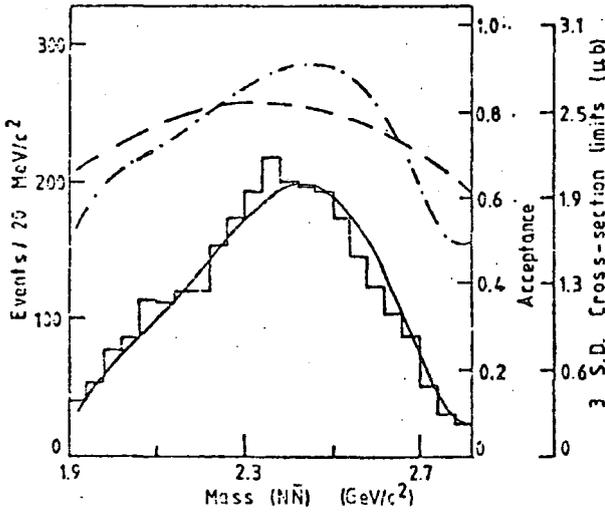
(f) $N\bar{N}$ mass for events including $N\bar{N}$.
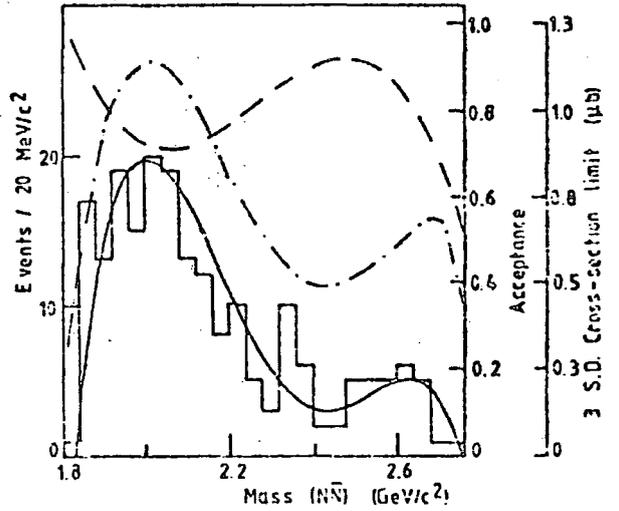
(g) $N\bar{N}$ mass for events including $N\bar{N}$, selecting mom.(N) > mom.($\bar{N}$).

Fig. 6.5 continued.

with a similar result. The 4 standard deviation effects are in the course of being examined.

6.1.2 Upper Cross-Section Limits

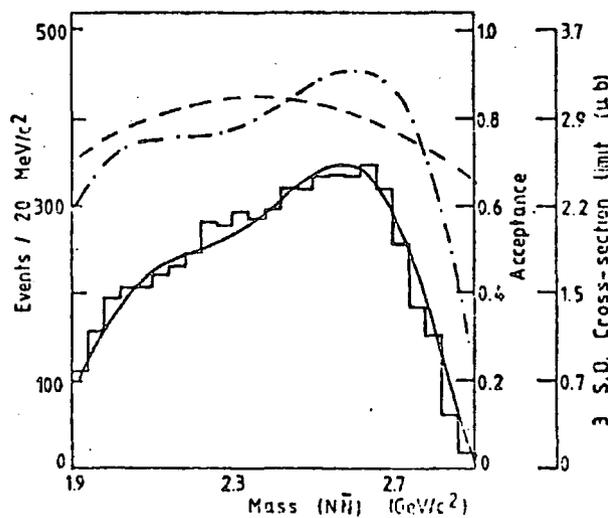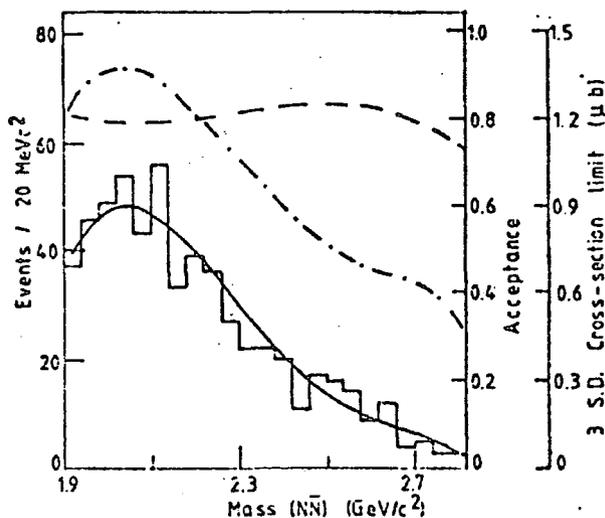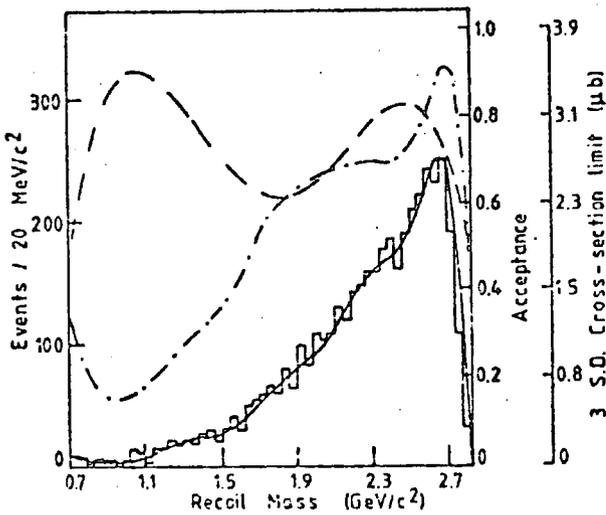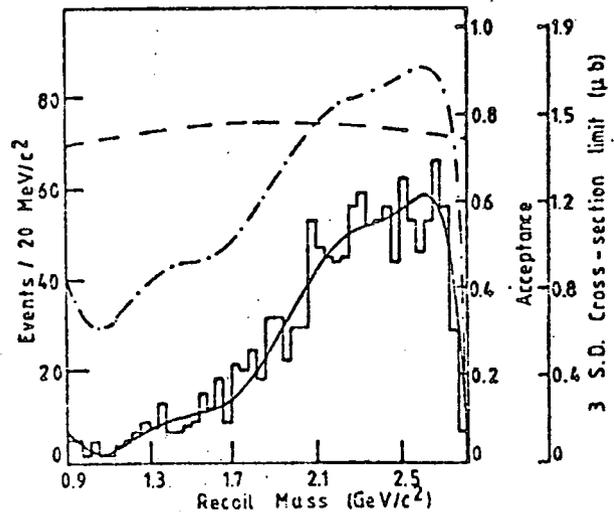The dot-dashed curves in Figures 6.4 and 6.5 represent the cross-section that any 3 standard deviation enhancement would have, as a function of effective mass. This should be qualified by noting that all cross-sections given are only for the region of phase-space accepted by the trigger. In order to give some idea of the effects of acceptance, the average acceptance of events in a bin is plotted against the mass (dashed curves). This is always smoothly varying.

The upper cross-section limits given in the figures are only valid if the supposed narrow resonance is produced with the same average acceptance as the background it lies on. In fact, baryonium may be produced more peripherally or less peripherally than the background events. As an alternative way of demonstrating the sensitivity of the experiment to narrow states, a model dependent method has been tried (Ref. 6.2). Monte Carlo events were generated with a very simple matrix element :

$$|M|^2 = e^{bt} \times \text{Breit-Wigner factors}$$

where t is the momentum transfer from the incoming antiproton to the fast outgoing pion, and b was set to 3 $(GeV/c^2)^{-2}$. The Breit-Wigner factors were applied using a variety of masses and widths for the baryonium resonance. The acceptances of these Monte-Carlo events were then determined so that the number of events could be found that would occur in a certain mass plot, for a given cross-section.

Although this work is still under way at the time of writing, preliminary results indicate that the experiment is good for detecting narrow states of cross-section $\gtrsim$ 1 μb at 6 GeV/c and $\gtrsim$ 0.35 μb at 9 GeV/c. These are the cross-sections predicted by Pennington (Ref. 1.39) for the M(2.02) and M(2.20) states ; they would appear in this experiment as enhancements of at least 5 standard

deviations (depending on the final state).

6.2 CENTRALLY PRODUCED STATES

A search has been made (Ref. 6.3) for baryonium states produced centrally ; that is, in the reaction

$$\bar{p} \, N \rightarrow \pi_F \, C \, \pi_S$$

where π_F is the fastest pion, π_S is the slowest pion, and C represents the remaining final state particles. Figure 6.3 is a quark-line diagram showing a possible mechanism for baryonium production is this reaction. A diquark from the target nucleon and an anti-diquark from the incident antiproton come together to form a four-quark state in the central rapidity region. The remaining quark and anti-quark carry the bulk of the momentum of their parent hadrons, resulting in one fast pion at the top vertex and one slow pion at the bottom vertex. The four-quark state decays into a diquark and anti-diquark which then recombine with single quarks to give a baryon and anti-baryon.

While this is necessarily oversimplified, the central region is well worth investigating, especially in view of the finding in Chapter 5 that central production appears to be the dominant mechanism in simple annihilation channels.

To enhance any signal from such events, a selection criterion was applied :

$$p_L^S \; < \; p_L^C \; < \; p_L^F$$

where p_L^I refers to the longitudinal momentum of respectively the slowest pion (S), the central system including $N\bar{N}$ (C), and the fastest pion (F). Whether p_L is taken in the C.M.S. or in the lab frame does not change the main qualitative results.

The only noticeable narrow effect found is a state at 1.96 GeV/c^2 which appears in more than one effective mass plot. It is mainly seen in the reaction

$$\bar{p} \, p \rightarrow \pi_F^- \, p\bar{p} \, \pi_S^+$$
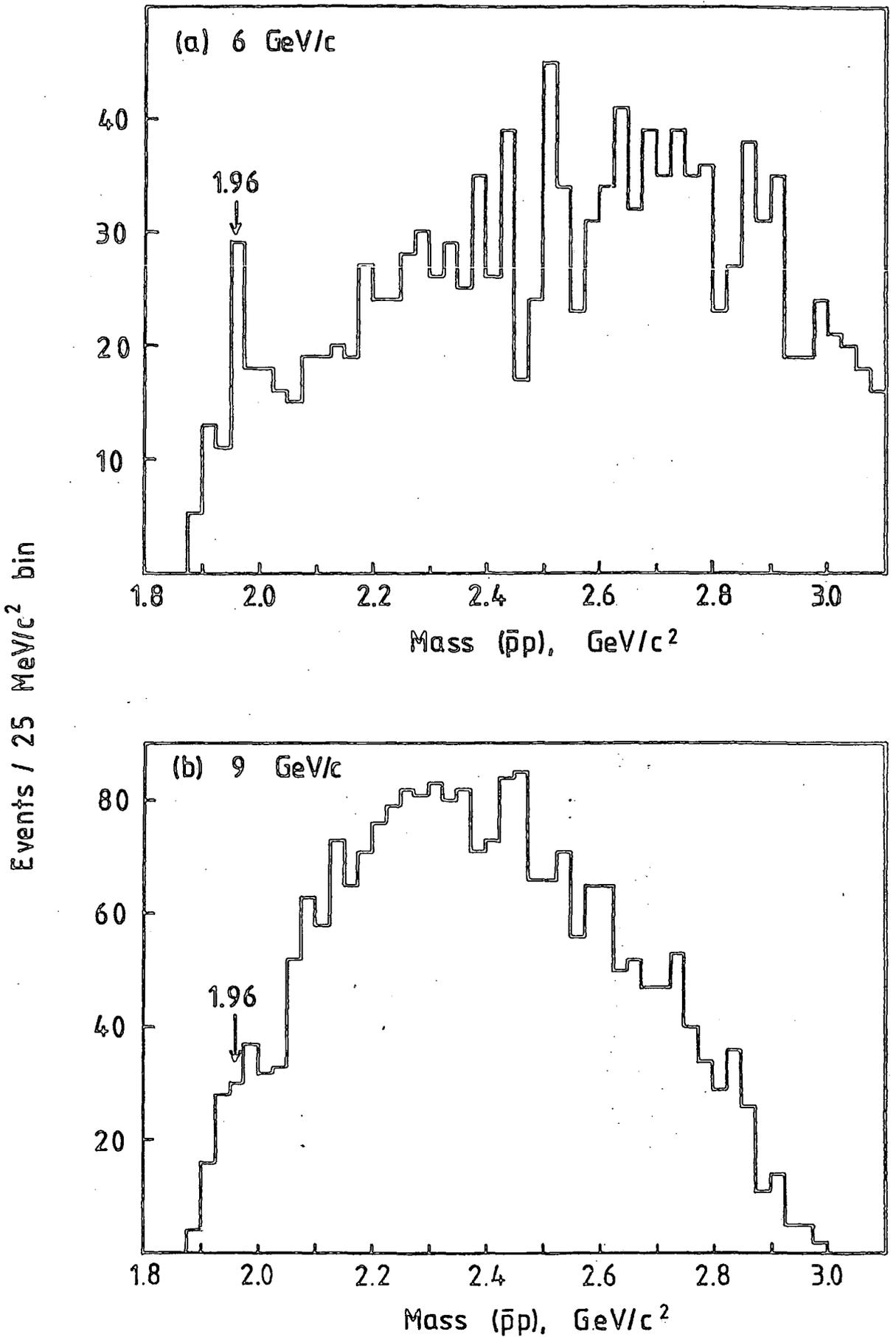
Fig. 6.6   Effective mass of $\bar{p}p$ produced centrally in the final state $\pi_F^- \bar{p} p \pi_S^+$ (from ref. 6.3)

so that C is a neutral object coupling to $\bar{p}p$ (see Fig 6.6). It is more

significant in the 6 GeV/c data but there are indications of its presence

in the 9 GeV/c data, and also in some other reactions. In particular, it is

seen in central $p\bar{n}$ and $\bar{p}n$ mass distributions, after adding up all the charge

combinations of pions, though it looks much wider here (not shown). Small

enhancements also appear at the same mass in the deuterium data.

In summary, while no very significant peak is seen in individual mass

plots, an effect at 1.96 GeV/c^2 recurs in a number of different distributions.

Although too high a mass for the S-meson, this is tentative evidence for

centrally produced baryonium.

6.3 EXCLUSIVELY PRODUCED STATES

A comprehensive search has been made for narrow effects in the invariant

mass distributions of all the common final states with constrained fits. As

will be seen, a number of effects have been found, but only a few of them

are significant enough to merit detailed investigation.

6.3.1 Method and Classification of Results

Invariant mass distributions have been examined for events having a

4C or 1C fit (that is, zero or one neutral particle in the final state) to

the channels

$$\bar{p} N \rightarrow m\pi \, , \quad m = 3, 4..9 \text{ i.e. up to 8 prongs}$$

and $\quad \bar{p} N \rightarrow \bar{N}N + m\pi \quad$ up to 6 prongs (m > 0)

where N represents proton or neutron. This corresponds to 33 distinct

channels. Final states with strange particles or more than one neutral

particle were not looked at for this purpose.

Data was used from the 6 and 9 GeV/c runs with a hydrogen target, and

from the 9 GeV/c run with deuterium. Because of the low sensitivity of the

6 GeV/c deuterium data, it was only used to look for effects already

suggested by data from other runs. Where an event had more than one

kinematic interpretation, only the "best fit" was used, that is the most

highly constrained and, within those, the one of highest χ^2 probability.

Histograms were made of all mass combinations of the final state particles, separately for each of the trigger particles π^+, π^-, and proton, as appropriate. They were not acceptance-weighted, but only events in a well defined kinematic region of good acceptance were used. The significance of any noticeable peak appearing in less than four 20 MeV/c^2 bins was measured as the number of standard deviations, $\sqrt{B}$, (strictly, this should incorporate the uncertainty in B, but this is ignored here), of the peak above the background level B (estimated by eye). All peaks of 3 standard deviations (s.d.) or more were recorded, except for well-known resonances such as ω^o.

In an exercise of this sort, in which more than 10^5 histogram bins were examined, one expects to see more than $\sim$ 100 3 s.d. peaks, a few ($\sim$ 5) 4 s.d. peaks, and $\sim$ 0.05 5 s.d. peaks (that is, the chance of seeing such a peak in the whole experiment is approximately 1 in 20). The numbers of 3 and 4 s.d. peaks seen correspond roughly with these expectations. A short list was made by discarding all 3 s.d. effects, except those seen at comparable masses in more than one final state, or at more than one energy. This is reproduced in Tables 6.1 and 6.2, with information on the masses, widths, statistical significance and production reactions of the surviving candidates.

6.3.2 Inspection of Particular Effects Found

In deciding which of the effects listed in Tables 6.1 and 6.2 are genuine manifestations of exotic resonances, one may be guided to some extent by the widths of the observed enhancements. In the table, the widths are roughly estimated from the number of bins occupied by the peaks. Broad enhancements may sometimes be caused by threshold effects, reflections of well-known resonances or contamination from other channels ; whereas narrow widths, especially below about 50 MeV/c^2 are much more difficult to explain this way. Furthermore, other experimental evidence for baryonium has mainly concentrated on narrow effects comparable with the experimental resolution, and this is the main aim of the present experiment. For these reasons, effects such as the four pion

(a) 6 GeV/c

Mass (GeV/c^2)	Reaction	Approx. width (MeV/c^2)	Significance (S.D.)	Seen* after cut?
1.93	$\bar{p}p \to (p_f p)\pi^+\pi^-\pi^0$	60	4.9	-
1.94	$\bar{p}p \to \pi^+_f(\bar{p}n)\pi^+\pi^-$	<40	3.5	No?
2.02	$\bar{p}p \to (p_f\bar{n})\pi^+\pi^-\pi^-$	<40	6.0	-

(b) 9 GeV/c

Mass (GeV/c^2)	Reaction	Approx. width (MeV/c^2)	Significance (S.D.)	Seen* after cut?
1.91	$\bar{p}p \to \pi^-_f(\bar{p}n)\pi^+\pi^+$	60	3.5	Yes - only
1.95	$\bar{p}p \to \pi^-_f(\bar{p}p)\pi^+\pi^0$	<20	3.0	Yes
2.01	$\bar{p}n \to \pi^-_f(\bar{p}p)$	40	3.6	No?
2.02	$\bar{p}p \to \pi^+_f(\bar{p}n)\pi^+\pi^-$	80	5.5	Yes
2.13	$\bar{p}n \to \pi^-_f(\bar{p}p)\pi^+\pi^-$	80	3.0	Yes?
2.15	$\bar{p}n \to \pi^-_f(\bar{p}p)\pi^0$	60	3.0	No
2.16	$\bar{p}p \to \pi^+_f(\bar{p}n)\pi^+\pi^-$	<40	3.1	Yes?
2.95	$\bar{p}p \to \pi^+_f(\bar{p}n\pi^+)\pi^-$	<20	4.0	No
4.00	$\bar{p}p \to (\pi^+_f\bar{p}n\pi^-)\pi^+$	<40	3.5	No
4.00	$\bar{p}n \to (\pi^+_f\bar{p}n\pi^-\pi^-)\pi^-$	<40	3.0	Yes?
4.02	$\bar{p}p \to (\pi^+_f\bar{p}p\pi^0)\pi^-$	<40	4.1	No?

Table 6.1 Effects seen in mass combinations including $N\bar{N}$

For each reaction, the particles bracketed comprise the mass combination in which the effect is seen. The fast (triggering) particle is denoted by subscript f.

* The cut referred to is that the laboratory momentum of the nucleon is to be greater than that of the anti-nucleon. A? indicates too few events to be sure.

(a)   6 GeV/c

Mass (GeV/c^2)	Reaction	Approx. width (MeV/c^2)	Significance (S.D.)
0.41	$\bar{p}p \rightarrow p_f(\pi^+\pi^-)\bar{p}\pi^0$	60	4.2
0.41	$\bar{p}p \rightarrow p_f(\pi^-\pi^0)\bar{p}\pi^+$	60	3.1
0.44	$\bar{p}p \rightarrow \pi^-_f(\pi^-\pi^0)2\pi^-4\pi^+$	<40	2.8
0.52	$\bar{p}p \rightarrow \pi^-_f(\pi^-\pi^-)\pi^-4\pi^+\pi^0$	<40	4.1
1.49	$\bar{p}p \rightarrow \pi^-_f(\pi^+\pi^+\pi^+\pi^-)\pi^-\pi^0$	100	5.5
2.00	$\bar{p}p \rightarrow (\pi^+_f\pi^+\pi^-\pi^-)\pi^+\pi^-$	<40	4.7
2.72	$\bar{p}p \rightarrow (\pi^+_f\pi^-\pi^+\pi^+)2\pi^-$	80	4.5
2.93	$\bar{p}p \rightarrow (\pi^+_f\pi^-\pi^+\pi^+)2\pi^-$	80	4.6

(b)   9 GeV/c

Mass (GeV/c^2)	Reaction	Approx. width (MeV/c^2)	Significance (S.D.)
0.36	$\bar{p}p \rightarrow \pi^-_f(\pi^+\pi^0)\bar{p}p$	<20	4.0
0.40	$\bar{p}p \rightarrow \pi^-_f(\pi^+\pi^+)\bar{p}n$	<40	3.5
0.44	$\bar{p}p \rightarrow (\pi^-_f\pi^0)\pi^+\bar{p}p$	40	3.2
0.51	$\bar{p}p \rightarrow (\pi^-_f\pi^0)\pi^+\bar{p}p$	<20	3.5
0.70	$\bar{p}p \rightarrow (\pi^+_f\pi^+)\pi^-\bar{p}n$	60	4.0
0.71	$\bar{p}p \rightarrow \pi^+_f(\pi^+\pi^0)\pi^+3\pi^-$	<20	3.0
1.13	$\bar{p}p \rightarrow (\pi^-_f\pi^+)\pi^-\bar{p}n$	<20	4.1
2.89	$\bar{p}p \rightarrow (\pi^-_f\pi^0)\pi^+$	<20	4.0

Table 6.2   Effects seen in mass combinations of only pions

For each reaction, the particles bracketed comprise the mass combination in which the effect is seen. The fast (triggering) particle is denoted by subscript f.

enhancements at 1.49, 2.72, and 2.93 GeV/c^2 are given low priority as claims for baryonium.

Conversely, some effects may be eliminated because they are too narrow and less than the mass resolution ; such effects can only be statistical fluctuations. This is true of the $\pi^-\pi^0$ enhancements at 0.51 and 2.89 GeV/c^2. The mass resolution has been determined for each channel separately, at each energy, and as a function of the effective mass of the particular combination being investigated. This is done by taking the individual track vector errors on each event and calculating the resultant error propagated into any mass combination. The r.m.s. error of events in a bin centred on a given mass is the estimate of resolution at that mass ; it is generally in the range 5 - 40 MeV/c^2. The bin width of 20 MeV/c^2 is therefore a suitable value, though sometimes histograms had to be re-plotted with a smaller bin width.

For the mass plots of combinations including a nucleon-antinucleon pair, the plots were repeated selecting only events where the nucleon has greater laboratory momentum than the antinucleon (a selection also used for the inclusive final states - see section 6.1.1) to reduce background from 'normal' processes. If, as a result of this cut, the peak is not seen (or greatly reduced in significance), it casts doubts on the nature of the enhancement. For this reason, the $\bar{p} n \pi^+$ state at 2.95 GeV/c^2 is not considered as a serious candidate for baryonium (though it is interesting to note that a narrow state at this mass has been found previously which, however, was not confirmed by a subsequent experiment - Ref. 1.52).

After applying these considerations, most of the remaining effects can be grouped together for states of similar mass. For the few effects that cannot be so grouped, there is no evidence to suggest that they are anything other than statistical anomalies (in particular, the complete absence of any peaks in related channels cannot be otherwise explained), and the statistical signific-ance is in any case often crucially dependent on where the background curve is drawn.

The following states then emerge as the most likely candidates for narrow meson resonances :

1.93	($\overline{N}N$)	(Fig 6.7)
2.02	($\overline{N}N$)	(Fig 6.8)
2.14	($\overline{N}N$)	(Fig 6.9)
4.00	($\overline{N}N$ $\pi\pi$)	(Fig 6.10)
0.41	(π π)	(Fig 6.11)

Of these, by far the most significant is the 2.02 ($\overline{N}N$) state. This has been investigated more fully, and further details are given in the next section. The other states are considered here briefly as, at the time of writing, only a preliminary investigation has been done.

1.93 ($\overline{N}N$)

This state is of special interest as it is at a mass consistent with that of the S-meson (1.936 GeV/c^2). The four relevant histograms are displayed in Figure 6.7 (a)-(d). Enhancements are seen in mass distributions for two channels : $\overline{p}p \rightarrow \overline{p}p \pi^+ \pi^- \pi^0$ and $\overline{p}p \rightarrow \overline{p}n \pi^+ \pi^+ \pi^-$. The usual way of confirming such effects is to examine the charge conjugate configurations ; however, this is not straightforward here, because of experimental acceptance, and a proper comparison would be model-dependent. Neither of the effects seen at 6 GeV/c is seen in the corresponding histograms at 9 GeV/c, and vice-versa. While it is always possible to account for this in terms of cross-section variation, it does cast considerable doubt on the interpretation as a resonance.

Furthermore, the enhancements all occur at slightly different masses and with different widths (although the resolutions are all similar). However, when the distributions are summed (Fig 6.7 (e) - (g)), the peak remains, and is particularly significant in the overall sum (g), where the width is estimated to be $\sim$ 40 MeV/c^2. Before claiming this to be an observation of the S-meson,

Fig. 6.7 Narrow Effects in Mass (NN) at ~1.93 GeV/c²

Number of events per 20 MeV/c² bin

(a) $\bar{p}p \rightarrow (p_f \bar{p}) \pi^+ \pi^- \pi^o$
6 GeV/c
245 events
1.93 $(\bar{p}p)$
Mass $(p_f \bar{p})$, GeV/c²

(b) $\bar{p}p \rightarrow \pi^+_f (\bar{p}n) \pi^+ \pi^-$
6 GeV/c
133 events
1.94 $(\bar{p}n)$
Mass $(\bar{p}n)$, GeV/c²

(c) $\bar{p}p \rightarrow \pi^-_f (\bar{p}n) \pi^+ \pi^+$
9 GeV/c, 102 events
1.91 $(\bar{p}n)$
Mass $(\bar{p}n)$, GeV/c²

(d) $\bar{p}p \rightarrow \pi^-_f (\bar{p}p) \pi^+ \pi^o$
9 GeV/c
641 events
1.95 $(\bar{p}p)$
Mass $(\bar{p}p)$, GeV/c²
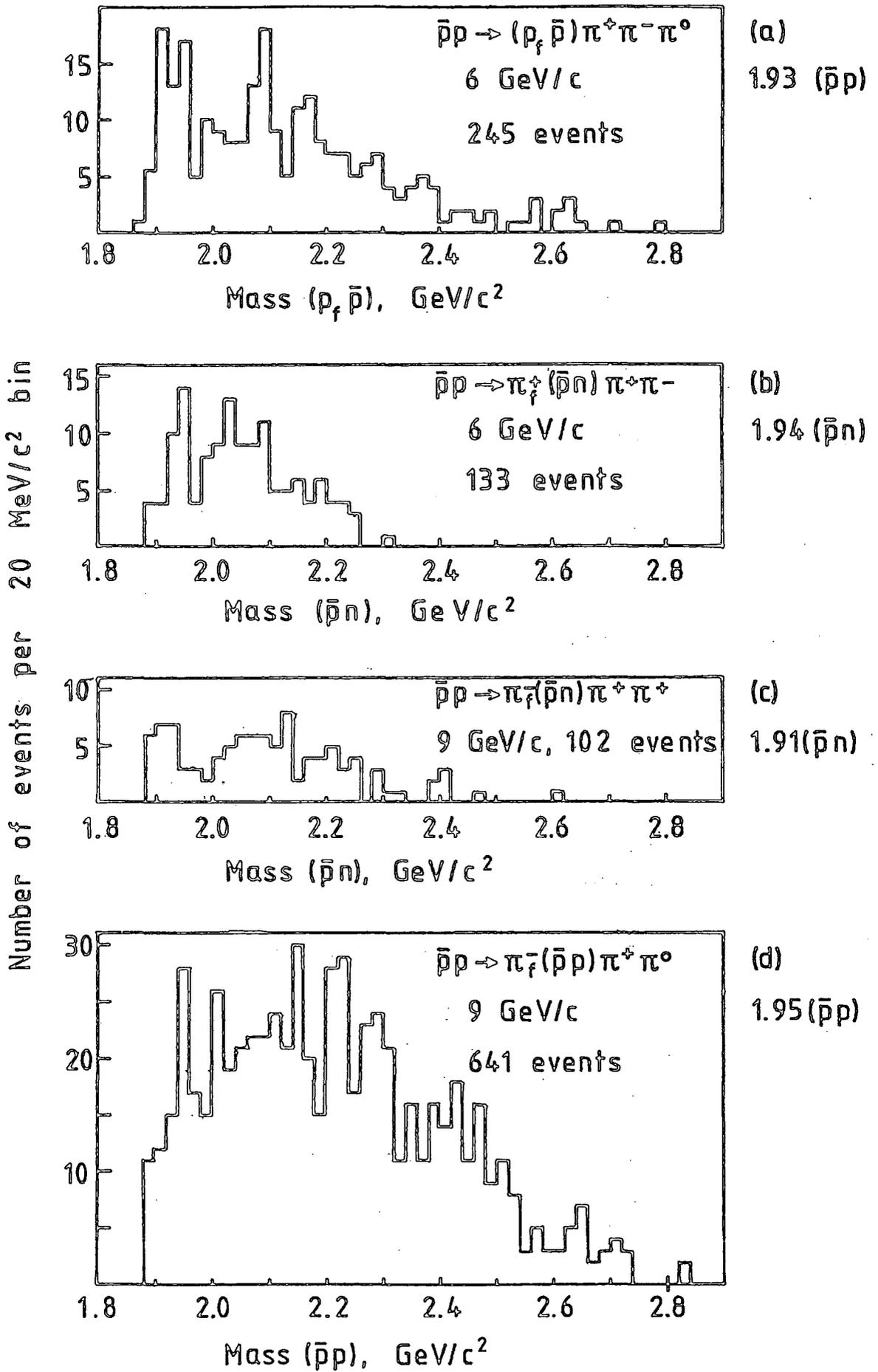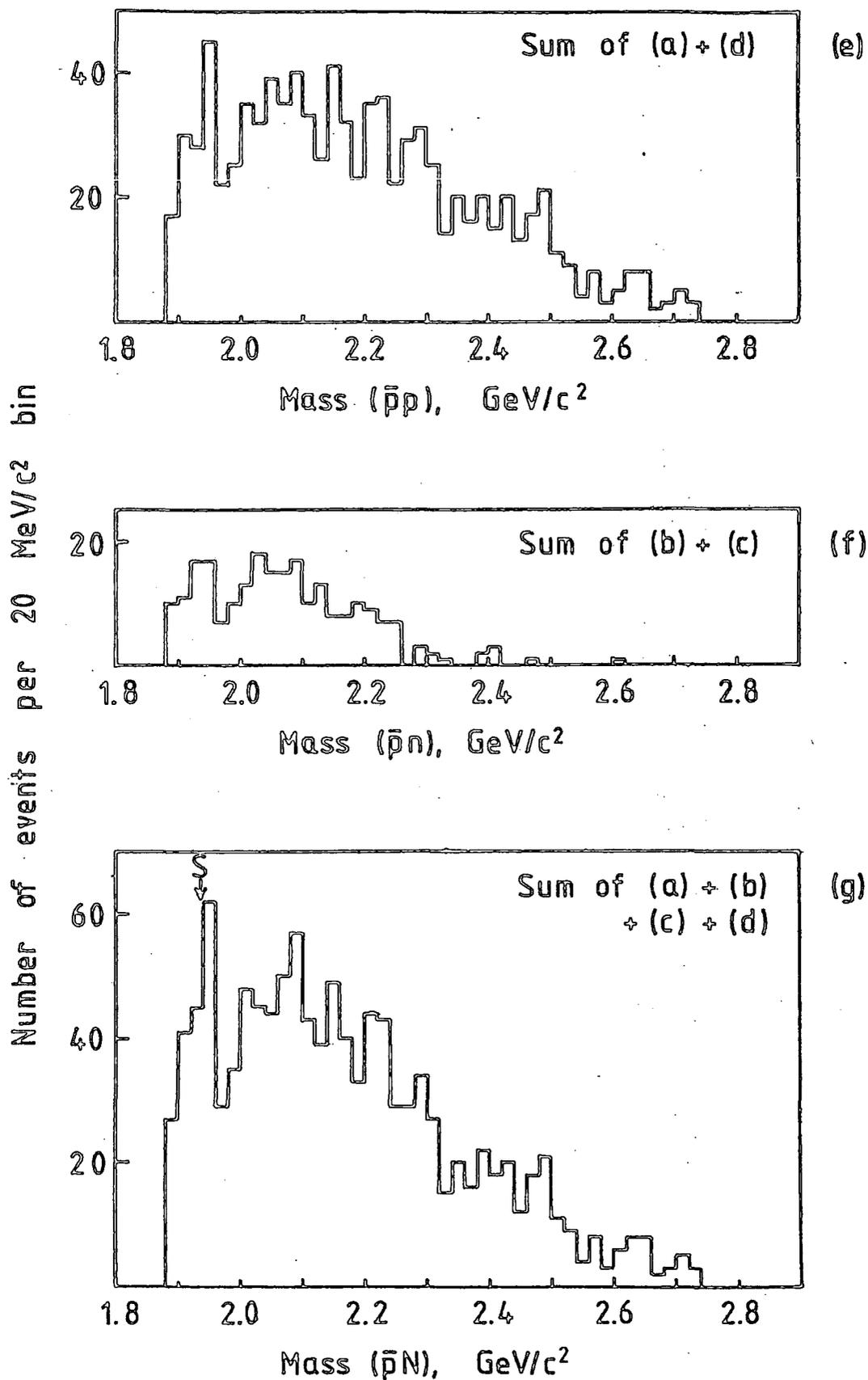
Fig. 6.7 (cont.) Sum of Histograms on Previous Page

Fig. 6.8 Narrow Effects in Mass (NN) at ~ 2.02 GeV/c²
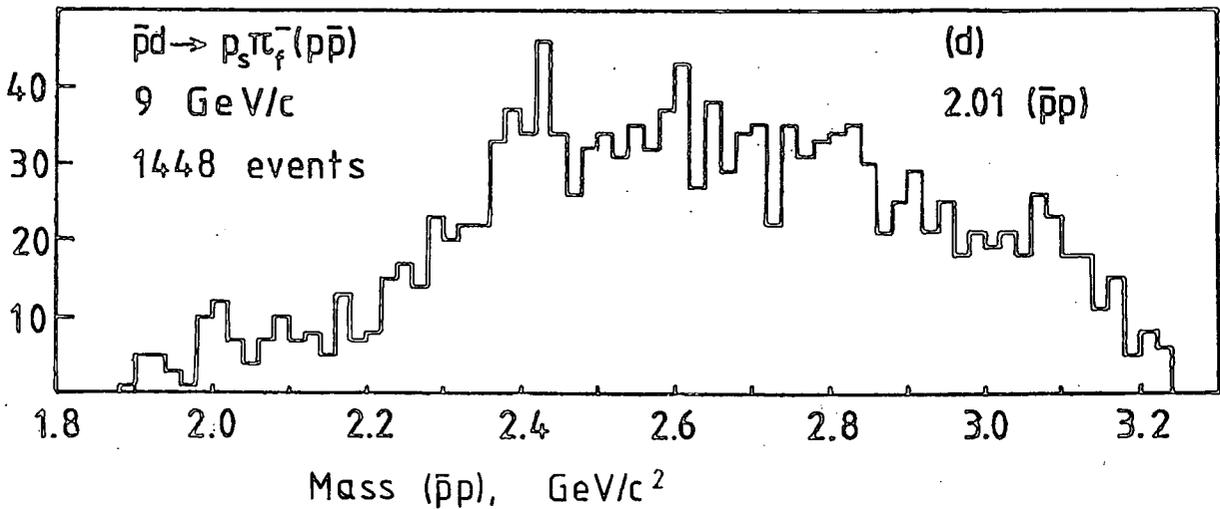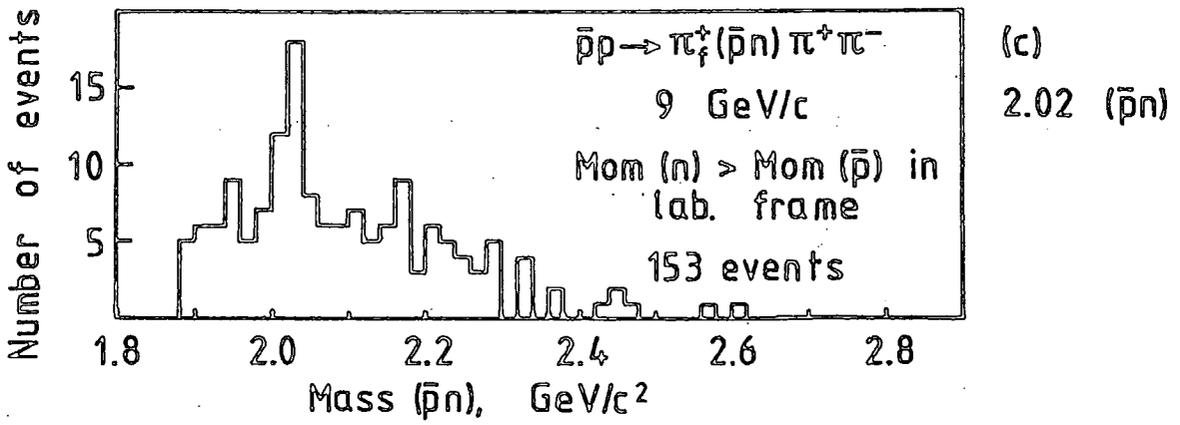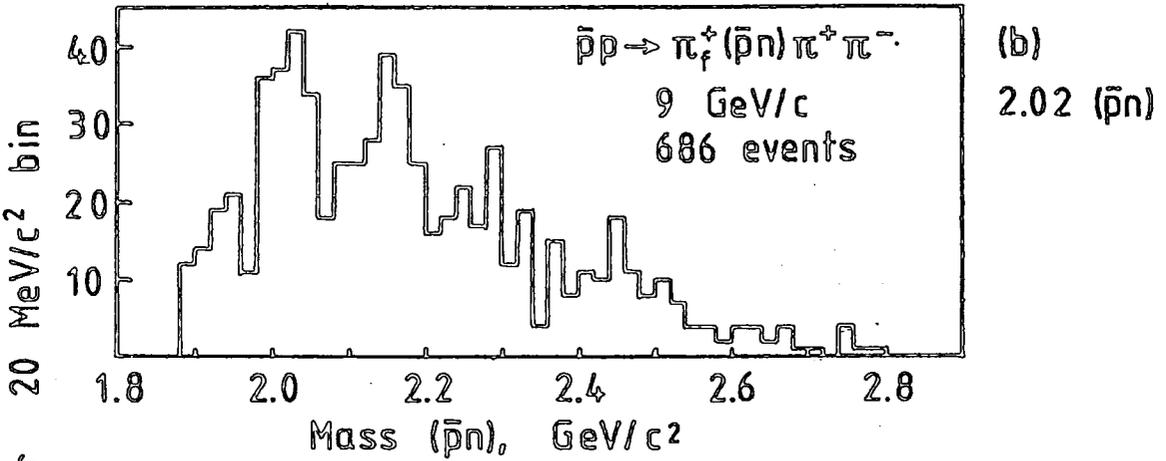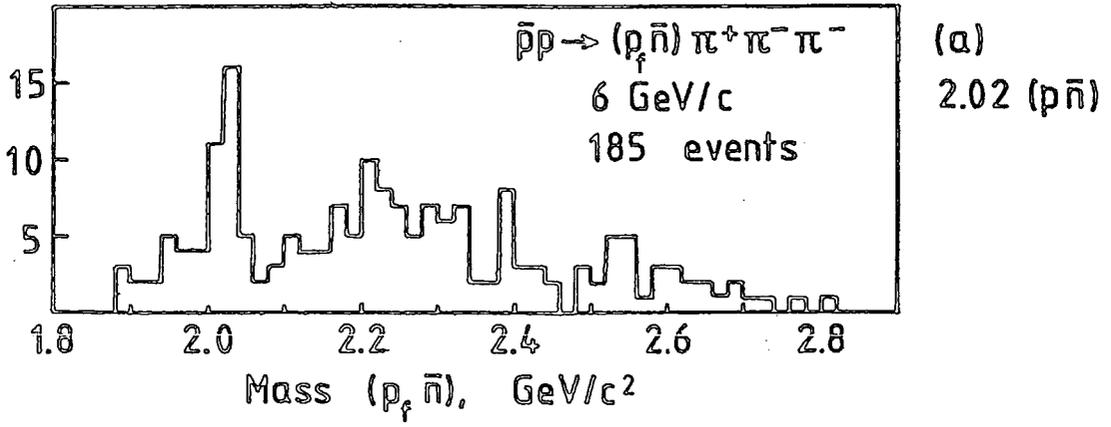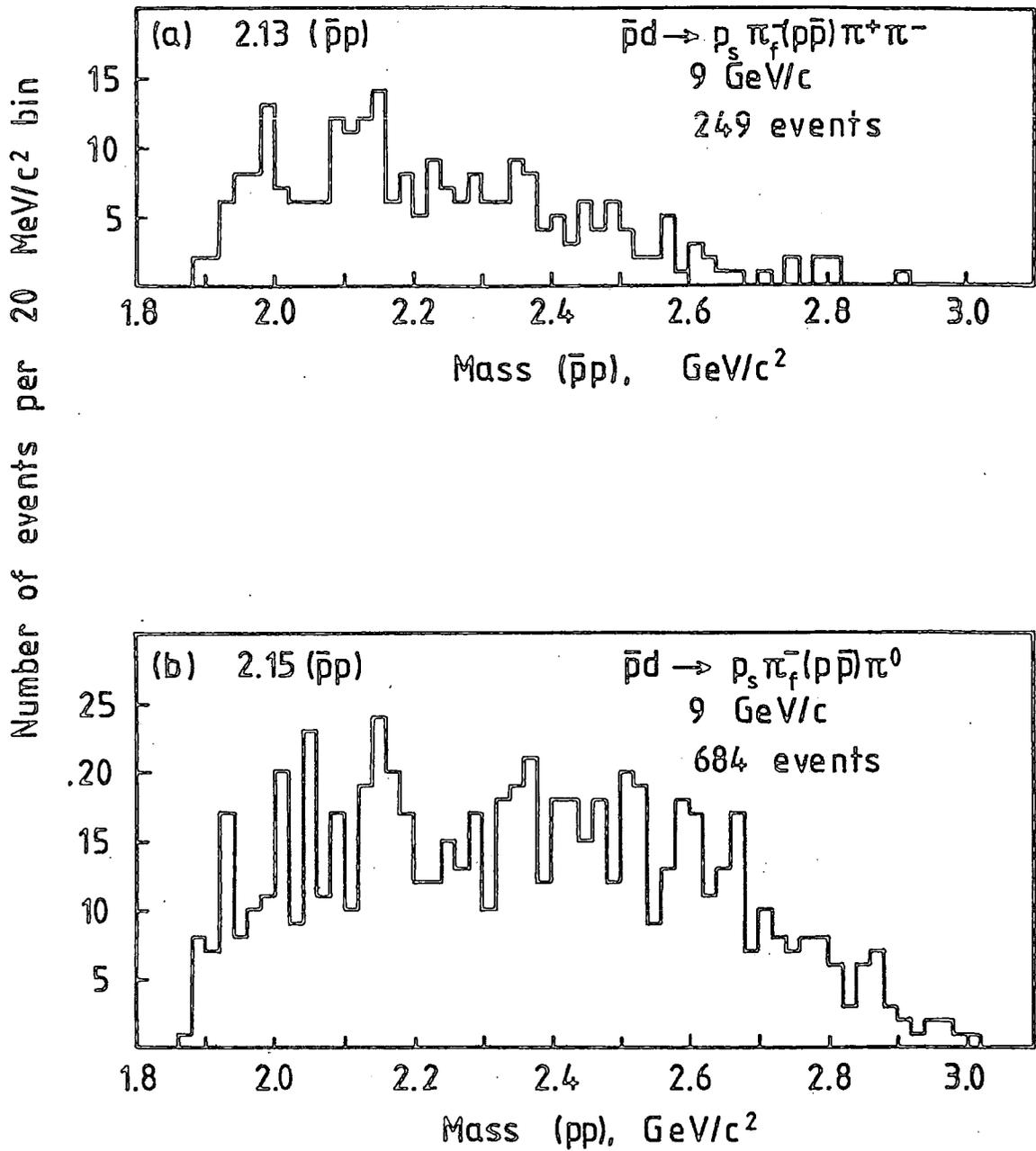
Fig. 6.9 Narrow effects in Mass ($\bar{N}N$) at ~ 2.14 GeV/c^2
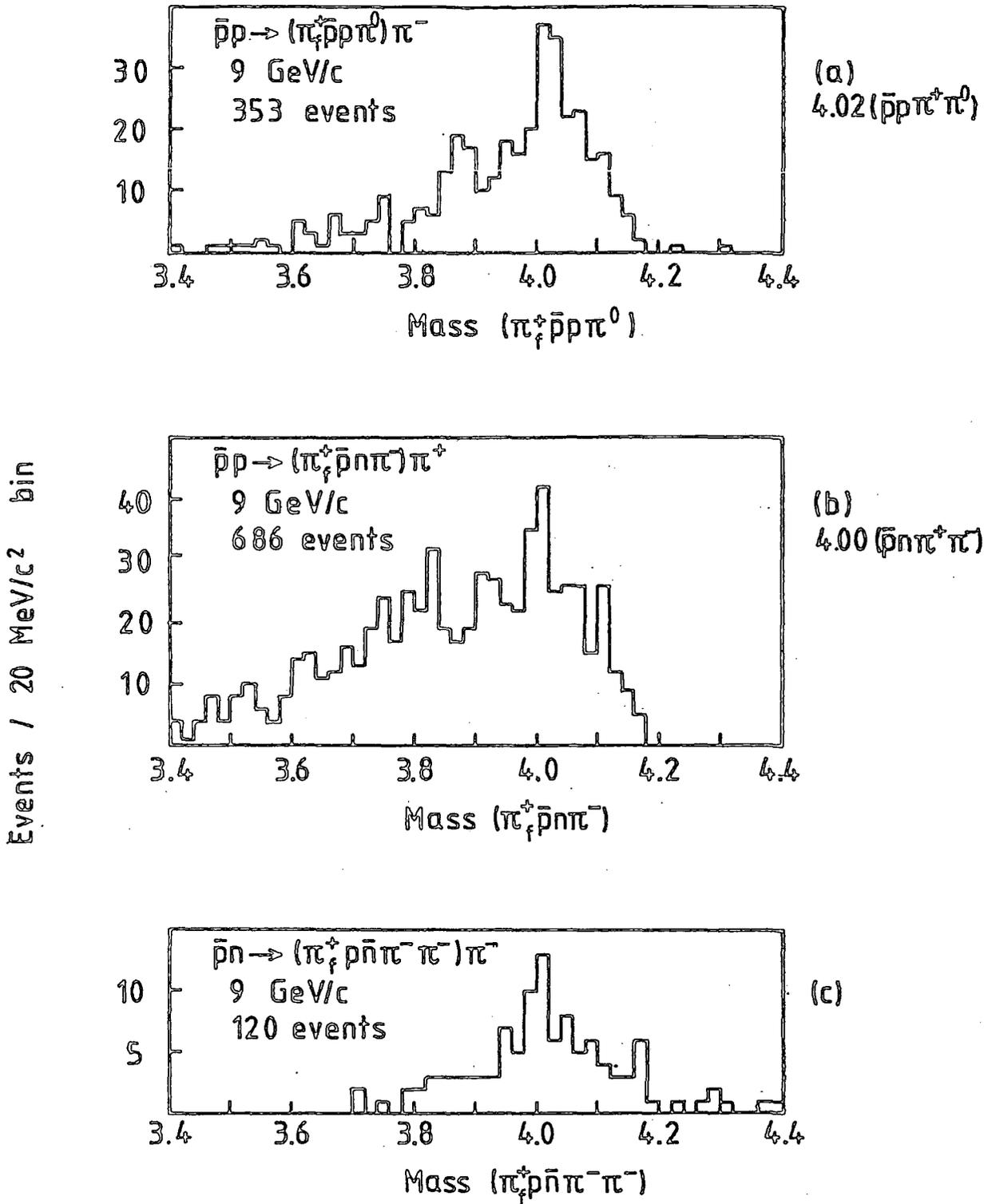
Fig. 6.10 Narrow effects in Mass ($\bar{N}N\pi\pi$) at ~4.00 GeV/c^2
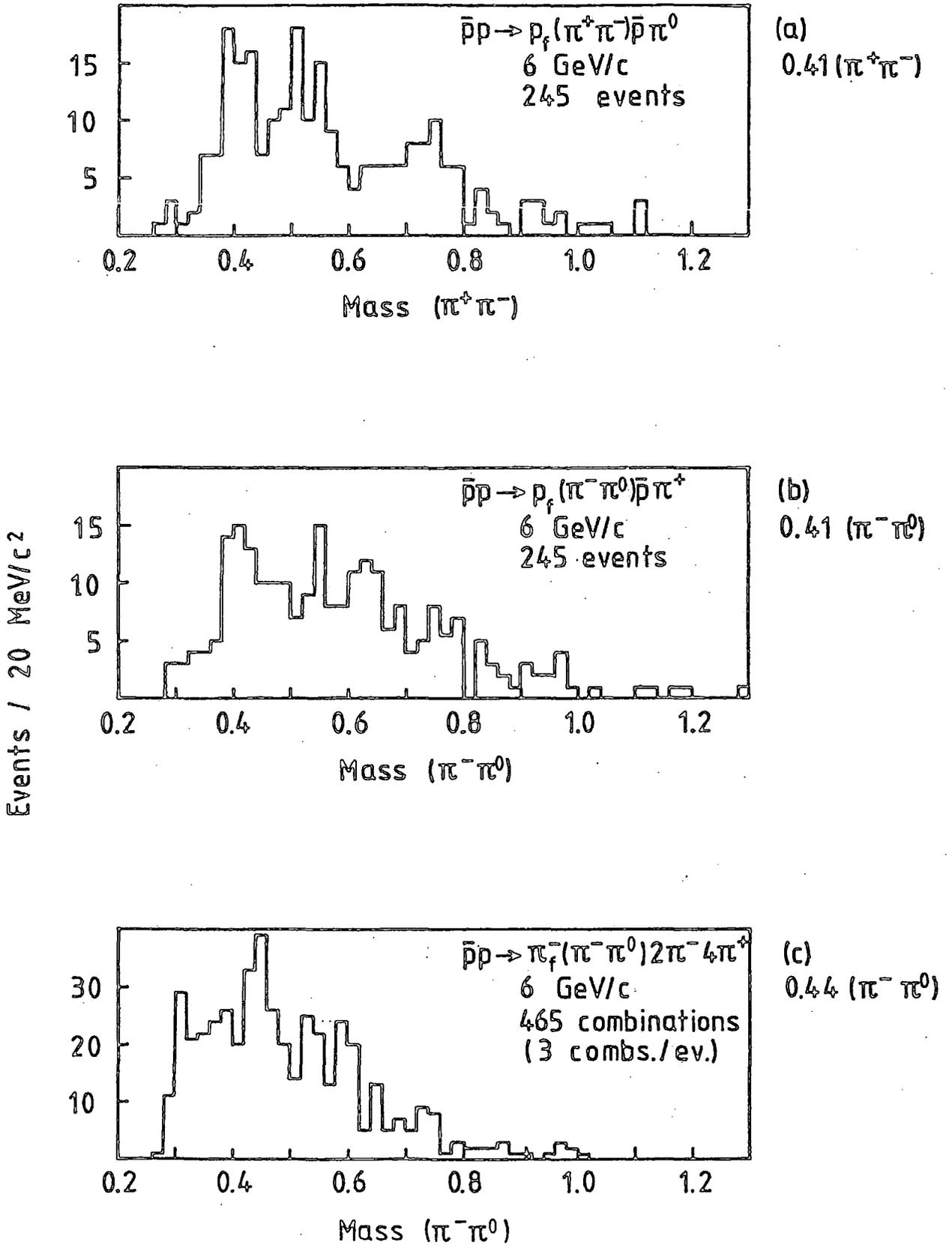
Fig. 6.11   Narrow   effects   in   Mass $(\pi\pi)$ at ~ 0.41 GeV/c^2
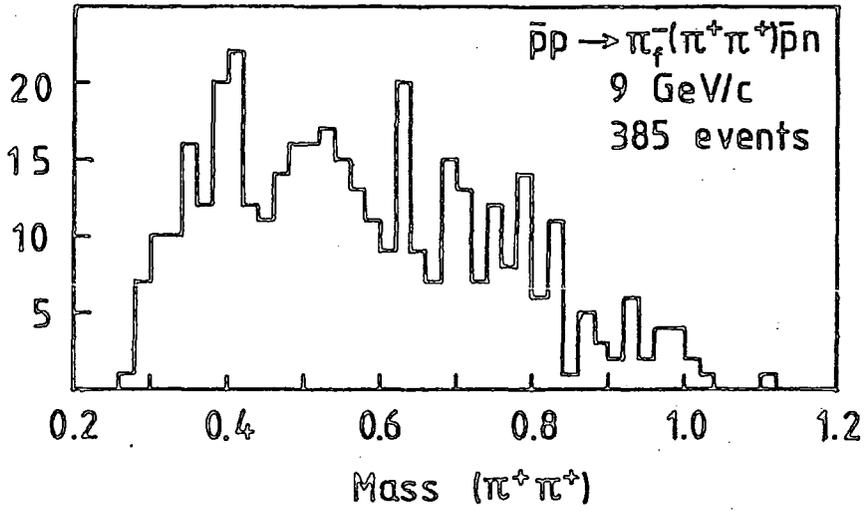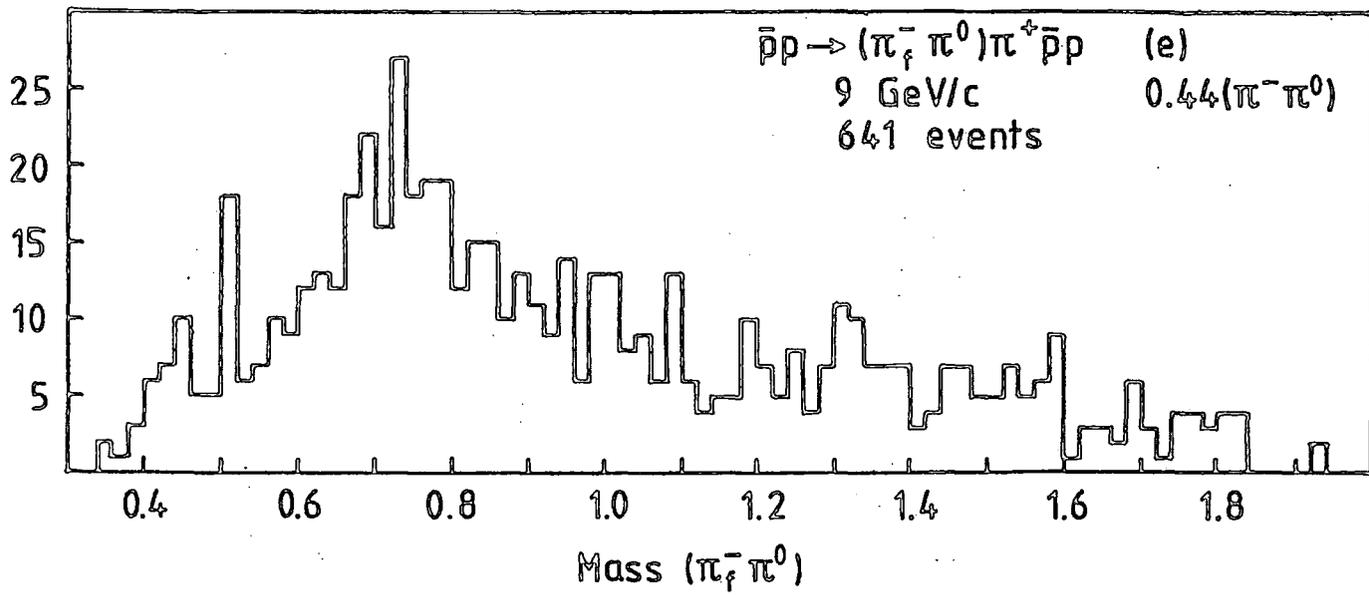
Fig. 6.11 (continued)

it would be necessary to examine the channels for contamination from other

kinematic interpretations, and to account for the absence of any signal

in other related channels. No effects are seen at this mass in any deuterium

data.

2.02 $(\bar{N}N)$

Figs 6.8 (a) - (d) show the effects found in $\bar{N}N$ mass distributions at

2.02 GeV/c^2. The first one (a) shows a striking 6 s.d. peak in the $\bar{p}n$ mass

for events with a proton trigger (p_f) in the channel

$$\bar{p}p \rightarrow p_f\bar{n} \ \pi^+ \ \pi^- \ \pi^- \quad \text{at} \quad 6 \text{ GeV/c}$$

No effect is seen in this channel at 9 GeV/c. However, in the charge con-

jugate channel, with π^+ triggered events, a rather broader structure is seen

at this mass in the 9 GeV/c data (Fig 6.8 (b)). After applying the cut that

the neutron should have higher laboratory momentum than the antiproton, the peak

becomes much narrower (< 40 MeV/c^2) though less significant (from 5.5 to 4.3 s.d)

because of the reduced number of events (c).

The final plot (d) shows perhaps a weak structure in the $\bar{p}p$ mass for a

deuterium channel. Nonetheless, taken together, these effects represent strong

baryonium candidates, particularly the one shown in (a). More reason for

interest in these states is the previous observation of a narrow peak in the

$\bar{p}p$ mass at 2.02 GeV/c^2 in $\pi^-p \rightarrow p_f \ \pi^- \ \bar{p}p$ (Benkheiri et al, see Chapter 1,

section 1.7.2). Further investigations of these effects are described in the

next section.

2.14 $(\bar{N}N)$

Three effects are seen in the 9 GeV/c data at a mass around 2.14 GeV/c^2.

Two of these are shown in Fig 6.9, the other one (at 2.16 GeV/c^2 in the table)

being in Fig 6.8 (b) together with a peak at 2.02 GeV/c^2. None of these

effects are very significant, especially as it is uncertain where one should

draw the background. One of the effects is removed by applying the cut

(nucleon faster than anti-nucleon in the lab). Since the peaks are all fairly

wide (40-80 MeV/c^2), these could well be reflections of other resonances.
In any case, there is no strong evidence that they are genuine baryonium
states.

4.00 ($\bar{N}N$ $\pi\pi$)

Two effects seen in the $\bar{N}N$ $\pi\pi$ mass at $\sim$ 4.00 GeV/c^2 are shown in Fig 6.10.
Also shown is an effect in the $\bar{N}N$ $\pi\pi\pi$ mass at $\sim$ 4.00 GeV/c^2 ; but this
channel has few events, and the peak is not by itself very significant.
Although fairly narrow (< 40 MeV/c^2), all three peaks lie on the maxima
of the mass distributions, and could be due to kinematic effects resulting
in a particularly sharp background function. After adding the histograms,
the peak is 4.7 standard deviations above a smooth hand-drawn background
(not shown in figures), and is clearly worthy of further investigation.

0.41 ($\pi\pi$)

Of all the effects seen in purely pionic mass distributions, those
around 0.41 GeV/c^2 are striking in that they appear in five distinct distribu-
tions (Fig 6.11) (the effect at 0.36 GeV/c^2 is considered to be of too low
mass to be included). One of the structures (d) is in the $\pi^+\pi^+$ mass distri-
bution which, if genuine, would imply the existence of explicitly exotic states.
The others are in $\pi^+\pi^-$ or $\pi^-\pi^0$ combinations. Only one of the states (c) occurs
in an annihilation channel, which is puzzling since one would expect that states
decaying predominantly to $\pi\pi$ would be produced most easily in annihilation
reactions. Moreover, this enhancement is at rather a high mass, as is the
one shown in Fig 6.11 (e). Omitting these two cases, the sum of the remaining
three histograms shows a prominent peak at 0.41 GeV/c^2 (not shown here) ;
however, this is an artificial selection, so it is not a fair way to judge the
significance of the effect.   Further analysis is clearly required before any-
thing definite can be said about these structures.

6.3.3 Further Investigation of a $p\bar{n}$ State at 2.02 GeV/c^2

A thorough examination of the events in the channel $\bar{p}p \rightarrow p\bar{n}\, \pi^+\pi^-\pi^-$

at 6 GeV/c has been made in order to check the peak found in the $p_f\,\bar{n}$ mass at

2.02 GeV/c^2. A rather surprising feature of this reaction is the high pro-

portion of events with a fast (triggering) proton (at least, in the sample

accepted by our apparatus) :

π^- triggers   56%

π^+ triggers   10%

p   triggers   34%

In order to check these mass assignments for the fast particles the Canute

information was examined in detail, and a portion of the events was 'choiced'

manually by considering the distribution of light in the Canute mirrors. Taking

the sample of events with a kinematic fit to this channel but which subsequently

fail to be accepted because the mass assigned to the fast particle disagrees

with Canute data, the mass distribution obtained from this sample shows no sign

of a signal at 2.02 GeV/c^2. This seems to show conclusively that the peak is

really associated with proton (or K^+) triggers.

The peak is not associated exclusively with data from one laboratory,

nor is there any multiple counting of events, so we are confident that there

is no error in the data analysis.

The most likely alternative explanation of this observation is that

the structure seen is caused by contamination from events belonging to another

channel. Therefore, the ambiguities have been considered in some detail.

The χ^2 - probability was required to be greater than 4% for all the 1C fits

examined in the baryonium search. When this cut was increased to 25%, the peak

was still present to the expected degree of significance.

By far the commonest ambiguity was with the unconstrained final state
$\pi^+\pi^+\pi^-\pi^-$ MM (where MM denotes the missing mass). Kinematically, this ambiguity
is always possible, but ionisation choicing reduces the proportion of ambiguities
to 45% for pion triggered events ; and Canute choicing reduces the proportion
to 22% for proton triggered events (it is not always possible to decide the
identity of the fast particle with Canute information). Even if the peak were
caused by Canute misidentifications, it would have to be ascribed to a new
narrow resonance at mass 2.02 GeV/c^2 decaying to π_f^+ MM. No such effect is seen
in events where this multi-pion final state is the only interpretation.

The other final states ambiguous with $p_f\bar{n}$ $\pi^+\pi^-\pi^-$ in the sample of events
used for Fig 6.8(a) are as follows, together with the numbers of events consistent
with these assignments :

p_f π^+ $\bar{p}$ π^- π^0 11 events

p_f π^+ $\bar{p}$ π^- MM   21 events

π_f^+ π^+ π^- π^- π^0 5 events

π_f^+ π^+ $\bar{p}$ π^- n   6 events

π_f^+ p π^- π^- $\bar{n}$ 1 event

In fact, out of the 185 events in the sample, 117 have a unique assignment
(the numbers given above are counted inclusively). The peak at 2.02 GeV/c^2
is still seen when only the unique events are plotted ; and it is present,
though less significant, in the ambiguous sample. Each of the above ambiguous
channels were tested by two independent methods, to see if they could account
for the narrow peak :

(i) Taking unique fits to p_f $\bar{n}$ $\pi^+\pi^-\pi^-$, the particle masses and energies were
changed to correspond to those in the supposed ambiguity (even though this usually

meant a kinematic imbalance in the energy). Appropriate effective mass

plots were then produced to look for signs of well known resonances which

could only be there if the original assignment were wrong. In particular,

the mass combination in which the 2.02 GeV/c^2 effect is seen was inspected

to see if it moved to the mass of a known resonance.

(ii) Taking unique fits to the "contamination" channels, the particle masses

and energies were changed to correspond to those in the $\bar{p}n\ \pi^+\pi^-\pi^-$ final state,

to see if a peak at 2.02 GeV/c^2 is generated in the (fast particle + neutral)

combination.

In each case, it was not possible to account for the observed enhance-

ment by any kind of known contamination. In addition to the ambiguities listed

above, the following channels were investigated in a similar way :

$$\bar{p}p \rightarrow K^+_f\ \pi^+\ K^-\ \pi^-\ MM$$

$$K^-p \rightarrow p_f\ \pi^+\ K^-\ \pi^-\ MM$$

$$K^-p \rightarrow \pi^+_f\ p\ \pi^-\ \pi^-\ MM$$

Again, there was no evidence of contamination from such events giving rise

to spurious peaks in effective mass plots. Finally, the momenta of the

particles identified as pions in the original channel are all found to be

quite low, and therefore it was generally possible to confirm the mass

assignments by ionisation data.

Properties of the Resonance

The experimental distribution of effective mass in which the $\bar{p}n$ (2.02)

resonance is seen has been fitted with a simple relativistic Breit-Wigner

function added to a background curve (see Fig 6.12). The fit was performed

by a maximum likelihood method, and a χ^2 was calculated to test the goodness-

of-fit by adding adjacent 5 MeV/c^2 bins until there were at least 5 events per
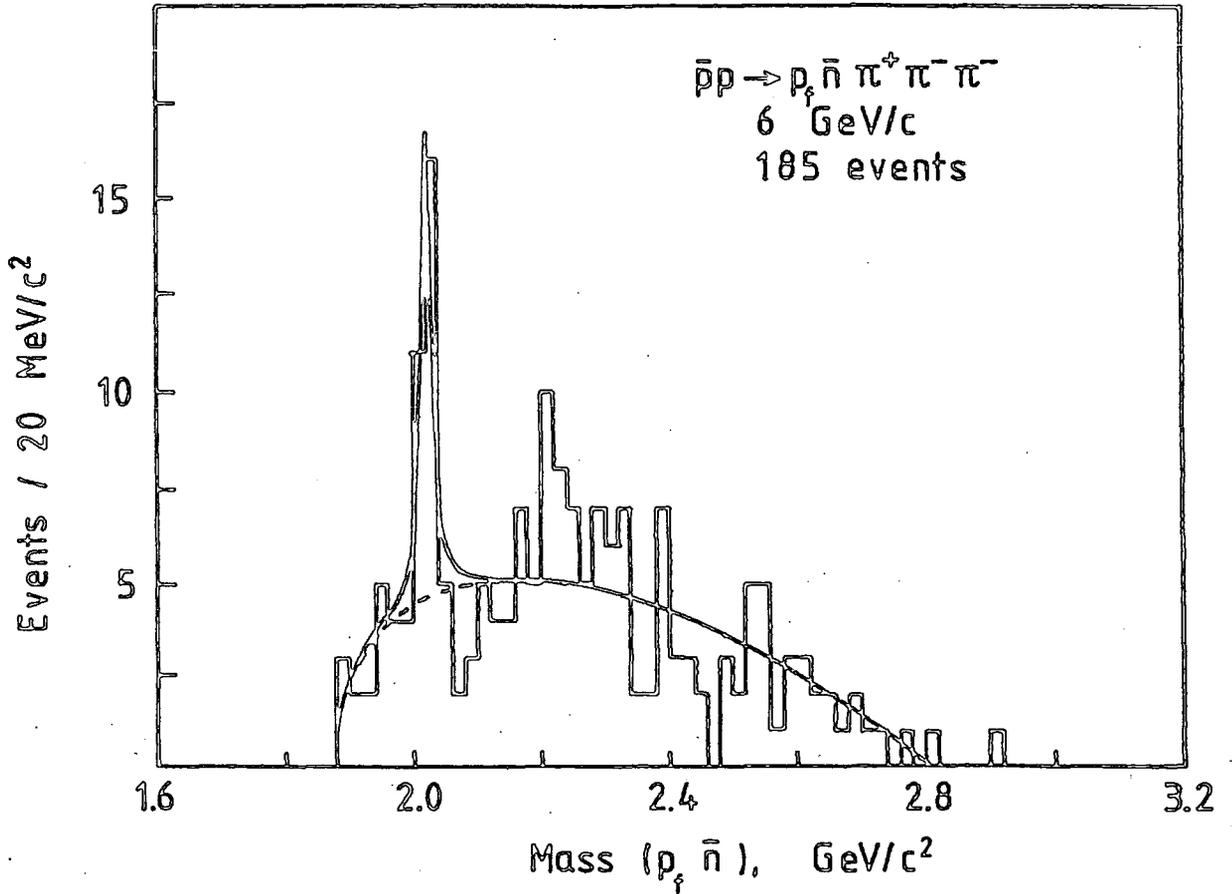
Fig. 6.12   Fit of a Breit - Wigner (solid curve) and
background (dashed curve) to the p̄n̄(2.02)
enhancement.

bin (a χ^2 was not used to obtain the fit because the bin width required would have artificially broadened the peak). The results of the fit are given in Table 6.3.

Table 6.3: Results of a fit to the $\overline{p}n$ (2.02) enhancement

Central mass (MeV/c^2)	2022.1 $\pm$ 3.8
Width, Γ (MeV/c^2)	19.6 $\pm$ 1.9
Accepted Cross-section (μb)	1.0 $\pm$ 0.25
Background parameter α	0.416
Background parameter β	0.924
χ^2 /d.f.	30.5/ 34

The width given in the table is the full width at half maximum and is consistent with the experimental resolution in this channel ($\sim$ 20 MeV/c^2). The background was represented by the function

$$y = (x - x_1)^{\alpha} (x_2 - x)^{\beta}$$

where x_1 and x_2 are the zero-points of the function, taken as the lowest and highest data values respectively. A fit was also made with just a background function and excluding events in the mass range 2.0 - 2.04 GeV/c^2. From this, the anticipated number of events in this range ($n_B \pm \sigma_B$) was determined to be 9.1 $\pm$ 0.5, which implies a signal (n_s) of 17.9 events. Hence the significance of the signal, given the null hypothesis that there is no physical effect, is

$$\frac{n_s}{\sqrt{n_B + \sigma_B^2}} = 5.9 \text{ standard deviations}$$

There are no outstanding features in the invariant mass of the $\overline{p}n$ (2.02) with any of the three pions in the final state ; nor are there any indications of resonances produced in association with this state, though the whole channel shows a little ρ^0 production in $\pi^+\pi^-$ combinations. Again, in the whole channel

(proton triggered events only), the distributions of nucleon + pion invariant mass are all peaked towards the lower mass region, though not strongly, indicating some production of Δ resonance but not especially favoured or disfavoured by events in the 2.02 peak.

Investigation of the decay angular distribution of the $\bar{p}n$ (2.02) state is severely limited by the experimental acceptance, but in a region of good acceptance, $\cos \theta_{decay} \gtrsim 0.3$, the data shows some concentration near $\cos\theta = 1$. However, there is little difference in the form of these distributions between the bin in $M(\bar{p}n)$ containing the peak and in neighbouring bands.

The distribution in momentum transfer, t, from the incident antiproton to the outgoing $\bar{p}n$ system is essentially flat up to the limit $t = -1.8$ GeV/c^2 imposed by the acceptance of the apparatus, implying a non-peripheral production mechanism. Examination of the rapidities of the $\bar{p}n$ system in comparison with the final state pions suggest that the former is produced centrally, which would support the findings of section 6.2. Clearly, the experimental acceptance removes a large fraction of events in this channel so the cross-section given in Table 6.3 is very much a lower limit ; though the selections made in data processing ensure that most events have acceptance > 65% and the events in the $\bar{p}n$ (2.02) bin do not have a particularly low acceptance. Evidently the reaction $\bar{p}p \rightarrow p_f \bar{n} \pi^+ \pi^- \pi^-$ has an unusual and interesting production mechanism. It should be added that pion triggered events from this channel show a much more peripheral behaviour than the proton triggered events.

If this effect at 2.02 GeV/c^2 is genuine, one would expect to observe it in the charge conjugate channel and other channels related by isospin, namely

$$\bar{p}p \rightarrow \pi^+_f \bar{p} n \pi^+ \pi^-$$
$$\bar{p}p \rightarrow p_f \bar{p} \pi^+ \pi^- \pi^o$$
$$\bar{p}p \rightarrow p_f \bar{p} \pi^o \pi^o \pi^o$$
$$\bar{p}n \rightarrow p_f \bar{p} \pi^+ \pi^- \pi^-$$
$$\bar{p}n \rightarrow p_f \bar{p} \pi^- \pi^o \pi^o$$

The only evidence for such an effect is the one reported in the last section, in the charge conjugate channel at 9 GeV/c. By making kinematic selections on the overlapping regions of accepted phase space between the final states $\bar{p}\,\bar{n}\,\pi^+\pi^-\pi^-$ and $\bar{p}\,n\,\pi^-\pi^+\pi^+$, it has been shown that the magnitude of the effects seen are consistent, within the very limited statistics. It therefore seems feasible to explain the non-observation of the enhancements at the other energy as due to the energy dependence of the acceptance. The formulation of a particular isospin model to account for these observations and non-observations is under way at the time of writing, and initial results are encouraging.

6.4 CONCLUSIONS

As the narrow effects reported here are still under investigation, any claim that these are baryonium resonances must be tentative, especially considering the history of previously claimed states. Nonetheless, the results are encouraging and are clearly worth serious consideration. The single most significant effect found is an enhancement in the $\bar{p}n$ mass at 2.02 GeV/c^2 in the reaction $\bar{p}p \to p_f\,\bar{n}\,\pi^+\pi^-\pi^-$ at 6 GeV/c, supported by a similar effect at the same mass in the charge-conjugate reaction at 9 GeV/c. This is at the mass of a previously found state (Ref. 1.37). The cross-section is at least 1 μb and the decay width is consistent with the experimental resolution of 20 MeV/c^2. The absence of a signal in other expected channels has yet to be explained ; but the channel with a fast proton must have an unusual mechanism in any case, and makes an interesting study of baryon-exchange.

Other prominent effects have been found at masses 1.93, 2.14, 4.00, and 0.41 GeV/c^2 for a variety of final states with a variety of fast "triggering" particles. Of these, the most promising baryonium candidate is the 1.93 ($\bar{N}N$), at the mass of the S-meson. It is interesting to note that this is seen in channels $\bar{p}p \to \bar{N}N\,\pi\pi\,\pi$, as with the 2.02 GeV/c^2 state. These could be favoured channels for central production, where the $\bar{N}N$ state is produced in the central region and the pions peripherally. Initial results from the limited sample of events in the 2.02 ($\bar{N}N$) channel vindicate this hypothesis. Additionally,

examination of mass plots made with selections to enhance centrally produced states reveal a possible effect at 1.96 GeV/c^2, and latest results are showing up yet more such states.

If central production is the dominant mechanism for baryonium production in baryon-antibaryon collisions, this is clearly of great interest and may well effect our picture of quark dynamics. Future experiments should be able to confirm this. Results of the investigations into the four pion final state suggest that central production is important even for "normal" non-exotic meson resonances.

APPENDIX A   CALCULATION OF VERTEX AND MOMENTUM BY THE ALGORITHM

Referring to figure 2.8, the simplifying assumptions are:

(i)   Magnetic field B is a function of X only in the region of the BC and downstream detectors.

(ii) Neglect B_Y and B_X, hence $B \equiv B_Z(X)$

(iii) Momentum in the Y-X plane, $P_T \sim P$

(iv) Small angle approximations, e.g. $\tan\theta \sim \theta$, $\cos\theta \sim 1$.

Then, for any two points A and B on the outgoing or beam track,

$$Y_B - Y_A \sim \int_{X_A}^{X_B} \theta(X)\ dX$$

where θ is the angle in the Y-X plane, measured from the X-axis, and is given by

$$\theta(X) \sim \theta_A + \int_{X_A}^{X} \frac{dX'}{R(X')}$$

with radius of curvature, R(X') given by

$$R(X') = \frac{P}{0.3\ B(X')}$$

for p in MeV/c, B(X') in kgauss, and R(X') in cm.

Hence,

$$Y_B - Y_A = \theta_A (X_B - X_A) + \frac{0.3}{p} \int_{X_A}^{X_B} \left[\int_{X_A}^{X} B(X') \, dX' \right] dX$$

This can be abbreviated to

$$\Delta Y_{AB} = \theta_A \Delta X_{AB} + I_{AB}/p \tag{A.1}$$

where I_{AB} is the double field integral:

$$I_{AB} = 0.3 \int_{X_A}^{X_B} \left[\int_{X_A}^{X} B(X') \, dX' \right] dX$$

Denoting the beam momentum p and the outgoing track momentum p', we have (ignoring PWC β for the moment).

$$\Delta Y_{12} = \theta_1 \Delta X_{12} + I_{12}/p$$

$$\Delta Y_{1V} = \theta_1 \Delta X_{1V} + I_{1V}/p$$

$$\Delta Y_{V\alpha} = \theta_V \Delta X_{V\alpha} + I_{V\alpha}/p'$$

$$\Delta Y_{V\gamma} = \theta_V \delta X_{V\gamma} + I_{V\gamma}/p'$$

Eliminating θ_1 and θ_V from these equations gives

$$\Delta Y_{12} \Delta X_{1V} - \Delta Y_{1V} \Delta X_{12} = (I_{12} \Delta X_{1V} - I_{1V} \Delta X_{12})/p$$

$$\tag{A.2}$$

$$\Delta Y_{V\alpha} \Delta X_{V\gamma} - \Delta Y_{V\gamma} \Delta X_{V\alpha} = (I_{V\alpha} \Delta X_{V\gamma} - I_{V\gamma} \Delta X_{V\alpha})/p'$$

In principle, equations (A.2) could be used to solve for p' (by eliminating Y_V); but this would require accurate knowledge of the relative origins of the Y planes and of the BC field, and it would involve large numbers which are difficult to handle on a 16-bit computer.

Therefore, non-interacting beam tracks were used to calibrate the system. At the beginning of each new run, a calibration program was run on the NOVA computer which took data from non-interacting beam tracks and found average values of the "offsets" i.e. ΔY^b_{12}, $\Delta Y^b_{\alpha\gamma}$, $\Delta Z^b_{\alpha\beta}$ etc...

Here, superscript b refers to a typical or average beam track. Hence we may define quantities such as

$$\delta Y_{12} \quad = \quad \Delta Y_{12} \quad - \quad \Delta Y^b_{12}$$

Hence, subtracting equations (A.2) for a typical beam track from those for an actual interacting track, we have:

$$\delta Y_{12} \, \Delta X_{1V} - \delta Y_{1V} \, \Delta X_{12} = 0$$

$$\delta Y_{V\alpha} \, \Delta X_{V\gamma} - \delta Y_{V\gamma} \, \Delta X_{V\alpha} = F_{\alpha\gamma} \, (X_V) \, \left(\frac{1}{p'} - \frac{1}{p} \right)$$

$$\left. \right\} \quad \text{(A.3)}$$

where $F_{\alpha\gamma} \, (X_V) = I_{V\alpha} \, \Delta X_{V\gamma} - I_{V\gamma} \, \Delta X_{V\alpha}$

and we have chosen X_V to be in the same place for the two tracks. In the experiment the beam was focussed to be accurately parallel in travelling through the SHF, therefore

$$\delta Y_{12} \quad = \quad \delta Y_{1V} \quad = \quad 0$$

$$\delta Y_{V\gamma} \quad = \quad \delta Y_{2\gamma}$$

$$\delta Y_{V\alpha} \quad = \quad \delta Y_{2\gamma} \quad - \quad \delta Y_{\alpha\gamma}$$

$$\left. \right\} \quad \text{(A.4)}$$

Hence, equations (A.3) simplify to

$$\delta Y_{2\gamma} \ \Delta X_{\alpha\gamma} - \delta Y_{\alpha\gamma} \ \Delta X_{V\gamma} \ = \ F_{\alpha\gamma} \ (X_V) \ \left(\frac{1}{p'} - \frac{1}{p} \right) \qquad (A.5)$$

A similar equation may be written for Z, putting $F_{\alpha\gamma} (X_V) = 0$:

$$\delta Z_{2\gamma} \ \Delta X_{\alpha\gamma} - \delta Z_{\alpha\gamma} \ \Delta X_{V\gamma} \ = \ 0 \qquad (A.6)$$

Equations (A.5) and (A.6) were used in the algorithm to determine X_V (if the dip was large enough) and p', using only the hits in PWC2 and two of the downstream chambers. $F_{\alpha\gamma} (X_V)$ was available as a table, obtained from a map of the magnetic field. Similar equations may be written using the other two pairs of downstream PWC's i.e. $\beta\gamma$ and $\alpha\beta$

APPENDIX B.   PREDICTION OF PULSE HEIGHTS IN CANUTE

Cerenkov radiation is emitted along a cone at an angle θ_c to the particle direction given by

$$\cos \theta_c = \frac{1}{\beta n}$$

Since β (the velocity /c) and n (the refractive index) are both close to unity, this is better expressed by

$$\sin^2 \theta_c = \frac{1}{n^2} \left(2\varepsilon + \varepsilon^2 - \frac{m^2}{p^2} \right) \tag{B.1}$$

where m and p are the particle's mass and momentum respectively, and $\varepsilon = n-1$. Thus, a light spot of radius $R = L \tan \theta_c$ falls on the mirrors, L being the radiator length which is assumed constant (= 218.7 cm) since all tracks are at small angles to the mirror normals. The maximum value of R (for p >> m and pressure = 4 atm) is 20.3 cm, and the mirrors are 55 cm x 70 cm, so the light is always shared by 1, 2, 3, or 4 mirrors. The light falling on an annulus of given width is independent of its radius (fig. B.1), and so the light intensity of the spot varies as 1/r out to the edge of the spot. Using the co-ordinates of the intercept of each track with the mirror plane, and the radius R, a geometrical calculation yields the fractions f_i in each mirror.
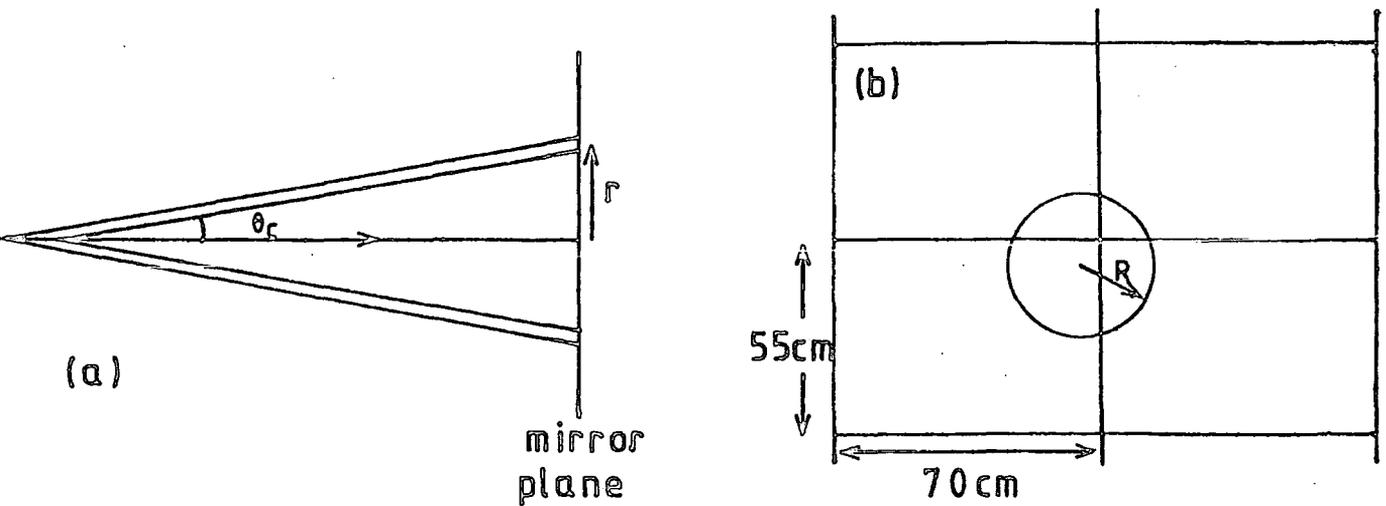
Fig. B.1 Diagrams showing (a) A Cerenkov light cone intercepting the mirror plane.

(b) A typical four-way split.

The number of photons emitted per cm of pathlength is given by (see, for example, ref. B.1)

$$\frac{dN_p}{dl} = \frac{2\pi\alpha}{c} \int \left(1 - \frac{1}{\beta^2 n^2}\right) d\nu$$

where the integral is over the frequency range ν for which $\beta n > 1$. Over the bandwidth of the photomultiplier n is practically constant and we can write for the total number of photons detected.

$$N_p = 2\pi\alpha L \sin^2\theta_c \left(\frac{1}{\lambda_2} - \frac{1}{\lambda_1}\right) \tag{B.2}$$

where λ_1 and λ_2 are the wavelength limits of the photomultiplier response (typically 400 to 600 nm). The average number of photoelectrons produced at the cathode is

$$N_e = \xi \eta N_p \tag{B.3}$$

where ξ is the light collection efficiency ($\sim$1) and η is the average quantum conversion efficiency (5- 10%). The actual number of photo-electrons varies statistica lly and follows approximately a Poisson distribution with standard deviation $\sqrt{N_e}$. Thus the pulse height in mirror i with gain A_i and fraction of light f_i is

$$A_i \, f_i \, N_e \quad \overset{+}{-} \quad A_i \, \sqrt{f_i \, N_e} \tag{B.4}$$

The factors in equations B.2 and B.3 are not all accurately known and ca n be combined into a single factor F:

$$N_e \quad = \quad F \sin^2 \theta_c \tag{B.5}$$

F has been determined empirically to be 7945 by accumulating the pulse height spectrum from beam particles of known momentum. N_e is then the square of the ratio of the mean to the standard deviation, and $\sin^2 \theta_c$ is given by equation B.1

APPENDIX C

APPLICATION OF MAXIMUM LIKELIHOOD FITTING TO AN AMPLITUDE

MODEL OF THE FOUR PION FINAL STATE IN A LIMITED REGION OF

PHASE SPACE

The number of events N of a process described by amplitude T is

$$N = A \int |T|^2 \, d\text{Lips} \tag{C.1}$$

where A is a constant for the experiment and dLips is an element of Lorentz invariant phase space.

The likelihood function L is defined as

$$L = \prod_i P_i \tag{C.2}$$

where P_i is the probability per unit volume of phase space of the i'th event according to the proposed amplitude. For a four body final state there are seven independent variables x_1, $x_2 \ldots x_7$ needed to define the event kinematically, so the normalisation condition is

$$\int P \, dx_1 \ldots dx_7 = 1$$

Hence we may write

$$P_i \, dx_1 \ldots dx_7 = \frac{A}{N} |T_i|^2 \, d\text{Lips} \tag{C.3}$$

Now, if the amplitude T_i can be expressed as the incoherent sum of a number of sub-processes, we have

$$|T_i|^2 = \sum_k |T_{ik}|^2 \tag{C.4}$$

where T_{ik} is the amplitude for the i'th event according to the k'th process, normalised in the same way as (C.1)

i.e. $N_k = A \displaystyle\int |T_k|^2 \, dLips$

Hence we have for the fraction a_k of process k

$$a_k = \frac{N_k}{N} = \frac{A}{N} \int |T_k|^2 \, dLips$$

Now, from (C.3) and (C.4),

$$P_i = \sum_k \frac{A}{N} |T_{ik}|^2 \frac{dLips}{dx_1 \ldots dx_7}$$

$$= \sum_k \frac{a_k |T_{ik}|^2}{\int |T_k|^2 \, dLips} \frac{dLips}{dx_1 \ldots dx_7}$$

The square of the amplitudes $|T_{ik}|^2$ are proportional to the unnormalised functions F_{ik} listed in Table C.1. To find the integrals of these functions over phase space, Monte-Carlo events were generated using program FOWL (ref. 5.47). In this way the unnormalised sums I_k were found for each process :

$$I_k = \sum_j F_{jk} \, w_j \tag{C.5}$$

where w_j is the phase space weight for the j'th event generated.

Hence

$$P_i = \sum_k \frac{a_k F_{ik}}{I_k} \text{ constant } \frac{dLips}{dx_1 \ldots dx_7}$$

Now, the constant factor and the phase space differential do not depend on the parameters of the fit (such as the slopes of the t-distributions or the density matrix elements), so we can write from (C.2)

$$\log L = \sum_{i} \log \left\{ \sum_{k} \frac{a_k F_{ik}}{I_k} \right\} + \text{constant} \qquad \text{(C.6)}$$

and the constant can be ignored.

Correcting for Acceptance

Since only events within a certain region R of phase space are accepted, the fractions a_k can only refer to that region, and the phase space integrals I_k must be determined by only selecting Monte-Carlo events within the same region. Furthermore, the real events have an acceptance weight u_i representing the effective number of events that would have been obtained in an untriggered experiment, at the same point in phase space.

Hence, we modify (C.6) thus :-

$$\log L = \sum_{i} u_i \log \left\{ \sum_{k} \frac{a_k^R F_{ik}}{I_k^R} \right\} + \text{const.} \qquad \text{(C.7)}$$

Constraints on the Fractions

Equation (C.7) was used to determine log L for each set of parameter values which were varied until log L reached a maximum (using program MINUI, ref.5.46). However, not all the fractions a_k^R were varied independently. The overall constraint is

$$\sum_{k} a_k^R = 1. \qquad \text{(C.8)}$$

Furthermore, some processes have the same form of amplitude (e.g. those

related by charge conjugation - see section 5.4.2). For these, we have the constraint

$$\frac{a^R_{k1}}{I_{k1}} = \frac{a^R_{k2}}{I_{k2}} \qquad (C.9)$$

which ensures that the functions F_{k1} and F_{k2} can be added directly, giving an overall amplitude that does not depend on which of the two processes is the correct interpretation.

Extending the Model to the Whole of Phase Space

If the model is applicable in the whole of phase space, W, we can predict the fraction B_k of events which are within the restricted region R, for each process k :-

$$B_k = \frac{N^R_k}{N^W_k} = \frac{\int_R |T_k|^2 \, dLips}{\int_W |T_k|^2 \, dLips} = \frac{I^R_k}{I^W_k} \qquad (C.10)$$

which is easily found because Monte-Carlo events may be generated over the whole of phase space.

Now, the fraction a^W_k of events of process k for the whole of phase space is

$$a^W_k = \frac{N^W_k}{N^W} \qquad \text{with} \qquad \sum_k a^W_k = 1$$

where N^W is the predicted number of events in the whole channel for an untriggered experiment of the same sensitivity,

Similarly,

$$a_k^R = \frac{N_k^R}{N^R}$$

where $N^R = \sum_i u_i$ is the effective number of events in the restricted region.

It is then easy to obtain from equation (C.10) expressions for a_k^W and N^W :-

$$a_k^W = \frac{a_k^R/B_k}{\sum_k a_k^R/B_k} \qquad (C.11)$$

$$N^W = N^R \sum_k a_k^R/B_k \qquad (C.12)$$

Description of the Functions

The complete set of Bose-symmetrised functions F_k are listed in Table C.1. The notation used is as follows.

Let the numbers 1,2 refer to the two π^+ 's

and 3,4 refer to the two π^- 's

then the vertex factors are represented by

$$v_{LP}^1 = \exp(b_{LP} \, t_p \rightarrow \pi_1)$$

$$v_{LP}^2 = \exp(b_{LP} \, t_p \rightarrow \pi_2)$$

$$v_{LP}^3 = \exp(b_{LP} \, t_p^- \rightarrow \pi_3)$$

$$v_{LP}^4 = \exp(b_{LP} \, t_p^- \rightarrow \pi_4)$$

$$v_{AP}^{1,3} = \exp(b_{AP} \, t_p^- \rightarrow \pi_1 \pi_3)$$

$$v_{AP}^{1,4} = \exp(b_{AP} \, t_p^- \rightarrow \pi_1 \pi_4)$$

$$v_{AP}^{2,3} = \exp(b_{AP} \, t_p^- \rightarrow \pi_2 \pi_3)$$

$$v_{AP}^{2,4} = \exp(b_{AP} \, t_p^- \rightarrow \pi_2, \pi_4)$$

Note that the first two are at the proton vertex ; the rest are at the antiproton vertex. The abbreviations LP and AP refer to the kind of model being described and are defined in section 5.4.1. They are chosen here to illustrate the notation.

The resonance decays are denoted thus :

$$\rho_{AP}^{1,3} = BW\ (\ \rho;\ \pi_1,\ \pi_3)\ W_{AP}\ (\rho;\ \pi_1,\ \pi_3)$$

$$f_{AP}^{1,3} = BW\ (f\ ;\ \pi_1,\ \pi_3)\ W_{AP}\ (f\ ;\ \pi_1,\ \pi_3)$$

and so on for the other combinations. Here $BW(R\ ;\ \pi_1,\ \pi_3)$ is the Breit-Wigner expression in terms of the given dipion mass and the central mass and width of the resonance R. $W(R\ ;\ \pi_1,\ \pi_3)$ is the angular distribution of the π^+ in the rest frame of the resonance, using the s-channel helicity frame. In this frame, the z-axis is defined as the direction of the resonance in the overall CM system. Then,

$$\hat{\underline{y}} = \underline{\hat{p}} \wedge \hat{\underline{z}}$$

$$\hat{\underline{x}} = \hat{\underline{y}} \wedge \hat{\underline{z}}$$

$$\cos \Theta_\pi = \hat{\underline{z}} \cdot \hat{\underline{\pi}}$$

$$\cos \phi_\pi = \hat{\underline{x}} \cdot \hat{\underline{\pi}} / \sin \Theta_\pi$$

where the $\bar{p}$ and π vectors are taken to be in the rest frame of the resonance. This enables $W(R\ ;\ \pi^+,\ \pi^-)$ to be expressed in terms of the density matrix elements, d_{mn}. If we assume the off-diagonal elements to be zero, there is no ϕ dependence, and we have

$$W(\cos \Theta) = d_{11} + (1 - 3\ d_{11})\ \cos^2\Theta \quad \text{for the } \rho$$
$$\text{(spin 1)}$$

and $\quad W(\cos \theta) = 1 - 2d_{11} + d_{22} + 6(d_{22} + 4d_{11} - 1) \cos^2 \theta$

$$+ 3(3 - 5d_{22} - 10d_{11}) \cos^4 \theta \quad \text{for the f} \\ \text{(spin 2)}$$

The Hermiticity condition requires that the elements d_{mm} are real, and the trace and parity conditions are

$$\sum_m d_{mm} = 1$$

$$d_{-m-m} = d_{mm}$$

TABLE C.1: Functions used in the Amplitude Model

(Refer to figure 5.9)

(a) $\quad F = 1$

(b) $\quad F = \rho_{AP}^{1,3}\,\rho_{AP}^{2,4}\,(V_{AP}^{1,3} + V_{AP}^{2,4}) + \rho_{AP}^{1,4}\,\rho_{AP}^{2,3}\,(V_{AP}^{1,4} + V_{AP}^{2,3})$

(c) $\quad F = f_{AP}^{1,3}\,f_{AP}^{2,4}\,(V_{AP}^{1,3} + V_{AP}^{2,4}) + f_{AP}^{1,4}\,f_{AP}^{2,3}\,(V_{AP}^{1,4} + V_{AP}^{2,3})$

(d) $\quad F = \rho_{AP}^{1,3}\,f_{AP}^{2,4}\,V_{AP}^{1,3}\quad \rho_{AP}^{1,4}\,f_{AP}^{2,3}\,V_{AP}^{1,4}$

$\qquad\qquad + \rho_{AP}^{2,3}\,f_{AP}^{1,4}\,V_{AP}^{2,3} + \rho_{AP}^{2,4}\,f_{AP}^{1,3}\,V_{AP}^{2,4}$

(e) $\quad F = f_{AP}^{1,3}\,\rho_{AP}^{2,4}\,V_{AP}^{1,3} + f_{AP}^{1,4}\,\rho_{AP}^{2,3}\,V_{AP}^{1,4}$

$\qquad\qquad + f_{AP}^{2,3}\,\rho_{AP}^{1,4}\,V_{AP}^{2,3} + f_{AP}^{2,4}\,\rho_{AP}^{1,3}\,V_{AP}^{2,4}$

(f) $\quad F = (\rho_{LP}^{1,3} + \rho_{LP}^{2,3})V_{LP} + (\rho_{LP}^{1,4} + \rho_{LP}^{2,4})\;V_{LP}^{3}$

(g) $\quad F = (f_{LP}^{1,3} + f_{LP}^{2,3})\;V_{LP}^{4} + (f_{LP}^{1,4} + f_{LP}^{2,4})\;V_{LP}^{3}$

(h) $\quad F = (\rho_{LP}^{1,3} + \rho_{LP}^{1,4})\;V_{LP}^{2} + (\rho_{LP}^{2,3} + \rho_{LP}^{2,4})\;V_{LP}^{1}$

(i) $\quad F = (f_{LP}^{1,3} + f_{LP}^{1,4})\;V_{LP}^{2} + (f_{LP}^{2,3} + f_{LP}^{2,4})\;V_{LP}^{1}$

(j) $\quad F = \rho_{DP}^{1,3}\,V_{DP}^{2}\,V_{DP}^{4} + \rho_{DP}^{1,4}\,V_{DP}^{2}\,V_{DP}^{3} + \rho_{DP}^{2,3}\,V_{DP}^{1}\,V_{DP}^{4} + \rho_{DP}^{2,4}\,V_{DP}^{1}\,V_{DP}^{3}$

(k) $\quad F = \rho_{DP}^{1,3}\,V_{DP}^{1,3}V_{DP}^{2} + \rho_{DP}^{1,4}\,V_{DP}^{1,4}V_{DP}^{2} + \rho_{DP}^{2,3}\,V_{DP}^{2,3}V_{DP}^{1} + \rho_{DP}^{2,4}\,V_{DP}^{2,4}V_{DP}^{1}$

(l) $\quad F = \rho_{DP}^{1,3}\,V_{DP}^{2,4}V_{DP}^{4} + \rho_{DP}^{1,4}\,V_{DP}^{2,3}V_{DP}^{3} + \rho_{DP}^{2,3}\,V_{DP}^{1,4}V_{DP}^{4} + \rho_{DP}^{2,4}\,V_{DP}^{1,3}V_{DP}^{3}$

(m) $\quad F = f_{DP}^{1,3}\,V_{DP}^{2}\,V_{DP}^{4} + f_{DP}^{1,4}\,V_{DP}^{2}\,V_{DP}^{3} + f_{DP}^{2,3}\,V_{DP}^{1}\,V_{DP}^{4} + f_{DP}^{2,4}\,V_{DP}^{1}\,V_{DP}^{3}$

(n) $\quad F \quad = \quad f_{DP}^{1,3} \, v_{DP}^{1,3} \, v_{DP}^{2} \quad + \quad f_{DP}^{1,4} \, v_{DP}^{1,4} \, v_{DP}^{2} \quad + \quad f_{DP}^{2,3} \, v_{DP}^{2,3} \, v_{DP}^{1} \quad + \quad f_{DP}^{2,4} \, v_{DP}^{2,4} v_{DP}^{1}$

(o) $\quad F \quad = \quad f_{DP}^{1,3} \, v_{DP}^{2,4} \, v_{DP}^{4} \quad + \quad f_{DP}^{1,4} \, v_{DP}^{2,3} \, v_{DP}^{3} \quad + \quad f_{DP}^{2,3} \, v_{DP}^{1,4} \, v_{DP}^{4} \quad + \quad f_{DP}^{2,4} \, v_{DP}^{1,3} v_{DP}^{3}$

REFERENCES

Chapter 1

1.1 L. Montanet, G. C. Rossi and G. Veneziano, Phys. Reports C 63 (1980) 149.

1.2 J. L. Rosner, Phys. Rev. Lett. 21 (1968) 950.

1.3 H. Harari, Phys. Rev. Lett. 22 (1969) 562.

1.4 O. D. Dalkarov et al, Nucl. Phys. B21 (1970) 88.

1.5 L. N. Bogdanova et al, Ann. Phys. 84 (1974) 261.

1.6 I. S. Shapiro, Phys. Rep. C35 (1978) 129.

1.7 G. F. Chew, 3rd European Symp. on antinucleon-nucleon interactions, Stockholm, July 1976.

1.8 M. R. Pennington, Nucl. Phys. B137 (1978) 77.

1.9 P. G. O. Freund, R. Waltz, and J. L. Rosner, Nucl. Phys. B13 (1969) 237.

1.10 P. Hasenfratz and J. Kuti, Phys. Rep. C40 (1978) 164-167.

1.11 R. L. Jaffe, Phys. Rev. D17 (1978) 1444.

1.12 M. Imachi, S. Otsuki, F. Toyoda, Prog. Theor. Phys. 57 (1977) 517.

1.13 G. C. Rossi and G. Veneziano, Nucl. Phys. B123 (1977) 507.

1.14 Chan Hong-Mo and H. Hogaasen, Phys. Lett. 72B (1977) 121.
     Chan Hong-Mo and H. Hogaasen, Nucl. Phys. B136 (1978) 401.

1.15 B. R. Karlsson and B. Kerbikov, Nucl. Phys. B141 (1978) 241.

1.16 B. Pietrzyk, 5th European Symposium on Nucleon-Antinucleon Inter-actions, Bressanone (Italy), June 1980.

1.17 I. M. Barbour and D. K. Ponting, Z. Phys. C5 (1980) 221.

1.18 A. S. Carroll, et al, Phys. Rev. Lett. 32 (1974) 247.

1.19 T. E. Kalogeropoulos and G. S. Tzanakos, Phys. Rev. Lett. 34 (1975) 1047.

1.20 Ch. d'Andlau et al, Phys. Lett. 58B (1975) 223.

1.21 V. Chapoupka et al, Phys. Lett. 61B (1976) 487.

1.22 W. Bruckner et al, Phys. Lett. 67B (1977) 222.

1.23 S. Sakamoto et al, Nucl. Phys. B 158 (1979) 410.

1.24 M. Alston-Garnjost et al, Phys. Rev. Lett. 35 (1975) 1685.

1.25 M. Alston-Garnjost, et al, Phys. Rev. Lett. 43 (1979) 1901.

1.26 R. P. Hamilton et al, Phys. Rev. Lett. 44 (1980) 1179.

1.27 R. P. Hamilton et al, Phys. Rev. Lett, 44 (1980) 1182.

1.28 T. Kamae et al, Phys. Rev. Lett. 44 (1980) 1439.

1.29 E. Jastrzembski et al, 5th European Symposium on Nucleon-Antinucleon Interactions, Bressanone (Italy), June 1980.

1.30 C. Defoix et al, Nucl. Phys. B162 (1980) 12.

1.31 E. Eisenhandler et al, Nucl. Phys. B113 (1976) 1.

1.32 C. Daum et al, Phys. Lett. 90B (1980) 475.

1.33 C. Daum et al, Phys. Lett. 100B (1981) 439.

1.34 S. Kooijman et al, Phys. Rev. Lett. 45 (1980) 316.

1.35 R. M. Bionta et al, Phys. Rev. Lett. 45 (1980) 1990.

1.36 D. Aston et al, Phys. Lett. 93B (1980), 517.

1.37 P. Benkheiri et al, Phys. Lett. 68B (1977) 483.

1.38 P. Benkheiri et al, Phys. Lett. 81B (1979) 380.

1.39 M. R. Pennington, CERN/EP/PHYS 78-44.

1.40 S. U. Chung et al, Phys. Rev. Lett. 45 (1980) 1611.

1.41 A. S. Carroll et al, Phys. Rev. Lett. 44 (1980) 1572.

1.42 C. Evangelista et al, Nucl. Phys. B184 (1981) 189.

1.43 B. G. Gibbard, et al, Phys. Rev. Lett. 42 (1979) 1593.

1.44 D. R. Green, 4th European Antiproton symposium, Barr (Strasbourg), June 1978.

1.45 A. D. J. Banks, et al. Phys. Lett. 100B (1981) 191.

1.46 R. M. Bionta, et al, Phys. Rev. Lett. 44 (1980) 909.
     D. R. Green, 6th International Conference on Experimental Meson Spectroscopy, Upton (New York), April 1980 (A.I.P. report).

1.47 A. E. Kreymer, et al, Phys. Rev. D22 (1980) 36.

1.48 H. Braun, et al, Phys. Lett. 60B (1976) 481.

1.49 M. Baubillier et al, Nucl. Phys. B183 (1981) 1.

1.50 W. E. Cleland et al, Phys. Lett. 89B (1979) 290.
     W. E. Cleland et al, Nucl. Phys. B184 (1981) 1.

References (Cont.)

1.51 A. Apostolakis, et al, Phys. Lett. 66B (1977) 185.
     G. W. van Apeldoorn et al, Phys. Lett. 72B (1978) No. 4.

1.52 C. Evangelista et al, Phys. Lett. 72B (1977) 139.
     T. A. Armstrong et al, Phys. Lett. 85B (1979) 304.

1.53 T. A. Armstrong, et al, Phys. Lett. 77B (1978) 447.
     D. Frame et al, Phys. Lett. 107B (1981) 301.

1.54 C. Evangelista, et al, Nucl. Phys. B153 (1979) 253.

1.55 R. V. Gavai and D. P. Roy, Phys. Lett. 88B (1979) 359.

CHAPTER 2

2.1 G. Hall, New Scientist, 20 July 1978, p. 189

2.2 J. Ballam and R. D. Watt, Ann. Rev. Nucl. Science 27 (1977) 75.

2.3 R. C. Field, SHF Note 67 (SLAC internal note).

2.4 T. M. Fieuguth and R. A. Gearhart, SLAC-PUB-1552, March 1975.

CHAPTER 3

3.1 CERN Hydra Application Library : GEOMPAM long write-up.

3.2 Rutherford Laboratory Kinematics Program Manual.

3.3 G. B. Bowden, R. C. Field, R. A. Lewis, C. T. Hoard, K. Skarpaas,
    P. Baker; Nucl. Instr. Meth. 138 (1976) 77-83.

CHAPTER 4

4.1 A. White, private communication.

4.2 Four-prong data kindly supplied by Dr. H. W. Atherton.

4.3 Data kindly supplied by Dr. G. Warren.

4.4 P. S. Gregory et al, Nucl. Phys. B119 (1977) 60.

4.5 H. W. Atherton, et al, Nucl. Phys. B113 (1976) 378 and Nucl. Phys.
    B103 (1976) 381.

4.6 G. Warren et al, Nucl. Phys. B130 (1977) 367.

4.7 H. Wald, Ph.D. thesis (Ch. 10), University of Tufts, Mass.

4.8 P. S. Gregory et al, Nucl. Phys. B78 (1974) 222.

REFERENCES (Cont.)

4.9   J. G. Rushbrooke and B. R. Webber, Phys. Reports 44 (1978) 55-66 or
      P. D. Gall, DESY report Fl - 76/02.

4.10 Chyla, Ph.D. thesis (1977), University of Prague.

4.11 R. Hagedorn, Nuovo Cim., Suppl. 3 (1965) 147.

4.12 T. F. Hoang, Nucl. Phys. B38 (1972) 333.

4.13 T. F. Hoang, Phys. Rev. D6, No. 5, p. 1328 (1972).

4.14 T. F. Hoang, D. Rhines, and W. A. Cooper, Phys. Rev. Lett. 27 (1971)
      1681.

4.15 G. W. van Apeldoorn et al, Zeit, Phys. C7 (1981) 235.

4.16 H. Braun et al, Phys. Rev. D20 (1979) 587 and H. Braun et al,
      Strasbourg preprint CRN/HE 80-12.

CHAPTER 5

5.1   D. R. Ward, 5th European Symposium on $N\bar{N}$ interactions, Bressanone
      (Italy), June 1980.

5.2   T.Fields and C. K. Chen, 3rd European Symposium on $N\bar{N}$ interactions,
      Stockholm, July 1976.

5.3   K. P. Das and R. C. Hwa, Phys. Lett 68B (1977) 459.

5.4   H. Goldberg, Phys. Rev. D.6 (1972) 2542.

5.5   C. J. Hamer, Nuovo Cimento 12A (1972) 162.

5.6   S. J. Orfanidis and V. Rittenberg, Nucl. Phys. B.59 (1973) 570.

5.7   R. Stenbacka et al. Nuovo Cimento 51A (1979) 63.

5.8   Chan-Hong Mo, J. Loskiewicz and W. W. M. Allison, Nuovo Cimento, 57A
      (1968) 93.

5.9   H. Miettinen, 3rd European Symposium on $N\bar{N}$ interactions, Stockholm,
      July 1976.

5.10 G. Warren et al, Nucl. Phys. B97 (1975) 381.

5.11 H. Braun, et al, Phys. Rev. D15 (1977) 1293.

5.12 D. R. Ward, et al, Nucl. Phys. B172 (1980) 302.

5.13 D. Everett, et al, Nucl. Phys. B73 (1974) 440.

5.14 A. Accensi et al, Phys. Lett. 20 (1966) 557.

REFERENCES (Cont.)

5.15   H. W. Atherton, et al, Nucl. Phys. B113 (1976) 378.

5.16   R. A. Donald, et al, Nucl. Phys. B6 (1968) 174.

5.17   J. Clayton, et al, Nucl. Phys. B22 (1970) 85.

5.18   D. Everett, et al, Nucl. Phys. B92 (1975) 78.

5.19   G. Warren, et al, Nucl. Phys. B130 (1977) 367.

5.20   R. Stenbacka, et al, Zeit. fur Phys. C4 (1980) 323.

5.21   Ch. De la Vaissiere, Nuovo Cim. 11A (1972) 185.

5.22   J. Debray et al, Nucl. Phys. B62 (1973) 13.

5.23   Ch. De la Vaissiere, Nuovo. Cim. 19A (1974) 118.

5.24   Ch. De la Vaissiere, Proceedings of the International Symposium on
       $\bar{p}p$ Interactions, Loma-Koli (Finland), June 1975.

5.25   G. Ranft, Nuovo Cim. 58A (1968) 425.

5.26   A. G. Frodesen, et al, Nucl. Phys. B18 (1970) 45.

5.27   C. Baltay, et al, Phys. Rev. 145 (1966) 1103.

5.28   J. Diaz et al, Nucl. Phys. B16 (1970) 239.

5.29   Z. Ming. et al, Nucl. Phys. B51 (1973) 77.

5.30   J. W. Chapman, et al, Nucl. Phys. B24 (1970) 445.

5.31   J. Davidson et al, Phys. Rev. D9 (1974) 77.

5.32   R. R. Burns, et al, Nucl. Phys. B27 (1971) 109.

5.33   R. R. Burns, et al, Phys. Rev. D7 (1973) 1310.

5.34   R. R. Burns, et al, Nucl. Phys. B73 (1974) 219.

5.35   T. Handler, et al, Nucl. Phys. B101 (1975) 35.

5.36   W. W. M. Allison, et al, Phys. Rev. Lett 24 (1970) 618.

5.37   T. Fields, et al, Phys. Rev. Lett 27 (1971) 1749.

5.38   G. W. Apeldoorn, et al, Nucl. Phys. B133 (1978) 245.

5.39   D. S. Rhines, Ph.D. Thesis, ANL/HEP 7146, December 1971.

5.40   'Review of Particle Properties' Rev. Mod. Phys. 52 (1980) No. 2.

5.41   T. Fields and R. Singer, 4th International Symposium on $\overline{NN}$ Interactions,
       Syracuse (New York), May 1975 (Vol. 2).

REFERENCES (Cont.)

5.42 R. Weill, et al, 4th European Antiproton Symposium, Barr (Strasbourg),
      June 1978, p. 147.

5.43 J. D. Jackson, Nuovo Cim. 34 (1964) 1644. R. D. Tripp, "Baryon
      Resonances", CERN Yellow Report 65-7.

5.44 L. Van Hove, Nucl. Phys. B9 (1969) 331.

5.45 F. T. Dao, et al, PEPR Programming note, Physics No. 101, (1971)
      M.I.T.

5.46 F. James and M. Roos, MINUIT Long Write-up, CERN Computer Centre
      Program Library.

5.47 F. James, FOWL Long Write-up, CERN Computer Centre Program Library.

5.48 Y. Oren, et al, Nucl. Phys. B71 (1974) 189.

CHAPTER 6

6.1   Figures kindly supplied by G. Gopal

6.2   R.L. Sekulin, Internal BC68 note

6.3   J.J. Dumont, Internal BC68 note

APPENDIX B

B.1   J.V. Jelley, "Cerenkov Radiation and its applications", Pergamon
      Press.

ACKNOWLEDGEMENTS